

FIRST MEASUREMENTS OF COSMIC RAY COMPOSITION FROM 1-50 PEV USING NEW  
TECHNIQUES ON COINCIDENT DATA FROM THE ICECUBE NEUTRINO OBSERVATORY

*by*

KAREN GRACE ANDEEN

A dissertation submitted in partial fulfillment of the  
requirements for the degree of

DOCTOR OF PHILOSOPHY  
(PHYSICS)

*at the*

UNIVERSITY OF WISCONSIN – MADISON

2011

© 2011 Karen Grace Andeen

All Rights Reserved

*I dedicate this work to Gen 3  
in loving memory of Gen 1  
who inscribed on our hearts  
a curiosity indomitable  
by even this weighty tome.*

## Acknowledgements

As in all things, more appreciation is deserved than can possibly be expressed.

To my advisor, Albrecht Karle, and my former advisor, Wesley Smith: I cannot give you enough thanks for believing in me when I needed it most.

To my mentor, Katherine Rawlins: without your kind support, encouragement, brilliant insights and straight-up know-how this document and all the work that it represents would never have been completed.

To my officemates, roommates, housemates, travel-mates, and just plain -mates, Josh and Lisa Reusch, Eric Brownson, Tom Danielson, Erich Urban, Jon Dumm, Erik Strahler, Sean Grullon, Matt Miller, Nick and Hillary Stephens, Elliot Kaplan, Dan and Jess Clayton, Sam and Cate (and Lucia!) Sangiorgio, Alberto Palmonari, Wei Wang, Laura Gladstone, Eric Nordberg and Matt Palotti, Brian and Rachael Lancor, Mark Krasberg, Freija Descamps and Naoko Kurahashi: you are the people to whom I owe my sanity—as well as my insanity!—and I have loved every minute.

To my many colleagues, old and new, in the cosmic ray working group: I truly appreciate the scientific examples you have set and the many stimulating and helpful discussions. To my patient guides, Peter Niessen and Chihwa Song: I cannot express enough thanks for the time and effort you took to get me started. Especially to my stalwart champions and good friends Arne van Overloop, Tom Feusels, and Jonathan Eisch: it was the thought of Arne's quiet perseverance, Tom's enthusiastic persistence, and Jonathan's good-natured pushiness that encouraged me all those nights at 4 AM. I could not help but try to live up to your strong examples and I certainly could not let you down.

To my family: of course I owe you everything. I could not have wished for more loving and supportive parents and it has been a true blessing to have you so close at hand. To my excellent older brother and friend, Tim Jr.: I must thank you for always being kind enough to set the bar just low enough that I have a shot, but just high enough that I'd be crazy to go for it. Clearly I chose the crazy route long ago, but it's comforting to know I'm not alone on this path.

And to my very best friend, Tim Tharp, who makes me stop when I'm working too hard and shoulders my load when I cannot carry on, who has kept me company these past seven years: you are my rock, and I can't believe you still put up with me!

# Contents

<b>Acknowledgements</b>	<b>ii</b>
<b>1 Introduction to Cosmic Ray Physics</b>	<b>2</b>
1.1 What Are Cosmic Rays? . . . . .	3
1.2 Where do Cosmic Rays Come From? . . . . .	6
1.2.1 Fermi Acceleration . . . . .	6
1.3 Possible Sources for Production of High Energy Cosmic Rays . . . . .	10
1.3.1 Bottom Up Models: Likely Galactic Origins in Supernova Remnants (SNRs)	11
1.3.2 Bottom Up Models: Likely Extragalactic Origins in AGNs, GRBs, and Galaxy Clusters . . . . .	13
1.3.2.1 AGNs . . . . .	13
1.3.2.2 GRBs . . . . .	14
1.3.2.3 Collisions of Galaxy Clusters . . . . .	14
1.3.3 Top Down Models . . . . .	15
1.3.4 Difference between Top Down Models and Bottom Up Models . . . . .	16
1.4 Propagation Models . . . . .	16
1.4.1 Galactic Diffusion and the Leaky Box . . . . .	16
1.4.2 Extragalactic Interactions . . . . .	19
1.5 Modeling the Knee . . . . .	19
1.5.1 Poly-Gonato Parameterization . . . . .	21

1.6	Extensive Air Showers . . . . .	22
1.6.1	Detectors . . . . .	24
1.6.2	Air Shower Observables . . . . .	25
1.6.2.1	Electromagnetic Component of EAS . . . . .	25
1.6.2.2	Muonic Component of EAS . . . . .	28
1.6.3	Extracting Composition Information . . . . .	28
1.6.4	Composition with IceCube and IceTop . . . . .	29
<b>2</b>	<b>Detectors</b>	<b>30</b>
2.1	Terminology . . . . .	30
2.2	What We Are Hoping To Find: Detector Goals . . . . .	30
2.2.1	Cherenkov Light . . . . .	31
2.2.2	Detection Medium and Environment . . . . .	33
2.3	Seeing the Light: Detectors . . . . .	34
2.3.1	DOMs . . . . .	34
2.3.2	Arrays of DOMs . . . . .	37
2.3.2.1	IceCube . . . . .	37
2.3.2.2	Drilling and Deployment of DOMs . . . . .	40
2.3.2.3	IceTop . . . . .	40
2.3.2.4	Data Acquisition . . . . .	42
2.3.2.5	Event Triggers . . . . .	44
2.3.2.6	Simple Majority Trigger . . . . .	44
2.3.2.7	Calibration . . . . .	45
2.3.2.8	Waveform calibration . . . . .	45
2.3.2.9	IceTop Tank Calibration . . . . .	45
2.3.2.10	Calibration . . . . .	47
2.3.2.11	Ice Modeling . . . . .	49

2.3.3	Goals Revisited . . . . .	49
2.3.4	Cosmic Ray Composition . . . . .	52
<b>3</b>	<b>Reconstruction of Cosmic Ray Air Showers</b>	<b>55</b>
3.1	General Reconstruction Principles . . . . .	57
3.2	Event Reconstruction in the Ice: Likelihood Fitting . . . . .	59
3.3	Methods of Reconstruction: IceTop . . . . .	60
3.3.1	First Guess Reconstruction: Shower COG . . . . .	60
3.3.2	First Guess Reconstruction: Plane Fit . . . . .	60
3.3.3	Likelihood Reconstruction: Lateral Fit . . . . .	61
3.4	Methods of Reconstruction In the Ice . . . . .	63
3.4.1	First Guess: Velocity of Line Fit . . . . .	63
3.4.2	Likelihood Fit: Muon Bundle Reconstruction . . . . .	63
3.5	Full Detector Reconstruction: Multiple Iterations . . . . .	68
3.6	Energy Estimators . . . . .	69
3.6.1	IceTop: $S_{125}$ . . . . .	69
3.6.2	InIce: $N_{ch}$ . . . . .	70
3.6.3	InIce: MUE . . . . .	70
3.6.4	InIce: $K_{70}$ . . . . .	70
3.7	A Choice of Reference Distances for $K_{70}$ and $S_{125}$ . . . . .	71
3.8	Comparison with Other Parameters . . . . .	76
3.8.1	Comparing $K_{70}$ to other In-Ice Energy Estimators . . . . .	76
3.8.2	Comparing $S_{125}$ and $K_{70}$ to True Energy and Each Other . . . . .	77
<b>4</b>	<b>Data Quality and Event Selection</b>	<b>80</b>
4.1	Experimental Data . . . . .	80
4.2	Simulation . . . . .	80
4.3	Definition of Terminology . . . . .	83

4.4	Basic Cuts . . . . .	84
4.4.1	Checking Basic Distributions . . . . .	84
4.5	Containment Cuts . . . . .	87
4.5.1	Containment of the Final Reconstructions . . . . .	88
4.5.2	Containment Using Independent IceTop and InIce Reconstructions . . . . .	88
4.6	Further Quality Cuts . . . . .	89
4.7	Angular Difference . . . . .	89
4.8	Direct Length: LDirC . . . . .	90
4.9	Length Parameter . . . . .	91
4.10	Timing . . . . .	92
4.11	Final Cut Evaluation . . . . .	92
<b>5</b>	<b>Spatial Mapping: A Neural Network Technique</b>	<b>99</b>
5.1	Introduction to Neural Networks . . . . .	100
5.2	Neural Networks for this Analysis . . . . .	105
5.2.1	Activation Functions: Sigmoid for Internal Layers, Linear for Output Layer . . . . .	107
5.2.2	Learning Algorithm: Broyden-Fletcher-Goldfarb-Shanno (BFGS) . . . . .	107
5.2.3	Architecture: 2:5:5:2 . . . . .	108
5.2.4	Training Cycles: 947 . . . . .	108
5.2.5	Neural Network Output . . . . .	110
5.3	Human vs Neural Network . . . . .	111
<b>6</b>	<b>Energy Spectrum</b>	<b>114</b>
6.1	Calculating Flux . . . . .	117
6.2	Checking the Calculation . . . . .	118
6.2.1	Step 1: Transforming the Generated Spectrum to a More Realistic Spectrum	118
6.2.1.1	Defining Some Notation . . . . .	119
6.2.1.2	The Basic Transformation . . . . .	120

6.2.1.3	A More Realistic Transformation . . . . .	120
6.2.1.4	Last Key Piece For Comparison to Raw Experimental Data Distribution . . . . .	121
6.2.2	Step 2: Calculate the Flux From the True Simulated Rates . . . . .	122
6.2.3	Step 3: Calculate the Flux From the Reconstructed Simulated Rates . . . . .	122
6.3	Energy Spectrum Results . . . . .	125
<b>7</b>	<b>Analysis of Mass Composition</b>	<b>127</b>
7.1	Determination of Appropriate Energy Slices . . . . .	130
7.2	A Closer Look at Characteristic Curves . . . . .	130
7.3	Minimizing Across One Slice in Energy, Protons and Iron Only . . . . .	131
7.4	Determination of the Appropriate Number of Independent Nuclei . . . . .	132
7.5	Results . . . . .	134
<b>8</b>	<b>Systematic Errors and Corrections for Known and Understood Problems</b>	<b>135</b>
8.1	Ice Model . . . . .	135
8.2	Hadronic Interaction Models . . . . .	137
8.3	VEM Shift . . . . .	138
8.4	Snow at the Surface . . . . .	140
8.5	Seasonal Atmospheric Variations . . . . .	141
8.6	DOM Efficiency . . . . .	145
8.7	Summary of Systematic Uncertainties . . . . .	145
<b>9</b>	<b>Results and Conclusions</b>	<b>147</b>
9.1	Results . . . . .	147
9.1.1	Energy Spectrum . . . . .	147
9.1.2	Mass Composition . . . . .	151
9.2	Lessons Learned and Future Work . . . . .	151

<b>A Glossary of Some Acronyms and Units</b>	<b>155</b>
<b>B Niessenian Energy Binning Scheme</b>	<b>158</b>
<b>C Energy Spectrum Results</b>	<b>159</b>
<b>D Mass Results</b>	<b>160</b>
<b>E Supplemental Details About Cuts</b>	<b>162</b>

## List of Tables

1.1	Different Experimental Techniques for Composition and Energy Spectrum . . . . .	29
3.1	Reconstruction Algorithms Used in Composition Analysis . . . . .	59
4.1	Cut Levels Defined . . . . .	93
4.2	Quality Cut Bias . . . . .	95
4.3	Quality Cut Statistics . . . . .	96
B.1	Niessenian Energy Binning Scheme . . . . .	158
C.1	Energy Spectrum Results . . . . .	159
D.1	Number of Simulated Particle Type by Reconstructed Energy . . . . .	160
D.2	Mass Composition Results with Systematic Errors . . . . .	160
D.3	Reconstructed Ratio of Particles vs Energy . . . . .	161

## List of Figures

1.1	Measured All Particle Spectrum of Cosmic Rays . . . . .	4
1.2	Hillas Diagram illustrating relationship between magnetic fields and source size . . . . .	9
1.3	Images of a SNR and an AGN . . . . .	11
1.4	Diagram of a Gamma Ray Burst . . . . .	15
1.5	Diagram of Galaxy . . . . .	17
1.6	Compilation of Many Composition Models Compared to Experimental Data . . . . .	20
1.7	The Poly-Gonato Model . . . . .	21
1.8	Diagram of an Extensive Air Shower . . . . .	22
1.9	Depiction of various methods of EAS Detection . . . . .	24
1.10	Longitudinal Distribution of Proton and Iron Showers by Atmospheric Depth . . . . .	26
2.1	Cartoon of Cherenkov Light . . . . .	31
2.2	Schematic of A Digital Optical Module (DOM) . . . . .	34
2.3	IceTop and IceCube Array Diagram . . . . .	38
2.4	A DOM being deployed . . . . .	39
2.5	Photos of an IceTop station and the interior of an IceTop tank. . . . .	41
2.6	IceTop Local Coincidence Diagram . . . . .	43
2.7	A schematic of the IceTop and IceCube DAQ . . . . .	46
2.8	IceTop muon spectrum calibration . . . . .	47
2.9	Detector Layout and Geometry . . . . .	48
2.10	Optical Properties of the South Pole ice . . . . .	50

2.11	Energy Range Covered by IceTop . . . . .	52
2.12	Composition by Rotation with SPASE-2/AMANDA-B10 . . . . .	54
3.1	IceTop/IceCube-40 Event Display . . . . .	56
3.2	Number of Muons vs Number of Electrons, from Ralph Engel . . . . .	58
3.3	IceTop Event Display with Signal and Curvature Fits . . . . .	62
3.4	Side view of IceCube Reconstruction Coordinates . . . . .	64
3.5	“Top” view of IceCube Reconstruction Coordinates . . . . .	65
3.6	Cartoon of Muon Bundle in the Ice with Lateral Distribution of Light Intensity . . . . .	66
3.7	Charge as a Function of Distance to the Track Axis, and Fit Signal . . . . .	68
3.8	“Bundle of Sticks”: The most stable distance for the $K$ -parameter . . . . .	72
3.9	Finding most reliable distance at which to evaluate $K$ and $S$ , for all simulated showers . . . . .	73
3.10	Check Energy Resolution and Composition of $S$ -Parameter . . . . .	74
3.11	Check Composition-Sensitivity and Resolution of $K$ -Parameter . . . . .	75
3.12	Check $K_{70}$ against other Energy Estimators . . . . .	75
3.13	Check $K_{70}$ against other Energy Estimators using Spread . . . . .	77
3.14	Comparing $K_{70}$ and $S_{125}$ with true Energy and With Each Other . . . . .	79
4.1	40-string geometry used for 2008 . . . . .	81
4.2	Detector Event Rates and Livetime from August 2008 . . . . .	81
4.3	A first look at simulated data, only very basic cuts . . . . .	85
4.4	Array of Useful Parameters Before Cuts . . . . .	86
4.5	Defining Containment . . . . .	87
4.6	Angular Resolution Cut Selection . . . . .	90
4.7	LDirC Cut Selection . . . . .	91
4.8	Length Parameter Cut Selection . . . . .	92
4.9	Array of Useful Parameters After Cuts . . . . .	94
4.10	Offsets After Cuts . . . . .	95

4.11	$K_{70}$ and $S_{125}$ comparing data and simulation after cuts . . . . .	97
4.12	Data and Simulation in $K_{70}$ - $S_{125}$ Space, Showing the Percentage of Protons and Contours of True Energy (the “pig plot”) . . . . .	98
5.1	Diagrams of Various Neural Network Activation Functions . . . . .	101
5.2	Fit a function to various polynomials . . . . .	104
5.3	Basic Neural Network Schematic . . . . .	106
5.4	Neural Network Structure and Error Function . . . . .	107
5.5	Some Basic Plots of the Neural Network Output . . . . .	109
5.6	Man vs Machine: Contours in Mass and Energy . . . . .	112
5.7	Man vs Machine: Errors in Mass and Energy . . . . .	113
6.1	Energy resolution, bias, and efficiency, for the neural network output energy . . . . .	115
6.2	Energy Resolution in Slices of Reconstructed Energy . . . . .	116
6.3	Apertures for True and Reconstructed Energy . . . . .	121
6.4	True Simulated Energy Spectrum . . . . .	123
6.5	Reconstructed Simulated Energy Spectrum . . . . .	124
6.6	Reconstructed Energy Spectrum from August 2008 Experimental Data . . . . .	126
7.1	Characteristic Curves for All Particle Types for Minimization Across One Slice in Energy . . . . .	128
7.2	Characteristic Curves for 2 Particle Types for Minimization Across One Slice in Energy	128
7.3	Test of Minimization Algorithm using a test simulation for 2 primary types only . . . . .	132
7.4	Result of 2-type minimization on test sample for all energies . . . . .	133
7.5	Result of 3-type minimization on test sample for all energies . . . . .	133
8.1	Comparison of SPICE-1 vs AHA . . . . .	136
8.2	EPOS vs SIBYLL Comparison . . . . .	138
8.3	Calculating the VEM Shift . . . . .	139

8.4	Snow Rates by Position and a Division of IC-40 by Year . . . . .	142
8.5	Drawing of the Snow Drifts at the South Pole . . . . .	143
8.6	Comparing $K_{70}$ vs $S_{125}$ before and after the Snow Fix . . . . .	144
8.7	Effect of Yearly Atmospheric Variations . . . . .	144
8.8	Composition Results With Systematic Errors . . . . .	146
9.1	All Particle Energy Spectrum . . . . .	148
9.2	Energy Spectrum Fits for Other Recent Experiments . . . . .	149
9.3	Mean Logarithmic Mass . . . . .	150
9.4	Comparison of $\langle \ln A \rangle$ Results with SPASE-2/AMANDA-B10 . . . . .	152
9.5	Comparison of $\langle \ln A \rangle$ Results with Other Like Experimentsl . . . . .	152
9.6	Comparison of $\langle \ln A \rangle$ Results with Poly-Gonato Knee Model . . . . .	153
E.1	Level1 Cuts . . . . .	163
E.2	Level1 Cuts, Cut on Ang. Res. . . . .	164
E.3	Level2 Cuts . . . . .	165
E.4	Level3 Cuts . . . . .	166
E.5	Level3 Cuts, Cut on Ang. Res. . . . .	167
E.6	Level4 Cuts . . . . .	168
E.7	Level4 Cuts, Cut on Ang. Res. . . . .	169
E.8	Level5 Cuts . . . . .	170

## Overview: Thesis Map and Useful Conversions

This thesis explores the first measurements of the cosmic ray energy spectrum and composition using coincident data between IceCube and IceTop. This work begins with an introduction to cosmic rays (Chapter 1), motivating this study. Detection principles are reviewed (Chapter 2), and cosmic ray reconstruction is discussed (Chapter 3), including a detailed formulation of the two major parameters used in this work,  $K_{70}$  and  $S_{125}$ . The present work begins with a selection of data quality cuts (Chapter 4), based on a thorough understanding of the specific data and simulation sets used for this analysis. Next, a novel analysis technique using a neural network has been developed (Chapter 5), which produces a direct mapping from the  $K_{70}$ - $S_{125}$  parameter space to a new parameter space of energy versus a mass-like quantity. The energy spectrum is directly accessible through this mapping and compares favorably to previous measurements of the all-particle cosmic ray flux (Chapter 6). The mass-like parameter is reduced to a measurement of cosmic ray primary mass through a minimization technique (Chapter 7), and is observed to increase through the knee. Systematic errors (Chapter 8) result in a mass-resolution which is comparable to previous measurements. The sources of these errors have been identified and a significant improvement to mass measurement may be anticipated with future analysis. Finally, results are summarized and compared with previous measurements (Chapter 9).

The standard units used in this analysis are GeV ( $10^9$  eV) and  $\log_{10}(E/\text{GeV})$ . However, for easy comparison to other standard results we will often refer to EeV ( $10^{18}$  eV), PeV ( $10^{15}$  eV), and TeV ( $10^{12}$  eV), as well as eV. For a quick reference of abbreviations, conversions, acronyms and terms, please see Appendix A.

# Chapter 1

## Introduction to Cosmic Ray Physics

Each second, the atmosphere above you is bombarded with thousands of relativistic particles. Some of these particles have incredibly high energies—each year, roughly one in a million people will be directly targeted by a subatomic particle with the same energy as a friendly slap on the back. Almost none of these particles will make it all the way to the earth’s surface. Instead, they form giant air showers, ionizing millions of air molecules and creating thousands of particles and a bright but ephemeral pulse of light, spreading their energy over vast areas. This light can only be detected by sensitive instruments in very dark places.

It is no wonder, then, that humankind was unaware of their existence until nearly 100 years ago when Victor Hess historically brought his electrometer into the atmosphere in a risky hot-air balloon ride outside Vienna, Austria, to clarify the source of the radiation many scientists had detected in their labs [1]. This radiation was thought to emanate from the earth itself, but previous measurements of the radiation at higher elevations had shown an increase in the level of radiation instead of the decrease which would have confirmed the earth as the source. Over seven trials, Hess observed that at elevations below 1 km the radiation decreased, but from elevations above 1 km to as high as 5 km the radiation *increased*, indicating that it was coming from above—rather than radiating from—the earth. This radiation therefore became known as *Höhenstrahlung*, or *cosmic rays*, and has been the subject of much investigation from the moment its existence was first discovered.

From the very beginning, the main questions surrounding the mystery of cosmic radiation

have been:

- What is it?
- Where does it come from?
- How does it get here?

and in the past 100 years much progress has been made to these ends.

## 1.1 What Are Cosmic Rays?

The first step was to identify the ionization Hess observed as coming from the heavens rather than the earth. Shortly after Hess' discovery, Werner Kolhörster made his own balloon ascents to measure the longitudinal distribution of the ionization. In 1929 Kolhörster and Walther Bothe, working together in Germany, measured the absorption characteristics of the cosmic radiation by placing an absorber between two Geiger-Müller tubes (a.k.a. Geiger counters): this led to the conclusion that cosmic rays are not actually rays but rather charged particles [3]. This result was in agreement with J. Clay's similar discovery that the intensity of cosmic rays is dependent upon the observer's magnetic latitude [4].

In the late 1930s, Pierre Auger set up an array of Geiger counters and Wilson cloud chambers to detect cosmic rays at the Jungfrauoch in Switzerland (where, in his honor, there is still a cloud chamber on display<sup>1</sup>) [5]. His detectors were separated by large distances but showed signals that were correlated in time. By 1939 Kolhörster had extended his own coincidence tests by gradually separating his Geiger counters and similarly discovered that even up to a 75 m separation the tubes displayed coincident signals [6]. Both Auger and Kolhörster came to the same conclusion: these coincident events could only mean that the particles being observed were secondary particles produced by a single primary interaction in the atmosphere.

The discovery that only secondary particles can be detected at the earth's surface led to a number of attempts in the 1940s to directly detect primary cosmic rays in the atmosphere by installing cloud chambers and photographic plates on balloons which carried them to high altitudes.

---

<sup>1</sup>Personally confirmed by K. Andeen, T. Andeen, and T. Tharp in March, 2010.

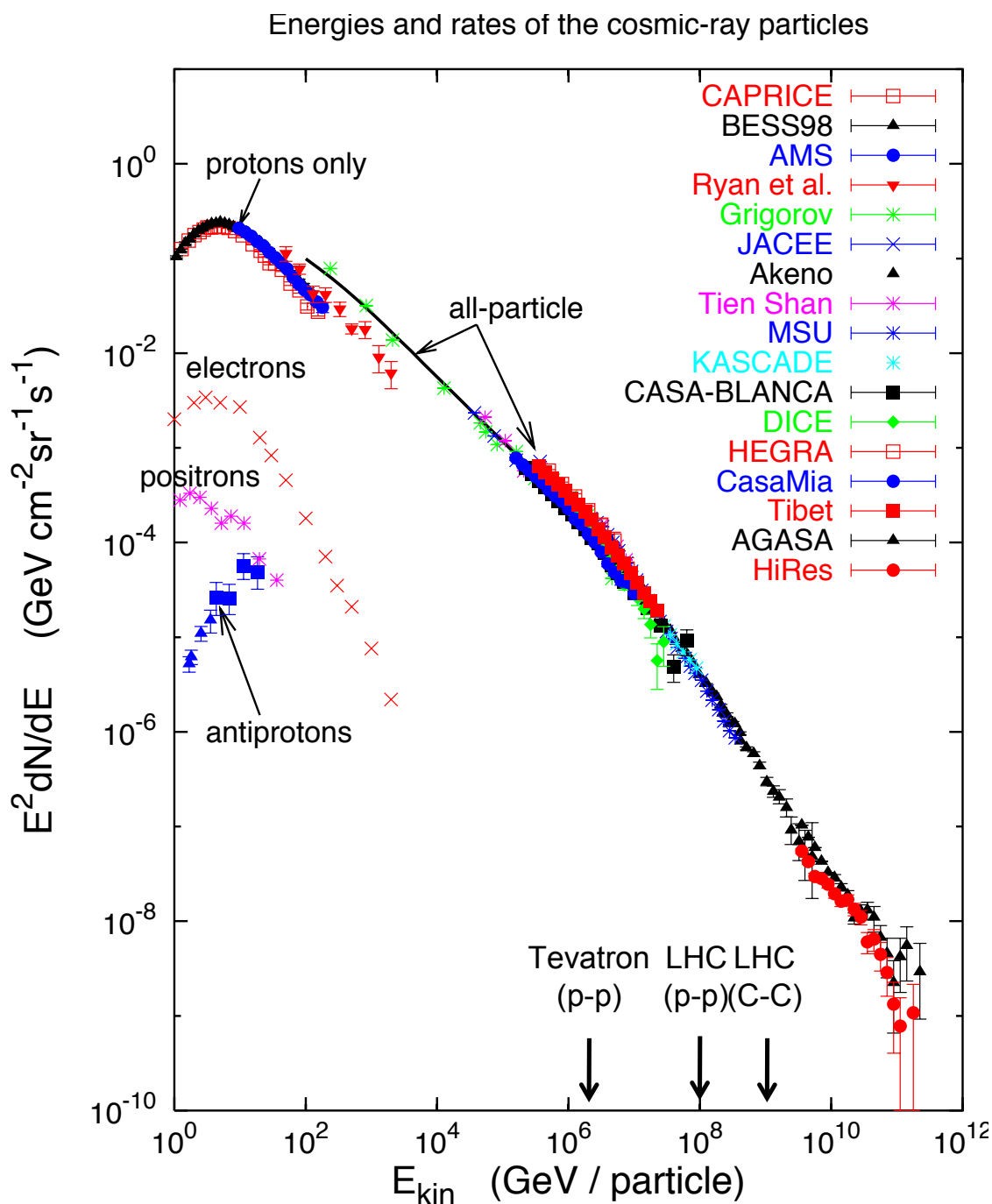


Figure 1.1: All particle energy spectrum of cosmic rays, as measured by various experiments. The flux is multiplied by a factor of  $E^2$  in order to bring out two major features: the “knee” just above  $10^6$  GeV, and the “ankle” around  $10^{10}$  GeV. (After [2].) Note that these naturally occurring cosmic rays reach energies even higher than those currently possible by man-made high energy experiments. Examples labeled above are the maximum energy attained by the proton-antiproton collisions at the Tevatron and the proton-proton collisions at the LHC, and a possible future upgrade to the LHC using crab cavities.

This proved to be a very successful technique (still in use today) and led to the discoveries that:

1. the charged cosmic ray primaries were predominantly protons [7], and
2. cosmic rays are primarily fully ionized nuclei, traveling at speeds close to that of light [8].

In the following years, nuclei from the periodic table up to  $Z = 40$  were observed and their abundances were determined. Particles with a mass greater than that of iron ( $Z = 26$ ) were discovered to be much less prevalent than the lighter elements such as helium and hydrogen (protons). In general, the number distribution of cosmic rays by mass was determined to be very similar to that in the solar system, which consists of  $\sim 89\%$  protons,  $\sim 10\%$  hydrogen, and  $< 1\%$  heavier elements [9].

Also during the 1940s the ground-based measurements of Auger and Kolhörster were extended through the construction of a number of large arrays for detection of Extensive Air Showers (EAS), as coincident secondary particles had come to be called. These arrays were commonly comprised of Geiger tubes, which later were replaced with scintillation counters coupled to photomultipliers and, most recently, Cherenkov detectors. These experiments revealed that the energy spectrum of cosmic rays observed on Earth follows a power law:

$$\frac{dN}{dE} \propto E^{-\alpha} \quad (1.1)$$

with index  $\alpha \sim 2.7$  over a large energy range. However, in 1958 by G.G. Kulikov and G.B. Khristiansen<sup>2</sup> (working with a hodoscope array in the U.S.S.R.) discovered that the spectral index steepens around several PeV to  $\alpha \sim 3.0$  [10]. This change in slope became known as the “knee” in the spectrum. The first evidence for a further change in the spectral index, called the “ankle”, was detected in 1963 in an analysis data from the Volcano Ranch detector in New Mexico, which was the largest detector of its time with 20 scintillator counter stations over an area of 12 km<sup>2</sup> [11]. The existence of the ankle was not confirmed until the 1990s by both AGASA [12] and Fly’s Eye [13] (the first detector to successfully detect the fluorescence light from the air shower). These two

---

<sup>2</sup>Note: Khristiansen, of the U.S.S.R., is sometimes cited as Hristiansen.

features can clearly be seen in Figure 1.1, which is a compilation of measurements of the energy spectrum multiplied by the factor  $E^2$  to emphasize the existence of the knee and the ankle.

The cause of these spectral index changes was mysterious and, though myriad theories have been developed and a multitude of measurements taken, still remains an important question in the field. Furthermore, while the ratio of elements composing incoming cosmic rays is relatively well known at energies below the knee, the composition at higher energies is less clear. These two unknowns are linked and can be better understood through a discussion of the next big question: where do they come from?

## 1.2 Where do Cosmic Rays Come From?

Anyone who has looked up at the night sky might guess that there are an abundance of potential sources of cosmic rays: the problem is one of distinguishing between the possibilities. Thus, important questions to consider are:

1. How can the cosmic rays be accelerated such that they produce a spectrum like the one we see on Earth?
2. Which of the astrophysical objects shining down on us can provide such an acceleration mechanism?

### 1.2.1 Fermi Acceleration

We know that the cosmic ray spectrum observed on Earth follows a power law with spectral indices currently measured to be  $\alpha \sim 2.7$  below the knee in energy and  $\sim 3.0$  above the knee. Thus, any complete model of cosmic ray origin, acceleration and propagation must explain the observed spectral index of this power-law in energy.

The current leading theory for acceleration of cosmic rays was proposed by Fermi in 1949 and is therefore known as Fermi Acceleration [14]. Fermi's basic idea was that a relativistic particle with initial energy  $E_0$  could gain energy within an acceleration region consisting of a moving, non-uniform, magnetic field off of which the particle elastically "collides" (where here a collision refers

to the reflection off the irregularities in the magnetic field itself—not with other particles—as in the case of a magnetic mirror). Following the derivation found in [15] let us assume the relativistic test particle suffers a change in energy  $\Delta E = \xi E$  with each “encounter” (which will be defined for different cases below). Thus, after  $n$  encounters the test particle has:

$$E_n = E_0(1 + \xi)^n \quad (1.2)$$

and the number of collisions required to reach a certain energy  $E$  is:

$$n = \frac{\ln\left(\frac{E}{E_0}\right)}{\ln(1 + \xi)}.$$

If the probability of the particle to escape the acceleration region after every collision is denoted by  $P_{esc}$ , the probability that the test particle remains in this region after  $n$  encounters is  $P_n = (1 - P_{esc})^n$ , and the proportion of particles accelerated to energies greater than  $E$  is:

$$N(> E) \propto \sum_{m=n}^{inf} (1 - P_{esc})^m = \frac{(1 - P_{esc})^n}{P_{esc}} = \frac{1}{P_{esc}} \left(\frac{E}{E_0}\right)^{-\gamma}, \quad (1.3)$$

or, in a differential form:

$$\frac{dN}{dE} \propto E^{-(1+\gamma)}.$$

The spectral index  $\gamma$  is:

$$\gamma = \frac{\ln\left(\frac{1}{1-P_{esc}}\right)}{\ln(1 + \xi)} \sim \frac{P_{esc}}{\xi}. \quad (1.4)$$

Assuming that there is a characteristic time for a single acceleration cycle,  $T_{cycle}$ , the total time to escape from the acceleration region can be written as  $T_{esc} = T_{cycle}/P_{esc}$ , and Equation 1.4 can be rewritten as:

$$\gamma = \frac{T_{cycle}}{\xi T_{esc}},$$

Furthermore, if the acceleration process has been running for a certain time,  $t_{accel}$ , the number of

possible reflections for a given particle is  $n \leq t_{accel}/T_{cycle}$ . Thus the maximum energy after  $t_{accel}$  (from Equation 1.2) becomes:

$$E = E_0(1 + \xi)^{t_{accel}/T_{cycle}} \quad (1.5)$$

Clearly this mechanism leads to a power law spectrum (Equation 1.3), as desired. Additionally, Equation 1.5 indicates that accelerating particles to a higher energy takes longer, and the maximum timeframe of an accelerator limits the maximum energy attainable.<sup>3</sup>

Which sources can provide this sort of acceleration mechanism? In Fermi’s original paper, he proposed particle acceleration in moving clouds of plasma, where the magnetic field irregularities in the cloud cause the reflections mentioned above. Let us assume the first reflection happens while the particle is moving with the flow of the magnetic field, i.e. a “tail-on” collision: the particle loses energy in this collision and is knocked back in the direction opposite to the flow of the field. The particle then makes a “head-on” collision (the second reflection), which causes a gain in energy, and the particle is again moving in the forward direction of the field. In a non-moving field there would be an equal number of collisions, resulting in neither a net increase nor a net decrease in energy. However, since the model assumes randomly moving fields, the probability of energy increases is higher than that of decreases and results in an overall gain in energy:

$$\xi \propto \beta^2 \quad (1.6)$$

where  $\xi$  is again the average fractional energy gain per “encounter” (where an “encounter” here is a pair of head-on and tail-on collisions) and  $\beta = V/c$  where  $V$  is the velocity of the plasma flow. This case has become known as “Second Order Fermi Acceleration” (since it is the second order term in an expansion of  $\beta$ ). This acceleration model, while initially promising, was found to be too “slow” (as in Equation 1.5) to provide the observed power spectrum.

Instead of turbulent variations in random magnetic fields, we can consider the shock front

---

<sup>3</sup>Beware: the maximum energy attainable would be given by Equation 1.5 if the cycle time,  $T_{cycle}$ , was independent of energy, which is NOT the case.

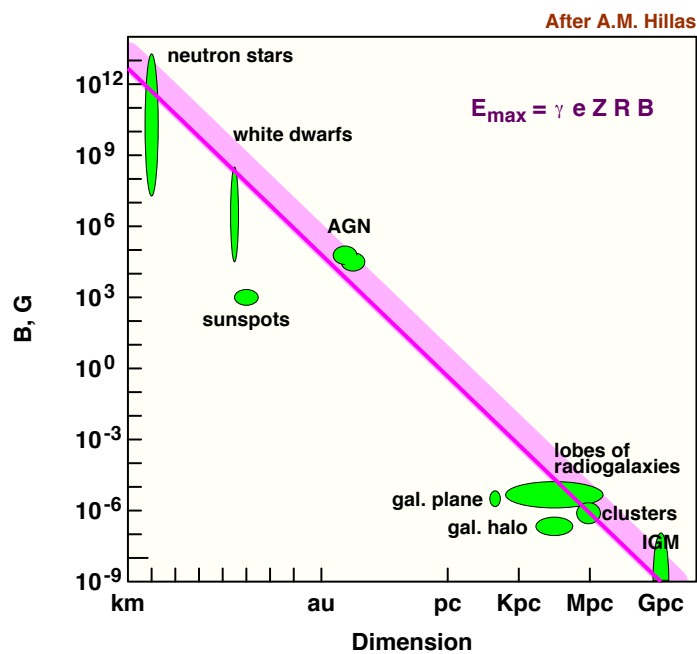


Figure 1.2: Diagram showing the relationship between the magnetic field strength and size of possible sources of ultra high energy cosmic rays. The shaded region depicts the minimum energy required to reach  $10^{20}$  eV, with the upper edge corresponding to the minimum magnetic field value for acceleration of proton nuclei as a function of the astrophysical object's dimension, and the lower edge corresponding to iron. (Note that GRBs are not shown due to the time dependence of their magnetic field and dimension.) [16]

produced when an exploding gas travels faster than the speed of sound of a medium [17, 18, 19, 20, 21]. In this model a particle bounces back and forth across the front and elastically collides with the magnetic turbulence both in front of (upstream) and behind (downstream) the shock<sup>4</sup>. The downstream edge of the front converges on (or catches up to) the upstream edge: in either the upstream or downstream rest frame the other side of the shock is approaching (as in the classic demonstration of a ping-pong ball bouncing back and forth between two paddles moving toward each other) [22]. Thus in both the upstream and downstream frame collisions with the particle are head-on, causing an increase in energy with every collision, not just every “encounter” (where an “encounter” in this case is defined as a crossing of the particle in both directions across the front):

$$\xi \propto \beta. \tag{1.7}$$

This is known as “First Order Fermi Acceleration”. In this case, the maximum energy acquired by a particle traveling in a medium with magnetic field  $B$ , Larmor radius  $r_L$ , and characteristic velocity  $\beta$  can be estimated as  $E_{max} \sim 2\beta cZeBr_L$ , which is sometimes referred to as the “Hillas criterion” [23, 24]. A maximum spectral index  $\alpha \propto 2.0$  can be calculated assuming very strong shocks (though in this case  $\alpha < 2.0$  is more likely due to nonlinear effects) while indices up to 2.5 can be obtained by incorporating much higher magnetic fields or larger acceleration regions, as depicted in Figure 1.2. The further interaction of the cosmic rays between the source and Earth allow for the remaining difference between the observed spectrum and that produced at the source.

### 1.3 Possible Sources for Production of High Energy Cosmic Rays

Now that we have a possible acceleration mechanism, the next step is to determine which sources could produce such a mechanism with the proper spectral indices. One category of models,

---

<sup>4</sup>The upstream and downstream terminology used here is theoretically meant to help clarify but in practice can be very confusing. For example, if one imagines a mountain stream, upstream should be against the flow, up the mountain *toward* the source of the stream, while downstream would be the direction *away* from the source (down toward the sea, usually). In the standard shock front descriptions, however, we are to work in the shock’s rest frame, imagining a “stationary” shock, which is fighting against a flow heading back in the direction of the shock’s source. Thus we follow the typical terminology here, using upstream to mean *away* from the shock’s source but *toward* the “source” of the flow, and downstream to mean *toward* the shock’s source and *away* from the “source” of the flow.

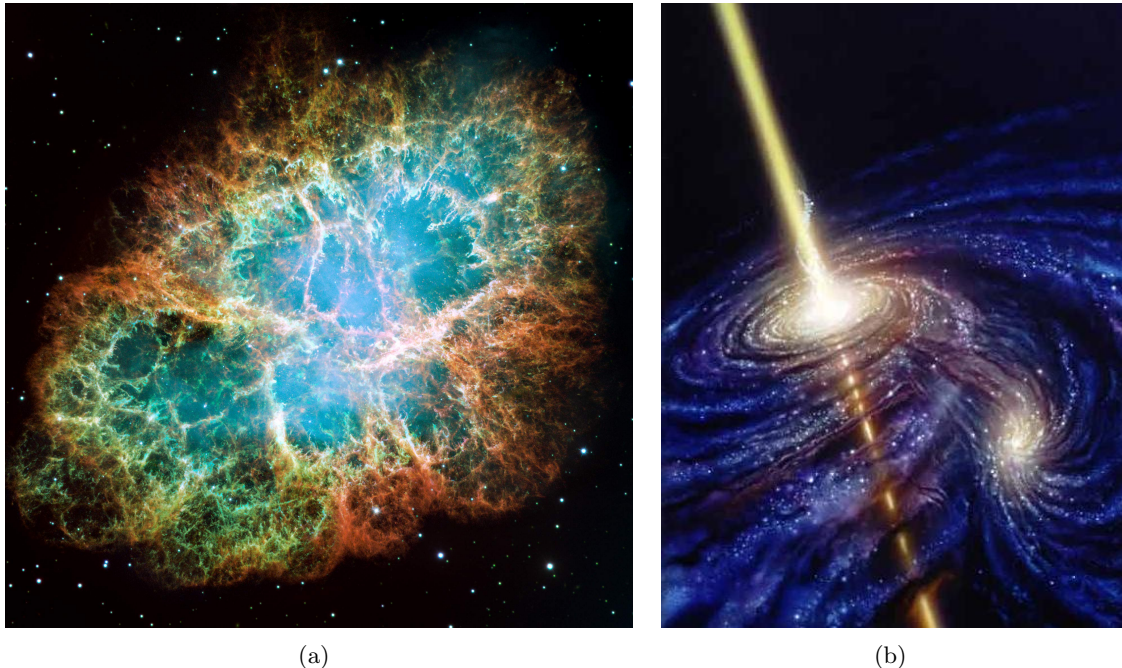


Figure 1.3: In Figure 1.3(a) we show an image of the Crab Nebula as an example of a supernova remnant (image from Hubble Space Telescope). In Figure 1.3(b) we show an artist’s rendition of an active galactic nucleus with a black hole in the center (painting by Don Dixon for “Scientific American”)

called “bottom-up” models, predict cosmic rays from a variety of both galactic and/or extragalactic astrophysical sources. Another category of models, called “top-down” models, consider the idea that the origin of cosmic rays might not be an astrophysical source, but rather exotic particle physics which we do not yet understand. We will discuss a few of these models below; however, a very comprehensive review article can be found in [23].

### 1.3.1 Bottom Up Models: Likely Galactic Origins in Supernova Remnants (SNRs)

The most commonly cited source of galactic cosmic rays up to a few hundred PeV are supernova remnants (SNRs), as discussed in [25, 26, 27, 28, 29]. Prior to a supernova, a star balances the inward gravitational pull of its own mass with the outward thermal pressure caused by the fusion of elements in its core. However, at some point this balance is tipped, initializing a chain of events which—if the circumstances are right—can result in an explosion of the star, called a supernova. The mechanism behind this explosion depends upon the initial mass of the star and/or the characteristics of the star system.

Supernovae were initially classified by their optical properties into two different types: Type II supernovae had Hydrogen Balmer lines, whereas Type I supernovae did not, indicating that Type II supernovae were caused by stars which had contained hydrogen. In the past century supernovae have been further categorized, with the most basic modern categories being Types Ia, Ib, Ic and II. Types Ib, Ic, and II supernovae are currently considered to be core collapse supernovas produced by very massive stars, whereas Type Ia supernovae are produced by thermonuclear explosions in relatively low-mass white dwarf stars.<sup>5</sup>

In all cases, the basic process begins when all hydrogen in the core of the star has been converted to helium and the initial fusion process comes to an end, throwing off the balance of thermal pressure against the force of gravity and causing a collapse. The collapse process heats the core of the star to a high enough temperature to begin helium fusion. This pattern is repeated through all elements as long as the star has enough mass to generate the temperature required for the fusion process of the next element in line.

For a star which is less than about five times the mass of the sun ( $M_{\odot}$ ), the process stops when helium has fully fused into carbon and oxygen. At this point, the star ejects its outer layers and becomes a very hot white dwarf surrounded by its planetary nebula. The star is once more supported in a balance between two forces: the gravitational pull and the electron degeneracy pressure. In the standard situation, the white dwarf cannot exceed  $\approx 1.4M_{\odot}$ , the Chandrasekhar limit which determines the mass supportable by the electron degeneracy pressure, and slowly cools to become a black dwarf. However, if the white dwarf acquires more mass (from, for example, a companion star in a binary system) its gravity can exceed the Chandrasekhar limit, causing a runaway thermonuclear reaction which releases enough energy to cause a supernova explosion.

On the other hand, in the case of sufficiently massive stars (greater than  $\sim 5 M_{\odot}$ )—such as those producing Type Ib, Ic, and II supernovae—the fusion process supporting the outward thermal

---

<sup>5</sup>Type Ib and Ic supernovae are called *stripped* core collapse supernovae, which implies that they follow very similar processes to Type II supernovae except that they are missing their outer layer of hydrogen gas, which is theorized to have been stripped by strong solar winds or companion stars. Type Ic supernovae are more stripped than Type Ib, missing also their helium layer. Both types lack the silicon absorption line which is apparent in the Type Ia supernovae.

pressure of the star comes to an end when the star has burned most fusable elements into an iron “ash” core. At this point, the fusion process again does not sustain the star against its own gravity and the star once more begins to collapse until at last it reaches the balance between the gravitational pull and the electron degeneracy pressure. The degenerate pressure, which stops the gravitational collapse, causes a recoil (like a wave smashing into a wall) which in turn causes the less-dense shell of the star to be ejected into the interstellar medium (ISM).

In both cases, the material ejected away from the star is known as the supernova remnant, which can be as large as several parsecs and can be traveling at speeds up to  $\sim 0.01c$ . These ejecta smash through the ISM, forming a shock wave that can accelerate cosmic ray particles up to a few hundred PeV. An example of an SNR can be seen in Figure 1.3(a).

### **1.3.2 Bottom Up Models: Likely Extragalactic Origins in AGNs, GRBs, and Galaxy Clusters**

While cosmic rays arriving at Earth with energies up to the region of the knee are commonly attributed to SNRs, cosmic rays in the region of the ankle are generally thought to require extragalactic origins (because the galaxy cannot contain cosmic rays of these energies) [15]. An overlap between the cut-off of the galactic sources and the turn-on of the extragalactic sources is then credited with the cosmic ray flux between the knee and the ankle. (This energy region is considered in more depth in Section 1.5.) Possible extragalactic sources could include Active Galactic Nuclei (AGNs), Gamma Ray Bursts (GRBs), and Galaxy Clusters [16].

#### **1.3.2.1 AGNs**

Active Galactic Nuclei are a very probable source of cosmic rays at energies above the knee [22]. They were first observed in the early part of the 20<sup>th</sup> Century as galaxies with stars which were extremely bright at certain wavelengths. The current theory is that all AGNs have the same basic elements: a supermassive black hole at the center, which sucks matter from nearby stars into a rapidly rotating accretion disk. This matter is subsequently heated to very high energies and is

eventually ejected in far-reaching jets along the rotational axis of the disk.

Over the past century AGNs have been classified into a number of different subcategories based on their observable properties outside the visible spectrum, the angle between their jet and the observation axis, the size of the accretion disk, and the mass of the black hole. The magnetic fields and shocks thought to be produced in jets and accretion disks in AGNs make them a strong candidate for cosmic ray acceleration; therefore, each type of AGN has an associated particle acceleration model, some predicting cosmic rays up to EeV energies.

### 1.3.2.2 GRBs

A Gamma Ray Burst [23, 30] is a brief astrophysical event which falls into one of two categories: long or short. The longer bursts (of duration  $> 2$  s) often appear with the core-collapse supernovae of massive stars in star-forming galaxies. Prior to the actual supernova explosion, a rapidly-rotating star which has run out of fuel will emit a jet of radiation (similar to that found in an AGN prior to its collapse into a black hole). The shorter GRBs (of duration  $< 2$  s) are thought to be symptomatic of the merging of two binary neutron stars (which are the compact cores resulting from core collapse supernovae, as described above).

Gamma rays resulting from these bursts are observed to have a falling spectrum. This feature is likely produced by the prompt-emission of gamma rays associated with the shocks produced in the jet from a GRB. This scenario implies the acceleration of electrons, which in turn should also indicate the acceleration of hadrons to energies high enough to be observed as ultra high energy cosmic rays on Earth. GRBs became popular as a model upon the realization that the arrival direction of the two most energetic cosmic rays ever detected coincide with the error circles of two powerful GRBs [16].

### 1.3.2.3 Collisions of Galaxy Clusters

Galaxy clusters [23, 16, 31] are clusters of 50 to 1,000 galaxies which are bound together by an unknown force (theorized to be the gravitational force of dark matter). Galaxy clusters also

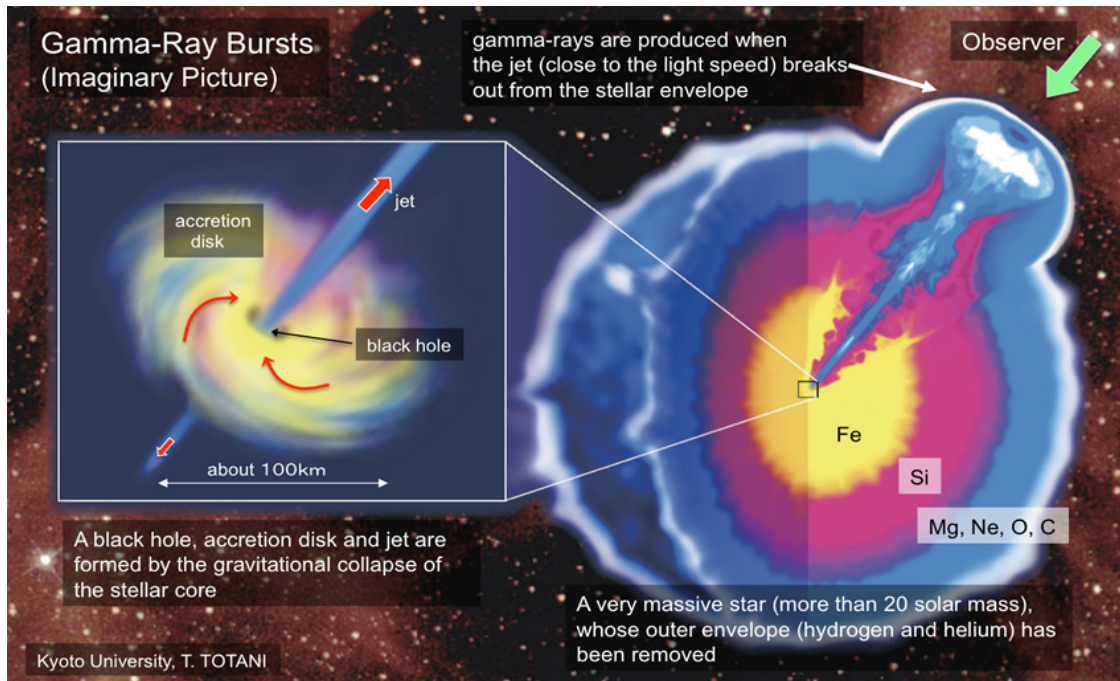


Figure 1.4: A diagram detailing the formation of a gamma ray burst.

contain large amounts of hot, intergalactic, x-ray emitting gas. When clusters of galaxies collide, it is expected that there will be accretion shock waves at their boundaries. Particle acceleration should take place if magnetic fields are present at these shocks; this can be expected to contribute to the flux of ultra high energy cosmic rays up to some tens of EeV. Recent X-Ray and radio observations of galaxy clusters seem to support this possibility.

### 1.3.3 Top Down Models

Alternative to the models postulating high energy cosmic rays being accelerated from astrophysical sources (bottom-up models) are top down models ([16, 23]), which theorize that high energy cosmic rays are actually the stable decay products of supermassive  $X$ -particles, called exotics. These particles are associated with the spontaneous symmetry breaking underlying grand unified theories and could either be remnants of the early universe or have as their source topological defects left over from phase transitions in the early universe (such as magnetic monopoles). In either case the mass of these particles is much higher than the observed cosmic ray energies: when

the exotic particle decays, its energy is split, resulting in the observed flux.

### 1.3.4 Difference between Top Down Models and Bottom Up Models

There are two significant differences between top-down models and bottom-up models [16]:

1. Top-down models would produce a high proportion of neutrinos and  $\gamma$ -rays and a small proportion of protons, whereas bottom-up models would produce predominantly charged nuclei.
2. The spectrum produced by the top-down models is relatively flat around  $\alpha \sim 1.5$ , whereas the bottom-up models produce a spectrum with  $\alpha \geq 2$ .

These differences do not imply that these models are mutually exclusive; in fact, there are a number of hybrid top-down/bottom-up models.

## 1.4 Propagation Models

In the above sections we mentioned that the observed flux of cosmic rays is not the same as the spectrum at the source. This is due to the fact that, once accelerated, the particles still need to cross a vast expanse of space, be it galactic or extragalactic. Within the galaxy the magnetic field is  $\sim 3\mu\text{G}$ . This both deflects cosmic rays from their initial trajectory and interacts magnetohydrodynamically with the ionized gas filling the galaxy. As the cosmic rays pass through this magnetohydrodynamic (MHD) fluid, they can generate Alfvén waves, a source of turbulent scattering for the cosmic ray. In the regime outside our galaxy the universe is filled with Cosmic Microwave Background Radiation (CMB), which cosmic rays must cross before reaching the galaxy and arriving at Earth. During this passage through the universe cosmic rays might undergo any number of possible interactions, the effects of which depend upon the source of the particle, its energy, and its composition [15, 32].

### 1.4.1 Galactic Diffusion and the Leaky Box

To determine an appropriate model for cosmic ray propagation in the galaxy the sources, the shape of the galactic halo, and the boundary conditions of the halo must be specified. (See

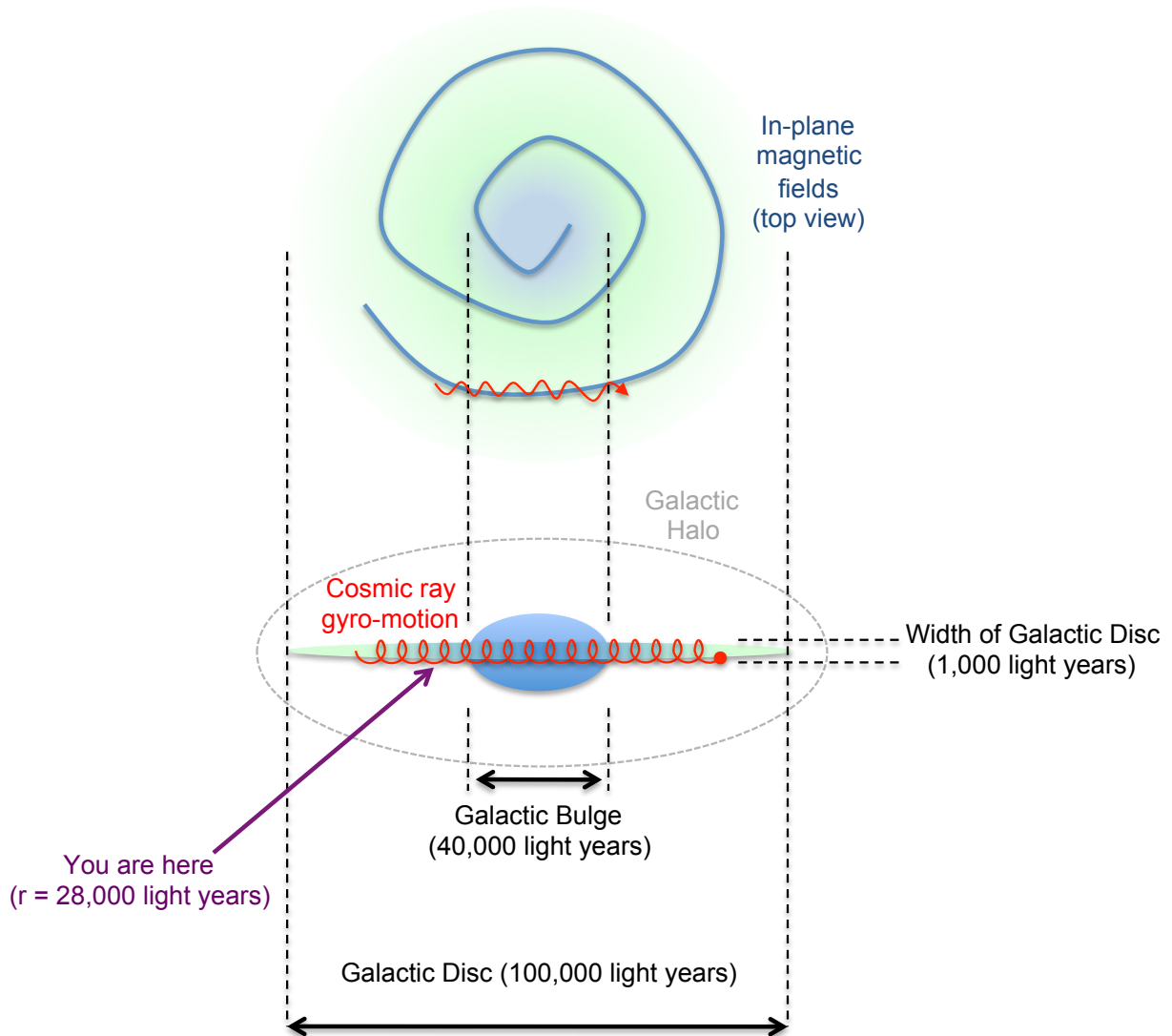


Figure 1.5: A diagram of the galaxy showing the basic dimensions of the galaxy, the motion with which a typical cosmic ray would traverse a magnetically homogeneous galaxy, and a view from above showing the galactic magnetic fields and a more realistic vision of how a cosmic ray traverses the galaxy.

Figure 1.5 for a schematic of the galaxy.) Possible energy loss and gain due to the interstellar medium, nuclear fragmentation, and radioactive decay of unstable nuclei must be incorporated into the diffusion equations. At this point the distribution functions can be calculated for different nuclei. Then a fit is performed to all available cosmic ray data to calculate the transport coefficients, the properties of their sources, and the size of the confinement region of cosmic rays in the galaxy. A full model of galactic diffusion can be as complex or as simple as the situation dictates [32].

A well-accepted approximation to particle diffusion in the Galaxy is the “leaky box” model [32, 33, 15]. This approximation assumes that cosmic rays propagate freely within the three-dimensional container of the galaxy which contains their sources. At each boundary there is a probability to escape the galaxy. On average, this escape will occur after time  $\tau_{esc}$ , when the particle has traversed on average  $\lambda_{esc}$  amount of matter. By definition,  $\lambda_{esc} = \rho_{ISM}\beta c\tau_{esc}$  for a particle of velocity  $\beta c$  crossing the interstellar medium of density  $\rho_{ISM}$ , where there is no dependence on spatial distribution, source density, and other energy dependent processes. However,  $\lambda_{esc}$  does depend on the particle energy. Since galactic magnetic fields are assumed to be the driving force behind the propagation and diffusion of cosmic rays, this energy dependence of the escape length is commonly fit as an inverse function of the particle rigidity,  $R = pc/Ze$ . This means that, with increasing energy, particles are more likely to escape the confines of the galactic magnetic fields; however, since the fundamental dependence is on rigidity, all particle types do not escape at the same energy. For a given energy, particles with more charge (like iron) have a smaller rigidity and are therefore more easily confined within the galactic box than particles with less charge (like protons). This causes the distribution of particles contained within the galaxy to become dominated by heavy particles as the energy increases, until at a certain energy the heavy particles also have a large enough rigidity to escape. This is, essentially, the “leaky box” model of cosmic rays. In many models the knee in the cosmic ray spectrum is presumed to be a result of the leaky box with different predicted cutoffs for particles of fixed rigidity, and therefore an increase in mass through the knee should be observed.

### 1.4.2 Extragalactic Interactions

The significant steepening of the power spectrum around 30 EeV is presumed to be a result of the increased interaction of charged nuclei with the cosmic microwave background (CMB) photons at EeV energies, due to the larger cross-section at those energies [33]. This causes the main feature of the GZK (Greisen, Zatsepin, Kuzmin) model, which is often called the “GZK Cutoff” or “GZK Limit”, above which only neutrinos, due to their nearly massless neutrality, are able to propagate without being bent or absorbed [34, 35].

### 1.5 Modeling the Knee

There are a variety of models describing the presence of the knee in the cosmic ray spectrum [36]. Figure 1.6 shows the customary parameterization of composition,  $\langle \ln A \rangle$ , vs energy for various theoretical models ( $\langle \ln A \rangle$  is described further in Section 1.6.3). Many models of the bottom up variety (described in Section 1.3.1) combine the acceleration and propagation effects described above, pointing to the limited acceleration power of SNR shocks (Figure 1.6(a)), the extragalactic contribution of acceleration in GRBs (Figure 1.6(b)), the increasing probability of escape in the diffusion models (Figure 1.6(c)), and other factors which could cause a change in the spectral index at increasing energies. Models of the top down variety (mentioned in Section 1.3.3) start on the other end, using the measurement techniques employed to explain the change in spectral indices along the cosmic ray spectrum. There are no data with which to check high energy cross-sections on which we base our model simulation; instead, extrapolations are used from lower energy accelerator data. However, it is entirely plausible that new (exotic) physics could exist in these regimes—such as interactions with background particles like massive neutrinos or photodisintegration in dense photon fields (Figure 1.6(d))—which could cause a misinterpretation of the particle distribution and, thus, the total energy of the shower of secondary particles which a primary cosmic ray incident on Earth’s atmosphere creates. These new physics phenomena could cause a miscalculation of the energy spectrum. The best way to distinguish between the two types of models, and the various models within those types, is to measure the cosmic ray composition. In the case of the exotic

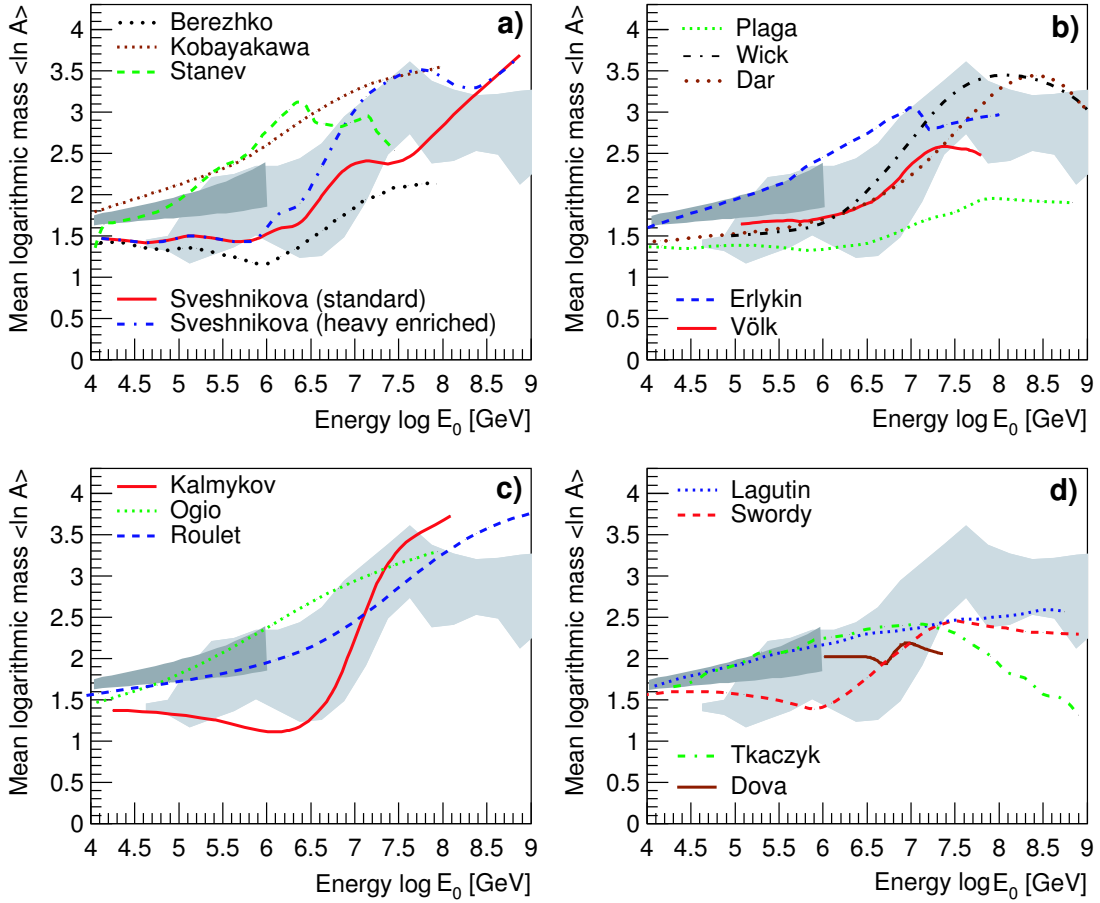


Figure 1.6: This figure compares  $\langle \ln A \rangle$  as a function of energy for a variety of different models. In each figure, the dark gray corresponds to a weighted average of all measurements made directly, while the light gray represents those measured indirectly. The lines are the expected  $\langle \ln A \rangle$  from a variety of models for cosmic ray sources and propagation: (a) acceleration in SNRs, (b) source and acceleration models including GRBs (Dar, Wick, Plaga), a single nearby SNR (Erykin), and reacceleration in the galactic wind (Völk) (c) galactic diffusion, and (d) propagation in the galaxy due to the Leaky Box Model (Swordy) or multi-scale galactic structures (Lagutin) combined with interaction with background photons (Tkaczyk) and massive neutrinos (Dova). It is clear that the different models predict a wide variety of mass results and the experimental results are not specific enough to pin down or rule out many of the theoretical models [36, 37].

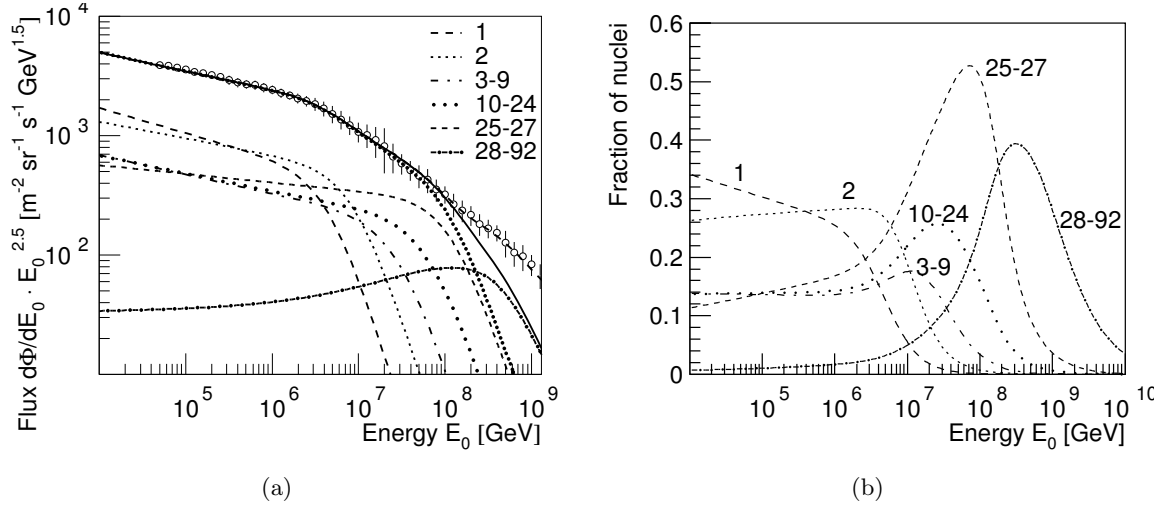


Figure 1.7: In Figure 1.7(a), the cosmic ray energy spectrum predicted by the poly-gonato model is shown for individual mass groups and as a sum for the all-particle spectrum. The points represent experimental data from many detectors. In Figure 1.7(b) the ratios of individual mass groups as expected by the poly-gonato model are shown [38].

models the knee position should scale by the atomic mass number of the primary type, whereas in models based on acceleration and diffusion the knee position is dependent on the charge number of the primary,  $Z = q/e$ . To measure cosmic ray composition at these energies, the extensive air showers produced by cosmic ray primaries incident on Earth's atmosphere are examined.

### 1.5.1 Poly-Gonato Parameterization

In an attempt to sort out which models are more appropriate, the measured spectral results for each particle type have been fitted to the all-particle spectrum and a many-knee (poly-gonato) model was developed, as shown in Figure 1.7 [38]. In this model, measured results provided the spectral indices and abundances of different particle types below the knee, while above the knee different indices were tested using three models for the knee position: a constant energy, a constant rigidity (i.e. a dependence upon  $Z$ ), and a dependence on  $A$ . In each case, the spectral index above the knee was tested to either be the same for all particle types, or to be a constant change for each type from the index below the knee. The best fit to the observed data is found with a choice of constant rigidity and constant change in index for each particle type. In this model the second knee corresponds to the cutoff of the highest mass particle, around  $10^8$  GeV. As seen in Figure 1.7(a),

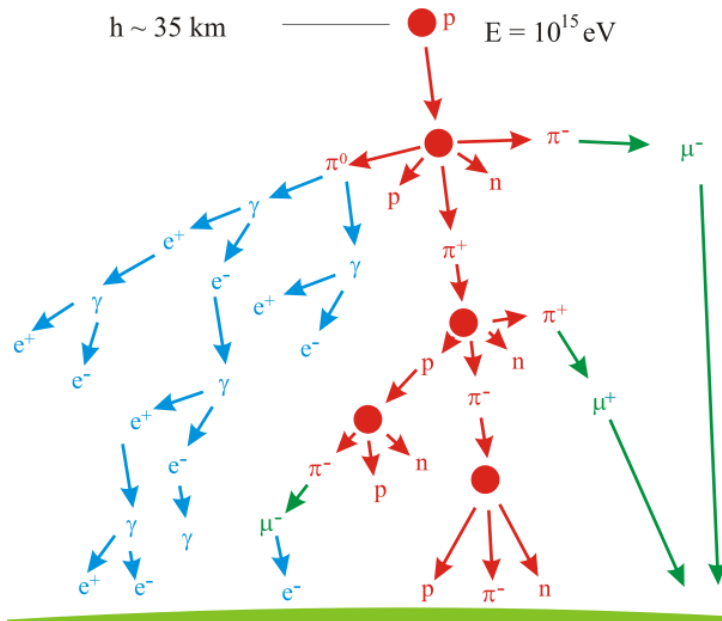


Figure 1.8: A diagram depicting an Extensive Air Shower. The shower begins with an incident proton of  $10^{15}$  eV. The proton collides with a nucleus in the atmosphere, resulting in three components which can be detected at the ground: shown at the left in blue is the electromagnetic component (photons, electrons and positrons), in the middle in red is the hadronic component, and to the right in green is the muonic component. Notice that the hadronic component further contributes to both the electromagnetic and muonic components, while neither of the other components contributes back to the hadronic component. A 1 PeV proton primary will produce on average 80% photons, 18% electrons, 1.7% muons, and 0.3% hadrons at sea level [39].

the spectrum from the model is much steeper beyond this point than the data indicates; however, this is often accounted for by including an additional ad-hoc extra-galactic component of cosmic rays at ultra high energies.

Though this model is phenomenological, it is an accepted and useful model for composition. In light of this, the poly-gonato model will be the primary model used for comparison to our measurements.

## 1.6 Extensive Air Showers

At energies around 1 TeV, the flux of cosmic rays falls to  $\sim 1$  particle per  $\text{m}^2$  per year: much too low to allow for feasible *direct* detection of primaries since the size requirement for the detectors to collect enough events to make a statistically significant measurement is simply too large for satellite or balloon payloads. However, when a cosmic ray crashes into Earth's atmosphere, it will interact with a (typically nitrogen) nucleus at heights of somewhere between 10 and 40 km

above the ground, producing a cascade of particles known as an air shower. If the energy of the incident particle is high enough, these showers will penetrate the atmosphere to ground level, where they can be detected using a variety of ground-based or underground detection techniques to gain information about the primary cosmic particles [39]. For example, an incident proton of 1 PeV typically produces around 500,000 charged secondary particles at the atmospheric depth of the South Pole Station (at a height above sea level of 2835 m, or  $\sim 680 \text{ g/cm}^2$  atmospheric depth) [40]. This strategy is known as *indirect* detection of cosmic rays.

The first interaction of the primary occurs at a depth in the atmosphere characterized by its interaction length  $\lambda \propto 1/\sigma$ , where  $\sigma$  is the cross-section for the interaction. The products of the first interaction include secondary hadrons, both charged and neutral pions, and kaons. The hadrons interact with other target nuclei creating an increasing shower comprised of hadronic energy (from the charged pions and kaons) and electromagnetic energy (from the neutral pions). The charged pions and kaons further decay into neutrinos (which pass unnoticed through the detectors) and muons, which only reach the surface if they do not decay in the atmosphere [15].

$$\begin{aligned}\pi^+/K^+ &\rightarrow \mu^+ + \nu_\mu \\ \pi^-/K^- &\rightarrow \mu^- + \bar{\nu}_\mu \\ \pi^0 &\rightarrow \gamma + \gamma \\ &\gamma \rightarrow e^+ + e^-\end{aligned}$$

Throughout the shower, the balance of particles is determined by the changing probabilities for interaction or decay. At the beginning of the shower secondary nucleons and electrons have high energies and the particle interaction rates are high, so the total number of particles is increasing. As the particles lose energy they drop below thresholds for further particle production, and the shower begins to thin out. In between these two phases of the shower is “shower max,” the point at which the particle count reaches its maximum.

This results in three components which can be detected at the ground: the electromagnetic

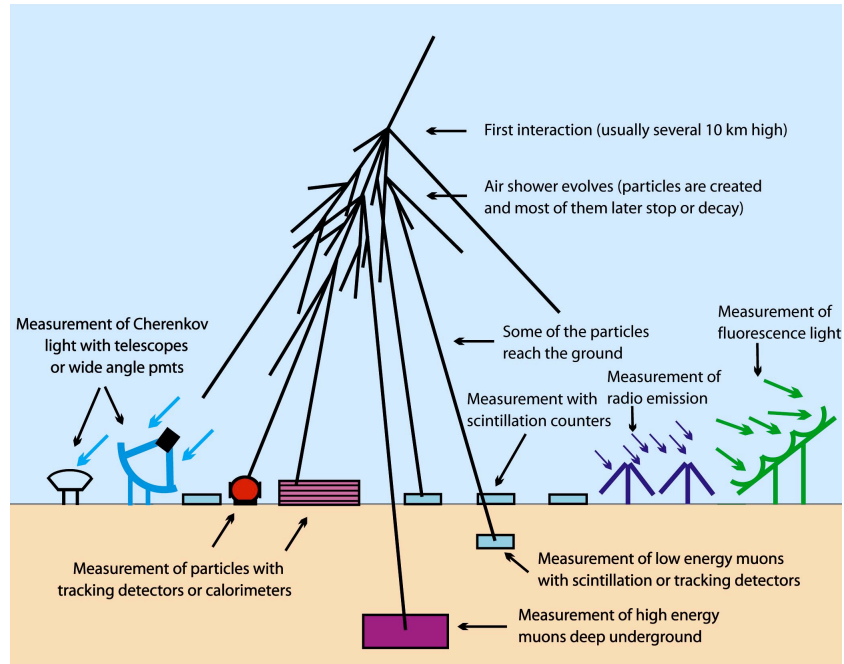


Figure 1.9: This diagram depicts a number of ground-based methods for detecting extensive air showers [41].

component (photons, electrons and positrons), the muonic component, and the hadronic component, as seen in Figure 1.8. A 1 PeV proton primary will typically produce on average 80% photons, 18% electrons, 1.7% muons, and 0.3% hadrons at sea level [41].

The secondary particles carry most of the kinetic energy and momentum of the primary and continue to further interact with nuclei in the atmosphere such that a hadronic cascade develops. (If the mesons do not interact, they decay quickly.)

In general, the direction of the shower resembles that of the primary, the particle number scales with its energy, and the secondary particle composition and position of the shower maximum vary with its nuclear mass.

### 1.6.1 Detectors

As the air shower produces a number of different particle types at ground level there are also a variety of indirect detection techniques [41, 39, 33]. Some common types of detectors include:

- Scintillators (usually in combination with photomultipliers), detecting the passage of charged

particles through a scintillating medium. At ground level the electromagnetic component is dominant, but if shielded from the electrons by some material (such as a mountain) they can also be used to detect muons.

- Ionization chambers, detecting hadrons
- Air Fluorescence detectors, detecting the fluorescence emitted by nitrogen molecules excited by the air shower particles.
- Air Cherenkov telescopes, detecting Cherenkov light from relativistic charged particles in the medium of the atmosphere.
- Water/Ice Cherenkov telescopes, detecting Cherenkov light from relativistic muons passing through the ice or water.

Most of these techniques are included in the diagram in Figure 1.9, which displays the different observation methods with respect to the part of the air shower they detect. Cross-checking across the wide variety of techniques for detecting air showers is crucial for elimination of errors in modeling or the detection technique itself.

## 1.6.2 Air Shower Observables

Extensive air showers (EAS)—the observable products of high energy cosmic rays—themselves form an important field of scientific study. Many observables are produced by air showers and measured by experiments, but we will restrict the present discussion to those which are directly applicable to this study:  $N_e$ , the number of charged particles and  $N_\mu$ , the number of muons.

### 1.6.2.1 Electromagnetic Component of EAS

The electromagnetic (em) component of an air shower is initiated by photons or electrons and is caused by bremsstrahlung and pair production. The number of charged particles in the electromagnetic component of an air shower depend upon how deep the shower is observed in the atmosphere. In terms of the depth in the atmosphere  $X$ , the function proposed by Gaisser-Hillas

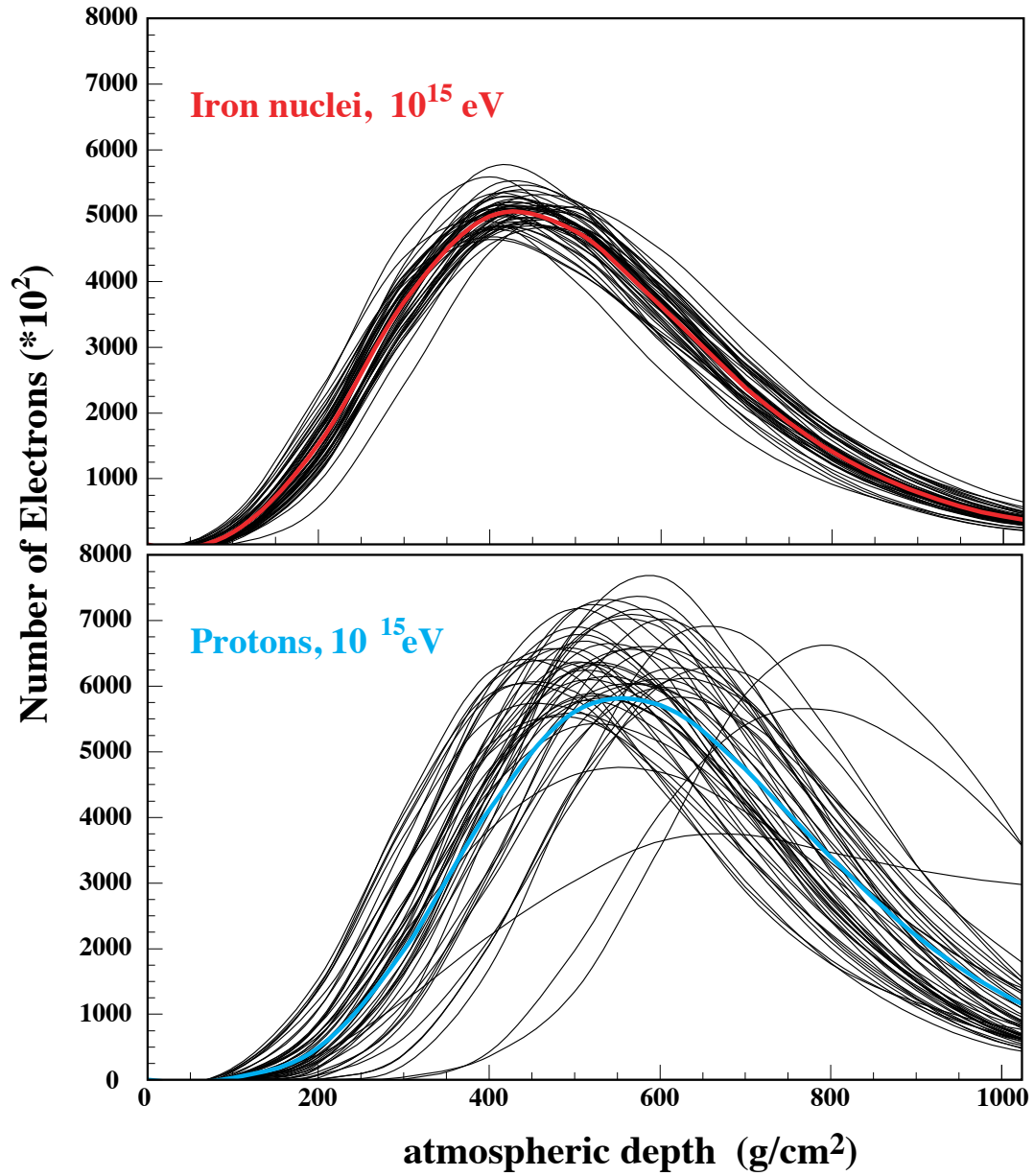


Figure 1.10: The longitudinal distribution by atmospheric depth of various proton and iron air showers generated using CORSIKA with the QGSJET hadronic interaction model [39].

to fit the longitudinal shower size profile is:

$$N_e(X) = N_{e,max} \left( \frac{X - X_1}{X_{max} - X_1} \right)^{\frac{X_{max} - X_1}{\lambda}} e^{-\frac{X_{max} - X}{\lambda}} \quad (1.8)$$

where  $X_{max}$  is the depth where the electromagnetic component of the air shower has the maximum number of charged particles,  $N_{e,max}$ ;  $X_1$  is the depth of the first interaction; and  $\lambda$  is the interaction length, approximately 70 g/cm<sup>2</sup> [42]. This function describes the longitudinal development of the air shower. At ground level, the lateral distribution of charged em-particles can be fitted by a function first established by Nishimura, Kamata, and Greisen (called the NKG function) [43, 44]:

$$\rho(r) = \frac{N_e}{r_M^2} C \left( \frac{r}{r_M} \right)^{S_{NKG}-2} \left( 1 + \frac{r}{r_M} \right)^{S_{NKG}-4.5} \quad (1.9)$$

where  $r_M$  is the Molière radius of the electrons, C is a normalization constant, and  $S_{NKG}$  is the shower age, which characterizes the longitudinal development of a shower, and is defined by:

$$S_{NKG} = 3 \left( 1 + \frac{2X_{max}}{X} \right)^{-1} \quad (1.10)$$

with atmospheric depth  $X$  and depth of the shower maximum  $X_{max}$  [33]. With the development of the shower, the age is defined such that it increases from 0 to 3, with 1 being the age at the shower maximum. The depth at shower maximum can be approximated as:

$$X_{max} \propto X_0 \left( \ln \left( \frac{E}{\epsilon} \right) - \ln A \right) \quad (1.11)$$

where  $\epsilon$  is the critical energy in air (where Bremsstrahlung losses dominate over ionization),  $X_0$  is the radiation length (the thickness over which an electron loses  $1 - (1/e)$  of its energy through bremsstrahlung) in air (37.1 g/cm<sup>2</sup>).  $X_{max}$  is dependent upon particle type, as shown in Figure 1.10. This is due to the fact that iron primaries are more likely to interact near the top of the atmosphere, whereas protons are more variable in their depth of first interaction. This is because an iron primary

is essentially a superposition of 56 proton primaries: therefore, the cross-section of the iron primary is larger and it is more likely to interact higher in the atmosphere, where the air is less dense. Furthermore, this implies that each individual nucleon has 1/56 of the energy, so it has less energy to lose in particle production. These effects combine to provide a much more predictable  $X_{max}$  for heavy primaries than for protons.

### 1.6.2.2 Muonic Component of EAS

The number of muons,  $N_\mu$  in an air shower as a function of the muon energy  $E_{mu}$  is parameterized as [45]:

$$N_\mu(E_\mu) = A \frac{14.5 \text{ GeV}}{E_\mu \cos\theta} \left( \frac{E}{AE_\mu} \right)^{0.757} \left( 1 - \frac{AE_\mu}{E} \right)^{5.25} \quad (1.12)$$

where  $A$  is the primary mass number,  $E$  is the primary energy, and  $\theta$  is the zenith angle of the air shower. This relationship can be simplified to:

$$N_\mu(> E) = KE^{-\gamma_\mu} \quad (1.13)$$

where  $\gamma_\mu$  is the muon spectral index of muons,  $\sim 0.757$ . Notice that  $K$  is highly dependent upon the mass of the primary, such that an iron shower has nearly a factor of two more muons than a corresponding proton shower [15].

### 1.6.3 Extracting Composition Information

While no single observable parameter can provide enough information to reconstruct both primary mass and energy, a wealth of techniques and parameters are available and can be combined to disentangle the primary mass and energy from the air shower observables. Different detectors have access to different parameters and use different analysis techniques to accomplish a composition study. A few recent examples are given in Table 1.1 below.

In all cases the observables are typically not used to identify primaries of individual showers, but rather to find a “typical” mass for each energy. Since the typical mass range covers more

than an order of magnitude in these studies, and because resolution of particle mass is limited, it is customary to discuss composition in terms of  $\ln(A)$ . This quantity is only measurable in a statistical sense and not shower-by-shower, so we are limited to measuring the mean-log-mass,  $\langle \ln A \rangle$ , as a function of energy.

Group	Detector type	Measured Parameters
KASCADE	Liquid Scintillator + PMTs Plastic Scintillator + PMTs Iron Sampling Calorimeter	Surface EM component Surface $\mu$ -component Surface Hadronic Component
Pierre Auger Observatory	Multi-faceted Fluorescence Systems Water Cherenkov Detectors	Air Fluorescence Surface EM Component
SPASE/ AMANDA	Surface Scintillators + PMTs Deep Ice Cherenkov Detectors	Surface EM component (S30) Deep Muonic component (K50)
IceTop/ IceCube	Ice Cherenkov Deep Ice Cherenkov Detectors	Surface EM component (S125) Deep $\mu$ -component (K70)

Table 1.1: A few recent experiments which incorporate multiple detectors acting in coincidence to help disentangle primary air shower properties from experimental observables.

#### 1.6.4 Composition with IceCube and IceTop

In this analysis we will use the new IceCube Neutrino Observatory to measure the surface electromagnetic component and the in-ice muonic component. We have access to parameters similar to those used for SPASE/AMANDA, our predecessor, although the surface array is of entirely different construction and the Observatory has a much larger detector volume ( $\sim 1 \text{ km}^3$ ). Furthermore, a novel analysis technique has been developed to allow for accurate reconstruction of primary mass and energy at energies from 1-50 PeV. The detector itself will be described in detail in Chapter 2, while the reconstruction of the observable parameters will be developed in Chapter 3.

## Chapter 2

### Detectors

As discussed in Chapter 1, one method to study cosmic ray composition involves an examination of two separate components of the air showers resulting from an incident cosmic ray interacting with the atmosphere. Currently near completion at the South Pole are two very large arrays with the capability to study the electromagnetic component of the air shower at the surface, and the muonic component in the ice. The goal of this analysis has been to develop a method to study cosmic ray composition using these two detectors. Before we discuss the analysis itself, we must have a complete understanding of the detectors we are working with; therefore, this chapter will be devoted to an overview of the IceTop and IceCube arrays.

#### 2.1 Terminology

Our detector is known as the “IceCube Neutrino Observatory”. The IceCube Neutrino Observatory involves three components: IceTop (IT), IceCube (IC, also referred to as “the in-ice array”) and DeepCore. This analysis uses only IceTop and IceCube with data from 2008, at which time DeepCore existed only as a future plan; thus, we will not discuss that particular sub-array.

#### 2.2 What We Are Hoping To Find: Detector Goals

The main goal of the IceCube Neutrino Observatory is to study neutrinos from extragalactic sources arriving at Earth. This goal was the driving force behind the design and location of the detector. Many models of the sources of cosmic rays (as described in Chapter 1) predict the production of neutrinos through interactions between high energy cosmic ray hadrons and the

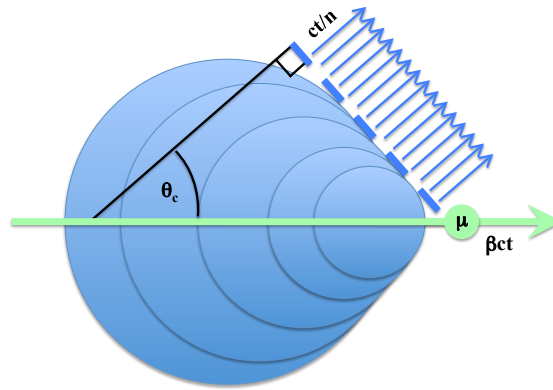


Figure 2.1: An incident neutrino, interacting in a medium with index of refraction,  $n$ , produces a muon  $\mu$ . The highly relativistic muon travels at a speed  $\beta = v/c$  which is greater than the speed of light in this particular medium, producing Cherenkov light, which radiates from the particle.

matter surrounding the source. Neutrinos therefore provide an additional way to search for the origins of high energy cosmic rays. Neutrinos are neutral, nearly massless, weakly-interacting particles; thus, while the cosmic ray hadrons will be isotropized between their source and Earth, the neutrinos observed on Earth will point directly back to their source. Therefore, from the perspective of a neutrino astrophysicist, the goal of IceCube is to reveal the source of high energy cosmic rays by “catching” neutrinos. Fortunately, not only are the sources of neutrinos and cosmic rays closely related, so are the techniques we use to detect them on Earth; therefore, the IceCube Neutrino Observatory can serve as a multi-purpose detector. To this end, the IceTop Air Shower Array was included for three reasons: for calibration purposes of the in-ice array, as a veto against high energy cosmic ray background events and—its main purpose—as a cosmic ray detector which can act either independently or in coincidence with the in-ice array.

### 2.2.1 Cherenkov Light

Although IceCube is designed as a neutrino detector, the neutrino itself is not actually detected. When a neutrino interacts, it produces charged secondary particles. For example, high energy muons will be produced by the interaction of a muon neutrino,  $\nu_\mu$ . These high energy muons are indistinguishable from the high energy muons produced in cosmic ray air showers, which

we focus on in this work. These charged particles travel faster than the speed of light in ice, thereby producing Cherenkov radiation. This bluish light is the result of transitions to the ground state of atoms excited by the electromagnetic field of the passing particle, and is shaped like a cone of light behind the particle, as seen in Figure 2.1. This cone is analogous to a wake behind a boat moving through water, or a sonic boom produced by a jet traveling at greater than the speed of sound. This conic shape is due to constructive interference, and its opening angle can be calculated:

$$\cos\theta_c = \frac{c}{v_{\text{particle}}n_{\text{medium}}(\lambda)}, \quad (2.1)$$

where  $n$  is the wavelength-dependent refractive index of the medium.

The number of photons emitted per unit length by a relativistic particle is given by the Frank-Tamm formula [46]:

$$\frac{d^2N}{dx d\lambda} = \frac{2\pi\alpha z^2}{\lambda^2} \sin^2(\theta_c(\lambda)) \quad (2.2)$$

(in terms of  $\alpha$ , the fine structure constant, and charge  $z$ ) and can be calculated for the relevant IceCube parameters, resulting in about 200 photons/cm (independent of the particle energy) in the relevant spectral range from 300 nm to 600 nm. In addition to producing Cherenkov radiation, as a muon passes through the ice it will also lose energy through various processes such as ionization, Bremsstrahlung, photonuclear interactions, and  $e^+e^-$  pair production. For highly relativistic muons, the dominant energy loss mechanisms result in the production of yet more relativistic particles, each of which will also produce Cherenkov radiation. This means that the total Cherenkov light yield (which is proportional to the number of relativistic particles) is a measure of the energy lost by the incident muon in the detector. In this sense, a Cherenkov detector acts as a muon calorimeter within which muons from air showers (and from neutrinos) create Cherenkov light, which our detectors collect. We then back-calculate the energy lost in our detector from the Cherenkov light deposited. This will be discussed further in Chapter 3.

### 2.2.2 Detection Medium and Environment

In order to observe the Cherenkov light we are interested in, we require a very large, very transparent medium. Man-made materials are too expensive on this scale; thus, neutrino astronomers took to the field, scouring the globe in search of large quantities of natural media in a sufficiently dark location (for low background), with high enough transparency (for high signal), and at sufficient depth (to avoid being dominated by the cosmic ray muon flux) such that a detector could observe the Cherenkov light derived from the original neutrinos. This search has led us to two materials: deep water and deep ice. There have been a number of experiments designed to use deep water (for example, DUMAND, ANTARES, BAIKAL, NESTOR, and the future KM3Net), but the only other detector to have used ice was IceCube’s predecessor, AMANDA [40]. Ice has a number of advantages: it is a very stable environment, it is easy to control the location of our detectors, and we can predict the state of the ice around them to reasonable accuracy. Another advantage of our experiment is its location. First, the South Pole already had the infrastructure necessary to support a large scientific endeavor like IceCube, which helps to increase efficiency and keep down costs. Additionally, the South Pole is very cold, with typical temperatures ranging from around  $-75^{\circ}\text{C}$  in the winter (July), to around  $-20^{\circ}\text{C}$  in the summer (January). The sun rises and sets once per year, which means that there is only a single day (the summer is marked by sun, the winter by darkness). Due to these very unique circumstances the environment of the detectors, though extreme, is very stable.

A further location-related advantage is that the South Pole is at an altitude of 2835 m, which means the surface array is at an atmospheric depth  $\sim 680 \text{ g/cm}^2$ , near that of the shower maximum,  $X_{max}$  (as defined in Equation 1.11) for energies in the region of the knee in the cosmic ray spectrum. We therefore expect a smaller energy resolution from our surface array, a distinct advantage over air shower arrays located at sea-level.

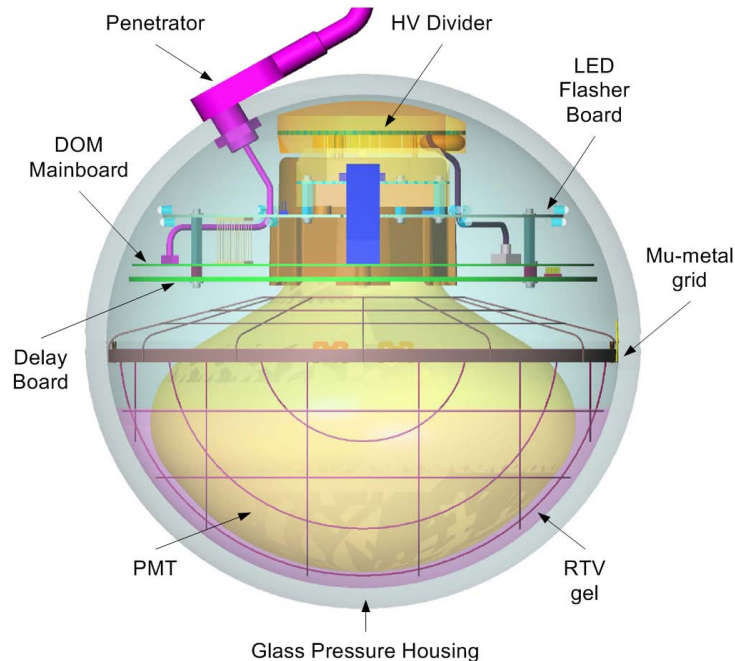


Figure 2.2: The Digital Optical Modules (DOMs) are the basic component of the IceCube Neutrino Observatory. They contain a 10 inch PMT (in gold), which is shielded from the Earth’s magnetic field by a mu-metal cage. The PMT is optically coupled to a pressurized glass housing, which also encloses the DOM readout electronics, a high-voltage flasher board with 12 LEDs, and a high voltage generator. The DOM acts as an independent data acquisition unit looking for Cherenkov photons in the South Pole ice.

## 2.3 Seeing the Light: Detectors

Now that we have reviewed our goals and discussed where to begin our search, the question remains: How do we “see” this Cherenkov light? For this express purpose we have developed eyes, called Digital Optical Modules (DOMs), as seen in Figure 2.2. These DOMs are deployed as the main working component of both the IceCube detector in the ice and the IceTop surface array.

### 2.3.1 DOMs

The basic component of a DOM is the photomultiplier tube, or PMT. A PMT is a high voltage device designed such that a (Cherenkov) photon, upon hitting the PMT’s photocathode, will interact via the photoelectric effect to produce an electron. This electron is accelerated toward an array of high voltage plates, initializing a cascade of electrons (thus “photo-*multiplier*”) such that for an incident photon of a given energy, a certain number of electrons will be produced. (This number is called the gain, and is determined by the applied high voltage.) The charged electrons

then arrive at an anode on the opposite end of the tube and are detected, meaning that a PMT is capable of observing a single photon.

The PMTs used for all DOMs are the (rather large) 25 cm Hamamatsu PMTs (Model R7081-02), which have a quantum efficiency of  $\sim 25\%$  at their maximum wavelength, meaning that only a fraction of all useful photons will be detected. The single photon time resolution of these particular PMTs is about 3 ns. The PMT is operated at a relatively low gain, typically  $10^7$ , allowing for very good linearity for large signals up to more than 300 photoelectrons/10 ns. Even very bright pulses of more than 5000 photoelectrons may be recorded while preserving the original photon arrival time distribution. The performance and characteristics of the PMT used in IceCube has been described in detail in [47].

The raw analog waveform resulting from each pulse is sent to a mainboard where it is split between a trigger discriminator and a delay board, which delays the signal by 75 ns using an 11.2 m long stripline. The delay allows for capture of the entire waveform—both before and after the trigger initialization. If the discriminator’s threshold (which is set to  $\sim 0.3$  photoelectrons) is exceeded, the delayed signal is given a rough time-stamp via a 40MHz high stability crystal oscillator with timing resolution of  $\sim 2$  ns, and continues on to an ATWD (Analog Transient Waveform Digitizer). In order to cover the entire dynamic range, the PMT signal is recorded by three ATWD channels independently with amplifier stages of 0.25, 2, and 16. If local coincidence (LC) conditions (described below) are met, the analog waveform is digitized. Additionally, since the digitization process takes  $\sim 100 \mu\text{s}$ , there is the possibility that a second event will occur during this timeframe. To this end a second ATWD substitutes for the first ATWD while it is occupied. The 2-ATWD system together with event rates of a few Hz provide us with a near-zero deadtime. The total amount of time to record an event is  $\sim 420$  ns [48, 49].

Of further note is that each DOM contains 13 LEDs: one ultraviolet LED on the mainboard, which can calibrate the transit times to the local PMT, and 12 LEDs on a dedicated flasher board, used for calibration of other DOMs. These components—the PMT (which is shielded from magnetic fields by a Mu-metal grid), mainboard, delay board, and flasher board—are all housed within a

13 mm thick, 35.6 cm diameter, pressurized glass sphere, as seen in Figure 2.2. This sphere is optically coupled to the PMT through a gel which was chosen specifically for its transmission properties. The glass sphere has a UV cutoff near 300 nm, and above 500 nm the ice begins to lose transparency (as seen in Figure 2.10 in Section 2.3.2.11). Once frozen, the glass sphere is considered completely optically coupled to the ice—in other words, there are no air-gaps which would allow for miscellaneous reflections of our precious light. As each DOM is intended for use in the Antarctic Ice this glass sphere is pressurized to 0.5 atm using dry nitrogen to ensure the structural integrity of the sphere (the DOMs are designed to operate reliably for at least 15 years in their cold, high-pressure environment) [49].

Since it is not feasible to access a DOM once it is frozen, each DOM is rigorously tested at least three times. Each DOM has a DOM-ID, a mainboard-ID and, to make the process easier for those involved, an actual name. (Usually DOMs are named for places, animals, or inanimate objects, but sometimes they are given names like “Karen\_Andeen”, see Figure 2.4.) First, each subsystem is individually tested prior to final assembly. Following assembly, the DOM is subjected to a full battery of performance tests in a special Dark Freezer Laboratory (DFL) over the course of 3-4 weeks. These tests can be thought of as DOM boot-camp: they mimic the data acquisition and optical duties of the DOM at the South Pole, and each test is run in succession at up to five different temperature settings between  $-55^{\circ}\text{C}$  to  $25^{\circ}\text{C}$ . Those that have problems at this stage are evaluated for repair and tested again—some DOMs were tested many times over and a few were found to be completely unreliable as detectors and have been put to work in the field of public outreach. Once this stage is passed, the DOM is shipped in specially designed packaging to the South Pole where it is put through a similar battery of tests one last time prior to deployment.

In summary, each DOM is a complete, autonomous, highly reliable data acquisition system, specifically designed to collect Cherenkov light (emitted by charged particles) as waveforms which can be used to analyze either the integrated charge (proportional to the number of photons collected), or to study the underlying physics of the time development itself.

## 2.3.2 Arrays of DOMs

As spectacularly self-sufficient as an individual DOM is, a single DOM by itself is not very useful in the grand scheme of searching for neutrinos or cosmic-rays—a very large volume containing many DOMs is necessary for particle detection. Thus, we are currently in the process of deploying 4800 DOMs in the deep ice to form IceCube and 160 DOMs at the surface to form IceTop. These DOMs are laid out in a configuration very similar to that shown in Figure 2.3 (the configuration has recently changed, so this figure is not completely up-to-date).

### 2.3.2.1 IceCube

When complete, the in-ice array will fill a volume of  $1 \text{ km}^3$  of ice with 80 vertical strings buried in the Antarctic ice at depths between 1450 m and 2450 m beneath the surface. Each string is separated from its neighbors by  $\sim 125$  m, in a triangular grid formation. This spacing defines the air shower detection threshold to be around 300 PeV (with the trigger conditions described below). Equally spaced at 17 m along each string are 60 DOMs which detect the Cherenkov light resulting from muons produced either by cosmic ray air showers, or by neutrinos.

Each DOM is connected to the surface via a single twisted copper wire pair which it shares with its neighboring DOM. The twisted wire pair is incorporated into the full “Surface to DOM Cable Assembly”, which spans 2540 m—the distance from the bottommost DOM to the Surface Junction Box (SJB)—and therefore requires two 25 kN strength members. (Notice that this is an extremely long cable. This length is one of the main motivations to digitize the signals onboard the DOMs. This allows for a transmission of data without the signal quality loss which would be a problem for analog signals.) At the DOM, the connection is made using a specialized connector which is waterproof to 10,000 psi—these connectors become very brittle below  $\sim 25^\circ\text{F}$  requiring great care not to crack them during installation. The SJB connections are made using military-grade round metal shell connectors, but these connections are not made until after the string is deployed.

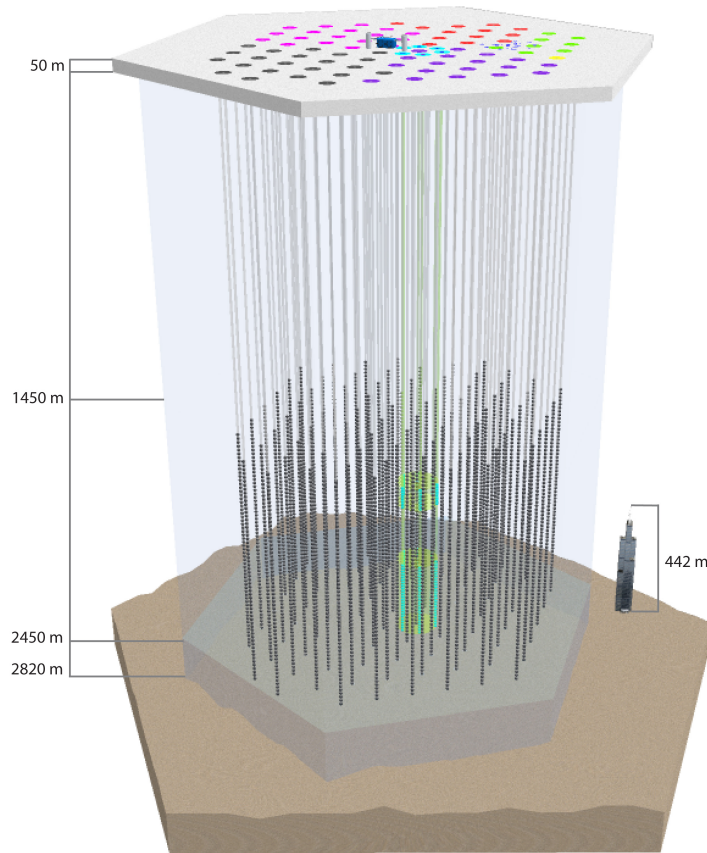


Figure 2.3: A schematic of the combined IceTop and IceCube arrays. *IceTop* is at the surface, where each colored dot represents a station containing two tanks and four DOMs, which is separated from its neighbors by 125 m. The *firn* layer, which is snow rather than ice, comprises the first 50 m below the surface. From the Surface Junction Box (SJB) at the IceTop station, the cables traverse 1450 m of ice before reaching the first *IceCube* DOM, and another 1000 m before reaching the 60<sup>th</sup> DOM at 2450 m depth, which indicates to a DOM separation of 17 m. The *bedrock* (i.e. Antarctica’s ground) begins only 170 m below the bottommost DOM. The green cylinder indicates *IceCube-DeepCore* (ICDC), a series of condensed strings of high quantum efficiency DOMs of 8 m DOM-spacing, concentrated primarily in the especially clear ice below the *big dust layer* (around 2000 m depth). For a sense of scale, a cartoon of the *IceCube Lab* (ICL)—the center for all computing—is drawn at the surface, and an image of the Willis (née Sears) Tower is placed on the bedrock next to the detector. (The Sears Tower is slightly over a quarter of a mile, or 442 m, in height.)



Figure 2.4: A DOM being deployed. Around the hole are a rim and lining which extend 1 m into the hole and are added during deployment for safety purposes and removed later. The large cable on the left is the Surface to DOM cable assembly which spans the entire depth of the detector and connects all the DOMs to the surface. The black tail, or *penetrator*, coming from the DOM is the cable which passes all DOM information to that main cable. The PMT is facing downwards and the boards with the readout electronics (as described in Figure 2.2 and in the text) are visible from the top. Around the DOM, at its “waist”, is a metal band connected to three cables coming up toward the main cable (there are also three cables heading downward which are not visible from this angle): these comprise the DOMs *harness*, which also attaches to the main cable assembly to support the weight of the DOM (~20 kg). Each DOM has a name. This DOM was known as Darrel Hamilton until the person in charge of checking the DOM database discovered that the DOM Darrel Hamilton already existed: hence it was renamed as Karen Andeen so as not to confuse the database. It has DOM-ID TL9P6721, which is a code: T indicates that it has a long (15 m) penetrator cable, L indicates that it’s a high quantum efficiency DOM, 9 indicates that it was assembled in 2009, P indicates that it was assembled at PSL in Stoughton, and 6721 indicates that it was one of the last DOMs assembled at that location. This DOM was deployed on string 86, a DeepCore string, number 8. *Photo by F. Descamps and A. van Overloop, courtesy of M. Krasberg*

### 2.3.2.2 Drilling and Deployment of DOMs

Once the DOMs are connected via the cable assembly, they are deployed into a hole which has been drilled using a hot water drilling system. The drilling technique is the most time-intensive step of the deployment process. The hot water is provided from a temporary drill camp consisting of 15 buildings dedicated solely to providing hot water—they contain heaters, generators, storage tanks and pumps. The hot water is then pumped out to the drilling location via a supply hose, which is connected to a 2.5 km drill hose. The end of the drill hose is connected to a nozzle designed specifically for this purpose, which is then lowered at a certain rate depending on the desired width of the hole. (Sometimes it is necessary to use a drill hole to run other tests prior to installing the DOMs, in which case it is crucial to make the hole slightly wider to prevent the string from becoming stuck part-way down due to refreezing, as was the case for one of the AMANDA strings.) The total time to drill a standard hole—which requires a minimum width of 45 cm at the time of string deployment—and ream the drill hose back to the surface is 28 hours on average (not including the time it takes to drill through the loosely packed firn layer at the surface, for which a separate drill is used) and requires a team of ice drillers working around the clock. The deployment itself—which consists of attaching the DOMs to the Surface-to-DOM Cable Assembly as the main cable is loosed down the hole—can be completed in 4.5-5 hours; however, some strings in recent years have taken 10 hours to deploy, and the deployment of the first IceCube string took 18 hours. The deployment team usually consists of a combination of scientists and drillers.

### 2.3.2.3 IceTop

Each in-ice string has a corresponding IceTop station (situated within  $\sim 25$  m of the in-ice hole), which means that IceTop will cover an area of  $1 \text{ km}^2$ . Each station consists of two ice Cherenkov tanks containing two DOMs apiece which will measure the electromagnetic component of the incoming cosmic ray shower. (A through-going muon produces  $\sim 130$  photoelectrons.) Each DOM is of adjustable gain, so to increase the dynamic range of the detector one DOM in each tank is operated at low gain (LG) while the other is operated at high gain (HG). (The specific settings

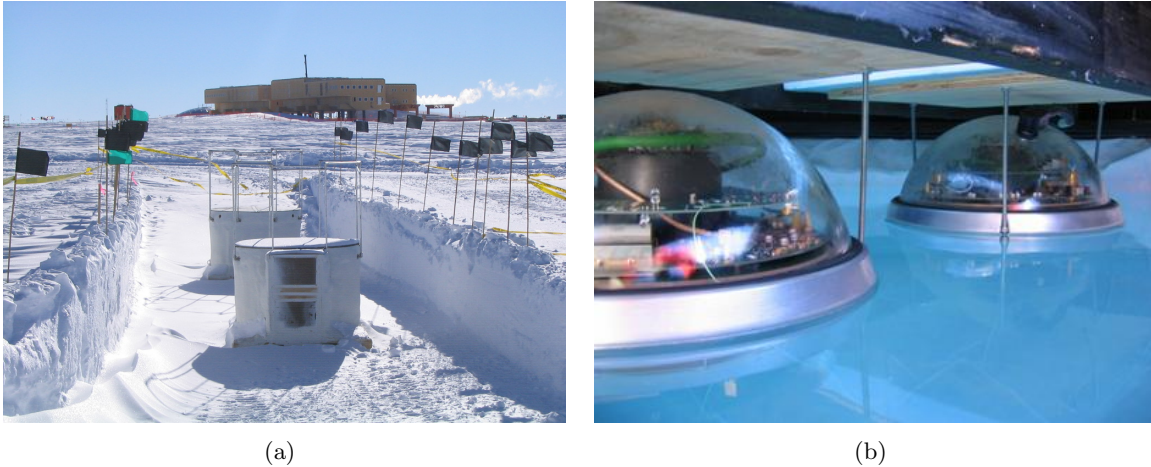


Figure 2.5: Figure 2.5(a) shows a view of a single IceTop station with the South Pole station in the background, about 1 km away. The station consists of two tanks which are 10 m apart and placed in a trench about 1.5 m deep to reduce snow drifting. The metal frames on top of the tanks are used to attach sun shades, which help to keep the freezing process uniform: both are removed at the end of the deployment season, once the tanks are completely frozen. The Surface Junction Box (SJB) was installed between the two tanks once the string corresponding to this station was deployed. Figure 2.5(b) offers a side view of the inside of an IceTop tank. Each tank consists of two DOMs, which are frozen using a complicated freezing technique to create crack-free bubble-free optically clear ice (note that in this the DOMs are imbedded in ice, not water). The DOMs are mounted to hangers below a wood platform, which is helpful during installation and provides some structural protection after deployment. The tanks themselves are lined with a reflective coating which can also be seen from this perspective. (*Photos by Daan Hubert*)

for the DOMs will be discussed below.) Each station is deployed in a shallow trench, as seen in Figure 2.5(a)—to minimize the buildup of snow (see Section 8.4)—in which a single tank is separated from its mate by 10 m, with the Surface Junction Box in between. This distance was chosen to allow for the detection of very small showers which will trigger a single station exclusively—these showers contain only one muon with enough energy to reach the deep detector and therefore can be used for calibration and veto studies of the in-ice array.

Each tank is cylindrical with a diameter of 1.9 m and a height of 1.1 m. The interior radius is 93 cm and the inner wall is lined with a light-proof diffusely reflective coating: in the first year a Tyvek lining was used for the four stations installed; in all following years an easier-to-install zirconium coating was used instead. The Tyvek has a reflectivity of  $\sim 90\%$  in the UV, while the zirconium has a reflectivity from 70-80%, which also prevented some of the signal smearing observed in the Tyvek tanks [50]. Once the lining is in place, the 2 DOMs are mounted looking downward into the tank with a center-to-center spacing of 58 cm. Similar to the in-ice array, each DOM is

then connected via a delicate waterproof connector to its own copper wire pair which runs from the tank to its associated SJB. Once all DOMs are connected, surface cable is laid which carries the wires for all 64 DOMs to the IceCube Lab for power supply and data taking (described below).

Once the tanks have power—required by the Freeze Control Units described next—they can be filled. Filtered water from the in-ice drilling system is used to fill each tank to a depth of 90 cm. The top of the water is just below the metal “waist” of the DOMs, as seen in Figure 2.5(b), for optimum optical coupling between the glass sphere and the ice (once frozen).<sup>1</sup> The water is then frozen using a specially designed Freeze Control Unit (FCU) to create optically clear and crack-free ice. This is necessary since the less-dense ice forms from top-to-bottom and would hence be filled with trapped air bubbles and cracked from the water pressure beneath the advancing ice front if the excess air and water were not removed. The freezing process takes  $\sim 50$  days. To top it all off, a 20 cm layer of perlite dust is spread across the frozen surface of the ice, which reflects the light from below while preventing light from entering the volume of the ice from above. The positions of each tank are later calculated using standard surveying techniques, and are known to within 5 cm, as seen in Figure 2.9.

From the perspective of someone working on a coincident analysis, the fact that IceTop uses the same hardware as IceCube cannot be emphasized enough. This was not the case with the predecessors, AMANDA and SPASE, and along with the immeasurable benefit of having more experts to help with IceTop, this allowed for uniform testing across the entire Observatory, saved design and development costs, and simplified the integration of IceTop signals into the IceCube Data Acquisition System (DAQ).

#### **2.3.2.4 Data Acquisition**

The Surface Junction Box (SJB), which collects the signals from the four IceTop DOMs and all 60 DOMs on the affiliated IceCube string, is connected to the surface cable which brings the signals to the IceCube Laboratory (ICL). There, the surface cable is connected to a single DOMHub

---

<sup>1</sup>This design also allows access to the DOMs from the top so, in theory, we could replace the inner-workings of a DOM if one were to fail. This operation has not been tested thus far.

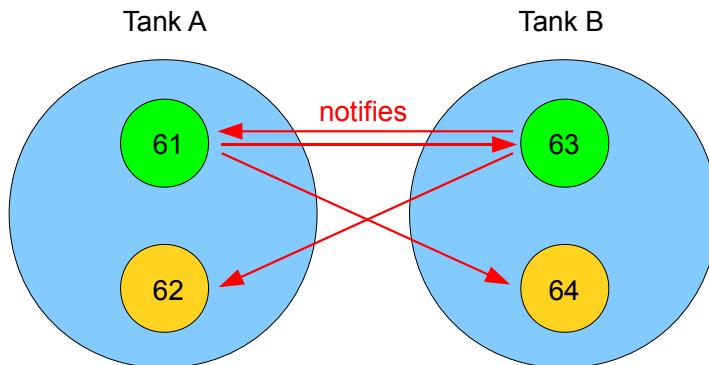


Figure 2.6: This figure describes IceTop Local Coincidence conditions for a single IceTop Station consisting of two tanks, A and B. The high gain (HG) DOMs are colored in green, the low gain (LG) DOMs are gold. The HG DOMs do the actual triggering, while the LG DOMs act as slaves and are only read out if the opposing HG is read out (ie, if the Local Coincidence trigger conditions are satisfied). *Diagram by A. Lucke*

which contains 8 DOR (DOM Readout) cards which control power and manage all communications (such as boot-up, calibration, data transfer and time calibration) to all DOMs. A master clock using GPS allows for absolute time stamping at this stage, which is recorded in UTC with an offset due to cable delays. This requires a team of around 15 people to literally *pull* the cables up from the level of the ice, through the ICL, to the DOMHubs so they can be connected in an orderly fashion.

Now that we've literally pulled everything together, we can consider our events. The event rate is so high in IceCube and IceTop that not all data can be read out. Therefore we make certain requirements so as not to occupy our DAQ with hits and events which are uninteresting for our analysis purposes. These requirements begin at the level of the DOMs with the local coincidence conditions, and continue to the full-detector event trigger requirements.

IceCube DOMs communicate with their vertical nearest neighbors via local coincidence (LC) links. This allows a hit DOM to transmit an LC signal to its neighbors. The DOM then waits for  $1 \mu\text{s}$  to see if one of the neighboring DOMs was also hit and returns a corresponding LC signal. If

a return signal is received, meaning at least two neighboring DOMs have both been hit, the local coincidence condition is satisfied. Until 2009 the detector ran in a hard local coincidence (HLC) mode, which only allowed LC hits to be digitized and sent to the surface, thereby eliminating isolated noise hits and freeing up valuable ATWD digitization time.

In IceTop the explanation is more complicated: see Figure 2.6. In this case, the HLC hits are defined as events where both HG DOMs in a station have detected a signal within the LC window of  $1 \mu\text{s}$ . The LG DOMs act as slaves to the HGs, meaning that they do not “notify” the DOMs in the other tank but only “listen” for a signal from the HG DOM in the complementary tank, in which case the full waveform information is read out.

Soft Local Coincidence (SLC) is also possible in both detectors. In this case, all hits are transmitted regardless of whether or not they satisfy the LC condition. In the case that they do not satisfy the LC condition, only the timing and charge stamps are transmitted—not the full waveforms. This mode was not used until 2009, and the SLC hits do not participate in the trigger conditions—they are simply read out with every triggered event.

### 2.3.2.5 Event Triggers

In addition to our LC requirements, we also require further trigger conditions to be met. To begin with, IceTop is always read out with any in-ice trigger and vice versa within a trigger window of  $\pm 10 \mu\text{s}$ . Furthermore, only LC hits, as defined above, participate in the trigger. Lastly, in-ice events are triggered if the in-ice Simple Majority Trigger condition (described below) is satisfied, and IceTop events are read out if the IceTop Simple Majority Trigger condition (described below) is satisfied.

### 2.3.2.6 Simple Majority Trigger

The Simple Majority Trigger, or SMT, is one of the basic physics triggers for both the IceTop and IceCube analyses. The IceCube conditions are satisfied if there are 8 DOMs satisfying the HLC conditions within a  $5 \mu\text{s}$  time window. The IceTop SMT condition is satisfied if there are 6 LC hits

(and therefore at least 2 stations) within  $5 \mu\text{s}$  of each other. The readout window is  $\pm 10 \mu\text{s}$ . The IC79 rate for this trigger is  $\sim 32 \text{ Hz}$ .

### 2.3.2.7 Calibration

The overall event rate for IceCube and IceTop is determined by two factors: the gain settings of the DOMs sets the base rate of available data, while the trigger settings reduce this base rate to something which is possible to record by selecting only useful events.

### 2.3.2.8 Waveform calibration

DOMs produce 420 ns long pulsed signals which undergo four main calibrations before they can be used for reconstruction:

- Droop Correction: DOMs from the first season suffer a droop at low temperatures. This was fixed after the first season of deployment.
- Baseline Subtraction: The short pulses may have some voltage offset due to noise. This noise floor is determined for each pulse using 40 bins of data before the pulse.
- Charge Integration: The time integral of the voltage waveform produces the total collected charge in Coulombs. This is then divided by a DOMs unique calibration voltage which corresponds to the signal of a single photoelectron (PE). This calibrated signal is now in units of PE which is proportional to the total number of measured photons.
- Leading Edge Time Extraction: This process determines the correct timestamp of the signal through a leading edge algorithm.

### 2.3.2.9 IceTop Tank Calibration

Even with calibrated DOMs, individual IceTop tanks may collect signals with varying efficiency, which could be due to variation in the tank materials (depending on year of deployment), cracks or bubbles in the ice, or variation in the amount of snow sitting on the top of each tank. To calibrate the tanks themselves, special muon calibration runs are used. In these runs, coincident trigger requirements are ignored and data is simply collected at a constant rate.

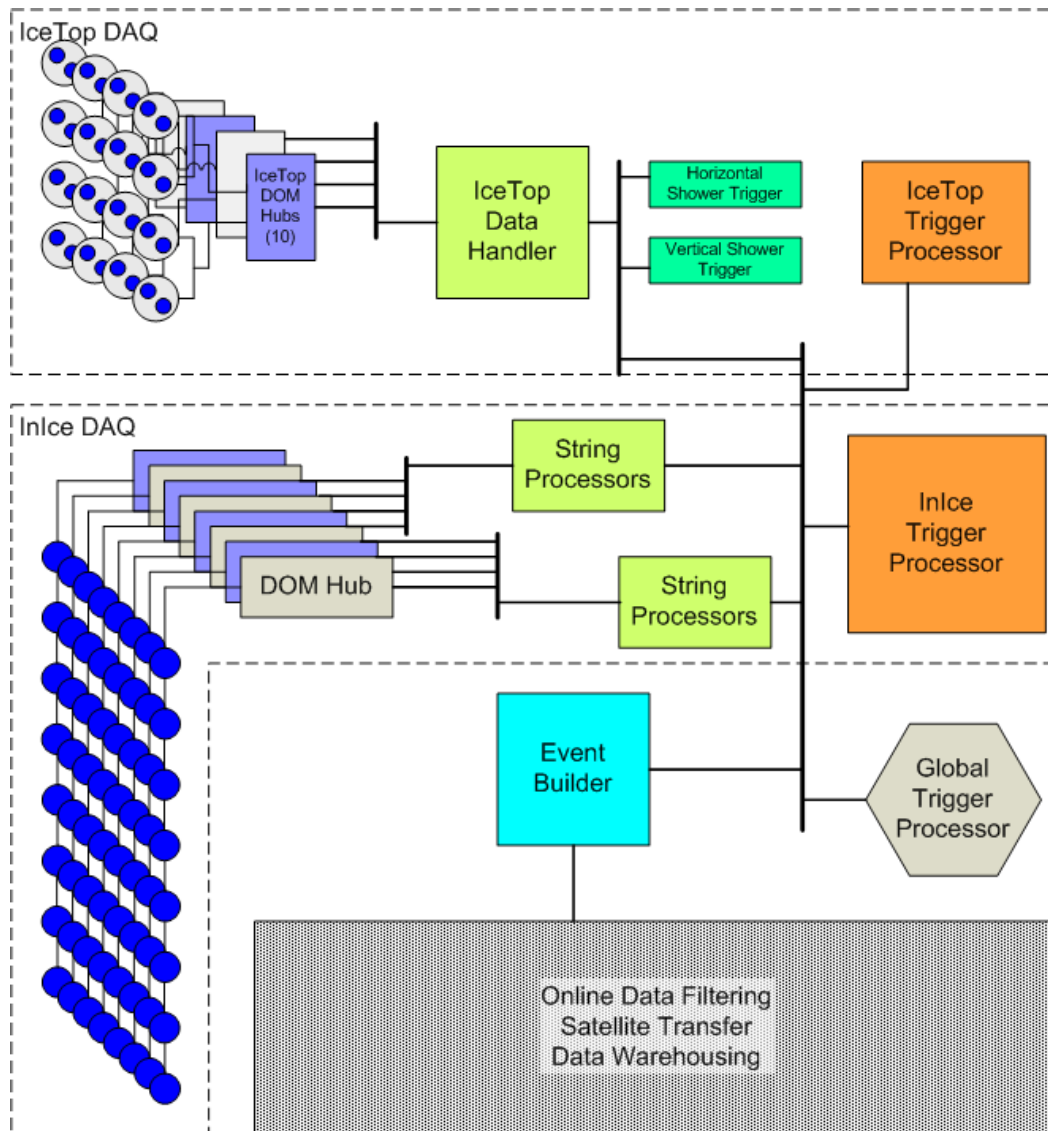


Figure 2.7: A schematic of the IceTop and IceCube Data Acquisition System. (Figure by T. Waldenmaier.)

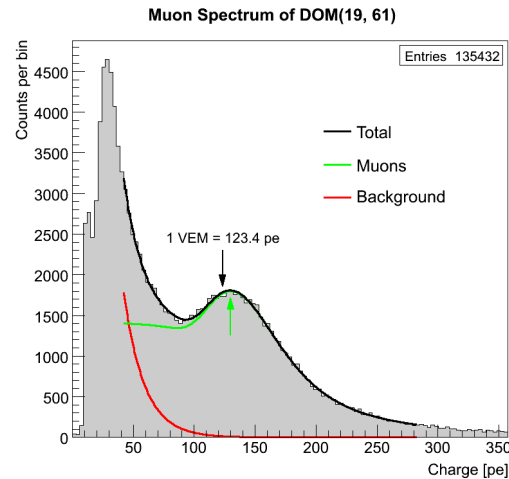


Figure 2.8: Muon calibration spectrum for a single IceTop tank. The peak corresponds to the voltage produced by a single muon traveling vertically through the tank.

Since muon energy deposition depends almost exclusively on the muon track length, a histogram of the tank output voltage has a sharp peak corresponding to the voltage associated with a track length equal to the height of the detector. Figure 2.8 shows this in detail. Application of this calibration results in a signal,  $S$ , in units of vertical equivalent muons (VEM).

### 2.3.2.10 Calibration

The first step in the geometric calibration uses different types of non-optical data (ie, that not recorded by the DOMs themselves) which is collected during drilling, deployment, and ground-based surveys. The next step uses data from flasher runs (where the flasher boards of the individual DOMs are flashed on) to determine relative depth offsets between strings. The final step is to check for deformations of the array over time due to ice shear, or movement of the ice at different rates at different depths. (It is known that the ice sheet is moving: at the current rate the detector will fall into the ocean at the edge of Antarctica in  $\sim 100,000$  years. However, the bottom of the array is thought to lag behind the top of the array.) In this case, the positions of the DOMs are determined



using down-going muon tracks which exclude the DOM (due to LC conditions) but from which there is data from the DOM. A likelihood technique is then used to find the best-fit position of the DOM [51, 52].

### 2.3.2.11 Ice Modeling

Once the position of each DOM is precisely known, we have one step left, which is to understand the ice around the DOMs. It is important to note that, while the South Pole Ice is the clearest in the world, that does not mean it is perfectly clear. The ice we use ranges from approximately 30,000 to more than 100,000 years old. Over the millennia, layers of particulate matter have been deposited on top of the ice sheet. Those layers are subsequently covered by more ice, thereby creating a horizontally layered dust-structure in the deep ice. These dust layers influence the absorption and scattering lengths of photons, so they must be well-mapped in order to properly understand our signals. To this end, a detailed, many-year study has been conducted to model the structure of the ice in our detector. This model is then compared with the data to be sure that we understand what we see. At wavelengths around 400 nm (the Cherenkov peak of our detectors), we find a typical absorption of  $\sim 110$  m and a scattering length of  $\sim 20$  m, which is defined as:

$$\lambda_s^{eff} = \frac{\lambda_s}{(1 - \langle \cos \theta_s \rangle)} \quad (2.3)$$

where  $\lambda_s$  is the scattering length and  $\theta_s$  is the scattering angle [51]. Figure 2.10 illustrates the optical properties by depth due to the dust layers in the ice within the volume of the IceCube array. An interesting feature in our ice is a large dust layer at a depth near 2000 m, which is marked on Figure 2.3 and which can be distinguished as a large peak in Figure 2.10. Below this dust layer, the ice is much clearer than anticipated [51, 53].

### 2.3.3 Goals Revisited

As discussed in the beginning of this chapter, the main goal of IceCube is to study neutrinos. Neutrinos are thought to come from a variety of sources. Some of these sources are expected to be

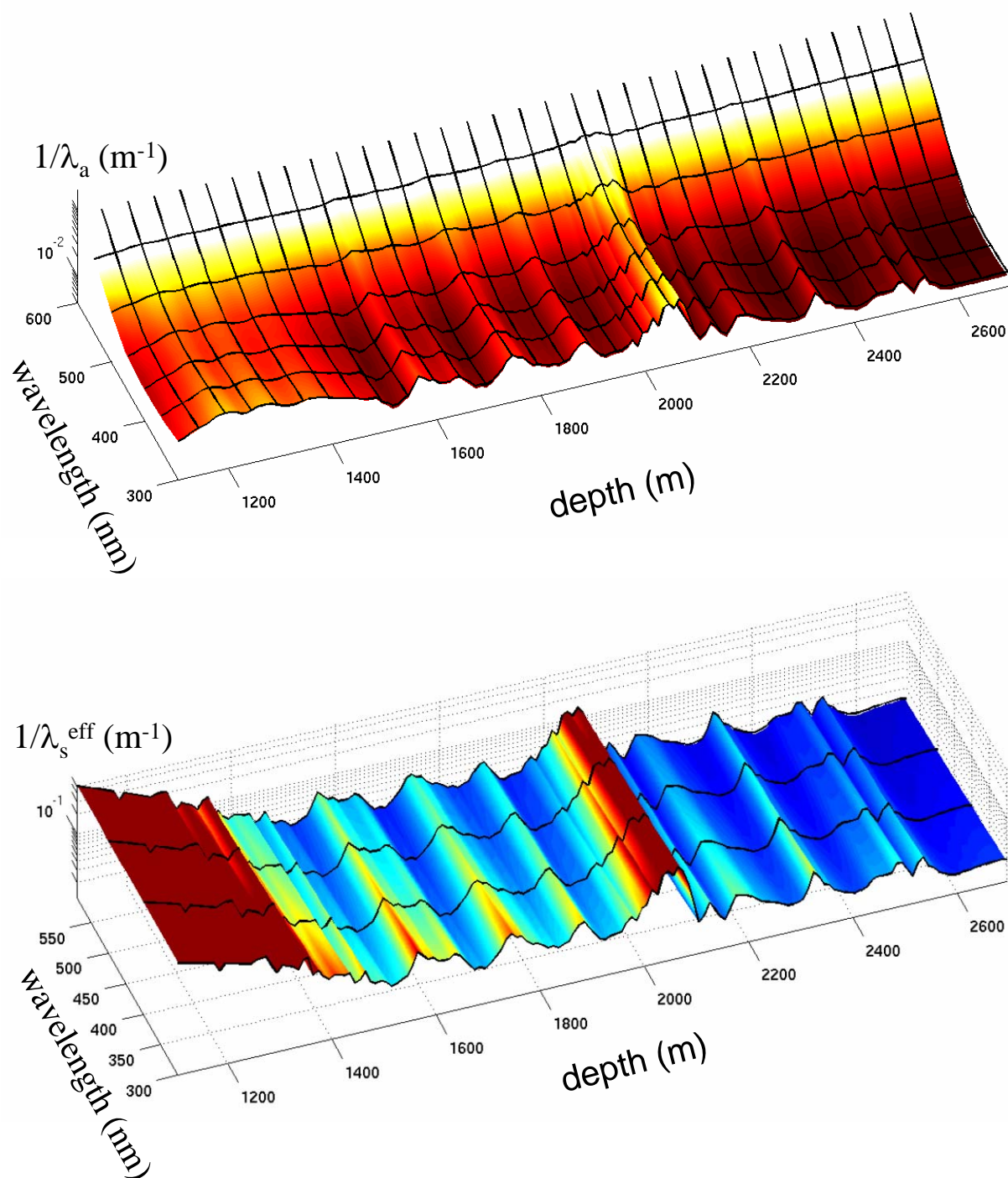


Figure 2.10: Inverse absorption length (upper panel) and inverse scattering length (lower panel) as a function of wavelength and depth. Notice that as depth increases, the clarity of the ice also increases. This is partly due to the integrated pressure of the ice above each depth; thus, at depths shallower than 1400 m there is a rapid increase in scattering due to the presence of air bubbles in ice, and below  $\sim 2100$  m there is much less scattering, indicating much clearer ice. The big spike in inverse scattering and inverse absorption around 2000 m is an indication of a very large dust layer [53].

transient, such as Gamma Ray Bursts and Supernovae bursts; thus, searches for these sources are based on time-dependent coincident observation with gamma ray observatories [54]. Other possible sources of neutrinos are more consistent in time: these are considered point-like and we search for them by location [55]. Still other sources, such as active galactic nuclei, are predicted to result in a diffuse flux of high energy neutrinos [56]. Any detection of neutrinos can rule out models of their production and help to develop new models for neutrino production and cosmic ray acceleration. Even a lack of detection (as is currently the case) will allow stringent limits to be set on the models that exist.

While the main goal of IceCube is to detect neutrinos, there are several other analyses that can be undertaken, such as searches for Weakly Interacting Massive Particles (WIMPs), magnetic monopoles, and other exotic particles, and of course, cosmic ray physics.

The main goal of IceTop is astroparticle physics, but it can also contribute to other fields. For example, a solar physicist might be interested to know that the untriggered discriminator rates in IceTop are related to the rate of low energy cosmic rays in the upper atmosphere, which is affected by disturbances in the solar wind caused by solar activity: in this way IceTop can be used as a solar neutron monitor [57]. IceTop can also be used to study high transverse momentum muon multiplicities—high- $p_t$  muons are produced by semi-leptonic decays of heavy quarks in the initial cosmic ray interaction [58], an analysis particle physicists would be especially interested in. It might also be possible to detect neutrinos with IceTop using very horizontal and therefore muon-dominated showers; however, these could be either very old showers which have passed through so much atmosphere that the electromagnetic portion of the shower has been stripped away, or they could be neutrino-initiated, and it might prove difficult to distinguish the two.

The main analyses coming from IceTop; however, will be related to the all particle energy spectrum and the cosmic ray composition. IceTop can identify a nearly-composition independent parameter related to the shower energy [50, 59]. This allows for various standard composition models to be tested: since the composition should be the same at all zenith angles, the data can be divided into three bins to check for consistency. This method provides a good handle on the com-

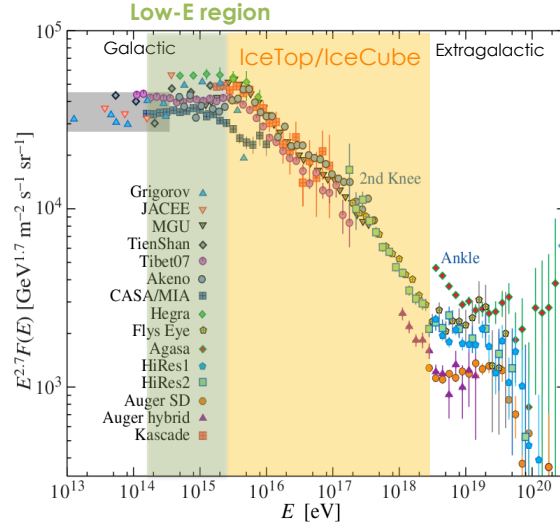


Figure 2.11: A depiction of the energy range spanned by the IceTop array: the transparent orange region is the standard range available to IceTop, while the transparent green depicts the range accessible using a new technique being developed especially to study these low energy showers [62]. (Figure from [63].)

position as well as a precise energy spectrum [60, 50]. Furthermore, with further study IceTop will be able to provide other composition-dependent parameters: the curvature of the electromagnetic component of the shower [61], which is dependent upon particle type, and a parameter measuring the low-energy muon content of the shower. These two parameters, together with the shower size parameter and a close look at zenith dependence, should provide enough information for a composition study with IceTop alone.

### 2.3.4 Cosmic Ray Composition

However, the most powerful technique for studying cosmic ray composition utilizes coincident data from both IceTop and IceCube. IceCube can measure the high-energy muonic component of the cosmic ray air shower, while the IceTop shower size is a measure of the electromagnetic component. Together, as discussed in Chapter 1, these two components can provide both the cosmic ray composition as well as the energy spectrum. An analysis was performed using the prototype detectors, SPASE-2 and AMANDA-B10, for which a parameter describing the muonic component of the air shower was developed (as is discussed in Chapter 3). A rotation technique was then employed to achieve a composition measurement, as shown in Figure 2.12(b) [40]. A new,

more flexible technique for this analysis was developed using data and simulations from SPASE-II and AMANDA-2, as found in other work [64, 65], and has now been applied to the IceTop and IceCube data from 2008. This new technique is the main focus of the analysis presented here.

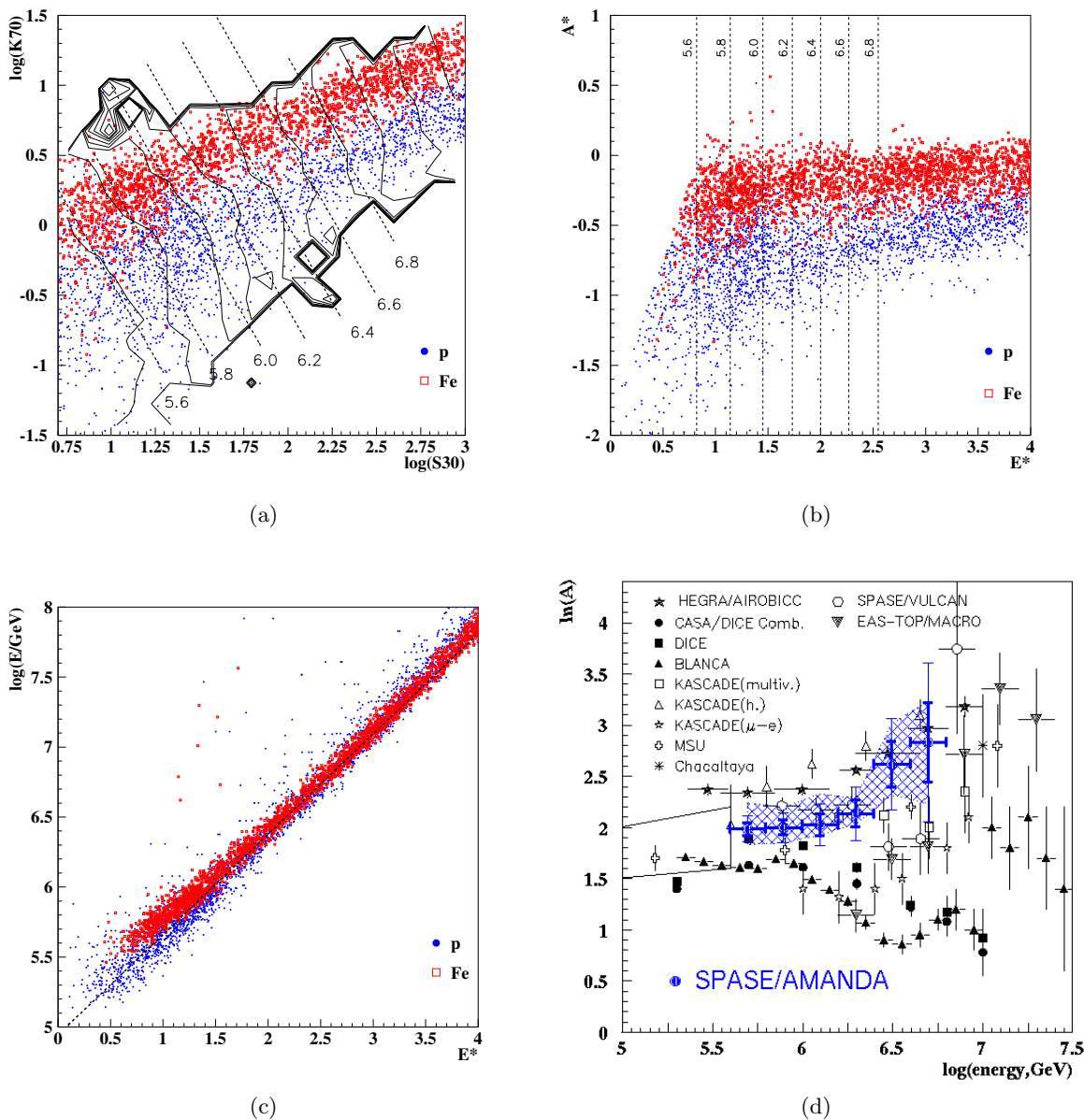


Figure 2.12: The previous method of achieving cosmic ray composition, developed using the SPASE-2/AMANDA-B10 detectors. Figure 2.12(a) shows constant contours in energy for proton (blue) and iron (red) simulations. The true energy contours are the jagged lines, which are then approximated by the dotted lines which denote the energy bins used for the analysis (in  $\log_{10}(GeV)$ ). Perpendicular to the approximate lines of constant energy is a line where the masses are approximately separated: these axes were called  $E^*$  and  $A^*$ . In Figure 2.12(b) shows the same simulation with approximate contours in energy after a rotation to the new  $A^*$  and  $E^*$  axes. Figure 2.12(c) shows a comparison of  $E^*$  to the true energy, and Figure 2.12(d) shows the final composition result, achieved by applying a maximum likelihood technique to the rotated  $A^*$  axis. [40]

## Chapter 3

# Reconstruction of Cosmic Ray Air Showers

For hundreds of years, archaeologists have been digging all over the earth to learn about civilizations past. With their patient hands and clever tools, they manage to piece together shards from a dig site that (to an untrained eye) appear to be no more than dust, into a pot, or a fountain, or a chair. When they've pieced together enough objects they can look at the collection and understand something about the people who used those objects: where they came from, what they knew, how they lived. When they have dug up enough sites around the world, and compared them with each other, and with other historical records, they can come to some consensus about the global interactions and understandings of civilizations past.

Event reconstruction is the physicists' version of an archaeological dig. As discussed in Chapter 2, our detector produces digital signals coming from photomultiplier tubes. Those signals correspond to light, and we know that the light comes from muons traveling faster than the speed of light in ice. In some cases the muons are the product of neutrinos (the background for this analysis). This is very unlikely. In most cases, the muons are the product of a cosmic ray smashing into the atmosphere and producing an air shower. The cosmic ray itself was produced by some astrophysical event long ago and far away, and has since propagated through the universe to us (as discussed in Chapter 1).

We start with our shards of light (seen in the event display shown in Figure 3.1), which we are trying to piece together to reconstruct the air shower. When we've pulled together a collection of air showers, we can study them and try to understand some new information about the initial

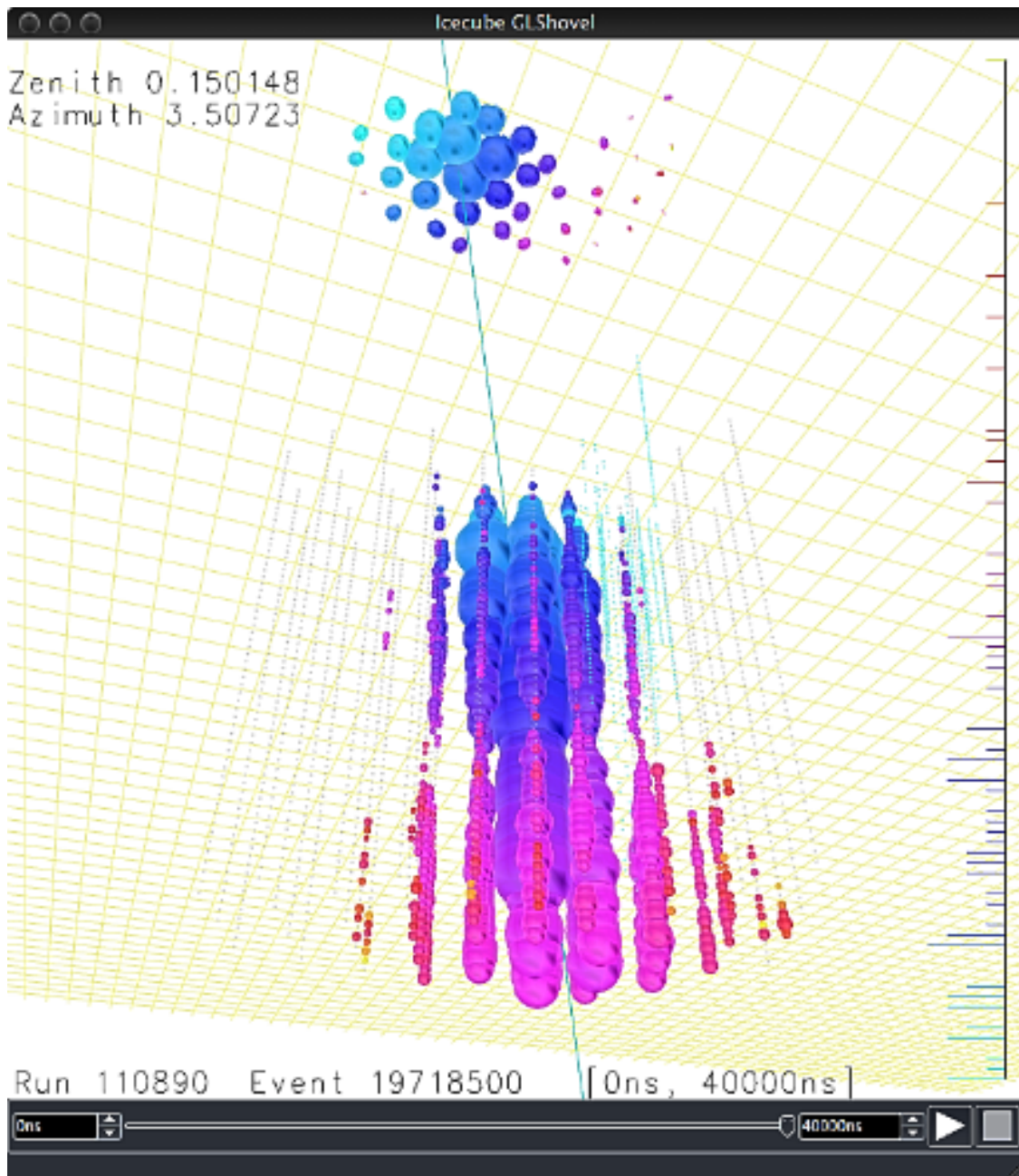


Figure 3.1: An event display from the IceTop/IceCube 40-string configuration of 2008. The colors represent the timing of the hits (light blue is earliest, dark red is latest), and the size of the sphere around a DOM represents the amplitude of light seen by that DOM. This was a very large event in which the “big dust layer” can clearly be distinguished as a ‘waist’ in the amplitudes just over half-way down the in-ice array.

astrophysical event that produced the cosmic rays, or about the way cosmic rays pass through the universe. When we've understood cosmic rays coming from multiple sources in the universe, we can begin to piece together the workings of the universe at large.

In summary, we need many trained eyes (DOMs), patient hands (currently typing), and clever tools to reconstruct the cosmic ray history of the universe. In this section we will be discussing the tools we use.

### 3.1 General Reconstruction Principles

In most detectors the size of IceCube and IceTop there is a large amount of raw data that we must understand. In our case, we can use the timing information across the entire array of PMTs to group the raw waveform amplitudes from each DOM into events. Each event—in the case of the composition analysis—is the result of a single air shower passing through the detector.

In Chapter 2 we reviewed how the events from the IceCube and IceTop detectors are processed at the lowest levels. This chapter will review the methods used for event reconstruction. To fully understand this discussion it is important to understand the two main goals of our reconstructions:

1. At the surface: the best possible measure of the electromagnetic component of the shower as discussed in Section 1.6.2.1)
2. In the ice: a parameter analogous to the muonic part of the air shower as discussed in Section 1.6.2.2).

Figure 3.1 shows an example of a shower in both IceTop and IceCube. One can easily see the interaction due to the electromagnetic component of the air shower at the surface, and the light deposit from the muons in the ice, along a track which we must reconstruct. High energy muons do not greatly deviate in the atmosphere (or the ice) from the path of the primary particle: they arrive at our detector tightly packed and are not distinguished as individual particles. We therefore refer to them as muon bundles.

The two most important things to focus on are the shower direction and the location of the shower's core in our detector. We will discuss what happens if the reconstruction does a poor job

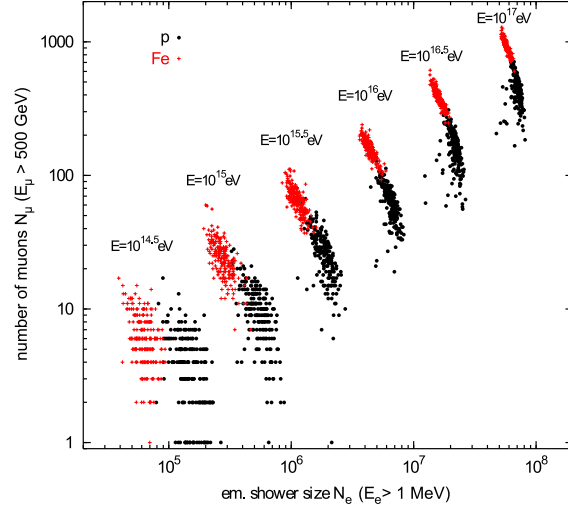


Figure 3.2: This is a well-known plot from Ralph Engel, in which a large number of proton and iron air showers were simulated with CORSIKA at distinct energies, as denoted in the figure. Along the y-axis is the number of muons above a muon energy of 500 GeV, a threshold which mimics that of the IceCube detector for muons in the ice (muons below 500 GeV tend to range out before reaching the in-ice array). It is notable that the proton/iron distribution become distinctly more vertical at higher energies. This is due to two effects: the electromagnetic portion of the shower is approaching shower max at the atmospheric depth of our detector, which occurs at different energies for protons and iron; and the Elbert effect [45] dominates the number of muons.

of finding these quantities later in this chapter.

A common technique to reconstruct a track is a maximum likelihood approach. Generally speaking, this is achieved by taking a first guess of the air shower’s track, then varying this track to find the most likely fit. In this analysis, the surface detector uses two algorithms to find an initial guess (COG and plane-fit), then uses a fitting algorithm to identify the track of maximum likelihood (Lateral Fit). The in-ice detector then uses the best-fit surface reconstruction as the “first guess” input to its maximum likelihood fitting algorithm (Muon Bundle Reconstruction). Alternatively, for typical in-ice analyses, an initial guess is used from the in-ice detector (LineFit). Though this first-guess in-ice algorithm is not used in the composition measurement reconstruction scheme, it does produce useful parameters for event selection which will be discussed in Chapter 4. These reconstruction algorithms (summarized on Table 3.1) are broadly used by the IceCube collaboration, and are not specifically the focus of this thesis, but for completeness we include a brief description of each algorithm in the sections to follow.

	First Guess Reconstructions	Likelihood Reconstructions
IceTop	ShowerCOG PlaneFit	LateralFit
In-Ice	LineFit	MuonBundleReconstruction

Table 3.1: Reconstruction algorithms useful for composition analysis. First Guess Reconstructions are simple algorithms which quickly produce the initial values for the much more accurate Likelihood Reconstructions.

### 3.2 Event Reconstruction in the Ice: Likelihood Fitting

The likelihood maximization technique is the basis of all sophisticated reconstruction algorithms in IceCube and IceTop. The basic idea behind a likelihood maximization is to develop a hypothesis track—described by free parameters such as the track direction  $(\theta_0, \phi_0)$  and vertex position  $(x_0, y_0, z_0)$ , which best describes a given event—with hits, amplitudes, and times provided by the DOMs. We begin with values for the track’s free parameters provided by a first-guess algorithm (as described below), and from there vary each free parameter in turn until the best fit is found.

The individual Poissonian likelihood,  $\mathcal{L}_{DOM}$ , that a photon *or lack thereof* as observed by a DOM,  $x_{DOM}$ , was caused by the hypothesis track  $\vec{a}$ , can be described with a probability distribution function, or PDF, and written as  $\mathcal{L}_{DOM} = p(x_{DOM}|\vec{a})$ . (Notice that most of our reconstructions use both DOMs that were hit and those that were not hit in our fit.) We define as the best fit among a given set of events the one that maximizes the overall likelihood  $\mathcal{L}$ , which is simply the product of the PDFs for the observations of all DOMs:

$$\mathcal{L} = \prod_{DOM's} \mathcal{L}_{DOM} = \prod_{DOM's} p(x_{DOM}|\vec{a})$$

For the in-ice array, instead of maximizing the likelihood we typically minimize the negative log likelihood

$$-\log(\mathcal{L}) = \sum_{DOM's} -\log(\mathcal{L}_{DOM})$$

which is the same idea but easier to manipulate. The two tricks to likelihood fitting are (a) to

find reasonable starting values for the tracks, and (b) to find an appropriate hypothesis fit to the distribution of hits. This will be discussed in more detail for each detector below.

### 3.3 Methods of Reconstruction: IceTop

#### 3.3.1 First Guess Reconstruction: Shower COG

The ShowerCOG fit calculates the center of gravity (COG) of the shower using a simple weighted average of the surface detector signals:

$$\vec{x}_{COG} = \frac{\sum_i \sqrt{S_i} \vec{x}_i}{\sum_i \sqrt{S_i}} \quad (3.1)$$

with signals,  $S_i$ , and distances from the shower axis,  $x_i$ . The ShowerCOG fit provides a first guess to the core location of the shower.

#### 3.3.2 First Guess Reconstruction: Plane Fit

The PlaneFit algorithm determines the approximate direction of shower propagation. This is accomplished by approximating the curved shower front as a simple plane propagating with speed  $c$  in the direction of  $\vec{n} = (n_x, n_y, -\sqrt{(1 - n_x^2 - n_y^2)})$ , where  $\vec{n}$  is optimized based on the arrival time of each signal relative to its neighbors. The  $\chi^2$  of the arrival times can then be written:

$$\chi^2(n_x, n_y, T_0) = \sum_i w_i \left( t_i^m - t_i^{plane} \right)^2 = \sum_i \frac{\left( t_i^m - \left( T_0 + \frac{n_x x_i + n_y y_i}{c} \right) \right)^2}{\sigma_i^2} \quad (3.2)$$

where  $t_i^m$  are the measured times,  $1/\sigma_i^2$  are their weights  $w_i$ ,  $(x_i, y_i)$  are the tank coordinates, and  $T_0$  is the arrival time of the plane. Here a constant height of all tanks is assumed, which is accounted for in a second iteration of the PlaneFit in which their relative heights are taken into account. The PlaneFit can be analytically minimized and provides a seed that is accurate within  $4^\circ$  of the true direction.

### 3.3.3 Likelihood Reconstruction: Lateral Fit

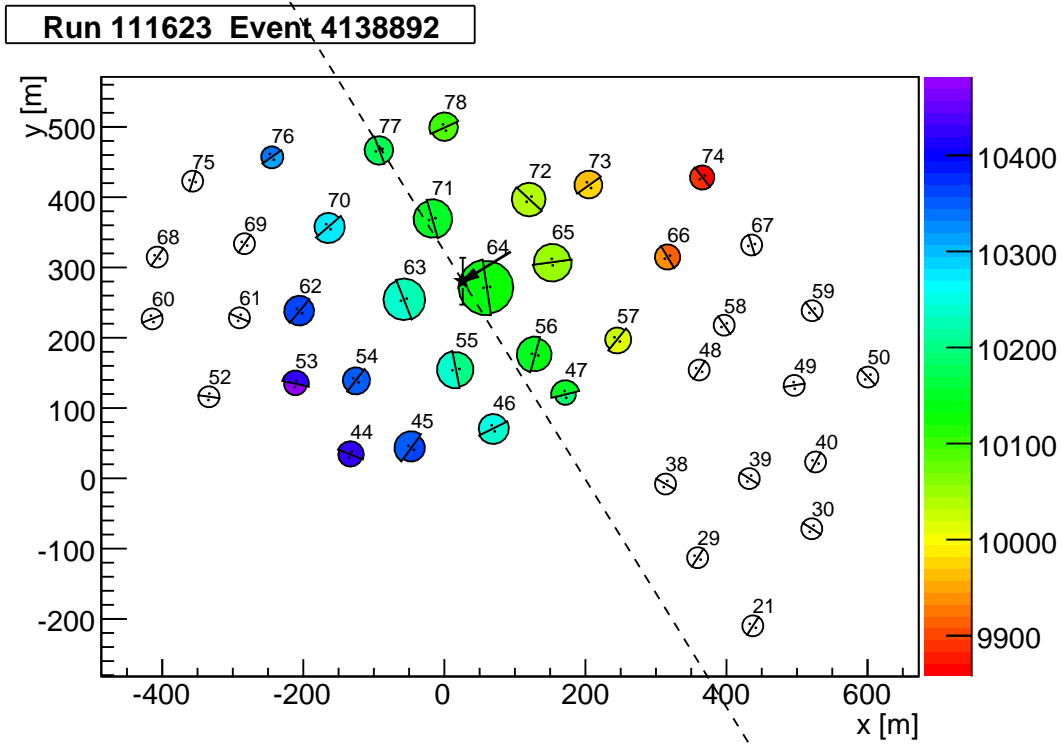
The surface array likelihood fit [59, ?] is a three-part likelihood reconstruction which combines information regarding the tank hit distributions, timing, and threshold behaviors of the detectors. The expected charge in a tank is expressed using a lateral distribution function, which describes the signal,  $S_{LDF}(R)$ , as a function of distance,  $R$ , from the shower core. Following the well-known likelihood for a normal distribution, the likelihood for a measured signal  $S_i$  in tank  $i$  at location  $\vec{x}_i$ :

$$\mathcal{L}_{hit}(\log_{10}(S_i), R) = \frac{1}{\sqrt{(2\pi)\sigma}} \exp\left(-\frac{(\log_{10}S_i - \log_{10}S_{LDF}(R))^2}{2\sigma(\log_{10}S_{LDF}(R))^2}\right) \quad (3.3)$$

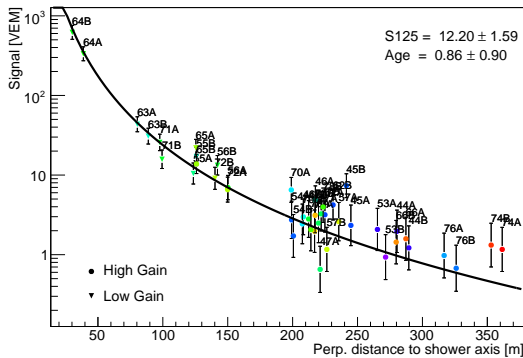
can then be maximized. Similarly, the timing and hit probability distributions are also maximized in the full likelihood reconstruction, as described in detail in [?]. Since the LDFs do not describe the showers well at small distances from the core, and signals from tanks within small radii can destabilize the fit, an iterative fit procedure was developed through which:

1. An initial fit is performed with all available tank signals, using the ShowerPlane and ShowerCOG as seeds for the shower core position and direction.
2. All stations within 11 m of the reconstructed core are eliminated.
3. The fit is repeated (with those stations removed).
4. Stations within 11 m of the new core location are eliminated in addition to those already removed.
5. The procedure is repeated.

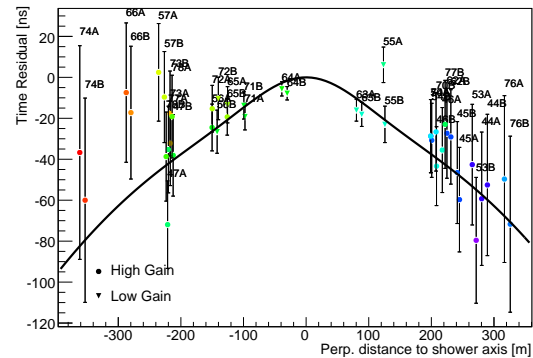
This fit method has been tested with Monte-Carlo simulations, and well-characterized to have reliably small and predictable reconstruction errors for showers which fall within the area of the surface array and have enough triggered tanks to perform the reconstruction. This algorithm reliably fits the lateral distribution of the air shower, which provides the most important parameter from IceTop data: the energy estimator  $S_{125}$ , which will be described in more detail below. An example event from the surface array can be found in Figure 3.3.



(a)



(b)



(c)

Figure 3.3: The IceTop event shown in Figure 3.3(a) is from a medium-to-large shower from September 11, 2008. The core location is denoted with a star in Figure 3.3(a) and the direction of the shower ( $\theta \approx 15^\circ$ ,  $\phi \approx 32^\circ$ ) is indicated by the arrow (the dotted line is the plane of the incoming shower front). The timing of the hits are represented by the colors, from red (earlier) to blue (later). The amount of signal observed by each *tank* in a given station is denoted by the size of the *hemi*-sphere closest to it. The lateral distribution of these hits is seen in Figure 3.3(b), where the station numbers are marked and color-coded for timing in the same scheme as for the event display. In Figure 3.3(b), the fit of the expected signal is shown in black, and  $S_{125}$  is the value of that fit at 125 m from the core of the shower or, in this case,  $\sim \log_{10}(10)$ . Similarly, the curvature is seen in Figure 3.3(c). Figures provided by Tom Feusels [66].

## 3.4 Methods of Reconstruction In the Ice

### 3.4.1 First Guess: Velocity of Line Fit

The LINEFIT reconstruction produces a rapid, analytical, first guess estimate of the vertex and direction of an in-ice track, which can then be used to seed more complicated in-ice reconstructions. This fit models the track using only the hit times and the positions of the DOMs, and ignores the Cherenkov cones and expected time delays due to scattering in the ice. The particle track is modeled as a single straight line,  $\vec{R}(t) \equiv \vec{r} + \vec{v}t$ , and optimized compared to some collection of hits,  $(r_1, t_1), (r_2, t_2), \dots (r_n, t_n)$ . At time  $t_i$ , the track is modeled to be at position  $\vec{R}(t_i)$ , and a hit is actually registered at position  $r_i$ . The distance between these two points can be regarded as an error of the track, and the best fit is defined to be the track which minimizes this error. As mentioned above, this fit will not be used as an input to the MuonBundleReconstruction; however, it is useful for certain quality cuts in this analysis.

### 3.4.2 Likelihood Fit: Muon Bundle Reconstruction

For this analysis we observe muon bundles in the ice which can vary in multiplicity from 1 to more than 1000 at the highest energies. Therefore, an improvement to the LINEFIT reconstruction technique was made by taking into account the expected amplitudes and arrival time distributions of photons (resulting from the muon bundles) at the DOMs [40]. As discussed in Chapter 1, the energy distribution of muons at the surface can be given by:

$$N_\mu (> E) = KE^{-\gamma_\mu} \quad (3.4)$$

where  $\gamma_\mu$  is the muon spectral index. For reconstruction purposes we are uninterested in the muon energy distribution at the surface; rather, we would like to know the muon energy distribution in the ice. Due to the fact that muons range out in the ice, only muons above a certain energy threshold,  $E_{min}$ , will survive passage through a given distance in the ice, called slant depth,  $X$ .

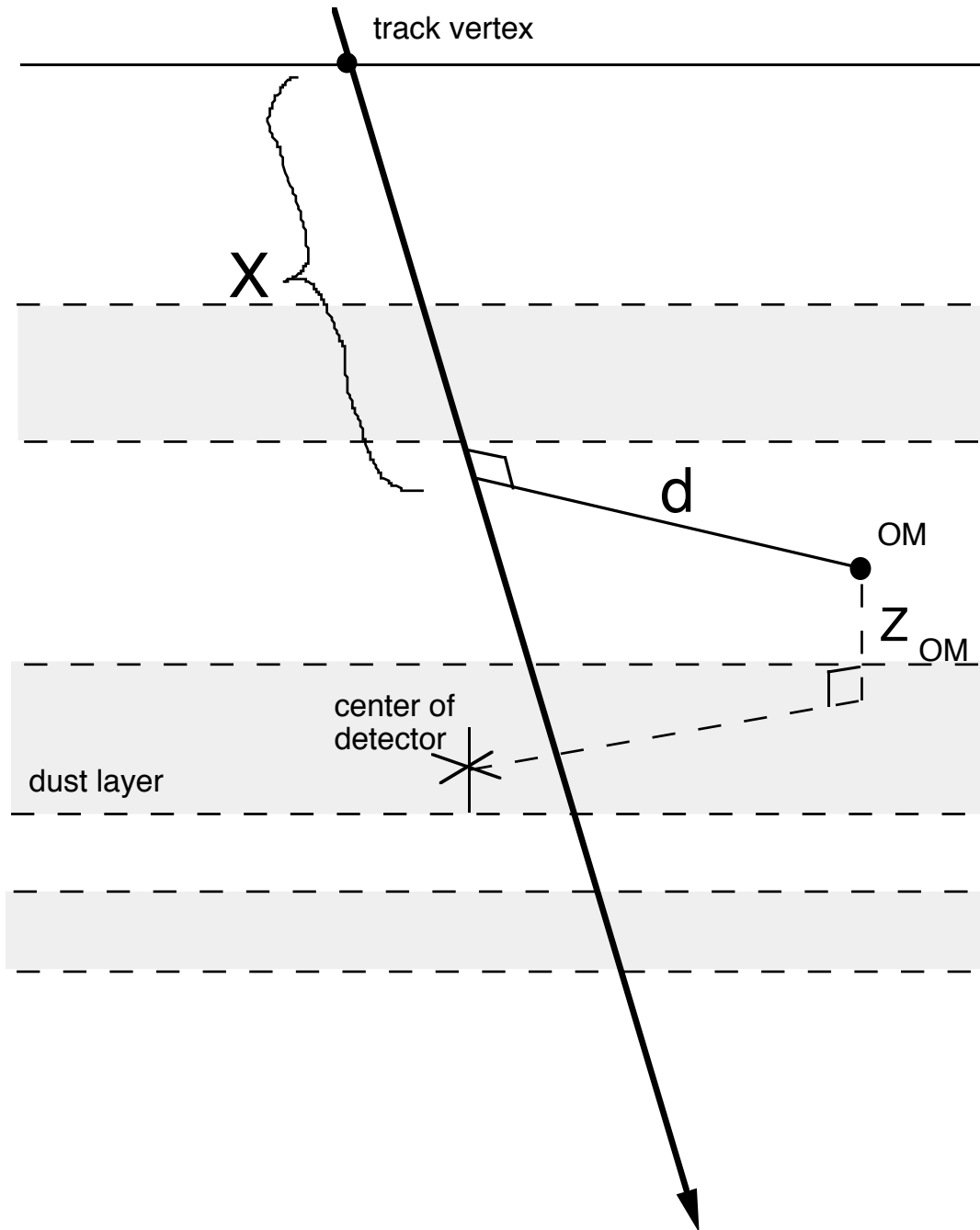


Figure 3.4: A side-view of reconstruction coordinates in the IceCube detector. The track vertex point is taken to be at the surface. The slant depth,  $X$ , is the thickness of the ice the muon bundle must pass through before it reaches the position of closest approach,  $d$ , to a given DOM. This distance,  $d$ , is the perpendicular distance from the track axis to the DOM [40].

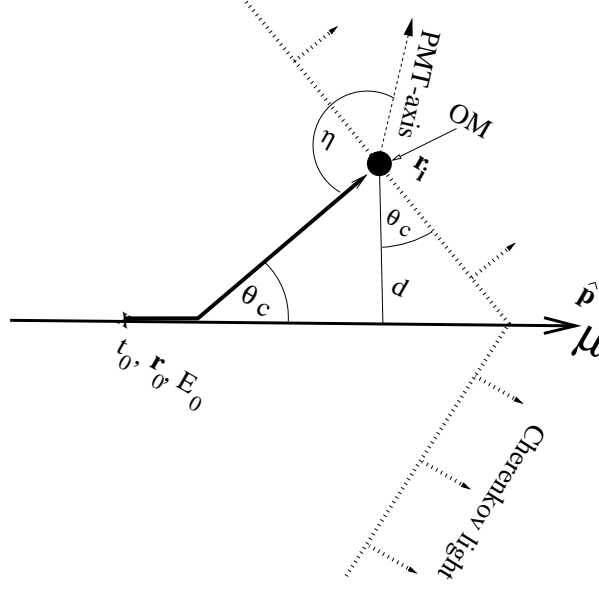


Figure 3.5: A “top” view of a muon track coordinate system. The Cherenkov light travels away from the track in a cone of angle  $\theta_c \approx 42^\circ$ . The distance,  $d$ , is once more the distance of closest approach of track axis to the DOM [54].

Thus, we take a well-known approximation of the muon energy loss in matter:

$$-\frac{dE_\mu}{dx} = a + bE_\mu \quad (3.5)$$

where  $a$  accounts for the continuous ionization energy loss and  $bE_\mu$  describes the stochastic loss due to a combination of pair production, bremsstrahlung, and photonuclear contributions [63]. We solve this differential equation for the minimum energy,  $E_{min}$ , required for a muon to reach slant depth  $X$ :

$$E_{min} = \left(\frac{a}{b}\right) \left(e^{bX} - 1\right) \quad (3.6)$$

and, substituting Equation 3.6 into Equation 3.4, we find the number of muons in a bundle at depth  $X$  to be:

$$N_{mu,depth}(X) = N_{mu,surface}(> E_{min}) = KE_{min}^{-\gamma_\mu} = K \left[ \left(\frac{a}{b}\right) \left(e^{bX} - 1\right) \right]^{-\gamma_\mu}. \quad (3.7)$$

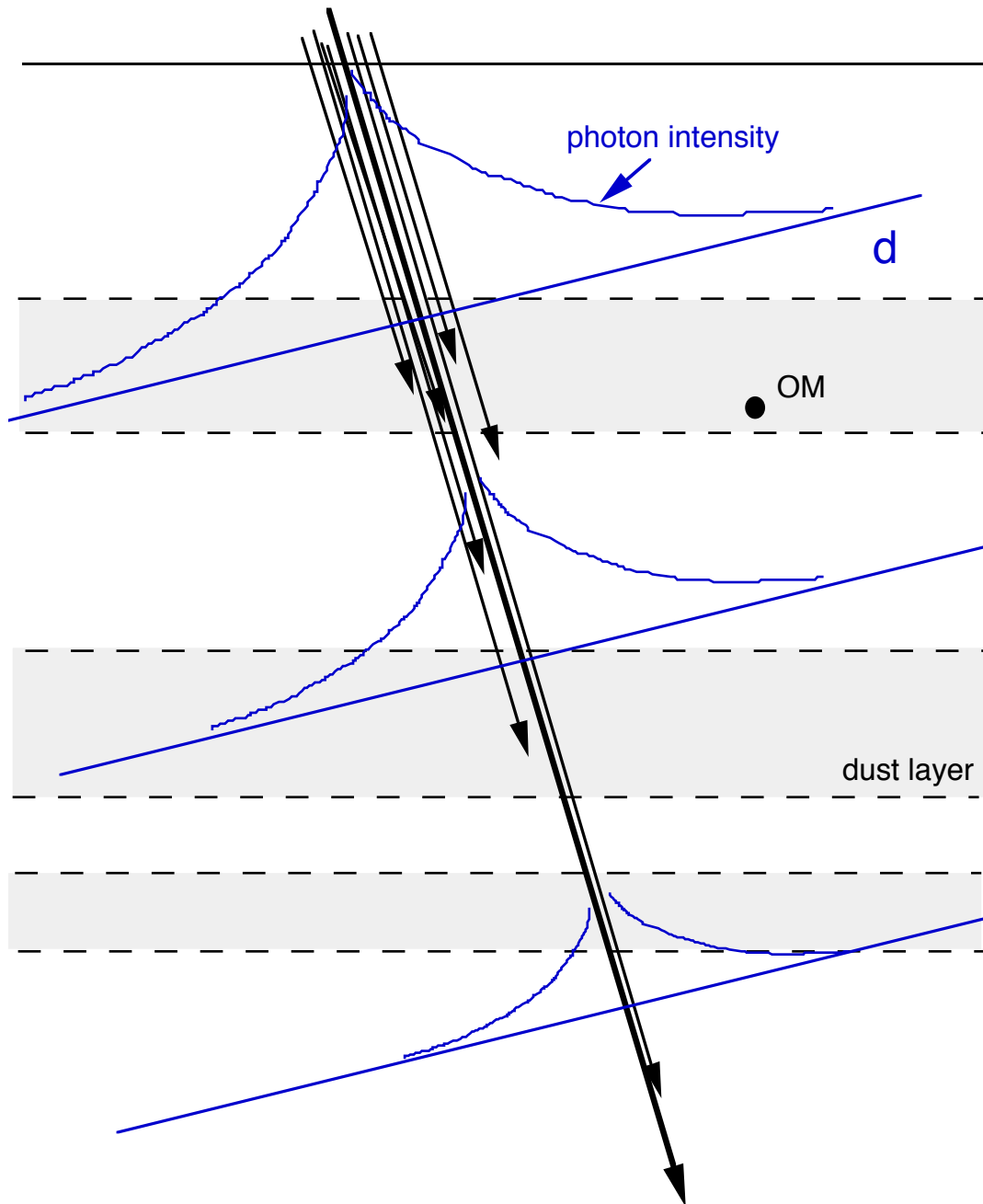


Figure 3.6: A cartoon of a muon bundle traveling through the ice. As it reaches deeper slant-depths, the muons in the bundle range out (where the arrows end). The Cherenkov photons which are emitted as the muons lose energy are drawn as curves. Their intensity is related to the number of the muons in the bundle, and decreases rapidly with the perpendicular distance from the track axis. This intensity is what we are actually fitting with the MuonBundleReconstruction [40].

To gain a complete idea of the signal expectation in each DOM, we need to also consider the lateral distribution of the photons around the bundle axis. The best-fit central track can be thought of as a line source of light, which produces an intensity of:

$$I_{photons} \propto \frac{1}{\lambda_e} K_0(d/\lambda_{eff}),$$

where  $K_0$  is a modified Bessel function of the second kind,  $d$  is the perpendicular distance from the DOM to the track, and  $\lambda_{eff}$  is the effective attenuation length of light in the ice due to the combined effects of scattering and absorption of (predominantly) dust, which is given by:

$$\lambda_{eff} = \sqrt{\lambda_e \lambda_a / 3}.$$

It can be shown that  $\lambda_{eff} \propto \lambda_e$  [40], and the Bessel function can be approximated for large distances,  $d$ :

$$I_{photons} \propto \frac{1}{\sqrt{\lambda_{eff} d}} e^{-d/\lambda_{eff}}.$$

Putting it all together, we can find that the expected signal for a given DOM at a perpendicular distance  $d$  from a central track of  $N_{\mu,depth}$  muons at slant-depth  $X$  with effective attenuation length  $\lambda_{eff}$  is:

$$\text{Expected Signal} = NN_{\mu,depth} \frac{1}{\sqrt{\lambda_{eff} d}} e^{-d/\lambda_{eff}}. \quad (3.8)$$

This function can be modified to take into account the dust layers of the ice by separating the fit into layers. For light which remains in a single ice layer, the calibrated effective attenuation length for that layer is used; for light which traverses multiple layers we cannot tell which layer the light originated in, we only know the distance from the DOM to the reconstructed track; therefore, the average effective attenuation length of the bulk ice is used instead, with a normalization,  $N$ , chosen to ensure continuity of the function. Thus, we now have an expected signal, which we can

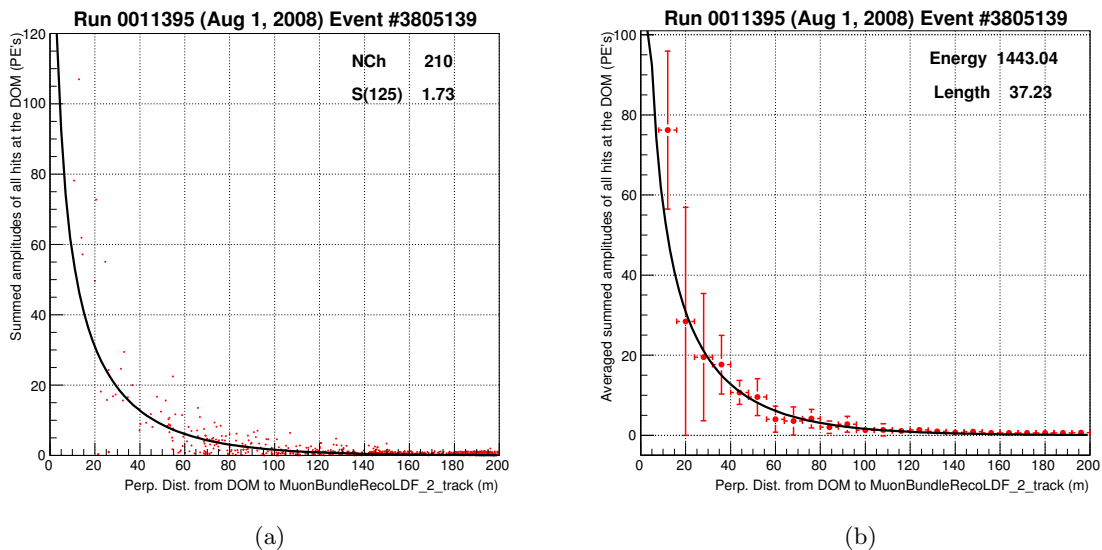


Figure 3.7: Figure 3.7(a) demonstrates the total amplitude of all hits in a given DOM, with respect to the DOMs perpendicular distance to the fitted shower axis, in red. The expected amplitude fit is shown in black. In Figure 3.7(b) we see the same distribution, but with the averaged amplitude at each distance shown in red. Again, the fit is shown in black.  $K_{70}$  is the  $\log_{10}$  of the value given by the fit at 70 m from the track axis, in this case  $\sim \log_{10}(4)$ .

compare with the actual hits using the likelihood method described above. This algorithm has been designed to take as starting values the core position and direction from the Lateral Fit. In most cases the core position is anchored at the surface, while the most likely direction is found. This allows for this track to use a very long “lever-arm”, due to the prior knowledge of the surface reconstruction, which leads to a much better angular resolution than other in-ice reconstruction algorithms which do not utilize this information.

Figure 3.7 shows an example of data fit to this function, which represents the analytic form expected for a line source of light.

### 3.5 Full Detector Reconstruction: Multiple Iterations

Now that we have a clear understanding of the main IceTop and InIce likelihood fitting algorithms, it is important to note that for this analysis we are using an iterative fit procedure which was developed and tested for IceTop/IceCube-40 [118]. This process follows on the tail of the standard filtering, described in Chapter 3, and the steps are as follows:

1. The PlaneFit and ShowerCOG first guess reconstructions are performed at the surface.
2. LateralFit likelihood reconstruction at the surface is seeded with core position and direction from the first guess reconstructions, and calculates a better core position and direction.
3. The core position and direction from the LateralFit are used as input seeds to the in-ice MuonBundleReconstruction, which provides an improved track direction.
4. The direction from the MuonBundleReconstruction is fed back into the LateralFit at the surface as a seed, which then recalculates our best-guess core position.
5. A final in-ice MuonBundleReconstruction is seeded with the core position from the 2<sup>nd</sup> iteration of the LateralFit, providing a best-guess track direction.

We use the 2<sup>nd</sup> iteration of LateralFit and MuonBundleReconstruction to calculate our two main input parameters for this analysis,  $S_{125}$  and  $K_{70}$ , as described below.

### 3.6 Energy Estimators

Now that we have reliably reconstructed our shower at the surface and our track in the ice, we can use those tracks to parameterize the energy deposited in our detector, which is proportional at the surface to the energy of the electromagnetic component of the air shower, and to the energy loss of the muon bundle in the ice. There are a number of energy estimators currently in use in IceCube and IceTop but, as we shall discuss shortly,  $S_{125}$  and  $K_{70}$  are the best choices available for this analysis.

#### 3.6.1 IceTop: $S_{125}$

The Double Logarithmic Paraboloid (DLP) function was developed specifically for the IceTop detector [59] to fit the signal lateral distribution,  $S_{DLP}(R)$ , in VEMs, as a function of radius  $r$  from the shower core:

$$S_{DLP}(R) = S_{ref} \left( \frac{r}{R_{ref}} \right)^{-\beta - \kappa \log_{10} \left( \frac{r}{R_{ref}} \right)} \quad (3.9)$$

where  $\beta$  is analogous to the shower age,  $\kappa$  is a measure of the curvature of the shower front (set to be a constant 0.303 in this analysis) and  $S_{ref}$  is a reference signal and energy-estimator measured

at a distance  $R_{ref}$  from the core. The DLP function was found to fit the signal lateral distributions in IceTop very well in the region between 30 m and 1000 m. The choice of 125 m as a reference point will be discussed in the next section.

### 3.6.2 InIce: $N_{ch}$

The most basic of the In-Ice energy estimators,  $N_{ch}$  is simply the number of channels which are hit in an event. It has primarily been used as an estimator of muon (i.e. neutrino) energy in diffuse limit analyses and is surprisingly robust, especially at low energies where the majority of the track is contained by the detector. However, at higher energies our detector can “see” muons from an event that lies well outside the physical volume of the array, meaning that we detect an unknown fraction of the light which is actually produced by the muon bundle causing  $N_{ch}$  to be less reliable.

### 3.6.3 InIce: MUE

MUE is a favorite in-ice energy estimator of the IceCube collaboration. In a similar fashion to the  $K$ -parameter, this algorithm extends a standard likelihood based track-reconstruction to also include a likelihood fit to the photon density around the hypothetical track. This provides the energy estimator MUE at the distance of closest approach to the center of gravity of hits in the event:

$$\text{MUE} = \frac{\langle N_\gamma \rangle}{L_{track}} A_{eff\ PMT} \quad (3.10)$$

where  $\langle N_\gamma \rangle$  is the average number of photons,  $L_{track}$  is the length of the track, and  $A_{eff\ PMT}$  is the effective area of the PMTs [67].

### 3.6.4 InIce: K70

The  $K$ -parameter is similar to the  $S$ -parameter from IceTop: it was developed for a similar composition analysis using the prototype detector, AMANDA-B10, and is used to fit the lateral distribution of Cherenkov photons from a muon bundle at a slant depth of 1950 m as a function of

perpendicular distance  $D_{ref}$  to the axis of the reconstructed track:

$$K(D_{ref}) = \frac{A}{\sqrt{D_{ref} \lambda_0}} e^{-D_{ref}/\lambda_0} \quad (3.11)$$

where  $A$  and  $\lambda_0$  are free parameters in the fit.  $A$  is the overall normalization, which is proportional to the total energy loss of muons in the ice, and  $\lambda_0$  is the propagation length of light in bulk ice, which is known to be  $\sim 26$  m, but which we fit because minor errors in the track reconstructions can change this best-fit slope of the LDF. A check to be sure this parameter still works the way it should, now that it has been ported to IceCube can be found in the next sections.

### 3.7 A Choice of Reference Distances for $K_{70}$ and $S_{125}$

The last important point of discussion is the choice to evaluate  $S$  at 125 m and  $K$  at 70 m. Before a choice is made, it is important to understand the physical arguments for near and far distances. Particles reaching DOMs at far distances from the core of the shower are subject to more scattering and decay, either in the atmosphere or in the ice. Furthermore, there are simply more hits at near distances than at far distances from the track. This means that DOMs near the track will have a more predictable behavior and will provide data points which the minimizer can use to find the best fit. However, though our track reconstruction is quite good, a directional misreconstruction of only half a degree corresponds to a  $\sim 20$  m shift of the track at 1950 m depth. This will cause an underestimation of the expected signal from the DOMs that are closer to the track than expected, and an overestimation of those which are further than expected, to the overall effect of flattening the slope of the signal expectation curve, especially at distances closer than the reconstruction error, as can be seen in Figure 3.8 where a single track of a given energy has been simulated and shifted by half a degree around its axis a number of times to see the effect of angular misreconstruction. A stable position can be found around 70 m for the high energy shower and at a slightly closer distance to the track for a lower energy shower. (This signal-flattening effect is less prevalent in the surface reconstruction, in part due to the fact that stations too close to the track

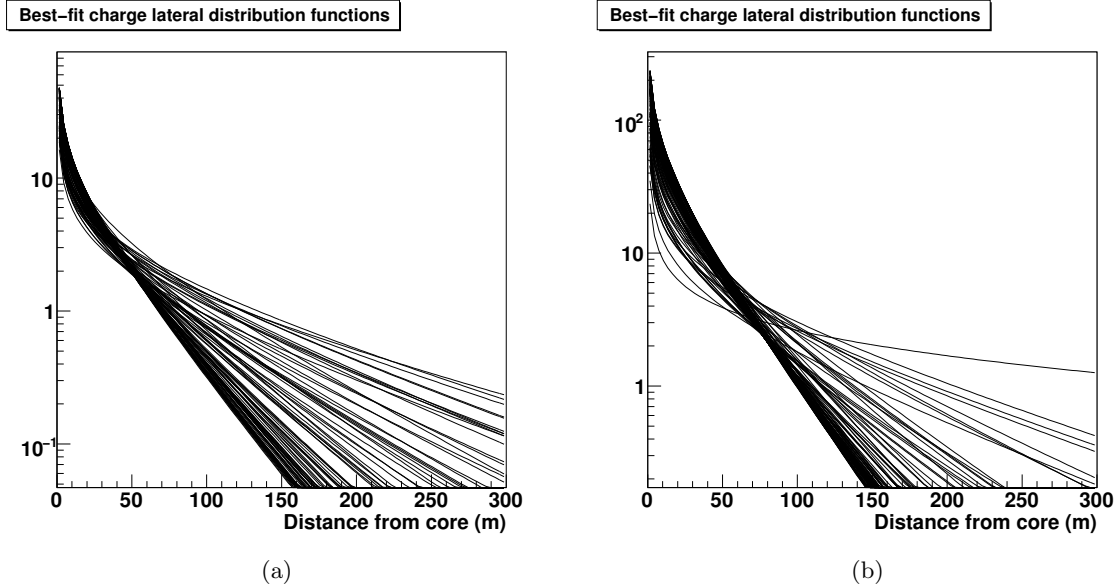


Figure 3.8: The “bundle of sticks” plot: for a single simulated shower at a given energy, the true track position is anchored while the direction is varied within  $0.5^\circ$  of the true direction. In Figure 3.8(a), an initial shower was chosen in the range  $5.66 \text{ GeV} < \log_{10}(E_{true}) < 6.0 \text{ GeV}$ , which is the lowest range available to our detectors, and below our efficiency threshold (as we shall see in Chapter 6. For this low energy, it seems the most stable distance at which to measure the K-parameter is between 50 and 60 m from the shower axis. In Figure 3.8(b), for a shower chosen in the range  $6.66 \text{ GeV} < \log_{10}(E_{true}) < 7.0 \text{ GeV}$  (where we are maximally efficient) the most stable distance appears to be around 75 m. Thus  $K_{70}$  seems like a reasonable compromise for showers at all energies.

are removed from the fit, as described above.)

The above plot is a nice way to consider angular misreconstruction on its own; however, there is also the idea of a poorly reconstructed core position to consider. A way to check the effect of overall misreconstructions is to simply assume that some of our showers are poorly reconstructed to a certain degree and look at the fits for all simulated, reconstructed showers to see where the most stable reference distance is, as can be seen in Figure 3.9, and which points to a reference distance of  $\sim 125 \text{ m}$  at the surface and, once again,  $\sim 70 \text{ m}$  in the ice.

Besides the simple physical considerations of the detector and reconstructions, it is also useful to consider the goal of these parameters in this analysis: to provide a good energy estimator and a parameter to distinguish particle type. Therefore, it is also interesting to simply check to see which distances work best for our given analysis goals. As seen in Figure 3.11, the reference distance for the  $K$ -parameter which provides the best separation of particle types, with the smallest spread, for the pertinent range in energy, is 70 m. In Figure 3.10, it seems that the reference distance for the

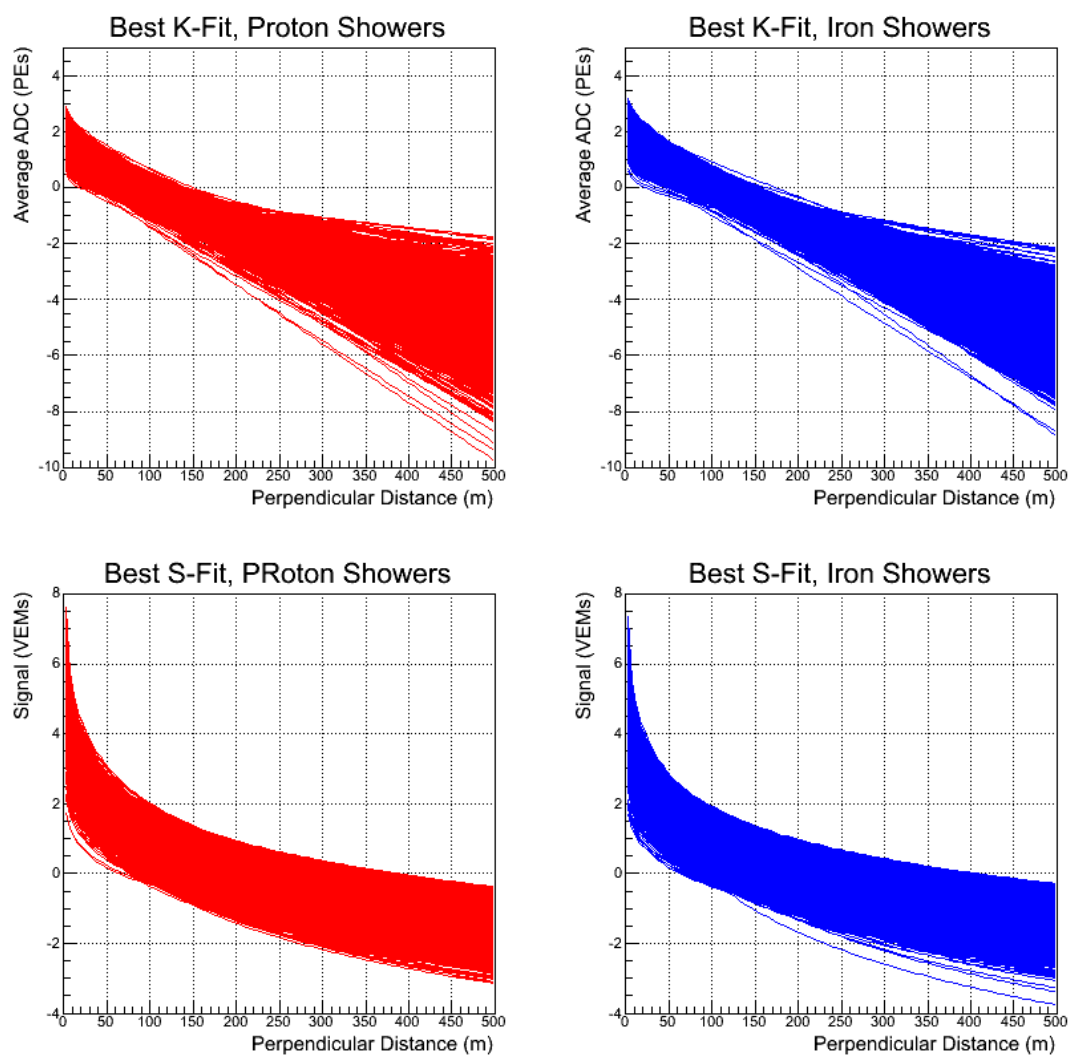


Figure 3.9: Though similar to the “bundle of sticks” plot, this plot is actually the fit results of all the simulated proton and iron showers which pass all of our cuts (as discussed in Chapter 4). As in the “bundle of sticks” plot, it is clear that the reference distance of 70 m for the  $K$ -parameter and the reference distance of 125 m for the  $S$ -parameter are good approximations of the most stable evaluation point of the fits for both protons and iron.

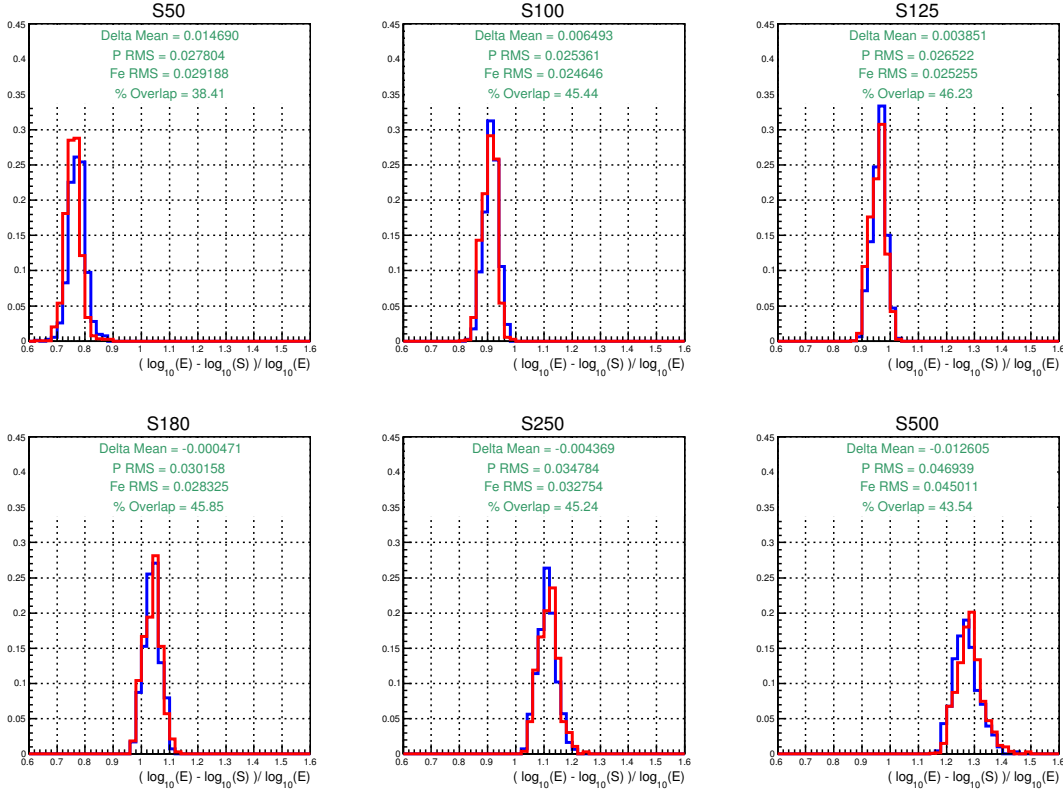


Figure 3.10: Another way to decide which  $S$ -parameter is most reliable is to consider that we are interested in acquiring a composition-independent parameter related to energy with tight resolution. Thus, we can simply evaluate the signal at different reference distances from the shower core, calculate the RMS of the showers, the offset between the means, and the amount of overlap they have. In this case, we are looking for the distance at which the overlap is maximized, but the offset and RMS are minimized. Of the distances chosen, 125 m is clearly the most type-independent with the tightest energy resolution. (Note: only showers with energies between  $6.3 < \log_{10}(E_{true}/\text{GeV}) < 6.8$  were used for this study.)

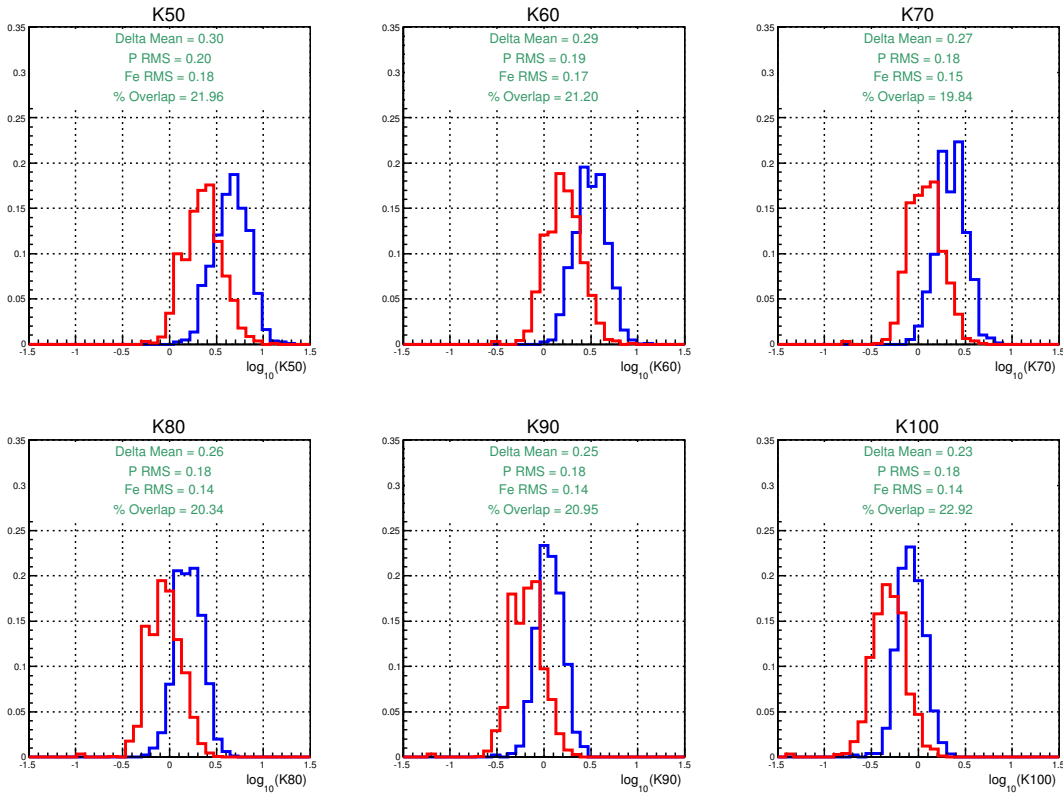


Figure 3.11: A way to decide which  $K$ -parameter is most reliable is to consider that we are interested in acquiring a parameter to help us separate particle type with great reliability. We can evaluate the signal at different reference distances from the shower axis and calculate the RMS of the showers, the offset between the means, and the amount of overlap they have. In this case, we are looking for the distance at which the offset is maximized, but the overlap and RMS are minimized (ie, we want good separation between tightly-defined proton and iron distributions). Of the distances chosen, 70 m clearly provides the least overlap and therefore best type separation. (Note: only showers with energies between  $6.3 < \log_{10}(E_{true}/\text{GeV}) < 6.8$  were used for this study.)

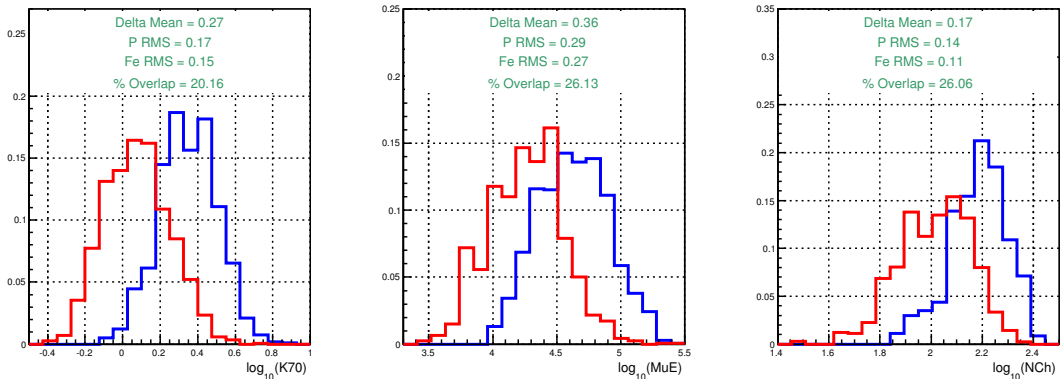


Figure 3.12: Similar to the way we choose the distance at which to evaluate the  $K$ -parameter, we can also check to see if one of the other In-Ice energy estimators could provide us with a similarly as strong parameter to accurately distinguish particle type. The answer is definitively “No”. (Note, only showers with energies between  $6.3 < \log_{10}(E_{true}/\text{GeV}) < 6.8$  were used for this study.)

$S$ -parameter which provides the most type-independent but tightly resolved relationship between  $S$  and true primary energy is 125 m. These two observations further confirm the distances indicated above.

Furthermore, an independent subarray analysis was performed at the surface to check the stability of the reconstruction method with respect to tank fluctuations. In this analysis, the array was divided into two subarrays, each containing one tank from each station. This analysis again concluded that a reference distance of 125 m provided the most stable fit [123].

### 3.8 Comparison with Other Parameters

At this point it is useful to make some very basic comparisons between the parameters chosen here and some other standard IceCube energy estimators, and between true and reconstructed parameters. (Note: for all of the following plots some very strict containment cuts were applied for the surface reconstructions, as well as for the LineFit reconstruction—no cuts were made on the MuonBundle reconstruction, as we were comparing that reconstruction to others. These are not the cuts used in the final analysis, but are meant to be easily understood basic cuts. The idea behind them will be fully explained in Chapter 4.)

#### 3.8.1 Comparing $K_{70}$ to other In-Ice Energy Estimators

In Figure 3.11 we look at  $K_{70}$ ,  $N_{ch}$  and MUE for a given slice in energy ( $6.3 < \log_{10}(E_{true}/\text{GeV}) < 6.8$ ) to compare the separation capabilities of each energy estimator for proton and iron simulated air showers. Once more, the best parameter for separating types will have the least amount of overlap between the types. It is clear that, for the purpose of separation,  $K_{70}$  is far superior to either MUE or  $N_{ch}$ .

Another method to check the superiority of different energy estimators is to identify the one with the best resolution and smallest systematic error. One of the only ways to do this is using coincident experimental data events (one advantage of this method is that no simulation is required): two independent energy measurements are available, the correlation between the two

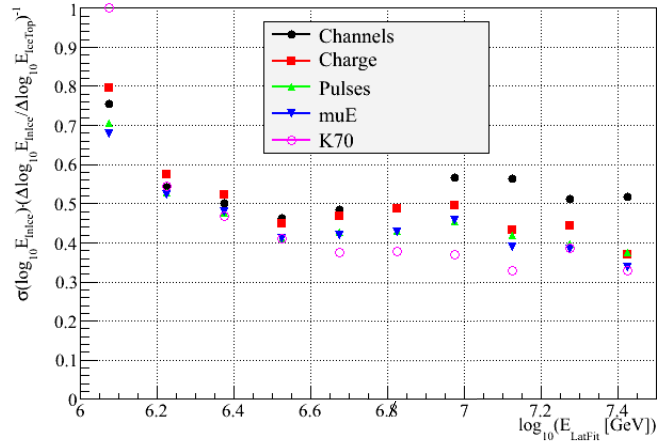


Figure 3.13: The spread of different in-ice energy estimators as a function of a surface energy estimator for experimental data. It is clear that  $K_{70}$  has the best resolution with the smallest systematic error, as compared with other standard IceCube energy estimators. (Courtesy of Patrick Berghaus)

detectors can be measured, and there is no concern about absolute normalization as there would be in simulation. Thus, a value for normalized  $spread = (\sigma * \Delta x) / (\Delta y)$  was used to compare the different energy estimators. The results are shown in Figure 3.13, and once again attest to the superiority of  $K_{70}$  over the other estimators as a parameter for use in this particular analysis.

### 3.8.2 Comparing $S_{125}$ and $K_{70}$ to True Energy and Each Other

The last check to make is to see exactly how well our parameters do what we want them to do. We intended  $S_{125}$  to measure the number of particles at the surface and we wanted  $K_{70}$  to measure the high energy muon component. Thus, using simulations, we can compare both to true energy to see how well we have accomplished our goal in the ideal situation, and lastly we can compare  $K_{70}$  and  $S_{125}$  to each other, to see how well our parameters separate mass in actuality. Figure 3.14(a) shows that  $S_{125}$  provides a very strong relationships with the true energy of the primary cosmic ray. There is a slight mass-dependence, which is marked by the slight difference in slope between protons and iron. In Figure 3.14(b) the mass separation capabilities of the  $K_{70}$  parameter are clear. At the highest energies there is very little overlap at all, which means that if we can measure

the energy well, we will be able to separate the mass well. In Figure 3.14(c) we can see that the combination of the two reconstructed parameters,  $K_{70}$  and  $S_{125}$  provide a very strong parameter space for studying cosmic ray composition, remarkably similar to that shown in Figure 3.2 for an ideal simulation (ie, without detector reconstruction).

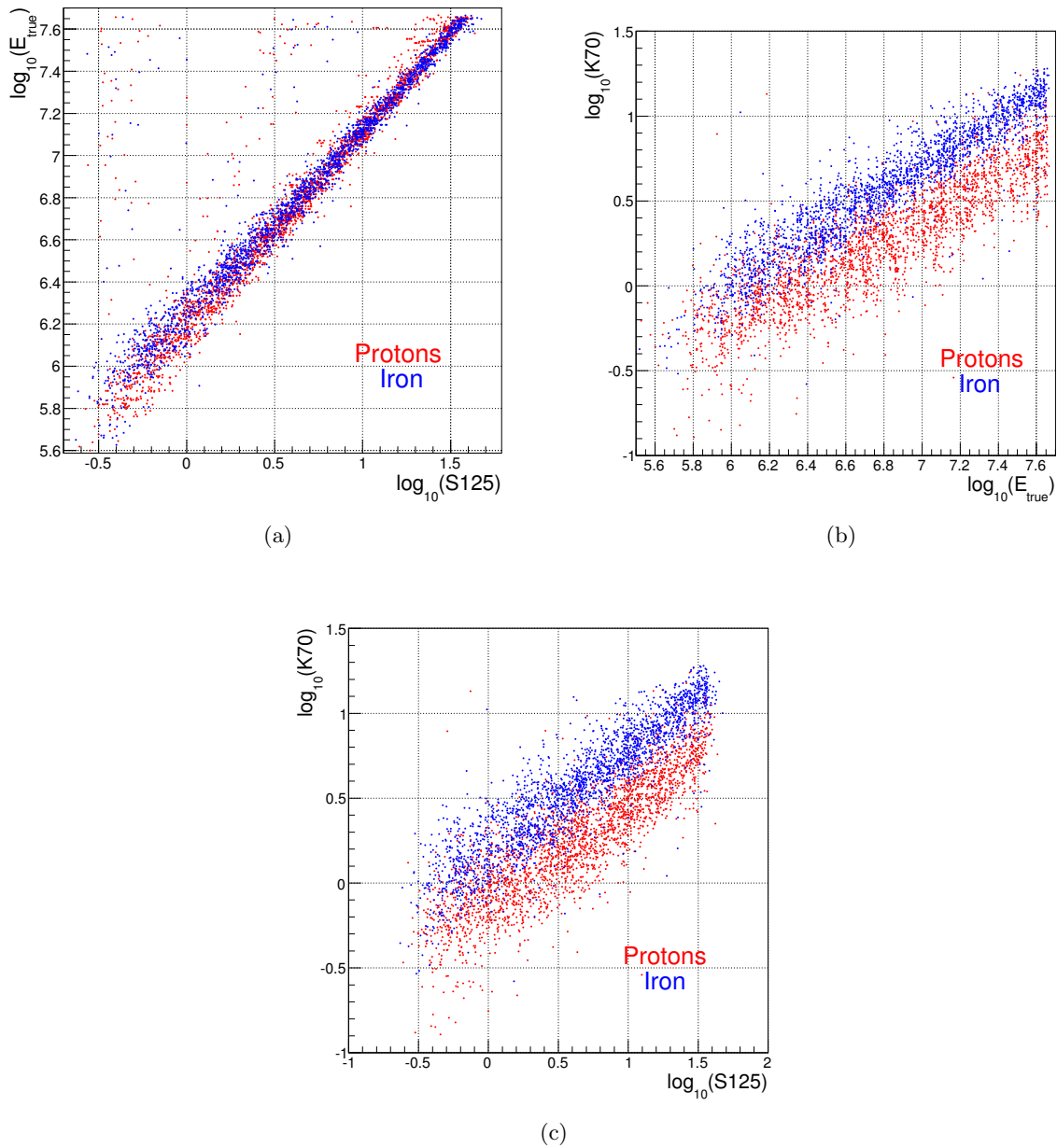


Figure 3.14: In Figure 3.14(a) we show a strong correlation between  $S_{125}$  and the true primary energy. In Figure 3.14(b) we show the type separation capabilities of the  $K_{70}$  parameter with respect to the true energy. In Figure 3.14(c) we show that the combination of the two parameters,  $K_{70}$  and  $S_{125}$ , provide a strong parameter space in which to study cosmic ray composition.

## Chapter 4

### Data Quality and Event Selection

In Chapters 1 through 3 we have reviewed methods for taking data and reconstructing parameters which are useful to study cosmic ray composition using IceCube and IceTop: it is time to discuss the data we are using for this analysis, develop some quality standards, and verify our detector simulation.

#### 4.1 Experimental Data

The latest data and simulation available to date are the IceTop and IceCube coincident data from August 2008 (referred to as the “burn sample”), when the detector was in its 40-station/40-string configuration, as shown in Figure 4.1.

The August 2008 data has been passed through all triggers and reconstructions described in Chapter 3, which means that we have selected down-going events which triggered both IceCube and IceTop within a certain time-window. We select only detector runs which are considered “good” (as defined for the collaboration-selected “Good Run List”), which eliminates any run with failures (for example, sometimes one of the DOMHubs has to be rebooted—the runs taken while the hub was down will be considered bad runs) and runs during which we were taking flasher data for calibration purposes. The event rate and livetime of this dataset can be seen in Figure 4.2.

#### 4.2 Simulation

In order to map out our  $K_{70}$ - $S_{125}$  parameter space we depend upon Monte Carlo simulations, which we then compare with data. The full simulation is done in multiple stages. The

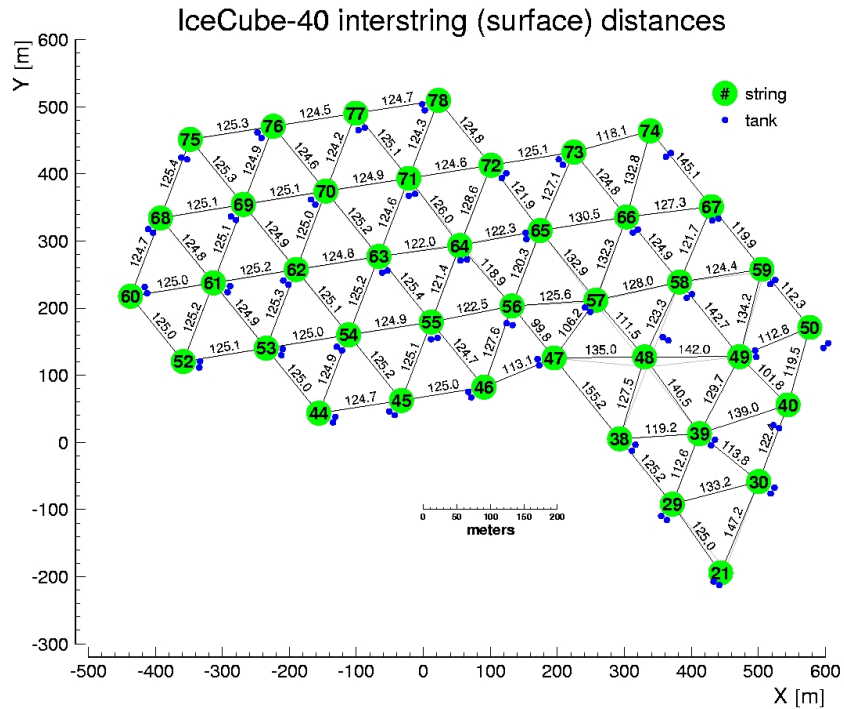


Figure 4.1: This is a map of each IceCube string and IceTop tank available for the 2008 40-string configuration, which was used for this analysis, in contrast to the current IC-79 geometry being used (Figure 2.9).

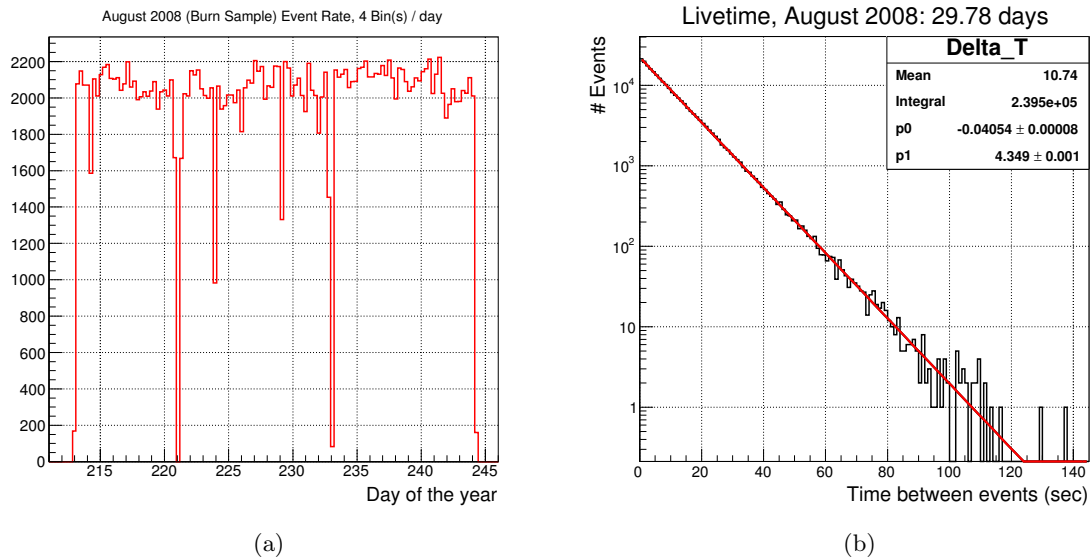


Figure 4.2: Figure 4.2(a) shows the event rates per 0.25 days for the IceTop/IceCube 40 string data from Aug. 2008. Dips correspond to known detector dead time and the average event rate is around 2000 events per 0.25 days. Figure 4.2(b) shows the livetime of the detector during August 2008, which is calculated by integrating over a line fit to the event rate vs the time between events (in seconds). We find a detector livetime of 29.78 days over the 31 day period.

process begins by generating air showers: we used the CORSIKA air shower generator with the Sibyll/FLUKA interaction models as our standard simulation. (For further discussion see Section 8.5.) The previous analysis using SPASE-2/AMANDA-B10 clearly showed that two primary particle types is not enough to describe the data well [40]; thus we chose to generate five particle types: protons, helium, oxygen, silicon and iron. For each particle type, we generated 3000 showers per energy bin, where the bins were 1/3 of a decade in  $\log_{10}(E_{primary})$  and spanned energies from 10 TeV  $< E_{primary} < 50$  PeV (see, for reference, Appendix B. We generate a flat (in log-scale)  $E^{-1}$  spectrum to ensure high statistics at the highest energies. We then reweight this spectrum to an  $E^{-2.7}$  spectrum below the knee at 3 PeV and to an  $E^{-3.0}$  spectrum above the knee. This weighting is further discussed in Chapter 6. The events were generated over  $360^\circ$  in azimuth, from  $0 - 65^\circ$  in zenith, and oversampled 100 times each over a radius of 1200 m. We chose to generate an atmospheric model to correspond to the Austral winter months.

Once the showers hit the surface, the response of the IceTop array is simulated using the TopSim software package, which accounts for all aspects of the tank response and was initially parameterized with a full GEANT-4 detector simulation. The DOM response is the same as described below for the in-ice detector (the ROMEO PMT Simulator produces the waveform, a full DOM response simulation is performed, and LC and trigger conditions are checked).

The muons are then propagated through the ice to the depth of the in-ice detector using the muon propagator Muon Monte Carlo (MMC) [68]. The Cherenkov photons from the muon tracks passing through the volume of the in-ice array are then simulated using the software package Photonics [69], which takes into account the full structure of the ice as described in Chapter 2 and stores the photon intensity and time residual information in lookup tables. This allows for quick access to the probability distribution functions of the simulated light patterns.

The detector response to Cherenkov photons is then modeled using a package called IceSim, which models each aspect of the DOM response (as discussed in Chapter 2). IceSim begins with the geometry and calibration files, which describe the location and operating status of each DOM. The DOM then accesses the Photonics tables to look up the photon distribution function for its location.

From the photon distribution, the ROMEO PMT Simulator produces an electrical waveform for the light which passes through a full simulation of the DOM response. A simple noise module adds random hits throughout the array and the local coincidence conditions and trigger settings are checked. Once an event is successfully triggered, it is read out and processed through the entire reconstruction chain as though it were data.

### 4.3 Definition of Terminology

After the data and simulation have passed through all levels of filtering and reconstruction, the last step in the processing chain is to identify and remove events which are of low quality and could cause an unnecessary bias in the final analysis.

The process of event selection is referred to interchangeably in a number of ways, of which “cut development” and “event selection” will primarily be used here. As mentioned above, the point of this process is to cut out events which are likely to be poorly reconstructed for known reasons, thereby selecting those events which are likely to be well-reconstructed. However, one must be wary of biasing the final event sample. As an illustration: in this analysis we determine the energy and mass composition of cosmic rays. Thus, we must be careful not to choose cuts which are dependent upon primary energy or composition. A cut on  $S_{125}$ , for example, would clearly be energy-dependent: such a cut must be avoided. In general, cuts are developed using simulated events in order to check if we are biasing our sample. Then the cuts are checked against the data to be sure the simulation and the data match well both before and after the cuts (unless, of course, there is an expected reason for a mis-match). This is also a good check of our simulation: if data and simulation match well, our simulation is doing what we expect.

In the following sections each cut will be described, a purpose for the cut will be given, and the result of the cut will be shown.

The two most important parameters in this analysis are  $K_{70}$  and  $S_{125}$ . The most important criteria for having a good reconstruction of  $S_{125}$  is the core location at the surface. If the core location is wrong, the fit of the shower profile will be poor and  $S_{125}$  will be less correlated to the

energy of the primary. The core location also affects the reconstruction of  $K_{70}$ , as the surface reconstruction is the first-guess for the in-ice fit. However, the biggest contributor to a bad fit of  $K_{70}$  is the angular resolution of the track. If the track is reconstructed as having a different angle from what is true, the averaged in-ice light profiles are no longer a good estimator of the light in the ice and  $K_{70}$  is misreconstructed. Thus the cuts below will focus on achieving a tight angular resolution and a good shower core resolution which, in turn, will lead to better energy resolution and mass separation.

#### 4.4 Basic Cuts

Basic cuts are made prior to the full multi-iteration combined reconstruction in order to save cpu processing time. The two basic cuts which were used for this analysis are:

1.  $N_{ch} > 5$ : this means that we have more than five hit DOMs in the ice. The reconstruction requires this many hits in order to perform a fit.
2. First and second iteration of the Lateral Fit must succeed: this means that the minimizer for the lateral fit must find a converging point. If the minimizer fails to converge in either iteration, the reconstruction fails and the event is thrown out.

After these initial cuts we examine the main parameters to gain a basic understanding for the necessity of further cuts. In Figure 4.3 we can see that the correlation between  $S_{125}$  and primary energy exists, and that in the  $K_{70}$ - $S_{125}$  parameter space we have some composition sensitivity, but in both cases the main features are obscured by outlying events. After these basic cuts, we have 1,141,590 experimental events and 62,954 simulated events left in our sample. By focusing on angular and position resolution we can develop a number of methods to select for high quality events.

##### 4.4.1 Checking Basic Distributions

In Figure 4.4 we make a quick but essential check of important parameters before making more cuts to be certain we are starting with a sample of data which is well-described by simulation.

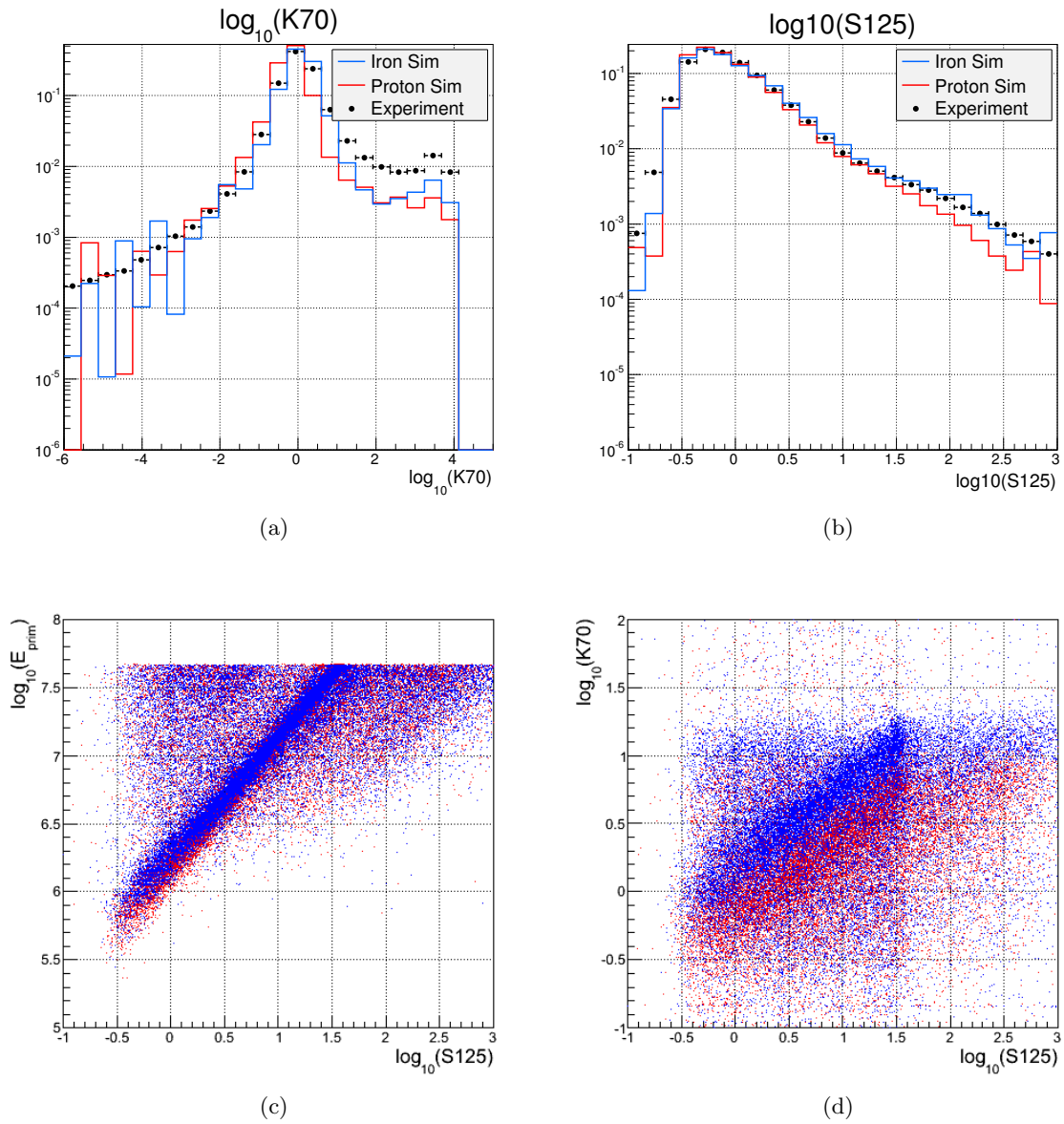


Figure 4.3: In Figures 4.3(a) and 4.3(b), we show the two main parameters for this analysis with only the most basic quality cuts. In Figures 4.3(c) and 4.3(d) we show the parameters at the same basic cut level with respect to true energy and compared to each other, respectively. Protons are red, and Iron are blue. It is clear that, without quality cuts, we have poor energy resolution and little visible composition dependence.

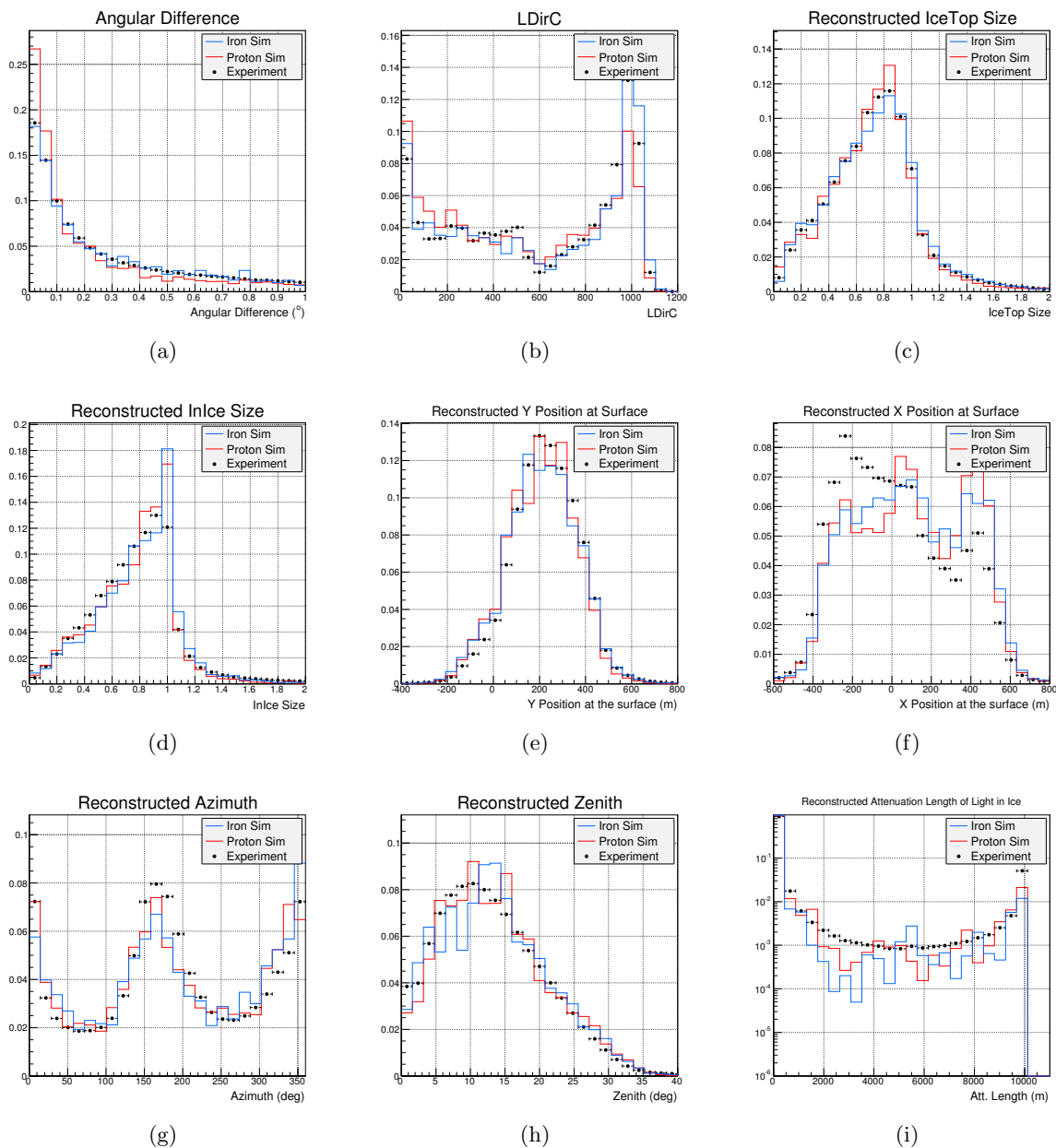


Figure 4.4: These are histograms of parameters which were either used to make the cuts or are useful diagnostic histograms. At this stage, only the basic cuts have been applied, and even though we will remove the majority of the events shown through quality cuts, the distributions agree quite well between data and simulation. The only discrepancy is found in Figure 4.4(f), an effect which is due to the drifting of the snow, as will be discussed further in Chapter 8. It is of note that the angles are restricted since the detector was only half built.

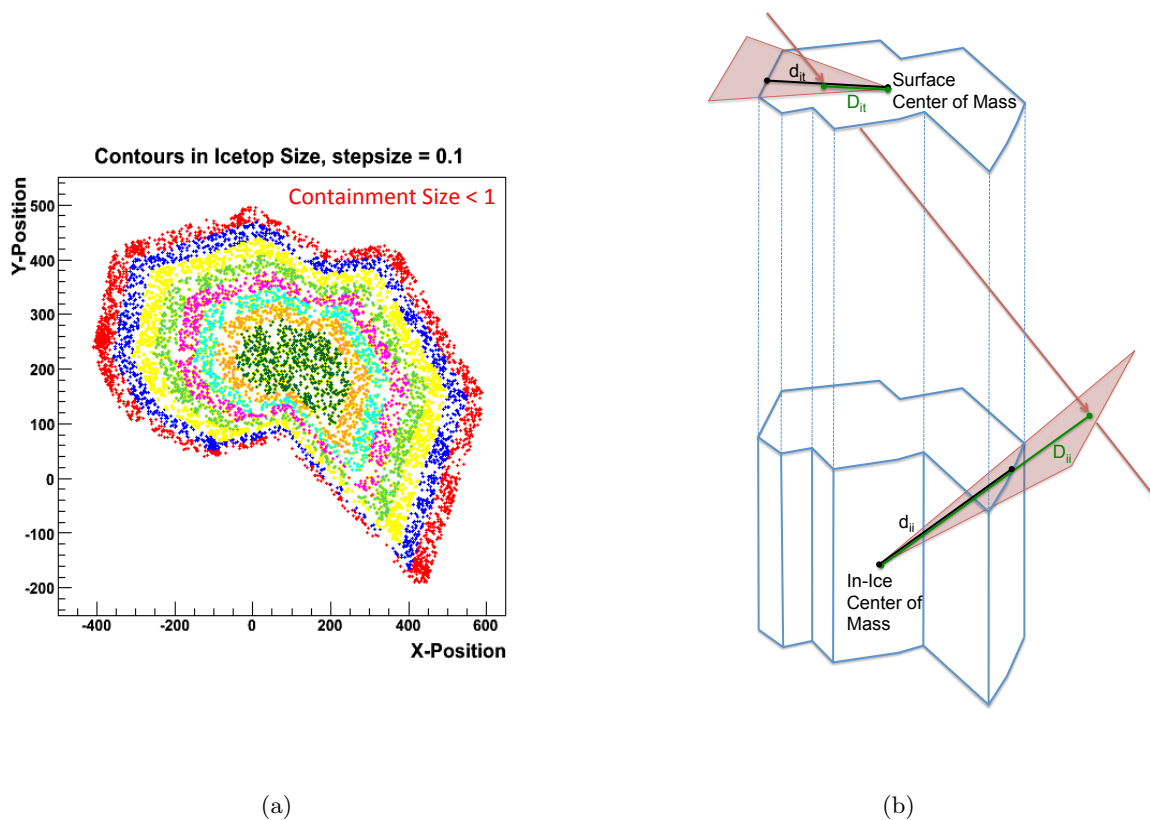


Figure 4.5: Containment cuts: Figure 4.5(a) shows the definition of containment using contours of IceTop containment size in steps of 0.1. The  $x$  and  $y$  axes are the true  $x$  and  $y$  position of the shower core, so this is the idealized situation only for demonstration of the idea. Figure 4.5(b) is a cartoon showing how containment is defined separately for the surface and the in-ice arrays. An event is considered contained for a given array if  $D/d < 1$ .

## 4.5 Containment Cuts

We begin with a selection based on containment to remove events which are not expected to be well-reconstructed: if the core of an air shower is not contained within the area (or volume) of the array, then the detector is viewing less than half of the complete profile of the shower. While the reconstruction algorithms can locate an expected core and direction with less than half of the shower information, the algorithms are significantly less likely to find the correct core location and direction. Thus, we require containment of shower cores. A parameter was developed to select for and eliminate any event with a core falling outside the detectors. Figure 4.5 demonstrates how this cut is defined in IceTop and IceCube. However, it is necessary to consider which track reconstructions to use for a containment cut. The name of the parameter used below to refer to

containment for a given fit is `InIceSize` for the in-ice array, and `IceTopSize` for the surface array.

#### 4.5.1 Containment of the Final Reconstructions

The first cuts are of the in-ice and ice-top containment from the final sample. The second iteration of our in-ice fit is the final reconstruction and is known to give the best angular reconstruction [118]; thus, the `InIceSize` from that reconstruction is required to be contained (i.e.  $< 1$ ). This means that our  $K$ -parameter is calculated from a track which appears to be contained after all reconstructions. Our  $S$ -parameter comes from the second iteration of our lateral fit, so we require the `IceTopSize` from that fit to be contained as well. Furthermore, we add an additional criterion that the second iteration of the lateral fit at the surface must reconstruct the `InIceSize` as being contained.

It may not be obvious why we cut on the in-ice containment when using the surface reconstruction. The events removed here will be showers that the surface reconstruction thought were pointing outside the volume of the in-ice array, but which the final in-ice algorithm reconstructed as within the array; i.e., there is a disagreement between the two final reconstructions as to where the track was pointing. While the angular resolution of the surface track is not as good as the final in-ice track, it is important to note that the in-ice track will try to reconstruct every event, as it is blind to whether or not the event is actually within the array; thus, it is possible for a nearby, but non-contained, event to be reconstructed as being contained. To be safe, we must remove those events which are considered by the surface reconstruction to be outside the volume of the *in-ice* array.

#### 4.5.2 Containment Using Independent IceTop and InIce Reconstructions

The second iteration tracks have been iterated through; thus, it is possible that an error from the first iteration could be propagated through to the final selection as something which looks like a good event but which is actually a nearby event that has repeatedly been “pulled” within the arrays. To solve this problem it is clear that we need to choose an independent surface

reconstruction to select for in-ice containment, and an independent in-ice reconstruction to select for IceTop containment. When the surface reconstruction reconstructs an IceTop event, a shower near the edge of the detector can be “pulled in” or reconstructed as falling within the area of the detector. Thus, events which are actually outside of the array will appear to fall within the array. The same is true for the in-ice detector. Therefore, it is a better choice to use the in-ice array to check for IceTop containment *and vice-versa*. The first iteration of the surface reconstruction is totally independent of the in-ice array, therefore we use this fit to select for containment as well. Our first in-ice reconstruction uses information from the first surface reconstruction; thus, as we have shown, it is biased and will not be used. However, there exist many other completely independent in-ice reconstruction algorithms specifically designed to find the best tracks using the in-ice detector by itself. One of the most commonly used is the LineFit reconstruction (as described in Chapter 3: this fit is used for the last IceTop containment cut).

#### 4.6 Further Quality Cuts

One goal of making cuts is to select events with good angular reconstruction; thus, the rest of this chapter includes several figures in which colored contours show the reconstructed angular error of the second iteration of the surface reconstruction with respect to the true track. The black dots represent simulated iron showers, while the gray dots correspond to simulated protons. The solid black line follows the chosen cut surface. The angular resolution contours demonstrate the usefulness of the cut and the proton and iron scatter plots to show that we are not biasing our sample.

#### 4.7 Angular Difference

Another way to catch events which are not well reconstructed, either in-ice or at the surface, is to calculate the opening angle—or *angular difference*—between the two final reconstructions:

$$\Delta\Psi = 90 - \sin^{-1}(\cos(\phi_1 - \phi_2) \sin\theta_1 \sin\theta_2 + \cos\theta_1 \cos\theta_2), \quad (4.1)$$

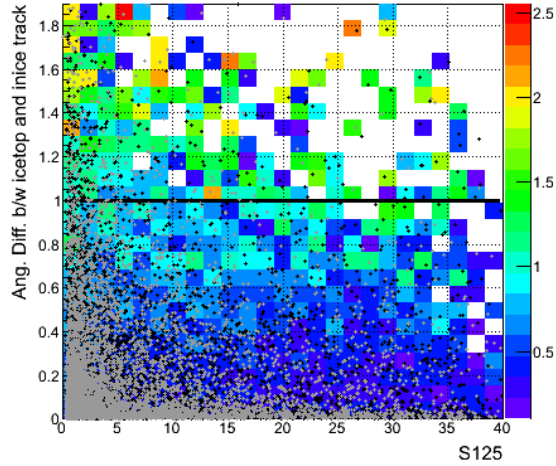


Figure 4.6: Angular difference between the surface and in-ice reconstructions (in degrees) vs S125. We keep only events with angular difference less than 1 degree (as marked by the solid black line). Shown are iron (black), protons (gray) and angular error of the second iteration (color).

where 1 and 2 indicate the two reconstructions which are being compared. If the surface reconstruction and the in-ice reconstruction have vastly different directionality, it is clear that one—or both—have a less-than-desirable degree of angular accuracy. Thus, as can be seen in Figure 4.7, the colored contours show a much larger angular difference between the true and reconstructed tracks above the cut at opening angle greater than 1 degree.

#### 4.8 Direct Length: LDirC

The longer the length of the track in the ice the better the reconstruction will perform, since longer tracks will have more data points for the in-ice track to fit. It is especially true that for well-contained high energy events the track lengths should be reasonably long. Thus, a two-dimensional cut on LDirC—the direct track length within a certain time window of the in-ice track—is performed as seen in Figure 4.8. This cut is defined by:

$$\begin{aligned}
 & \text{for}(S_{125} > 5.625) : LDirC > 850 \\
 & \text{for}(S_{125} \leq 5.625) : \frac{LDirC - 400}{S_{125}} > 80
 \end{aligned} \tag{4.2}$$

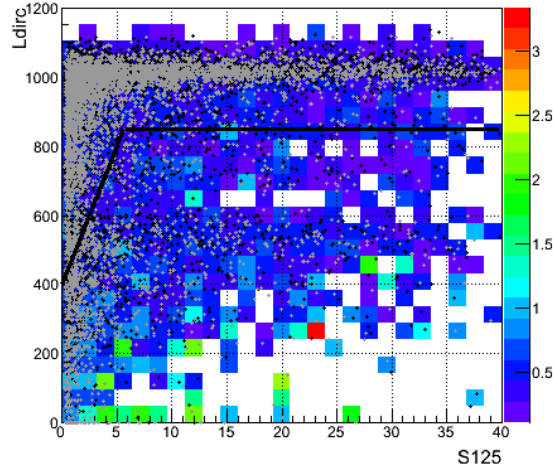


Figure 4.7: Direct length (LDirC, in meters) vs S125. We keep only events above the line marked by the solid black line. Shown are iron (black), protons (gray) and angular error of the second iteration (color).

## 4.9 Length Parameter

The length parameter from the Cherenkov lateral fit is another way to check the in-ice reconstruction. The average of the fitted attenuation length parameter is 26 m. The lateral distribution function used in the in-ice reconstruction fits this quantity. It is expected that it will not perform well for lower-energy showers; however, since this quantity does have a slight primary-mass dependence we make a loose two-dimensional cut on the length parameter with respect to both  $K_{70}$  and  $S_{125}$  in an attempt to restrict ourselves to events in which the  $K$ -parameter is well-reconstructed, as seen in Figure 4.8.

$$20m < \text{Length} < 150m$$

$$\text{Length} < \frac{100}{K_{70}} + 40 \quad (4.3)$$

$$\text{Length} < \frac{150}{S_{125}} + 40$$

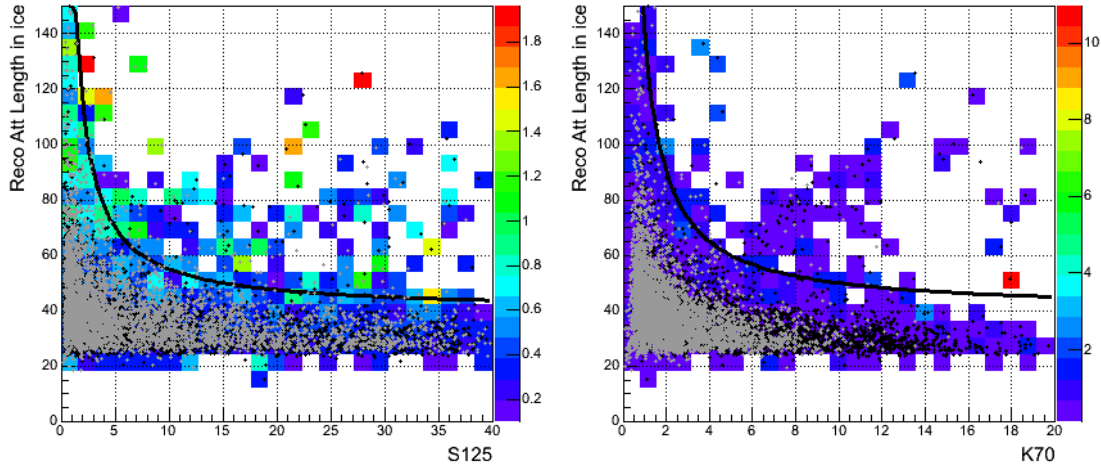


Figure 4.8: Reconstructed attenuation length of light in ice (in meters) vs S125 and K70. In each figure we keep only events below the solid black line. Shown are iron (black), protons (gray) and angular error of the second iteration (color).

#### 4.10 Timing

The final cut only applies to data. In data, random coincidences can occur, i.e. events which pass through the detectors within the time-window we use for coincidence, but which are completely unrelated. We do not simulate such events. The time difference between hits in IceTop and hits in the deep detector should correspond approximately to the time of flight of the muons. Events which do not match this basic criteria can be filtered out using the timing of the hits to verify the reconstructions by quantifying the difference between the arrival times of each track hypothesis at the surface:

$$\Delta t = \frac{z_{surface} - z_{inice}}{c \cdot \cos(\theta_{inice})} - (t_{inice} - t_{surface}). \quad (4.4)$$

To eliminate these events, we require  $\Delta t$  less than 3000 ns [122].

#### 4.11 Final Cut Evaluation

To summarize, we have developed the cuts listed in Table 4.11. These cuts have been constructed to achieve four goals:

1. To remove misreconstructed events by requiring events to pass through both detectors with

- good confidence in angular resolution and core position.
2. To avoid a bias in the composition measurements by cutting on one type of particle more than another.
  3. To avoid a bias in the energy spectrum by preferentially cutting on high or low energies.
  4. To retain as many events as possible, as simulation generation is an extremely time-consuming process.

Table 4.1: A definition of the different cut levels used for this analysis.

Cut Level	Description
1	Basic cuts: success of the minimizer for the first and second iteration of the surface LateralFit, and $N_{ch} > 5$
2	Containment $< 1$ for the first and second iteration of LateralFit, the second iteration of MuonBundleReco, and from LineFit
3	Angular Difference (as defined in Equation 4.1) between LateralFit and MuonBundleReco $< 1^\circ$
4	Restriction on the Direct track Length (LDirC) as in Equation 4.2
5	Restriction on the reconstructed attenuation length of light in the ice, as in Equation 4.3
6	Timing requirement so that (unsimulated) random coincidences are removed from the data

Figure 4.9 demonstrates the excellent agreement between data and simulation after cuts. Figure 4.10 shows the effectiveness of the chosen cuts in finding well-reconstructed events. Here, the reconstructed position and angle resolutions are shown to be extremely narrow. We have achieved a resolution less than 10 meters in position and less than 1 degree in angle—a considerable feat considering that the average detector separation is 125 meters.

This careful effort is rewarded by a clean, reliable, particle-independent energy spectrum through  $S_{125}$ , and a strong separation of particle type in  $K_{70}$ , while maintaining the excellent agreement between data and simulation that was observed before. The strong dependence of  $K_{70}$  and  $S_{125}$  on particle type and the clear correlation of  $S_{125}$  to primary energy can be seen

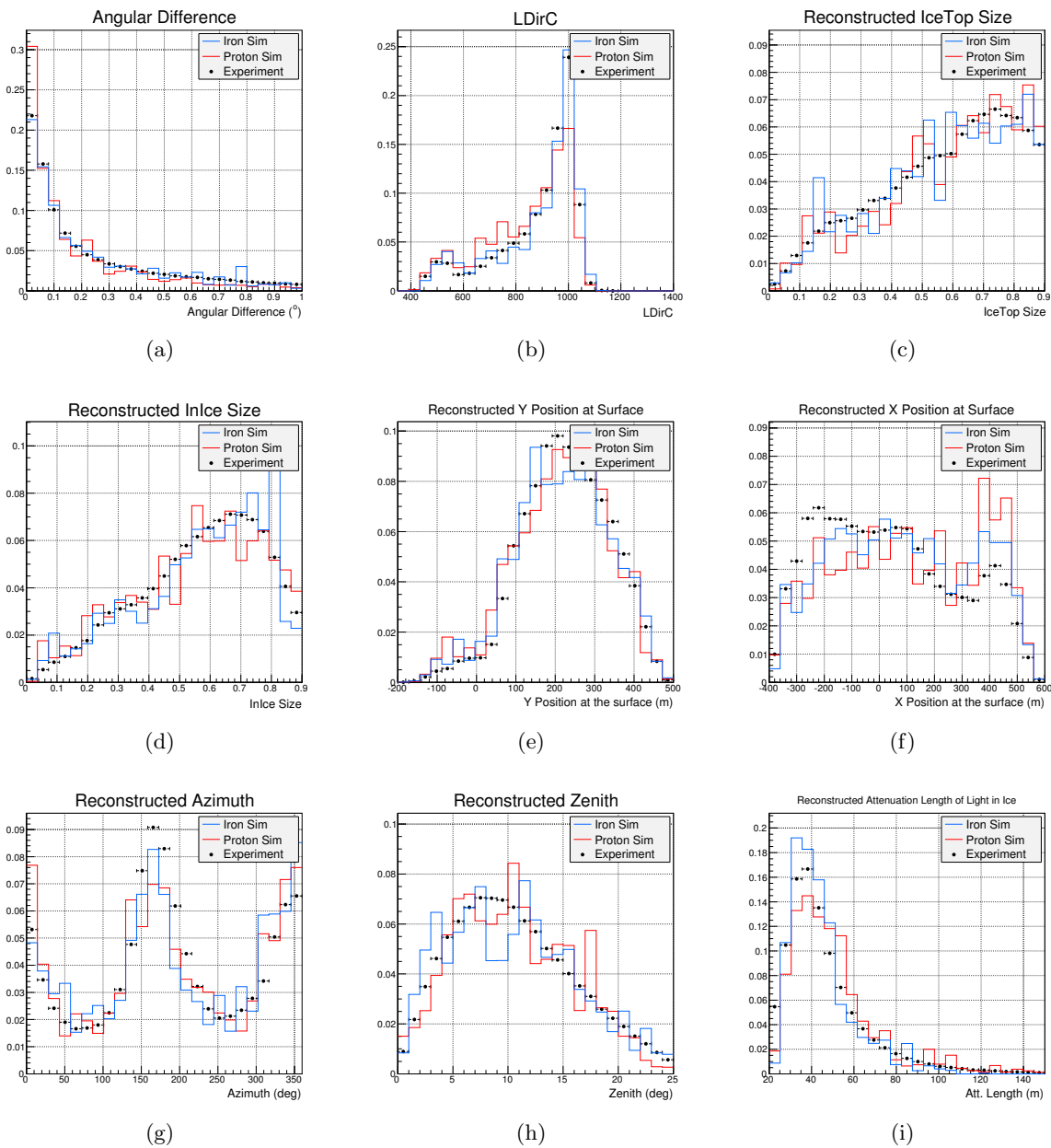


Figure 4.9: These are all histograms of parameters which were either used to make the cuts or are useful diagnostic histograms. At this stage, all the cuts have been applied. The data clearly matches the simulation in all but one plot: the x-position, Figure 4.9(f). This is due to the drifting of the snow in data, which is not simulated, and will be discussed further in Chapter 8.

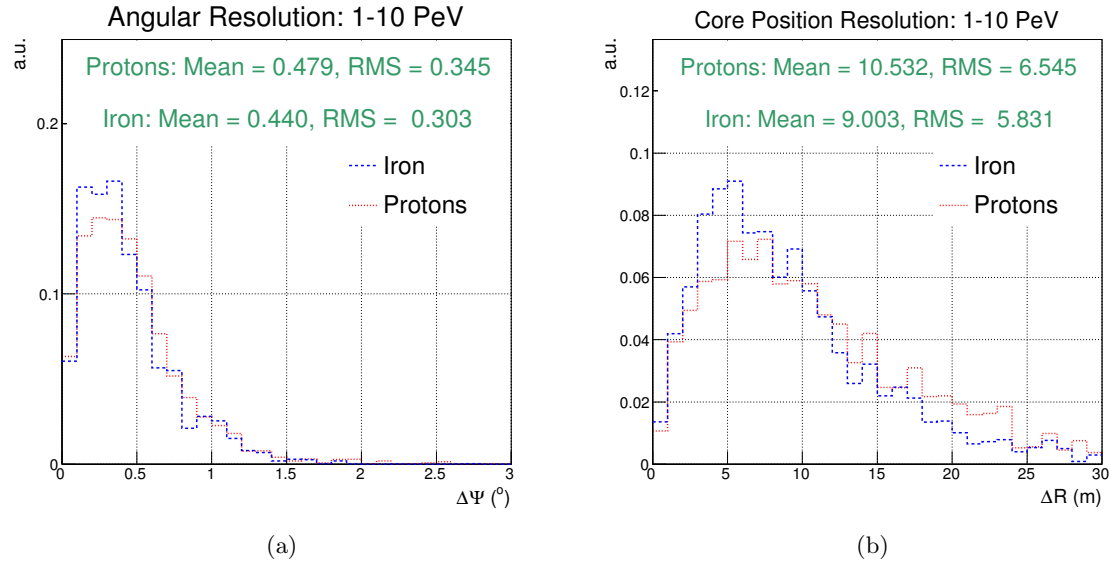


Figure 4.10: The opening angle (Figure 4.10(a)) and core position difference (Figure 4.10(b)) between the true track and the final in-ice reconstructed track.

in Figure 4.11. This cannot be achieved without some loss of events, demonstrated in Tables 4.2

Table 4.2: Cut biases for experimental data and simulated proton and iron.

Cut Level	# experimental data events remaining	total # simulated proton and iron events remaining	#p	(%)	#fe	(%)
1	1141590	62954	29945	47.6	33009	52.4
2	368815	11737	6053	51.6	5684	48.4
3	325685	10959	5679	51.8	5280	48.2
4	259717	8392	4196	50.0	4196	50.0
5	239902	8122	4039	49.7	4083	50.3
6	239797	8112	4036	49.8	4076	50.2

and 4.3. Here it can be observed that the sample remains unbiased and the sample resolution is improved with each cut, but overall efficiency plummets, producing a final simulation sample size of 8,112 proton and iron events, as compared to 239,797 events in a single month of data. We have worked hard to retain as many events as possible but this will eventually prove to be a limiting factor of this analysis.

Table 4.3: Cut reconstruction statistics for simulated protons and iron only.

Cut Level	total # simulated proton and iron events remaining	# truly contained	(%)	# within $1^\circ$ accuracy	(%)	$\Delta r < 25m$	(%)
1	62954	16601	26.4	25490	40.5	35313	56.1
2	11737	11201	95.4	10443	89.0	11190	95.3
3	10959	10484	95.7	9993	91.2	10532	96.1
4	8392	8129	96.9	7872	93.8	8074	96.2
5	8122	7868	96.9	7694	94.7	7815	96.2
6	8112	7859	96.9	7685	94.7	7808	96.3

Figure 4.12, which will be referenced numerous times in the coming chapters, shows the mass-separation and energy-dependence of the  $K_{70}$ - $S_{125}$  parameter space, and includes an RMS profile of the August 2008 data, to provide an initial indication for how these two parameters lead to the results.

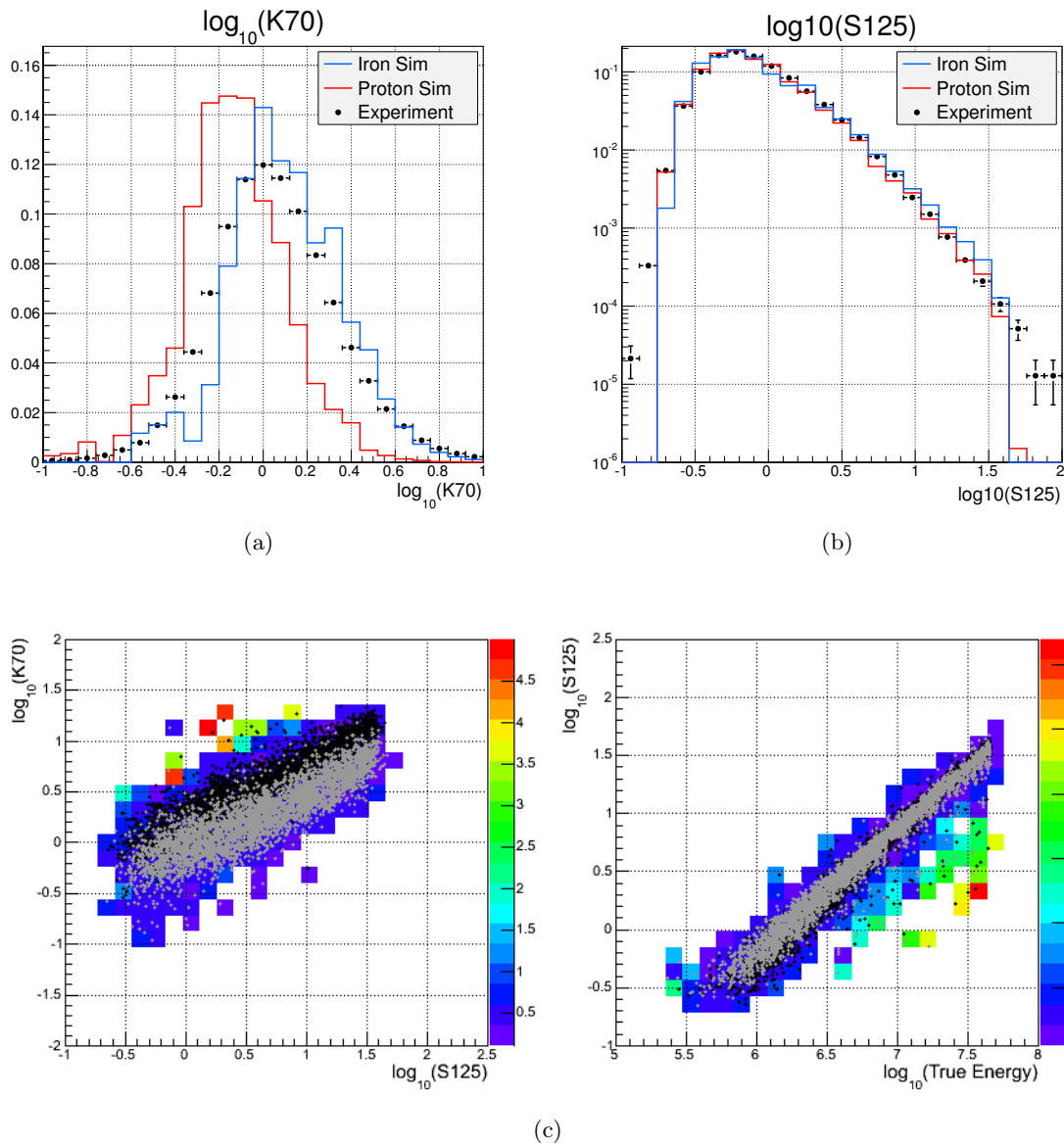


Figure 4.11: Figures 4.11(a) and 4.11(b) show  $K_{70}$  and  $S_{125}$  after the final cut level in simulation and data: there is clearly good agreement. In Figure 4.11(c) the colored contours show the angular error of the second iteration of the surface reconstruction with respect to the true track. The black dots represent simulated iron showers, while the gray dots represent simulated protons. Our cuts have managed to eliminate most of the events which have a large angular resolution. It has proven impossible to eliminate those that are left without also removing a disproportionate number of useful events, and those few that are left are not expected to bias our sample.

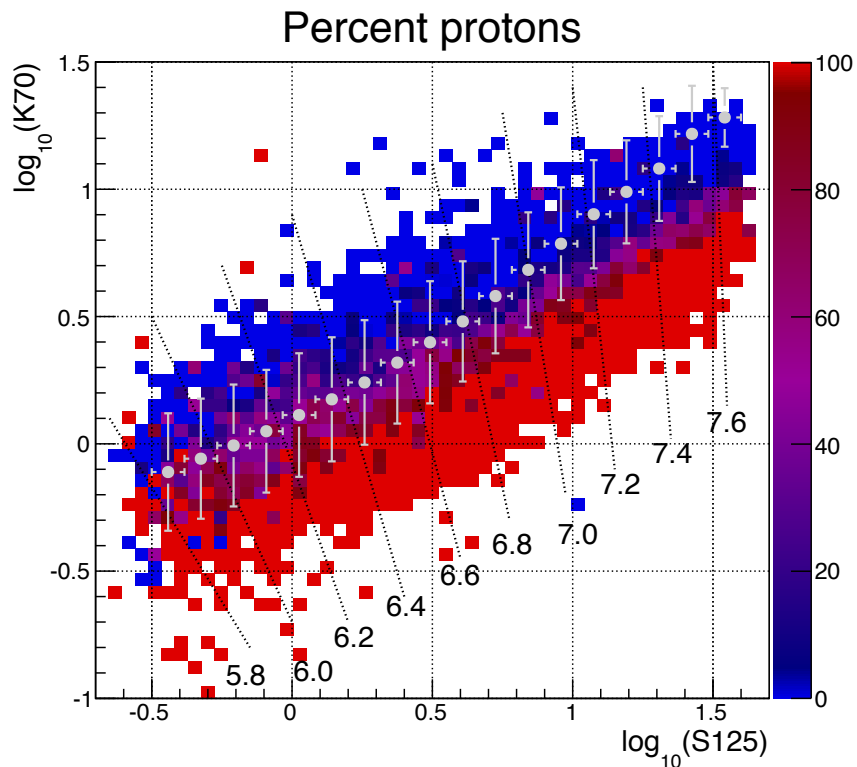


Figure 4.12: This is a plot of the  $K_{70}$ - $S_{125}$  parameter space after cuts. The colored contours depict the percentage of protons in each bin for simulated proton and iron showers ONLY. A bin which has more protons than iron will appear reddish, whereas a bin containing more iron than protons will be shaded in blue. Regions with the most overlap are colored in purple. The dotted black lines depict approximate contours of constant primary energy and are labeled in  $\log_{10}(E)$ . It is clear that the lines are not parallel. The data is shown as a gray profile with RMS error bars. There is clearly a good separation of proton and iron, especially at the highest energies. Furthermore, a comparison with Figure 3.2 shows a similarity which is remarkable due to the fact that this figure includes a detector simulation, whereas Figure 3.2 is theoretical only.

## Chapter 5

### Spatial Mapping: A Neural Network Technique

In the previous chapters we have developed parameters for IceCube and IceTop which provide information related to the primary energy and mass of individual cosmic ray air showers. The task remains to find the exact relationship between the  $K_{70}$ - $S_{125}$  parameter space and the  $\langle \ln A \rangle$ - $\log_{10}(\text{Energy})$  space. This is a problem of non-linear mapping, as was expected from Figure 3.2, and has been shown to be the case in Figure 4.12.

There are a number of techniques one can choose to use for non-linear mapping from one two-parameter space to another; however, while in the case of this particular analysis it is not difficult to find a mapping by hand, there are currently a variety of input parameters being developed to lend better separation capability to the muonic and electromagnetic air shower components in future analyses. Thus, with an eye to the future, it makes sense to develop a new technique on the simple case used here so that the mapping tools will be available to future generations who wish to use more than two input parameters. One obvious choice for mapping from multiple continuous input parameters to multiple continuous output parameters in a non-linear fashion is a neural network.

A common misconception about neural networks is that they are simply glorified black boxes with cranks attached which we can turn and pop out the correct answer without understanding anything. But, indeed, this is not the case: as we shall see, a neural network is not so different from a polynomial fit. But before we get ahead of ourselves with analogies, let us take a step back for a moment to understand what a neural network really is. (The reader who is very familiar with

neural networks may wish to skip ahead to Section 5.2.)

## 5.1 Introduction to Neural Networks

If I can learn to ride a bike, pick out a face among thousands, and identify a voice in a crowd, simply through trial and error, can I teach my computer to learn in the same way? This basic idea was the breath of life to computer learning algorithms in the first half of the 20<sup>th</sup> Century. By that time it was known that the human brain learns by using a highly connected network of *neurons*, which communicate with each other via electrical impulses over a complicated wiring structure consisting of axons, synapses, and dendrites. A simplistic idea of such a neuron is a switch which is either on or off depending upon the input from its connected neurons. If the input changes, the neuron can be activated or inactivated. The input is “weighted” and therefore depends on its source. For example: say you have two friends, Kris and Pat. If Kris is a known liar and Pat has typically been found to tell the truth, you are more likely to believe information coming from Pat. In biological terms, it could be said that you have a stronger “synaptic connection” to Pat, and information coming from Kris you will likely discredit entirely. In other words, input coming from a neuron to which the original neuron has a strong synaptic connection is weighted more heavily in the positive direction, whereas input from a neuron with a weak connection is given a negative weight. If the sum of the weighted inputs exceeds a certain threshold, the neuron will switch its state from activated to inactivated or vice versa. The total input from a given unit can be written mathematically as:

$$a = \sum_{i=0}^d w_i x_i \quad (5.1)$$

where  $w_i$  is the weight given to the input  $x_i$ . This first model of a neuron, as a simple switch, was proposed in 1943 by McCulloch and Pitts. It is mathematically very basic and can be thought of as a non-linear function which first transforms a set of inputs by weighting each input parameter (by either a positive or negative weight, as above), adding the weighted inputs together, and operating on this sum with an *activation function* such as those shown in Figure 5.1. The neurons, or *nodes*,

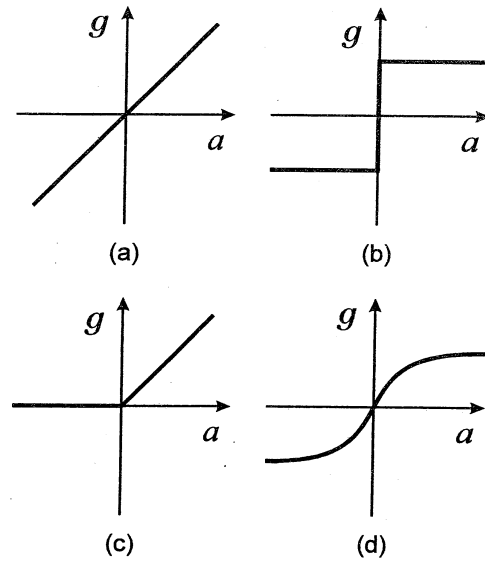


Figure 5.1: This diagram shows four types of activation functions that are either presently used or were previously used in neural network training. Figure 5.1(a) shows a linear activation function, Figure 5.1(b) shows a simple step function, as was used in the first neural networks modeling a switch, Figure 5.1(c) shows a linear function with a threshold below which the node is not activated, and Figure 5.1(d) shows a sigmoid type activation function which is in common use today [70].

can be combined as follows:

$$z_j = g(a) \quad (5.2)$$

$$z_j = g\left(\sum_{i=0}^n w_{ij}x_i\right) \quad (5.3)$$

$$(5.4)$$

where  $g$  and  $w_{ij}$  are the activation function and weight, respectively. To step back to the biological analogy, the input parameters are similar to the dendrites, the synaptic strength is the weight, and the output would be the average firing rate of the neuron.

The McCulloch and Pitts model of a neuron sparked an active time in the research of neural networks, during which the first hardware neural network system, called the *perceptron* was built by Rosenblatt. The perceptron was trained using the *perceptron learning algorithm*, which was

based on the idea from Hebb that learning is basically a series of modifications of the weights, or synaptic interconnections, between neurons. In other words, if there are two neurons which often trigger together, the weight of their connection should be increased. From understanding gained through his experiments, Rosenblatt was able to demonstrate theoretically the astounding fact that the perceptron learning algorithm was *guaranteed* to find a solution, in a finite number of steps, to any problem that was solvable in principle by a perceptron.

This era of intense development in the field of neural networks ran until the late 1960s, when it was shown by Minsky and Papert that a simple switch-type network using the step-type activation function in Figure 5.1(a) could only solve a very limited class of linearly separable problems. (In the case of a linear activation function, as in Figure 5.1(b), the method reduces further to simple multiplication.) However, interest was renewed in the 1980s when new learning algorithms based on the idea of *error back-propagation* breathed new life into the networks of the past. Error back-propagation can be thought of as learning from mistakes: for example, when a child touches a hot stove and gets burned, that child learns that stoves can be hot and will be more careful in the future. Learning methods using this technique allowed for *multi-layer perceptrons* or MLPs. Where with the *perceptron* the structure is:

$$\text{input layer} \rightarrow \text{weights} \rightarrow \text{activation function} \rightarrow \text{output layer} \quad (5.5)$$

the idea of an MLP is to combine more than one layer of weights to map from the input parameter space to the output parameter space, so, for the simplest case:

$$\text{input layer} \rightarrow \text{weights} \rightarrow \text{activation function} \rightarrow \text{intermediate layer} \quad (5.6)$$

$$\rightarrow \text{weights} \rightarrow \text{activation function} \rightarrow \text{output layer}. \quad (5.7)$$

Each intermediate layer is called a *hidden layer*, which has a *hidden node*. There can be as many

hidden layers and hidden nodes as necessary. This can be written mathematically as:

$$y_k = \tilde{g} \left( \sum_{j=0}^m \tilde{w}_{jk} z_j \right) \quad (5.8)$$

$$y_k = \tilde{g} \left( \sum_{j=0}^m \tilde{w}_{jk} g \left( \sum_{i=0}^d w_{ij} x_i \right) \right) \quad (5.9)$$

$$(5.10)$$

where  $\tilde{g}$  and  $\tilde{w}_{jk}$  are the activation function and weight from the output layer  $k$ , and  $g$  and  $w_{ij}$  are now the activation function and weight from the hidden layer  $j$ , and  $\tilde{g}$  does not need to be the same function as  $g$ .

In either a simple perceptron or an MLP, it is helpful to think of the weights as analogous to the coefficients in a polynomial where  $x$  is the input variable, and  $y$  is the desired output.

$$y = w_m x^m + \dots + w_1 x^1 + w_0 = \sum_{j=0}^m w_j x^j \quad (5.11)$$

In the same way that we would fit a polynomial to a set of data-points, we can fit a neural network to a parameter space. These are both non-linear mappings; however, there are two significant differences:

1. neural networks can have many inputs and outputs whereas the polynomial has only one of each; and,
2. a large class of polynomial functions can be approximated by a neural network very efficiently.

In principle, one can develop a multivariate polynomial which accomplishes the same non-linear transformation between two parameter spaces as a neural network; however, neural networks offer a much more practical approach as they use far (exponentially) fewer parameters. In fact,

“a sufficiently large network can approximate any continuous function, for a finite range of values of the inputs, to arbitrary accuracy” [70]

Although, while that statement may lead to the naive assumption that one should always use a

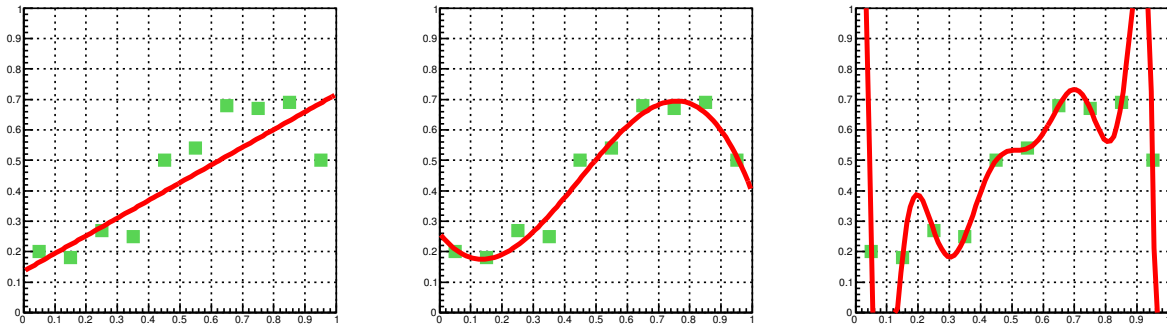


Figure 5.2: A collection of data can be fit to a variety of polynomial functions, in a similar way to neural network fitting. In this case, the best fit is to a  $3^{rd}$  order polynomial. While the  $9^{th}$  order polynomial is an exact fit, it fits all the random noise as well as the underlying distribution. (After [70].)

very large neural network because it will always find a solution, in practice we must deal with a finite data set with a certain precision. Therefore, this statement brings up an important pitfall to a neural network analysis: *overfitting*. Overfitting can happen in two ways: from training the network too well on a given data set, and from fitting the data set with too large a network. Thus, in order to find a generalizable mapping to describe the trends in the underlying distributions without fitting the noise in the data set, it is better to choose the *smallest* neural network for the precision of the dataset available. For example, consider a set of ten data-points following a sine function with artificial noise (as in Equation 5.2). This data can be fit to any number of polynomials: a  $1^{st}$  order polynomial can be fit, but does not describe the data well; a  $3^{rd}$  order polynomial fits quite well, but not perfectly; a  $9^{th}$  order polynomial is an exact fit. Now, it might be tempting to choose the  $9^{th}$  order polynomial to represent the data, but the underlying function is sinusoidal, so the  $9^{th}$  order polynomial is actually fitting a bunch of noise—clearly not the desired choice. In the same way, we should not automatically choose the largest network which can fit our sample, since this will not be generalizable to a larger set of data.

To help avoid the problem of overfitting we must determine the best network *architecture* (i.e., the number of internal layers and nodes) and produce a generalizable network. Thus we divide the data into three independent sections: one to *train* the network, one to *test* the network and a third to *validate* the performance of the network once it has been trained and tested. (The third is

absolutely necessary for any analysis of the network since the test set is used in the optimization of the network and is therefore no longer unbiased.) Then, considering an MLP network, the process of choosing architectures and checking generalization is as follows:

1. Select a network architecture and initialize the network weights randomly.
2. Using one of the standard learning algorithms, minimize the error of the training data.
3. Repeat the training beginning with different random weights in order to find a good minima.  
Select the network with the smallest error at the end.
4. Evaluate the error function from the resulting network with the test data set.
5. Change the architecture and run through the entire process again. The best network has the smallest error for the test set.

This process may seem a bit daunting: fortunately there are a number of software packages to help with this process, for example: ROOFit, SNNS, and the TMultilayerPerceptron class in ROOT. In the development of this analysis we tested all three packages and, upon finding similar results in all cases, settled on the ROOT package simply for ease of use (the root file format is the standard for the IceCube collaboration).

## 5.2 Neural Networks for this Analysis

Now that we have set up the basic structure of a network and a process for choosing useful architectures, we should return to our discussion of the current analysis. As we discussed above, our task is to find a multi-dimensional, non-linear mapping from  $K_{70}$ - $S_{125}$  space to  $\langle \ln A \rangle$ - $\log_{10}(\text{Energy})$  space, as in Figure 5.3. We have learned that in multi-dimensional mapping, as in polynomial curve fitting, we are often working with noisy data; thus, we are looking for a function which provides a smooth representation of the underlying trends, but does not necessarily pass exactly through each data point. This can be called an *interpolation* problem. It is important to note that the most common use for neural networks in our field is that of classification—for example, an analyses in which each data point is categorized by a network as either a signal event or a background event—thus, a common misconception is that a neural network will not work for an interpolation



Figure 5.3: This is the basic layout we begin with when choosing a neural network. We know that our input parameters will be  $K_{70}$  and  $S_{125}$  and that we are looking for true energy and mass. The appropriate number of hidden layers and the number of nodes within each hidden layer is determined through extensive testing to avoid overtraining of the network on one end, and oversimplification on the other.

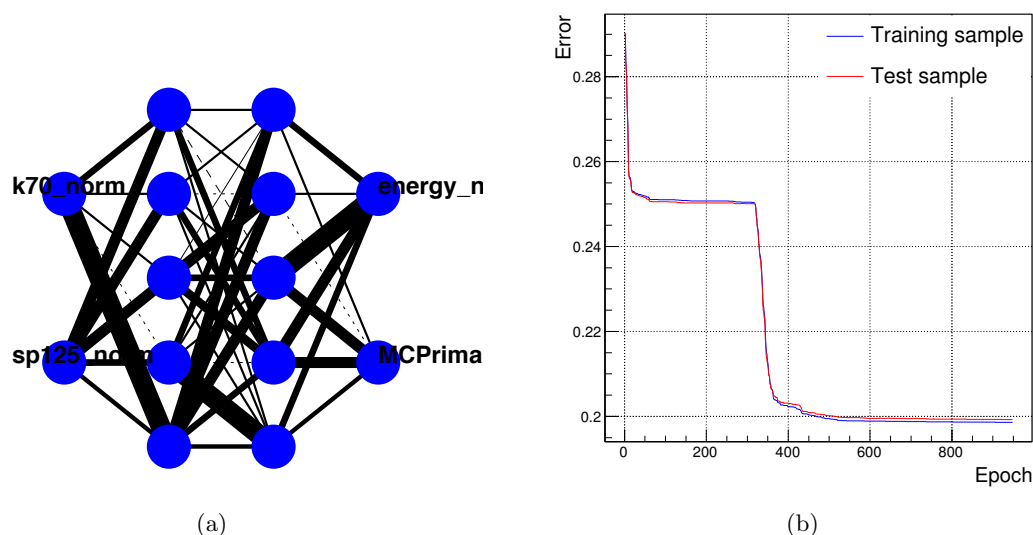


Figure 5.4: Figure 5.4(a) shows the structure of the final neural network we chose, with structure 2:5:5:2. The black lines depict the weights between the nodes—the thicker the line, the stronger the connection. Figure 5.4(b) shows the error in the training (blue) and testing (red) sample. Both errors decline steadily through all 947 training cycles. If we were to train this network for more than 947 cycles it would become overtrained, a state which would be indicated by an increase in the error of the test sample, while the error in the training sample was still decreasing—this implies that the network has started to fit the random noise as well as the underlying distribution, as discussed in Figure 5.2.

problem. However, as we will see, neural networks can indeed be applied to interpolation problems, even those in which there may be several input and several output variables (such as ours).

### 5.2.1 Activation Functions: Sigmoid for Internal Layers, Linear for Output Layer

After testing a number of activation functions for our internal and output layers (such as tanh, softmax, linear and gaussian), we have decided to choose the default activation functions for the ROOT `TMultilayerPerceptron` class, which are also those recommended by Bishop [70]: sigmoid for the internal layers, and linear for the output layer.

### 5.2.2 Learning Algorithm: Broyden-Fletcher-Goldfarb-Shanno (BFGS)

In the process of testing learning methods, we came to the same conclusion as the developers of the ROOT software: BFGS seems to be the fastest training method and provides good results. This is expected as BFGS is a quasi-Newtonian method, and Newton’s method for finding the point of a function where the gradient is zero approximates the function as a quadratic in the region in

close proximity to stationary point, and then calculates the first and second derivatives to find the optimum value. In other words, it uses the curvature of the function as well as the slope, whereas other commonly used methods, called *gradient descent*, basically use the slope only and therefore take longer. The difference between Newtonian algorithms and quasi-Newtonian algorithms is that the quasi-Newtonian methods do not actually calculate the second derivatives of the function being minimized; instead, they use a finite difference approximation, which means that it should be even faster than a standard Newtonian method. (In summary, it turns out that an approximation to an approximation is faster than doing the full calculation, and in most cases—like this one—it is just as accurate.)

### 5.2.3 Architecture: 2:5:5:2

After much trial and error, it was discovered that the best architecture had two hidden layers of five nodes each. One hidden layer was not sufficient for the interpolation of the mass gradients, and more hidden layers appear to be redundant and provided no improvement (and in most cases a slight degradation in quality) to the mapping. The final structure can be seen in Figure 5.4(a), where the black lines denote the weights connecting the nodes.

### 5.2.4 Training Cycles: 947

The `TMultilayerPerceptron` class provides a useful tool to analyze the errors, as shown in Figure 5.4(b). In the case shown, the error in the training and test set have been minimized. When this same network was trained through more iterations, the error in the test set began to increase, while the error in the training set continued to decrease, a clear indication of overtraining—or learning the training sample too well to be generalizable to the test sample. It might be interesting to note that the plateau, which ends around 350 epochs, appears to be a trait of having two hidden layers. When three hidden layers were used, a second plateau was observed, when a single hidden layer was used, no plateau was observed.

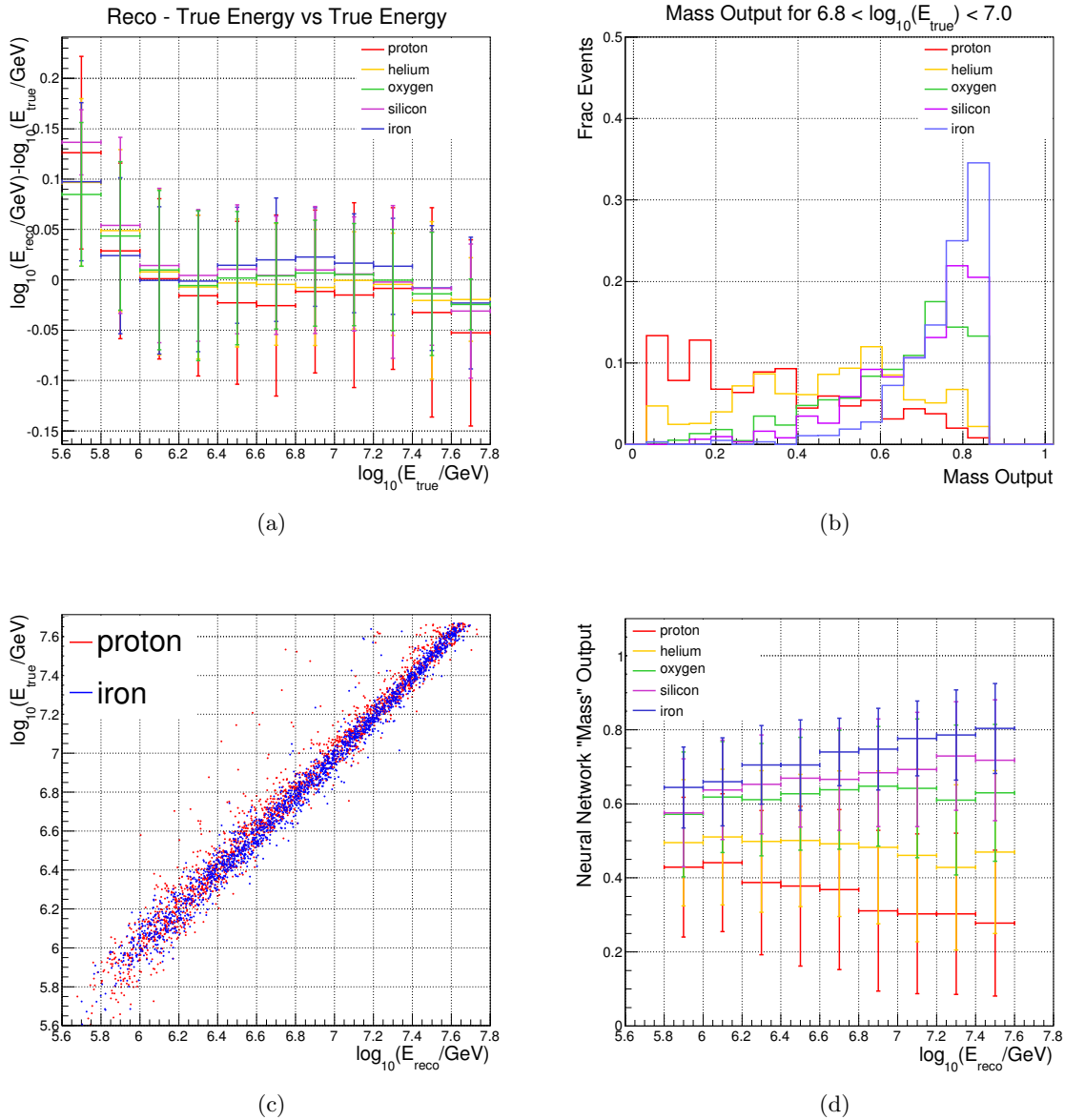


Figure 5.5: These are some basic plots of the neural network output parameters. In all plots, the colors denote the particle type: protons are red, helium is gold, oxygen is green, silicon is purple and iron is blue. Figure 5.5(a) we show the energy misreconstruction for all 5 particle types. Another way to look at this is in Figure 5.5(c), where we simply show the true vs the reconstructed energy: clearly we have remarkable energy resolution. In Figure 5.5(b) we show the mass output parameter for a single slice in energy ( $6.8 < \log_{10}(E_{\text{true}}) < 7.0$ ), which is equivalent to taking a slice from Figure 5.5(d) which shows the Mass vs Energy parameter space (similar to the  $A^*$  and  $E^*$  parameter space shown for the previous rotation analysis in Figure 2.12(b)) and expanding it in the third-dimension out of the paper. In both of those figures there is a great deal of overlap between the silicon and the iron, which makes silicon nearly redundant. All other primary types (p, he, o, and fe) have nearly equal mass separation at all energies.

### 5.2.5 Neural Network Output

In Figure 5.5 we show the output of the neural network mapping technique. The energy output is relatively easy to understand: it maps directly to the true energy that the network was trained on, as is clear in Figure 5.5(c). The misreconstruction of the energy reconstruction is shown in Figure 5.5(a): clearly we do an excellent job of estimating the primary energy of the particle in a nearly composition independent way. This will be discussed more in Chapter 6.

The mass deserves a bit more attention. For training the network, we assigned each particle type a mass defined as:

$$\text{mass} = \frac{\ln(\text{particle mass number})}{\ln(56)}, \quad (5.12)$$

where 56 is the mass number of iron. This was a way to quantify and normalize the mass of the particles between 0 and 1. In Figure 5.5(b) we show the mass output for all five particle types for a single slice in true energy:  $6.8 < \log_{10}(E_{\text{true}}) < 7.0$ . This shows where the particles of different types will be reconstructed in the mass-output parameter space. A common misconception is that the particles should span the entire Mass Output space, from 0 to 1. However, this is not true. The mass output basically represents how confident the neural network is that it has found a particle of a given type. At this energy, which corresponds to a slice shown in Figure 4.12, there is enough overlap with the other particle types that the network is not able to distinguish iron from silicon and oxygen: thus, for this slice in energy the network will never have an iron shower located at the mass output of 1.0, and the same is true for protons. Notice that the distributions become more peaked as the mass increases: this is also visible in Figure 4.12, which is due almost entirely to the fact that the lighter particles are subject to more fluctuations at the first interaction in the atmosphere. Figure 4.12 is essentially the input to the neural network, and the neural network cannot do better than the information it is given. This point is very important, and is very clear in Figure 5.5(d) which depicts profiles of mass output in slices of reconstructed energy. (This figure is essentially Figure 5.5(b), for all energy slices, as viewed from the top.) This figure shows that the type separation capabilities are limited at the lowest energies and are quite good at the highest

energies. Essentially, the network has performed a non-linear rotation from the  $K_{70}$ - $S_{125}$  space shown in Figure 4.12, to a mass-like and energy-like space. Since the input parameters have a significant amount of overlap at the lowest energies, the output also has significant overlap. Thus, more work will need to be done to transform the neural network mass output into  $\langle \ln A \rangle$ , the desired output for comparison with other experiments. This technique will be discussed in Chapter 7.

### 5.3 Human vs Neural Network

A measure of confidence is gained by comparing the neural network approach and an analytic (but less accurate) polynomial fit. In this comparison, we can see that the mapping function developed by hand is very similar to that fit by the neural network and, furthermore, that the energy and mass offsets are very similar between the two methods, with the neural network being slightly more predictable. As stated earlier, the main advantages to using a neural network are that it is expandable to many more input parameters (which conveniently eliminates the complicated task of developing n-dimensional mappings by hand), and that it is an automated and easily reproducible procedure, whereas the human-fitting technique would vary from human-to-human. We think that these two points make a strong case for the choice of a neural network to perform the non-linear mapping necessary for this analysis.

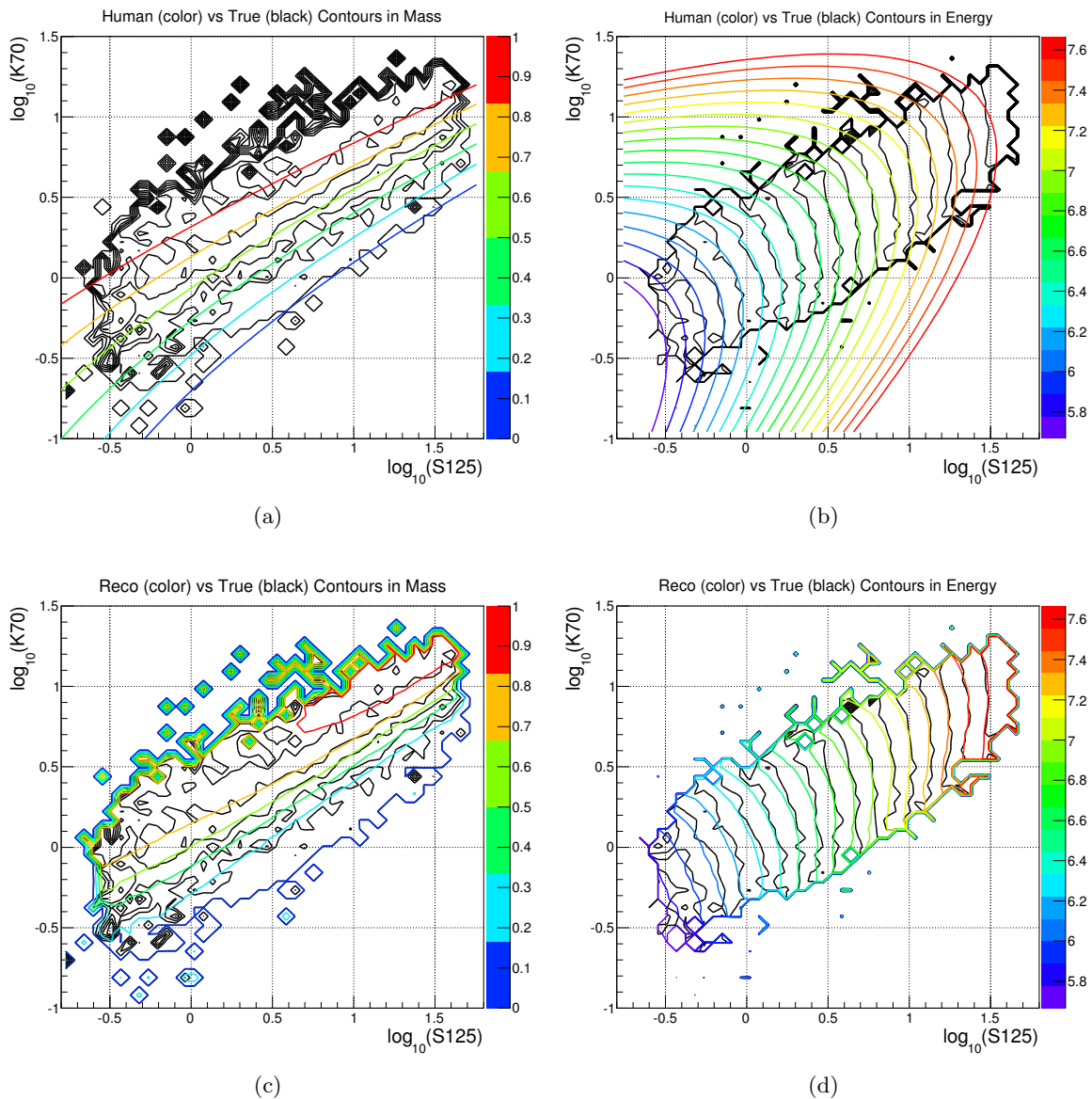


Figure 5.6: These contour plots indicate the mapping schemes we developed. In all figures, the black lines depict the true contours, while the colored contours indicate those achieved using either a neural network or the human function. In Figures 5.6(a) and 5.6(b) we show the mass and energy mappings, respectively, as generated by hand, which are directly comparable to Figures 5.6(c) and 5.6(d), the corresponding mappings as generated by the neural network. It is also clear that the two mappings are very comparable. It is also clear that this would become much more difficult to do by hand if there were more than two input parameters.

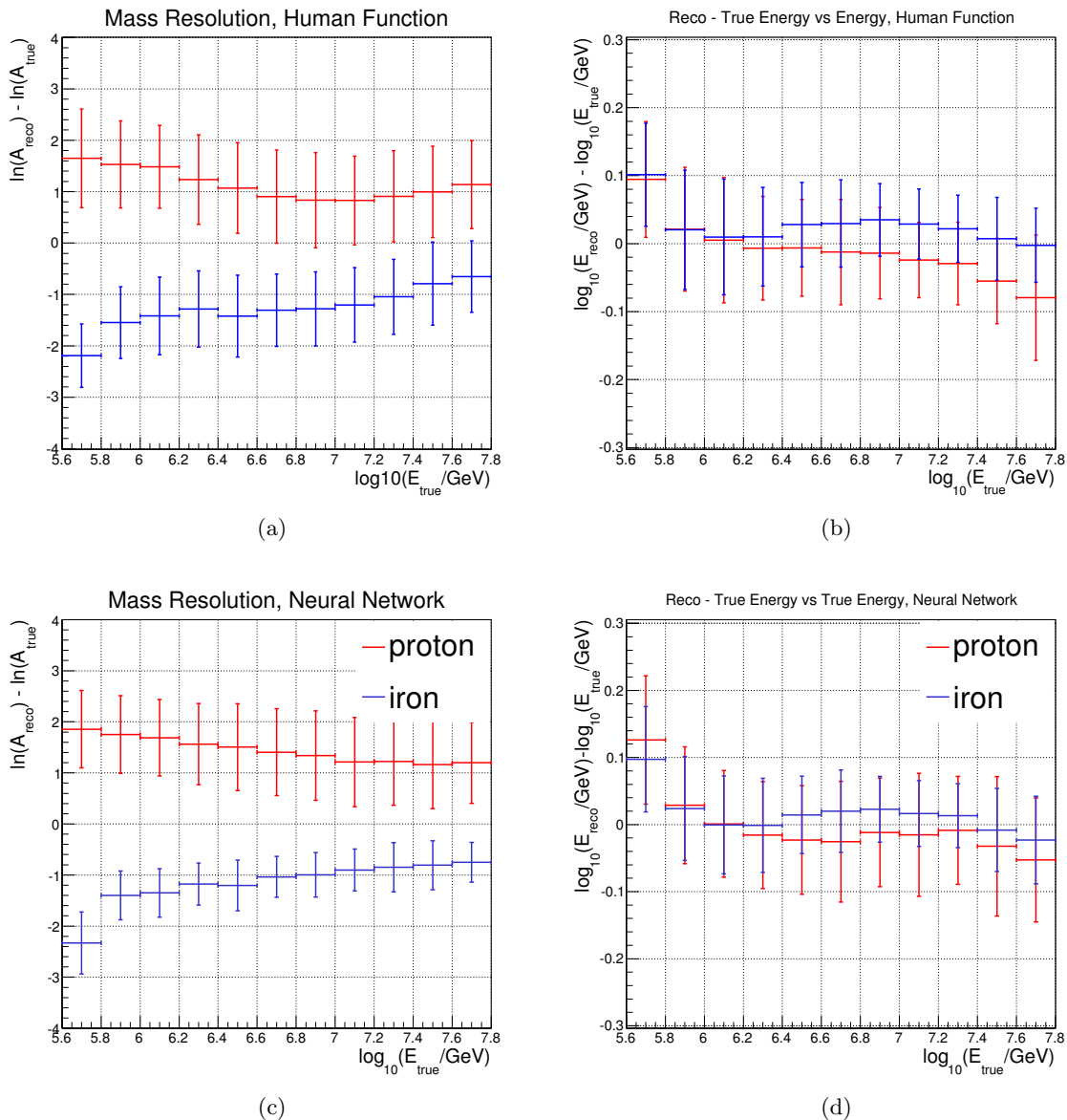


Figure 5.7: These plots indicate errors from the mapping schemes we developed in Figure 5.6. In these figures we have chosen to show only the two extreme masses: protons (red) and iron (blue). In Figures 5.7(a) and 5.7(b) we show the mass and energy misreconstructions, respectively, from the mapping generated by hand, which are directly comparable to Figures 5.7(c) and 5.7(d), the corresponding misreconstructions from the neural network generated mapping. It is clear that the two mappings are very comparable; however, the neural network does a slightly better job and has smaller error bars for both the mass and energy mappings.

## Chapter 6

### Energy Spectrum

At this point, we have used a neural network to find a mapping from  $S_{125}/K_{70}$ -space to mass/energy-space. As we can see in Figure 6.1, the energy resolution from the neural network output is very tight, so an obvious first step is to calculate the energy spectrum. The energy spectrum measurement is very important in cosmic ray physics, as discussed in Chapter 1. Furthermore, a complete energy spectrum analysis is being performed with IceTop alone, as seen in [50] and [60].

However, the focus of this analysis is composition and not the energy spectrum; thus, we perform a somewhat simplistic calculation of the spectrum, following the method developed by C. Song [71]. Since we have a very good energy resolution and very small bias, as seen in Figures 6.1(a), 6.1(b) and 6.2, we do not take these errors into account. Furthermore, we constrain ourselves to energies at which our detector has full efficiency:  $\log_{10}(E_{NN}) > 6.3$ . (The working definition of efficiency will be discussed in more detail below).

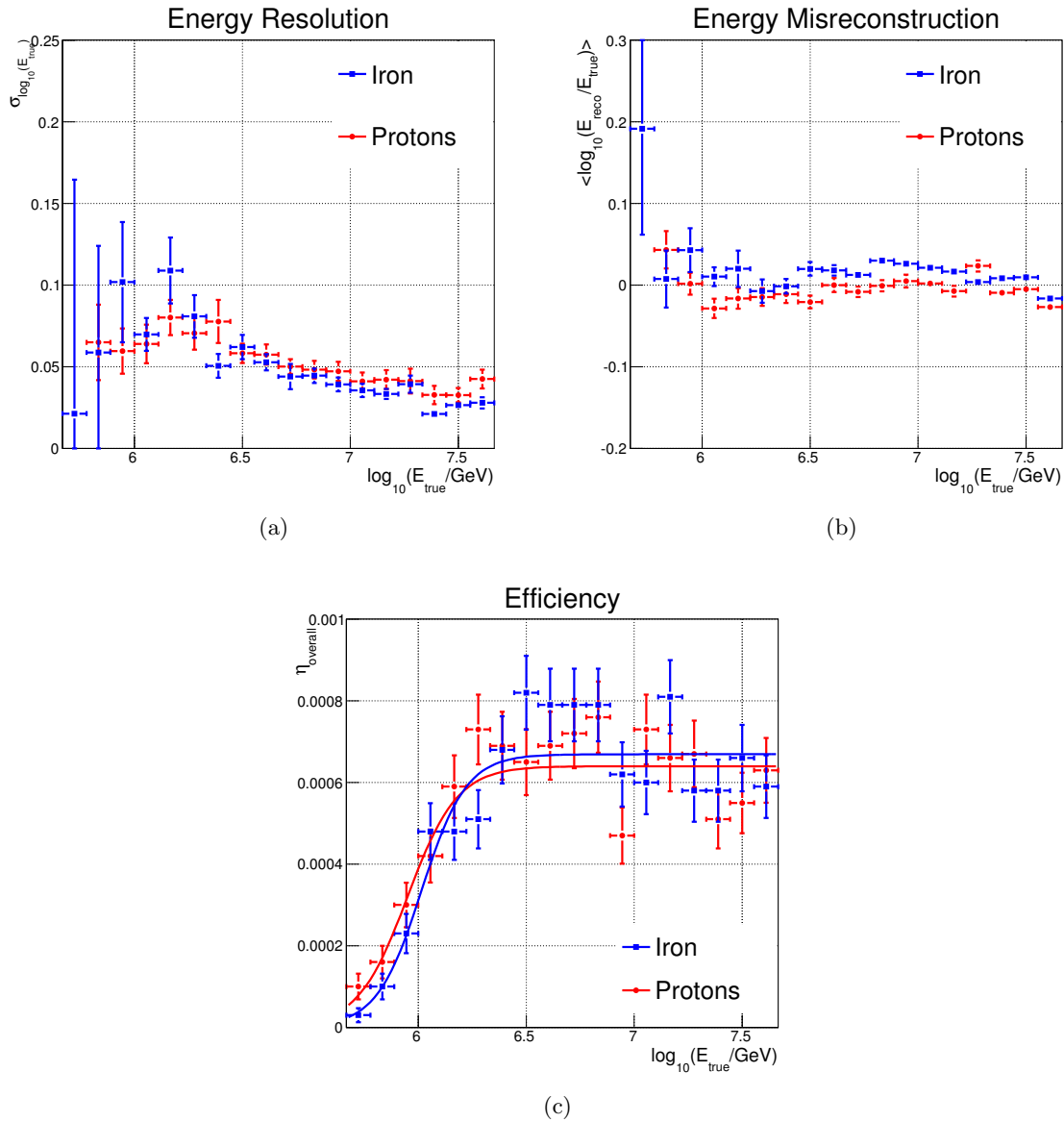


Figure 6.1: Figure 6.1(a) shows the response of the IceTop/IceCube 40-string detector in terms of energy resolution, Figure 6.1(b) shows the energy bias (also referred to as energy misreconstruction) and Figure 6.1(c) shows the overall efficiency from the energy output of the neural network. Red circles mark protons and blue squares denote iron. Figure 6.1(c) is used to define the energy at which our detector reaches full efficiency. Note that the efficiency is much smaller than 1: this is due to the requirement of coincidence between the two detectors. One of the main advantages of using both the IceTop and IceCube detectors for the composition analysis is that our energy reconstruction has a very tight resolution and is nearly primary-type independent, as can be seen in Figure 6.1(a) and Figure 6.1(b).

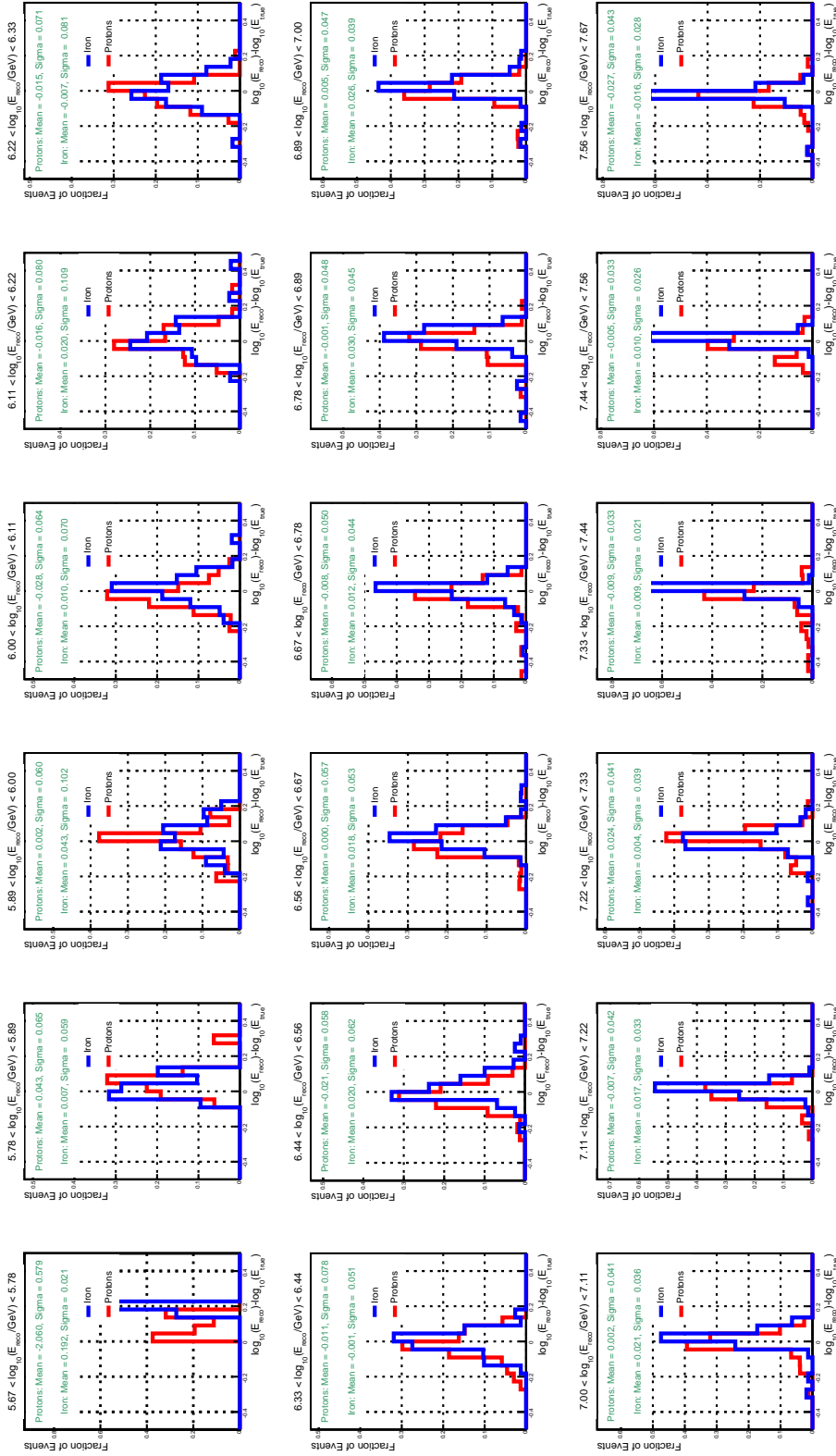


Figure 6.2: The difference between the reconstructed (from the neural network) and true energy for each bin in energy, labeled with a mean and sigma from a gaussian fit for each type of particle. These are the fits which were used to produce Figure 6.1(a) and Figure 6.1(b). It is clear that in the lowest energy bin we have too few statistics to reliably fit the gaussian.

## 6.1 Calculating Flux

For a given flux,  $\vec{J}(E)$ , the number of events,  $\Delta N$ , in a single slice in energy,  $\Delta E$ , is given by:

$$\Delta N_i = \eta_{overall} \tau \int_{E_i + \Delta E/2}^{E_i - \Delta E/2} dE \int \vec{J}(E) \cdot d\vec{s} d\Omega \quad (6.1)$$

$$\simeq \eta_{overall} \tau |\vec{J}(E_i)| A \Omega \Delta E, \quad (6.2)$$

where  $A$  is the effective core area, defined here as  $\pi(1200 \text{ m})^2$ , the area over which the CORSIKA air showers were oversampled;  $\tau$  is the exposure time, or livetime, of the detector, approximately 30 days as calculated in Figure 4.2(b);  $\eta_{overall}$  is the overall detector efficiency for each slice in energy, defined as:

$$\eta_{overall} = \frac{N_{\text{events after all cuts}}}{N_{\text{events generated}}}; \quad (6.3)$$

and  $\Omega$  is the stereo angle, given by:

$$\Omega = 2\pi \int_0^{\theta_{max}} \cos(\theta) \sin(\theta) d\theta = \pi \sin^2(\theta_{max}), \quad (6.4)$$

where  $\theta_{max}$  in our case is  $65^\circ$ . Rewriting, it is easy to see that:

$$J(E) = \frac{dN}{dE} \frac{1}{\eta A \Omega \tau}, \quad (6.5)$$

and, using

$$\frac{dN}{d \log_{10}(E)} = \frac{E}{\log_{10}(e)} \frac{dN}{dE} \quad (6.6)$$

(where  $e = \text{const.} = 2.7182\dots$ ) to convert to  $\log_{10}(E)$ , we find:

$$J(E) = \frac{1}{\eta A \Omega \tau} \frac{\log_{10}(e)}{E} \frac{dN}{d \log_{10}(E)}. \quad (6.7)$$

In other words, the flux can be found by dividing the energy distribution by the detector aperture,  $\eta_{overall}A\Omega$ , and the exposure time,  $\tau$ , with some care to account for the log scale. The overall efficiency from Equation 6.3 can be found in Figure 6.1(c) for protons and iron separately. The aperture for all particles generated (again  $\eta_{overall}A\Omega$ ), can be found in Figure 6.3(a).

## 6.2 Checking the Calculation

Before using our flux calculation above to obtain the observed cosmic ray flux in the data, we perform a numerical verification using simulation. We give our simulation a realistic flux (based on observations from other experiments) and test that the above calculation successfully reproduces the flux we give the simulation.

### 6.2.1 Step 1: Transforming the Generated Spectrum to a More Realistic Spectrum

Cosmic ray air shower simulation events are often generated using a spectrum of  $f \sim E^{-1}$ . However, the measured spectrum is very different, generally following  $E^{-2.7}$  below the knee and  $E^{-3.0}$  above a knee around 3 PeV. Therefore, to convincingly compare simulation to experimental data, the simulation must be reweighted to match the expected distribution in the experimental data. This means that we multiply the “observed” rate in simulation by a weight, and from the reweighted distribution, which reproduces what we generally expect to see, we can calculate the flux for the simulation following the same method used for the data.

To begin, we need to weight our simulated events properly. This requires a good understanding of what we expect to see compared to what we have generated, so that we can convert our generated rate to a realistic “observed” rate. To be perfectly clear, let us review what we generated:

- 3000 events for each particle type, for each 1/3 of a decade in energy (via the Niessenian binning scheme described in Appendix B), with each event oversampled 100 times,
- 5 particle types,
- flat (on a log scale)  $E^{-1}$  spectrum.

We would like to end up with:

- realistic all-particle flux,
- realistic spectrum:  $E^{-2.7}$  below a knee around 3 PeV, and  $E^{-3.0}$  above the knee.

In order to write this in mathematical terms, we must first develop some formulations for observed rates. Below, we will define some terms, following the notation used by Peter Niessen [72] for ease of comparison.

### 6.2.1.1 Defining Some Notation

A power law energy spectrum is governed by:

$$\frac{dN}{dE} = \Phi_0 \left( \frac{E}{E_0} \right)^{-\gamma}$$

where  $\gamma$  is the spectral index (a positive number) and  $\Phi_0$  is the flux normalization for a given energy  $E_0$  (in GeV) as observed by other experiments. Now, if we let  $\tilde{E} = \frac{E}{E_0}$ , it follows that:

$$\begin{aligned} d\tilde{E} &= \frac{1}{E_0} dE, \text{ and} \\ \frac{dN}{d\tilde{E}} &= E_0 \frac{dN}{dE}, \text{ so we can rewrite as:} \\ \frac{dN}{d\tilde{E}} &= \Phi_0 E_0 \tilde{E}^{-\gamma} = \eta. \end{aligned}$$

We are interested in the logarithmic representation, so we further define  $\tilde{L} = \log_{10}(\tilde{E}) = \log_{10}\left(\frac{E}{E_0}\right)$ . Then,

$$\frac{dN}{d\tilde{L}} = \ln(10) \Phi_0 E_0 \tilde{E} \tilde{E}^{-\gamma} \tag{6.8}$$

$$= \ln(10) \Phi_0 E_0 e^{\ln(10)(1-\gamma)\tilde{L}}. \tag{6.9}$$

### 6.2.1.2 The Basic Transformation

In Equation 6.8, let  $\ln(10)\Phi_0 E_0$  be a normalization,  $\eta$ . For the generated spectrum (with  $\gamma_{gen} = 1$ ), it can be shown that  $\eta$  is simply:

$$\eta = \frac{N_{\text{total events generated}}}{N_{\text{bins generated}}}, \text{ such that:} \quad (6.10)$$

$$\left(\frac{dN}{d\tilde{L}}\right)_{\text{gen}} = \eta e^{\ln(10)(1-\gamma_{gen})\tilde{L}}. \quad (6.11)$$

A new spectrum of the desired simulation index ( $\gamma_{sim}$ ) can be created by applying a weighting function  $w(E)$  to the generated spectrum (which has index  $\gamma_{gen} = 1$ ), such that

$$\left(\frac{dN}{d\tilde{L}}\right)_{\text{sim}} = \left(\frac{dN}{d\tilde{L}}\right)_{\text{gen}} w(E).$$

The weighting function is then:

$$w(E) = \frac{1}{\eta} \ln(10)\Phi_0 E_0 e^{\ln(10)(\gamma_{gen}-\gamma_{sim})\tilde{L}}, \quad (6.12)$$

which correctly transforms the generated spectrum to have the desired index  $\gamma_{sim}$ . This can be seen by explicit multiplication:

$$\begin{aligned} \left(\frac{dN}{d\tilde{L}}\right)_{\text{gen}} w(E) &= \left(\eta e^{\ln(10)(1-\gamma_{gen})\tilde{L}}\right) \left(\frac{1}{\eta} \ln(10)\Phi_0 E_0 e^{\ln(10)(\gamma_{gen}-\gamma_{sim})\tilde{L}}\right) \\ &= \ln(10)\Phi_0 E_0 e^{\ln(10)(1-\gamma_{sim})\tilde{L}} \\ &= \left(\frac{dN}{d\tilde{L}}\right)_{\text{sim}}. \end{aligned}$$

### 6.2.1.3 A More Realistic Transformation

Notice that the above Equation 6.12 reweights our simulated distribution to a spectrum with a single spectral index. However, as we discussed above, a more realistic cosmic ray spectrum has a knee at which the spectral index changes from  $\gamma_1$ , below, to  $\gamma_2$ , above (both positive numbers).

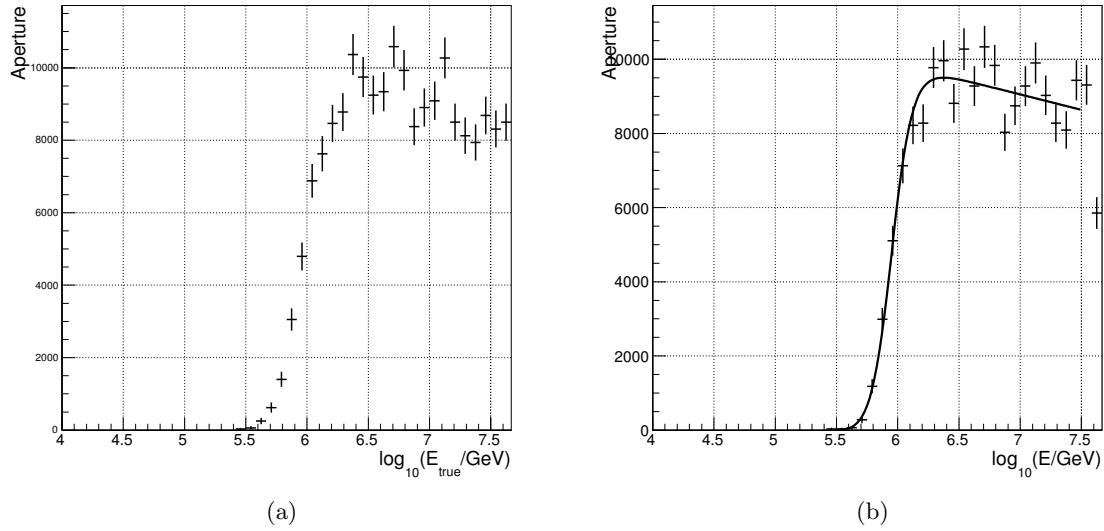


Figure 6.3: Figure 6.3(a) is the aperture calculated for the true energy—the exact bin content of this plot is used to calculate the true spectra in the simulation as seen in Figure 6.4, and Figure 6.3(b) is the reconstructed aperture—the fit is used to calculate the reconstructed spectra as seen in Figures 6.5 and 6.6.

Thus, our actual weighting function is a piecewise power law:

$$w(e) = \begin{cases} \frac{1}{\eta} \ln(10) \Phi_0 E_0 e^{\ln(10)(1-\gamma_1)\tilde{L}} & \text{below the knee} \\ \frac{1}{\eta} \ln(10) \Phi_0 E_0 \left(\frac{E_{\text{knee}}}{E_0}\right)^{(\gamma_2-\gamma_1)} e^{\ln(10)(1-\gamma_2)\tilde{L}} & \text{above the knee} \end{cases} \quad (6.13)$$

where  $\left(\frac{E_{\text{knee}}}{E_0}\right)^{(\gamma_2-\gamma_1)}$  is a term to account for the new normalization required above the knee. It is important to note that Equation 6.13 corresponds directly to the first order approximation of Equation 6.16 (Equation 2 from [38]).

#### 6.2.1.4 Last Key Piece For Comparison to Raw Experimental Data Distribution

The weighted spectrum then has units of inverse area, time, solid angle and energy. But what is observed experimentally is a rate of particles,  $f(E)$ , for a given energy, over a given amount of time. By multiplying the weight above by an area, a stereo angle, and the livetime of the data, we

can achieve something directly comparable to the observed spectrum we will find in the data:

$$f(E) = A\Omega\tau w(E) \left( \frac{dN}{d\tilde{L}} \right)_{\text{gen}}. \quad (6.14)$$

### 6.2.2 Step 2: Calculate the Flux From the True Simulated Rates

Now that we have figured out how to correctly weight the simulated events to a realistic spectrum, we can use the simulation to check our flux calculation, which was the goal. Thus, we simply use Equation 6.14 in place of  $\frac{dN}{d\log_{10}(E)}$  in Equation 6.7, which can then be rewritten as:

$$J(E) = \frac{1}{\eta_{\text{overall}}A\Omega\tau} \frac{\log_{10}(e)}{E} f(E). \quad (6.15)$$

To check first that we simply get out what we put in, we should divide  $f(E_{\text{true}})$  by the true aperture, Figure 6.3(a), the livetime in seconds, and the term to account for the log scale (again with respect to true energy). We can then fit the resulting plots to the function found in Eqn. 2 of [38]:

$$\frac{d\Phi_Z}{dE_0}(E_0) = \Phi_Z^0 E_0^{\gamma_Z} \left[ 1 + \left( \frac{E_0}{\hat{E}_Z} \right)^{\epsilon_c} \right]^{\frac{\gamma_c - \gamma_Z}{\epsilon_c}}. \quad (6.16)$$

The results of the fit are labeled in Figure 6.4 and should exactly match  $E_{\text{knee}} = 3PeV$ ,  $\alpha = 2.7$ , and  $\beta = 3.0$ , remembering that  $\epsilon$ , the term for the curvature of the knee, was ignored in the weighting function, so it should be as large (i.e. sharp) as possible. Fortunately, as seen in Figure 6.4 the input is nearly exactly recovered. Thus, it is clear that our calculation is performed correctly.

### 6.2.3 Step 3: Calculate the Flux From the Reconstructed Simulated Rates

The last part of our check involves switching from our true simulated distribution to the reconstructed distribution—in other words, replacing the true energy with the energy as reconstructed by the neural network. This will tell us how accurately we can expect to retrieve  $\alpha$ ,  $\beta$ ,  $E_{\text{knee}}$ , and

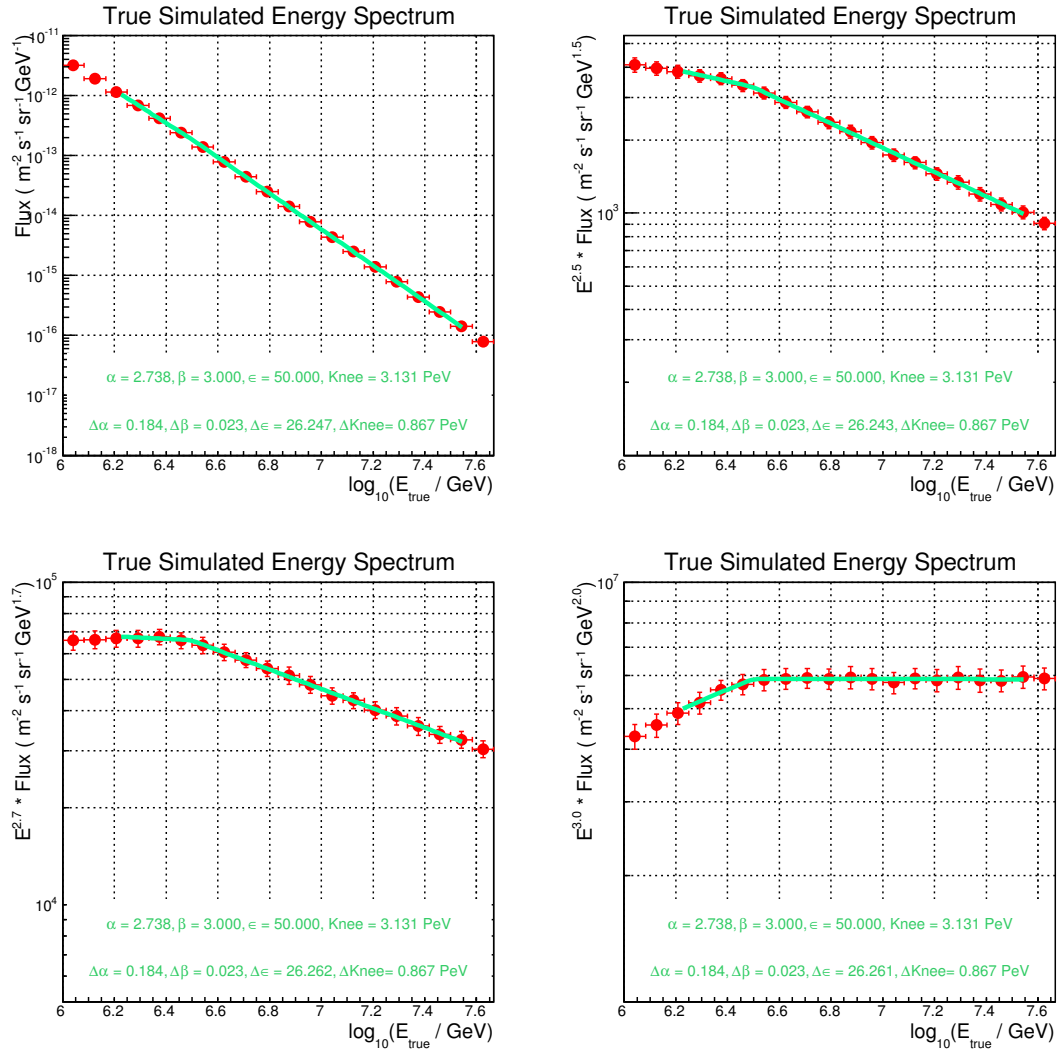


Figure 6.4: These plots all depict the *true* energy spectrum (in red), fitted to the Hörandel spectrum (green), as reproduced by the simulation. The neural network has no effect on these plots: they are simply the true energy after all cuts, which is then passed through the calculation of the energy spectrum. Two main points of this check were to (a) test the energy spectrum algorithm to be sure that it does what we expect it to do, and (b) check to see if the fitting algorithm actually reproduces the indices and knee energy that the simulation was given. The aperture used for this calculation is found to be the exact aperture found in Figure 6.3(a). A quick glance at the parameters and their errors reveals that, indeed, the input indices and knee energy are reproduced by the fit.

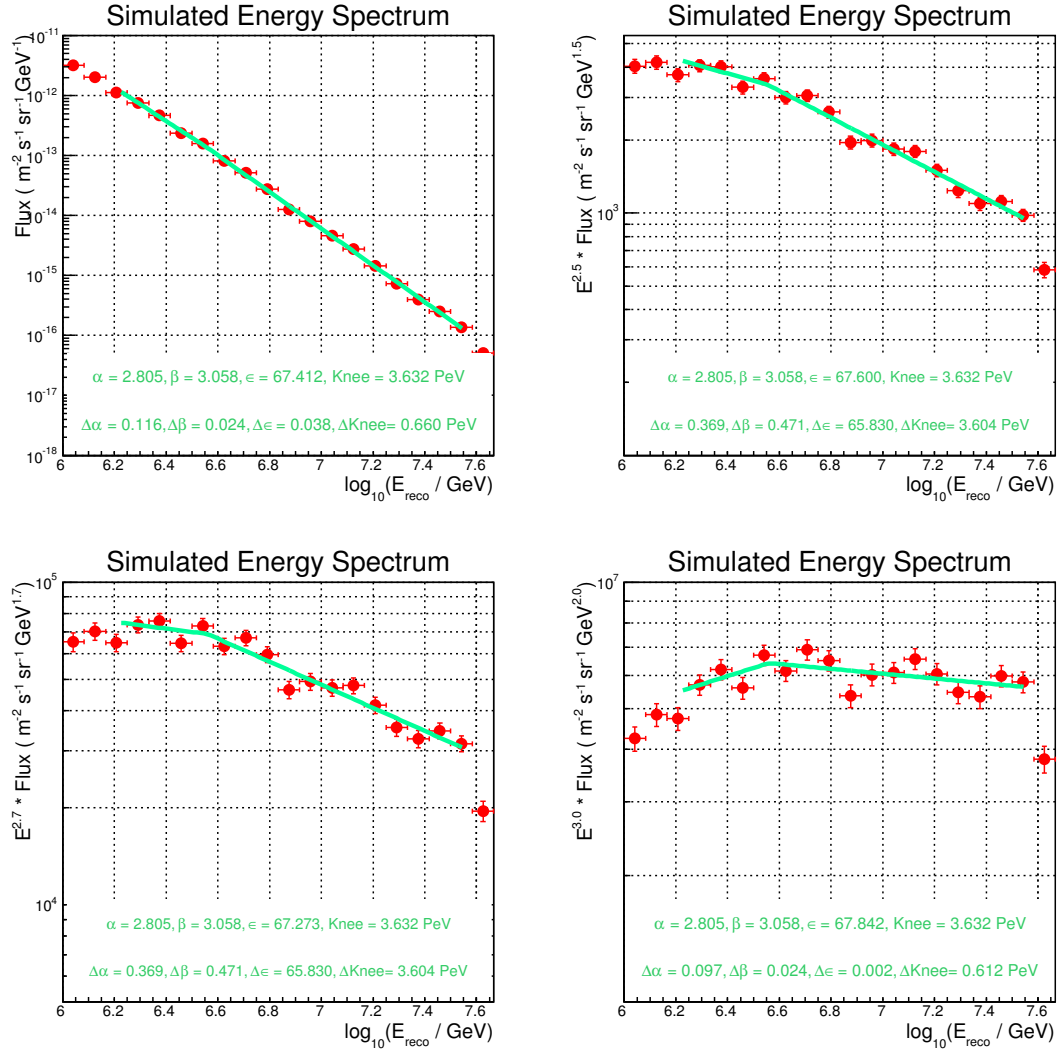


Figure 6.5: These plots all depict the *reconstructed* energy spectrum (in red), fitted to the Hördel spectrum (green), as reproduced by the simulation. These events initially have the same energy distributions as in Figure 6.4 but are shown here using the energy as reconstructed by the neural network and passed through the calculation of the energy spectrum. At this stage we can compare to Figure 6.4 to see how well our network reconstructs the true energy, and how well our *slanted* aperture fit can be relied upon, since for this calculation we used the slanted aperture fit as found in Figure 6.3(b). A look at the parameters and their errors reveals that, indeed, the input indices and knee energy are still reproduced by the fit within errors.

$\epsilon$  from our data, which clearly also uses the reconstructed energy. The only change we will make to the procedure described in Section 6.2.2 is that, to account for the fluctuations caused by the comparatively small statistics found in the simulated aperture distribution, we will fit the aperture to a sigmoid function modified by a line, of the form:

$$aperture = \frac{p_0}{1 + e^{-p_1(E-p_2)}} + (p_3E + p_4), \quad (6.17)$$

as can be found in Figure 6.3(b).

The fits to the reconstructed simulated distributions, again using Equation 6.16 can be found in Figure 6.5. From this check it becomes clear that we can retrieve our true parameters  $\alpha$ ,  $\beta$ ,  $E_{knee}$ , and  $\epsilon$  within errors.

### 6.3 Energy Spectrum Results

In Section 6.2 we have shown that we can calculate the energy of the knee, the curvature of the knee, and the spectral indices above the knee to reasonable accuracy. All that remains is to perform the same calculations on the data to see what we find. Using the aperture fit as in Equation 6.17, and the distribution  $\frac{dN}{d\log_{10}(E)}$  from the data, we can calculate our energy spectrum, as seen in Figure 6.6. (A table of the values found can be located in Appendix C.) We find spectral indices around 2.55 below, and 3.27 above a gradual knee around 5 PeV. The discussion of the implications of these results, and a comparison to other similar experiments, follows in Chapter 9.

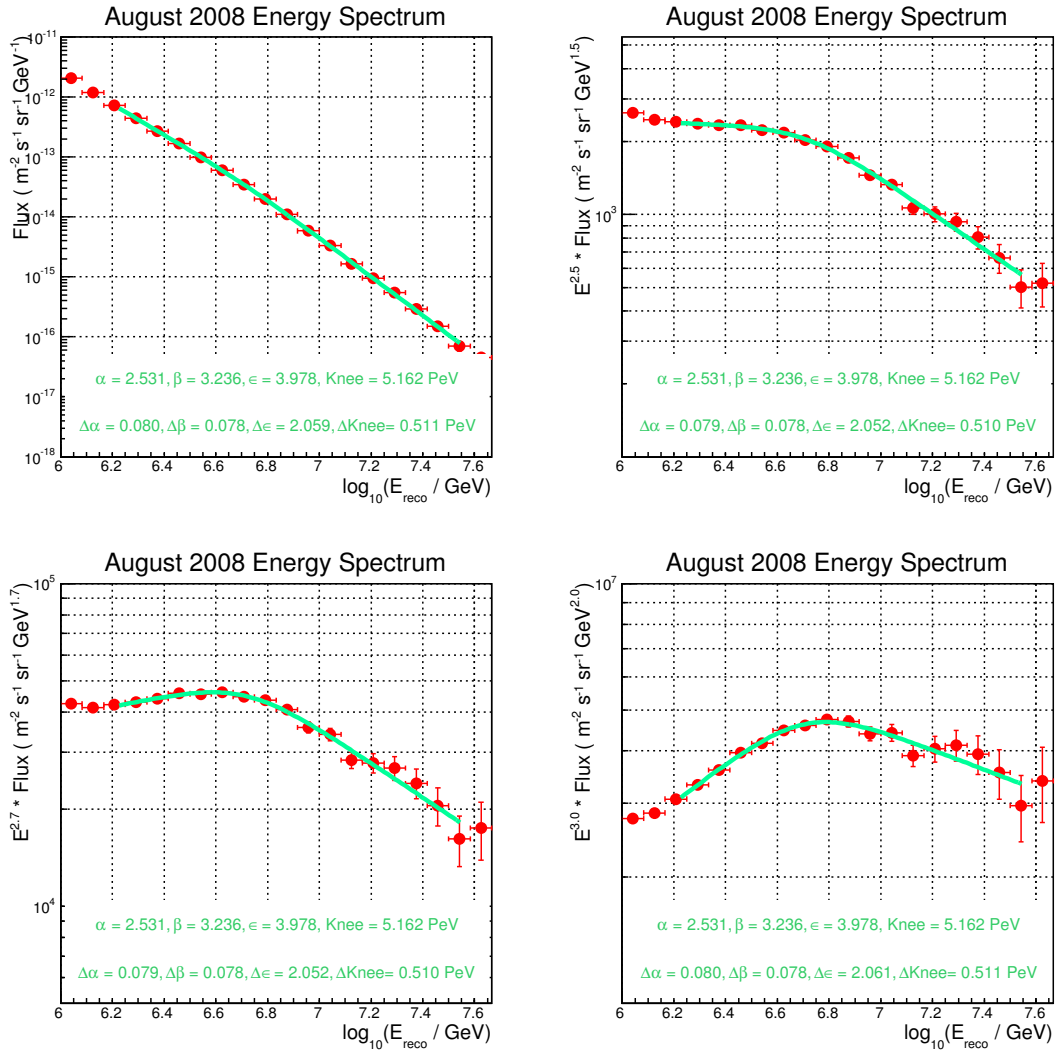


Figure 6.6: These plots all depict the *reconstructed* energy spectrum (in red), fitted to the Hörandel spectrum (green). These are the results of the energy spectrum calculations for real data. The indices indicate a power law of 2.5 below, and around 3.27 above a slowly turning knee around 5 PeV.

## Chapter 7

### Analysis of Mass Composition

In the previous chapter we learned that the neural network reconstructs the primary energy of an air shower with remarkable resolution. The reconstructed energy from the network was then used to calculate a simple energy spectrum.

With respect to mass reconstruction, however, the neural network output is a bit more complex. The network can only do as well as the parameters that it is given for training. For example, a finite number of iron nuclei will produce proton-like signatures, while a finite number of protons will produce characteristically iron-like signatures. There is some inevitable overlap in the  $K_{70}$ - $S_{125}$  space (Figure 4.12), which is propagated through the neural network to the mass and energy space, as seen in Figure 7.1. The input parameters are the limitation of the neural network analysis technique. It is notable that the overlapping tails of the particle distribution functions are statistically predictable. This means that, while we cannot precisely determine the mass of each individual particle, we can gain a good understanding of our overall mass by combining the neural network with a minimization technique to find a combination of particle types which best fits the data.

To do this, we use simulated particles of each mass type to reconstruct the characteristic mass output curve of the data. As discussed in previous chapters, the neural network produces a “most-likely mass” for each cosmic ray shower. Though the value of most likely mass for a particle of a given type may reconstruct anywhere in the spectrum, it is more likely to reconstruct near the particle’s true mass, and a histogram of most likely mass for a given particle type follows a very

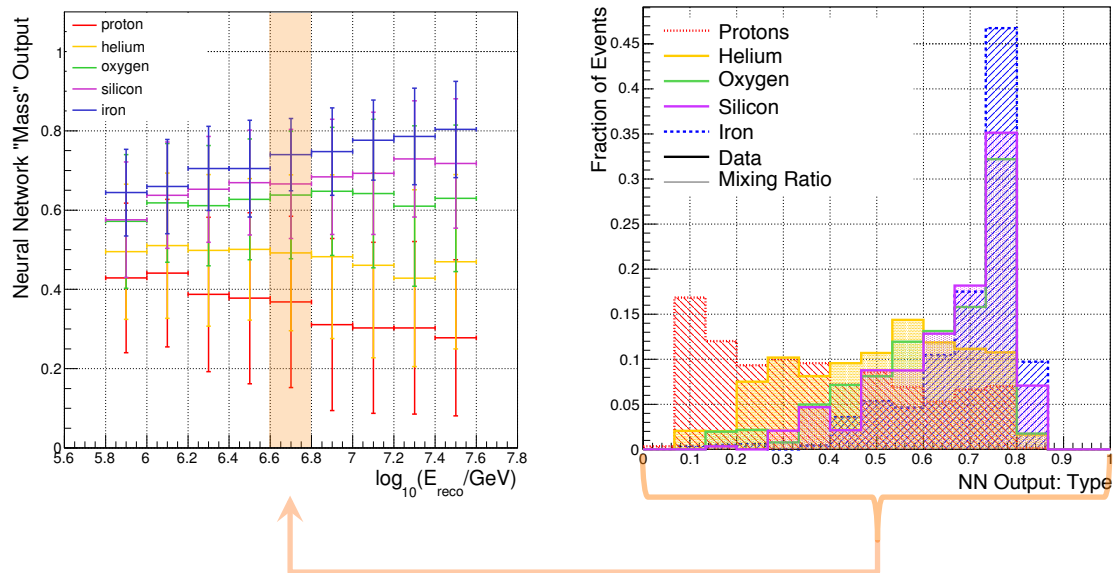


Figure 7.1: On the right, we show the “characteristic mass output curves” for all 5 particle types in a single slice in energy, which corresponds to the slice shown on the left, where we depict the mass output as RMS profiles in slices of the reconstructed energy.

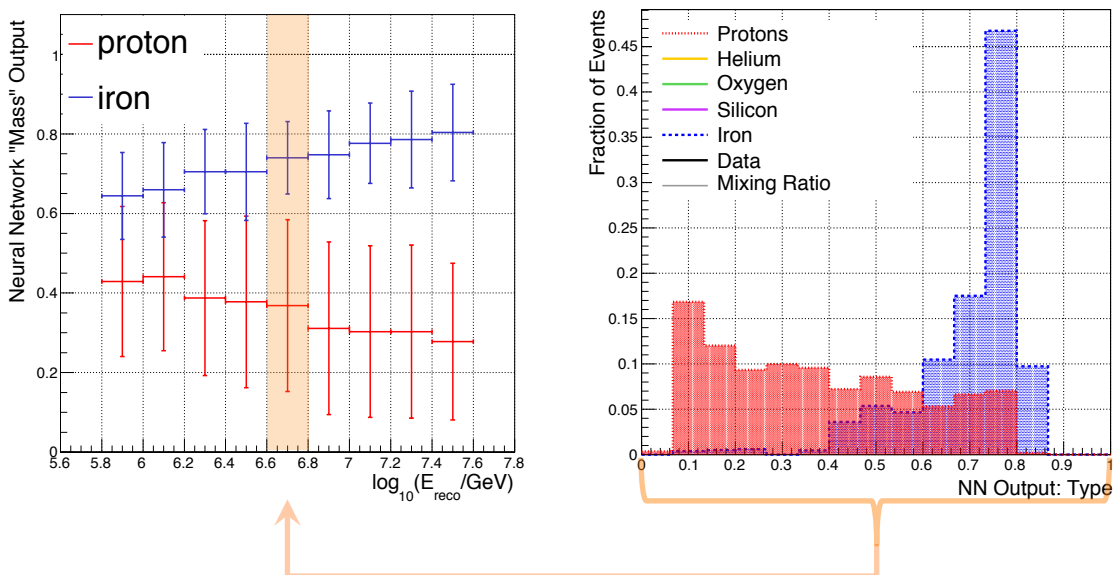


Figure 7.2: This figure is the same as Figure 7.1 only with the intermediate primaries removed for easier viewing. On the right, we show the “characteristic mass output curves” for proton and iron in a single slice in energy, which corresponds to the slice shown on the left, where we depict the mass output as RMS profiles in slices of the reconstructed energy.

predictable curve for a given particle mass. We will call this curve the “characteristic mass output curve,” or simply “characteristic curve”. (The curves may even vary by the details of the neural network construction; indeed, reproducibility of this curve is one factor which defines an acceptable neural network.)

Data, composed of particles with an unknown spectrum of masses, can be decomposed into linear combinations of characteristic curves. The minimization technique discussed here is the method by which the best-fit linear combination can be found. For example, a two-type minimization (for protons and iron only) will find the best fraction of protons,  $p_p$ , for which the linear combination of the proton and iron curves best matches the data:

$$1 = p_p(\text{proton curve}) + (1 - p_p)(\text{iron curve}). \quad (7.1)$$

This fit is easily expandable to include more particle types:

$$\begin{aligned} 1 &= p_p(\text{protons}) + (1 - p_p)((p_{fe})(\text{iron}) + (1 - p_{fe})(\text{oxygen})) \\ 1 &= p_p(\text{protons}) + (1 - p_p)((p_{fe})(\text{iron}) \\ &\quad + (1 - p_{fe})((p_o)(\text{oxygen}) + (1 - p_o)(\text{helium}))) \\ &\vdots \end{aligned}$$

(Using this particular construction naturally incorporates the fitting range constraints for easier manipulation of the minimizer.) Further, we show that an analysis consisting of as few as two characteristic curves (an analysis using only protons and iron) can be used to find a reasonable agreement with the general trend of  $\langle \ln A \rangle$  vs energy. By including more primaries, a more confident value for  $\langle \ln A \rangle$  can be obtained. Our best case (given the available simulation) uses three characteristic mass output curves: proton, iron, and a known mixture of helium and oxygen. In the future, with more statistics in our simulation, it may be possible to improve the analysis to include a larger number of characteristic curves, which ultimately could translate to a better average mass

resolution.

## 7.1 Determination of Appropriate Energy Slices

The number of slices in energy across which we can minimize are constrained by two factors: firstly, by the degree to which we can resolve our energy; secondly, by the number of statistics in the simulation.

We cannot use smaller bins than the resolution with which the network reconstructs the primary energy. As we determined in Chapter 6, in the region where we are fully efficient our energy resolution is around 0.06 in  $\log_{10}(E_{\text{reco}})$ . Thus, for the energy spectrum we conservatively used slices in energy that were  $\frac{1}{12}$  of a decade in  $\log_{10}(E_{\text{reco}})$ , or roughly 0.08. For mass we should definitely not use slices that are narrower.

Our second limitation is based on the amount of simulation we have. Ideally, we would have as much simulation as we have data in each slice in energy. However, even if that were the case, we need enough events of each particle type within a given energy range to be able to successfully minimize across that slice. If our resolution allowed for infinitely small slices in energy, the number of events simulated in each slice would limit us to a significantly wider slice. This limitation is significant and has had a great impact on the method chosen for this analysis (a problem which will need to be rectified for future analyses). With these two points in mind, we chose one bin in energy per 0.2 in  $\log_{10}(E_{\text{reco}})$ .

## 7.2 A Closer Look at Characteristic Curves

A characteristic mass curve for one slice in energy can be found in Figure 7.1. Note that each particle type has a distinct curve for a single slice in energy. However, if the binning is too fine this plot will simply be a jagged mess. On the other hand, if the binning is too wide the types will all run together and become indistinguishable. Thus, we must pay attention not to use too large or too small a number of bins. This is especially critical at the lowest and highest energies where the statistics are lower. In this case, we found that a reasonable choice for number of bins for the

slices in energy we have chosen is 15, as shown in this figure.

### 7.3 Minimizing Across One Slice in Energy, Protons and Iron Only

Below we will discuss each step of the minimization process. For clarity, the next figures have the intermediate primaries (helium, oxygen, and silicon) removed, and the analysis is described with protons and iron only using a single slice in energy as seen in Figure 7.2. We will test the method using a set of “hand-mixed” simulation (simulation in which all particle types have been included but where the average mass at a given energy has been modified to fit a specific model). We will then extrapolate to include as many primaries as possible given the statistics we have in simulation.

For a single slice in energy, the combination of primaries that best reproduces the distribution of the data must be determined. Therefore, we use a  $\chi^2$  test to find, in this case, the ratio of iron and protons that best matches the data. The value of  $\chi^2$  is determined as follows:

$$\chi^2 = \sum_{i=1}^N \frac{(\text{data distribution} - \text{functional fit to data})^2}{\text{variance of the data}} \quad (7.2)$$

where the functional fit is described by Eqn. 7.1, the linear combination using protons and iron only.

The performance of the fit for a single slice in energy can be found in Figure 7.3, where the hand-mixed sample of “data” is marked with black hashes and statistical error bars. The minimizer then tries to fit this distribution within the errors with different ratios of protons and iron. The result of the fit is marked in gray seen in Figure 7.3. It is clear that the fit performs reasonably well, even though it is constrained to only two choices—proton or iron—with which to match the “data”. In Figure 7.4, we show the result of the minimization technique in all energy bins. The gold is the true  $\langle \ln A \rangle$  for this hand-mixed simulation, and the red is the result from the minimizer with statistical error bars. We can see that this technique works reasonably well for two types only and that the minimizer finds the correct overall trend of the hand-mixed simulation. The true  $\langle \ln A \rangle$  does not always fall within the error bars of the minimized output and it does not follow

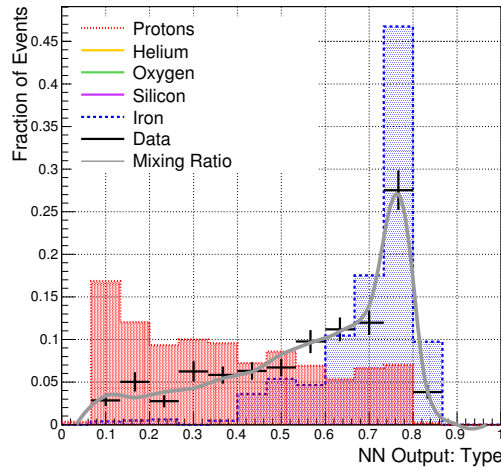


Figure 7.3: The results of the fit (in gray) as determined by the minimization algorithm. The hand-mixed sample of “data” (black) is marked with black hashes and shows statistical error bars. The fit matches the data quite well even though only 2 primary types were used.

a smooth trend, which indicates that the technique would benefit from the use of intermediate primaries.

#### 7.4 Determination of the Appropriate Number of Independent Nuclei

Fortunately, we have 5 primaries available to us in our simulation: protons, helium, oxygen, silicon and iron. However, as we are limited by statistics within each slice in energy, it is possible that five is too many primaries to use for this analysis. Thus, a number of tests were performed and it was found that silicon was completely extraneous at this level, and that while helium and oxygen were both necessary for a good fit, we do not have enough statistics and not enough mass resolution to reliably distinguish them individually. Thus, the helium and oxygen curves in each slice in energy were mixed together to have equal weighting (50% helium, 50% oxygen). So, for our final minimization we used protons, iron and the helium-oxygen mixture. The left plot in Figure 7.5 shows the neural network output for the proton, helium/oxygen mixture, and iron vs reconstructed energy, where it is clear that the choice of proton, helium-oxygen mixture, and iron cover the entire parameter space. The right-hand plot in that Figure 7.5 shows the result of the test of this minimization choice for proton, helium-oxygen mixture, and iron, once more with statistical

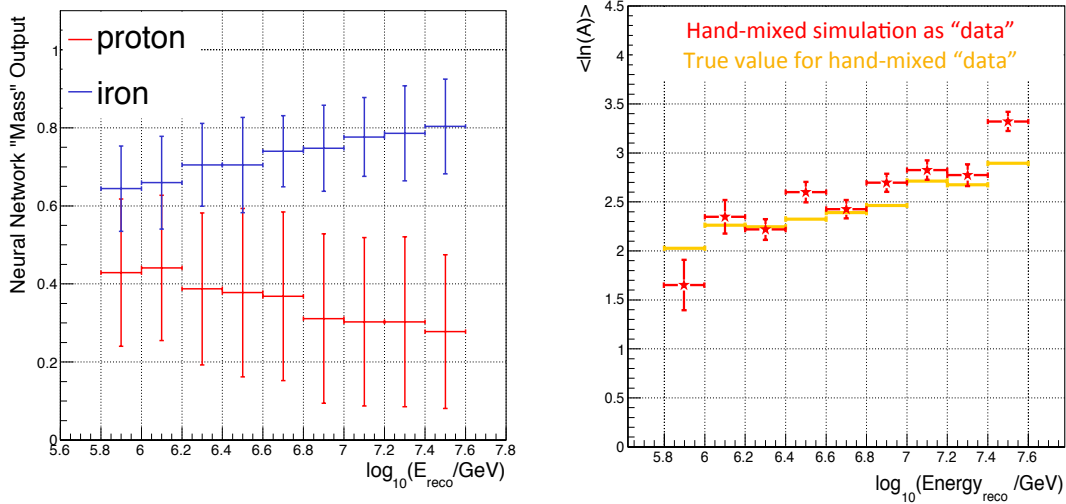


Figure 7.4: (Left) Profiles of mass output vs reconstructed energy for the chosen types used in the minimization: protons and iron. The parameter space is well-covered by these distributions, as demonstrated by the overlap. (Right) The result of the 2-type (pfe) minimization scheme for all energies. The true  $\langle \ln A \rangle$  for each slice in energy is marked in gold, while the  $\langle \ln A \rangle$  chosen by the minimizer as the best match for the hand-mixed simulation is shown in red, with statistical error bars. The minimizer finds a reasonable fit to the input values which follows the proper general trend, but more particle types should improve the quality of the result.

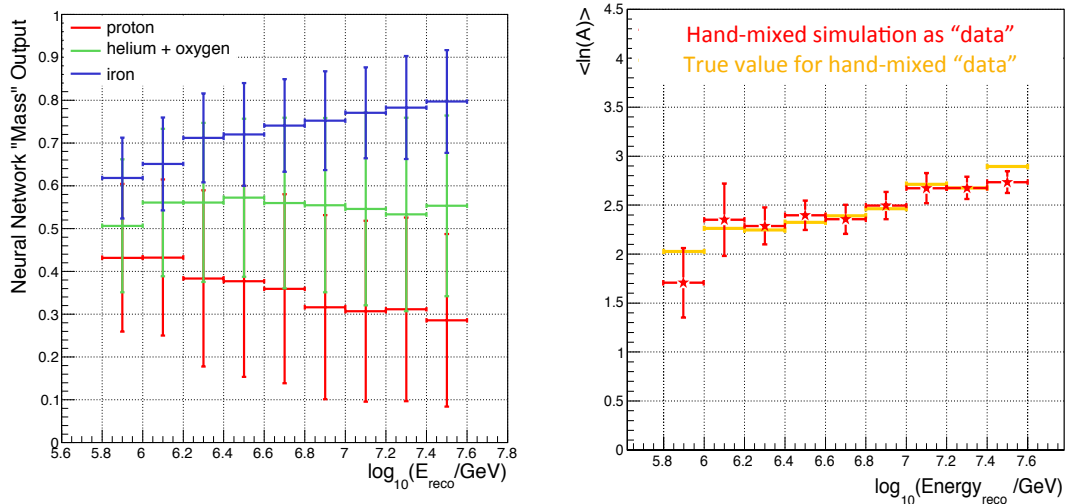


Figure 7.5: (Left) Profiles of mass output vs reconstructed energy for the chosen types used in the minimization: protons, helium/oxygen mixture, and iron. The parameter space is well-covered by these distributions, as demonstrated by the overlap. (Right) The result of the 3-type (p/he-o/fe) minimization scheme for all energies. The true  $\langle \ln A \rangle$  for each slice in energy is marked in gold, while the  $\langle \ln A \rangle$  chosen by the minimizer as the best match for the hand-mixed simulation is shown in red, with statistical error bars. The minimizer finds a very good fit to the input values at energies where the detector is fully efficient (i.e., above 6.2 in  $\log_{10}(E_{\text{reco}})$ ), a clear improvement over Figure 7.4).

error bars. The choice of using a linear combination of proton, helium-oxygen mixture, and iron to minimize clearly improves the technique, bringing our reconstructed test results to values well within the error bars of the true at energies where the detector is fully efficient (ie, above 6.2 in  $\log_{10}(E_{reco})$ ).

## 7.5 Results

Before we show the results of this technique for data from August 2008 a number of corrections and systematic effects will need to be taken into account. These will be discussed in Chapter 8. The results will be presented in Chapter 9.

## Chapter 8

# Systematic Errors and Corrections for Known and Understood Problems

Every analysis is limited in some ways. If discovered early enough, some problems can be corrected, such as the VEM to GeV conversion in our simulation. Other problems, like the snow, have caused serious dilemmas to this analysis, resulting in a complete elimination of part of the detector. This chapter will be a discussion of these important factors.

### 8.1 Ice Model

The way we model light propagation in the South Pole ice is a crucial component to every IceCube analysis, and has been the topic of much discussion. Over the years, our collaboration has developed very sophisticated techniques for modeling the South Pole ice [51]. The standard model used to simulate the 40-string detector is called AHA. However, there is also a new model called SPICE, which some collaborators believe reflects the properties of the ice more accurately [73]. The collaboration is currently planning to use the latest SPICE model for the IC-59 simulation, for the sake of comparison. In light of this there was a small set of simulation generated with SPICE for IC-40 for testing purposes.

For this analysis, the important quantity we measure is the amplitude of the light in the ice; therefore, the ice properties could potentially have a very large effect, particularly on the slope of this distribution. However, one of the reasons we measure the amplitude of light at a certain reference distance from the track (in this case, 70 m, in a previous analysis, 50 m) is to reduce

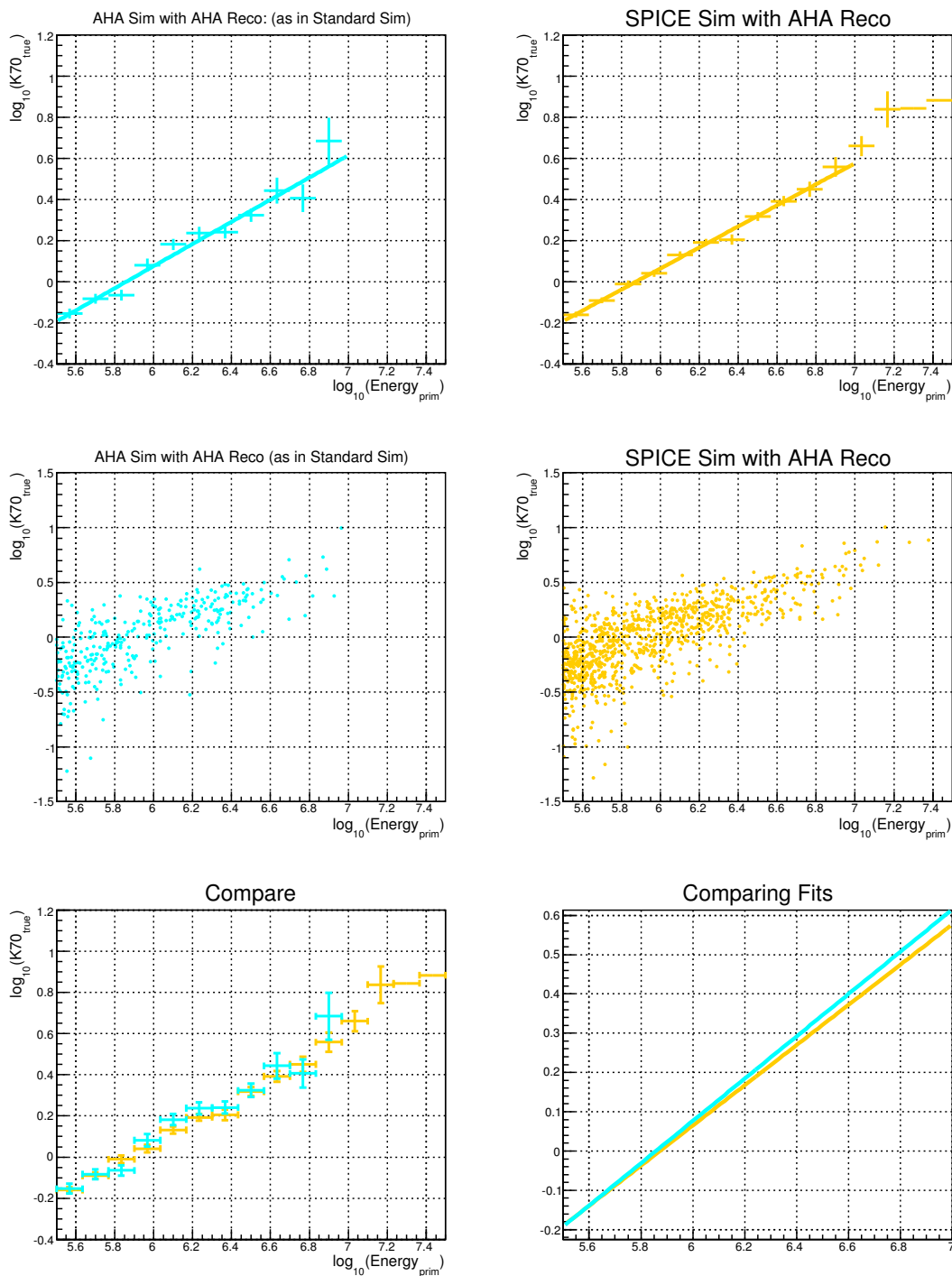


Figure 8.1: Simulation generated for in-ice alone. The gold is SPICE simulation with AHA reconstruction—if the SPICE ice model reflects the true ice at the South Pole better than the AHA model, this should be more comparable to our data. The cyan is AHA simulation with AHA reconstruction—if the AHA ice model better reflects the South Pole ice, this should be more comparable to our data. In either case, the cyan AHA simulation with AHA reconstruction is what we have for our standard simulation. This means that there is a possibility that the data (analogous to the gold fit) has less light in the ice than the simulation (in cyan) predicts at high energies, which corresponds to a maximum systematic decrease in  $K70$  of  $\sim 0.04$  for the data with respect to the simulation.

the potential systematic effects due to the choice in ice model [40]. Reduction is not the same as elimination, though, so we have made a comparison between two datasets which were generated with exactly this purpose in mind: one for AHA and one for SPICE. These datasets were generated for the InIce array only, and weighted to an  $E^{-2.7}$  Hörandel spectrum. It is important to remember that there is an assumption of ice model in the reconstruction of the  $K_{70}$  parameter. Therefore, to best see what the effect is we have used the same ice model for reconstruction—AHA—in both datasets, since AHA has been our assumption in the reconstructions for our standard simulation and experimental data as well. This will show us what the effect on  $K_{70}$  will be if the true ice model is more correctly described by the SPICE model. Unfortunately the statistics are low, but the results of this comparison (in Figure 8.1) show only a small effect at high energies, and no visible effect at low energies. This means that there is a possibility that the data (represented by SPICE simulation with AHA reconstruction) has less light in the ice than the simulation (which used AHA simulation and AHA reconstruction) would predict at high energies. This corresponds to a maximum systematic decrease  $K_{70}$  of  $\sim 0.04$  for the data with respect to the simulation. In the future, with larger data sets, it will be easier to make this comparison.

## 8.2 Hadronic Interaction Models

All cosmic ray analyses face the choice of hadronic interaction model. For this analysis we chose to use SIBYLL (a current favorite in the field) as our standard simulation. However, there is no way to know if SIBYLL correctly describes the propagation of high-energy muons, a vital component to this analysis. There have been many investigations into this problem, but the truth is that we are simply unsure of our hadronic interactions at the energies important to cosmic ray physics. We are working with energies that are as yet irreproducible on Earth. The current models will be tested with the new LHC detectors LHCf and TOTEM, which, though still not reaching to the energies most interesting to cosmic ray physics, will provide valuable new restrictions which will greatly help the field of cosmic ray physics. However, for now there is some error due to the knowledge gap in this regime.

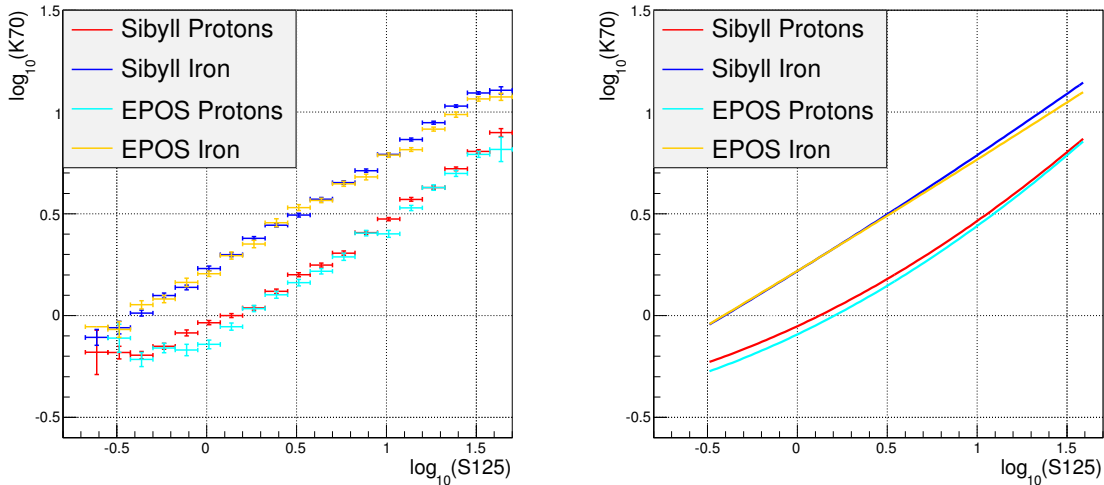


Figure 8.2: In Figure 8.2(a) we show profiles for the simulated protons and iron. The standard simulation is denoted by the usual red for protons and blue for iron. The EPOS simulation is marked using complimentary colors: yellow for iron and cyan for protons. A parabolic fit was then made to the different simulations to quantify the differences. The fits are shown with the data in Figure 8.2(b). Note that this is the Aug 2008 data without any correction for the snow or the VEM calibration discussed below. It is clear that the difference between the two models is slight and only significant for iron at high energies and protons at low energies. This generally corresponds to an increase of  $\sim 0.04$  in  $K_{70}$  with respect to  $S_{125}$  for the data.

In an attempt to get a handle on this systematic effect, we generated a dataset which uses EPOS, a different model than our standard SIBYLL simulation. We can compare the two in our  $K_{70}$ - $S_{125}$  space, as shown in Figure 8.2. The difference between the two interaction models is more evident for protons at low energies and iron at high energies and generally corresponds to an increase of  $\sim 0.04$  in  $K_{70}$  with respect to  $S_{125}$  in the data. For future analyses it is also important to compare with QGSJET-II, another standard algorithm which is thought to have a slightly higher muon-rate than the other two commonly used models.

### 8.3 VEM Shift

An offset in the VEM to GeV conversion in our simulation at the surface was discovered. The effect of this offset is a constant shift of 0.085 in  $S_{125}$ , which can be quantified by comparing a new test simulation with no snow included—which uses the updated VEM to GeV conversion—to our standard simulation, as in Figure 8.3. As a result, we simply shift  $S_{125}$  in the data, with respect to the simulation, by a factor of  $-0.085$ , prior to the neural network mapping.

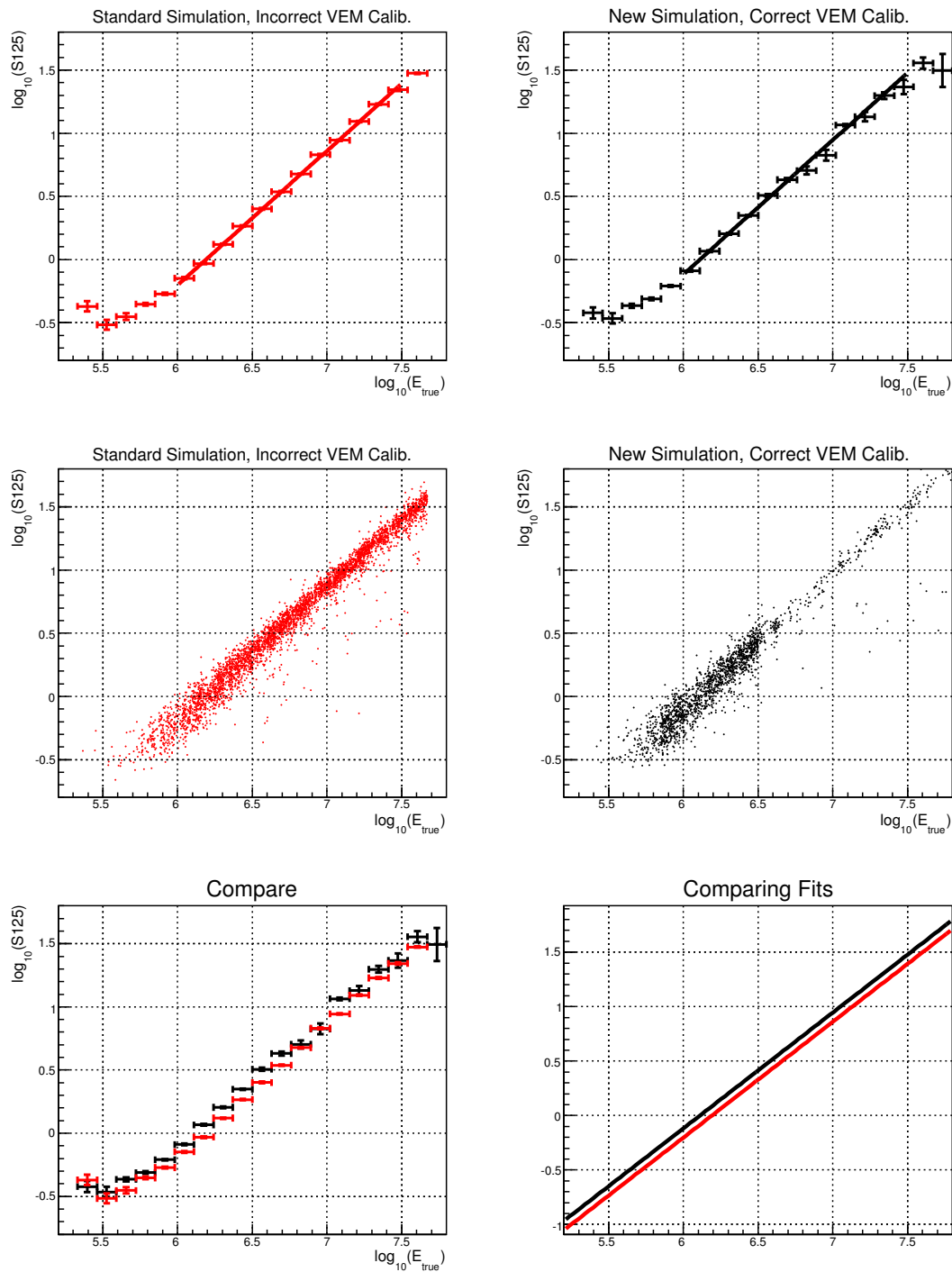


Figure 8.3: A constant VEM shift for the standard simulation (red, which had the wrong VEM to GeV conversion), was calculated by comparison with the new test simulation (black) set which had the correct VEM to GeV conversion. The result is a constant shift in the simulation by a factor of 0.085 in  $\log_{10}(S_{125})$ .

## 8.4 Snow at the Surface

By far the largest and most surprising effect we have seen is that of the snow at the surface. The snow has drifted in the newer half of the detector much less than in the older half of the detector, as seen in Figure 8.4. It makes sense that there is more snow covering the part of the detector that was built first, but the amount of drifting observed was unexpected. However it has become clear that the drifting is due to the buildings in the vicinity (see Figure 8.5) and thus there is no way to prevent it from happening. Furthermore, the extra snow has the effect of making the data from the older half of the detector look much more “iron-like” in the  $K_{70}$ - $S_{125}$  space, as seen in Figure 8.6(a), since the added snow causes attenuation in the electromagnetic part of the air showers that doesn’t occur in the newer half of the surface detector and which has no effect on the high-energy muons which pass through to the in-ice array. Thus, the  $S_{125}$ -parameter is shifted with respect to the  $K_{70}$ -parameter in a convoluted fashion that depends on the depth of the snow in the part of the array through which it passed, and therefore the angle of the shower, as well as the energy of the shower. (For example, a high energy shower with a core well-within the newer half of the array will be affected since the shower is likely large enough that it should trigger the full detector, while a similar lower energy will be unaffected as it isn’t expected to trigger the older half of the array.)

In light of this, there has been no small amount of time dedicated to investigating what we should do. In the future the snow can be added to the simulation; however, the snow does not exist in the standard IC-40 simulation, and our CORSIKA showers were too large to store on disk, so it is not a matter of simply retriggering our CORSIKA showers, but of regenerating an entirely new simulation. As this was not feasible due to the amount of processing time it would take, we have generated a small amount of IC-40 simulation with snow in order to examine the effect and develop a method to “remove” the snow from the data in the older half of the array. This process requires an adjustment of the signal expectation values by a factor which depends upon the measured snow

depth above each tank and, therefore, upon the snow density itself (lately measured to be about  $0.04 \text{ g/cm}^2$ ). This study revealed a best-fit attenuation length of snow of approximately 1.5 m. While this effort has been effective, as seen in Figure 8.6(b), the threshold of the older half of the detector is well above the knee in energy and will be different for different particle types. This remains a serious, insurmountable, problem for this study. Thus, for the results of this analysis, after this snow correction we still only use events with shower cores within the newer half of the array (surface x-position of the core  $<200 \text{ m}$ ). This slightly reduces the highest energy attainable with this analysis, but it safely mitigates the threshold effects of the snow in an unbiased way.

## 8.5 Seasonal Atmospheric Variations

A possible source of error which we have not yet discussed is the variation of the atmospheric conditions by season over the course of the year. It is well-known that the rates at the surface are highly dependent on the pressure and temperature of the atmosphere. For example, a cold atmosphere is less dense, which causes a decrease in the interaction rates, while a warmer atmosphere is more dense and has higher rates of interaction.

In Figure 8.7 we show the effect of increasing snow depth over the course of the year, as indicated by the decrease in  $S_{125}$  in the data between May 1, 2008 and May 1, 2009. This is not accounted for in a snow correction since the snow depth measurements are taken only once yearly. However, there is a further effect which is likely due to atmospheric variations, as can be seen by comparing the data from December 1, 2008 to May 1, 2009: the decrease in  $S_{125}$  between May 1, 2008 and Dec 1, 2008 is *greater* than the decrease between May 1, 2008 and May 1, 2009. Therefore, the snow cannot account for this change and, from a small study, seems likely to be a result of atmospheric variations throughout the year. This problem is not well understood and, furthermore, it is difficult to decouple from the effect of increasing snow at the surface. To mitigate the effects of this systematic, we have chosen to use only one month of data, August 2008, as we have simulated an atmosphere which is meant to approximate the South Pole atmosphere in the Austral summer.

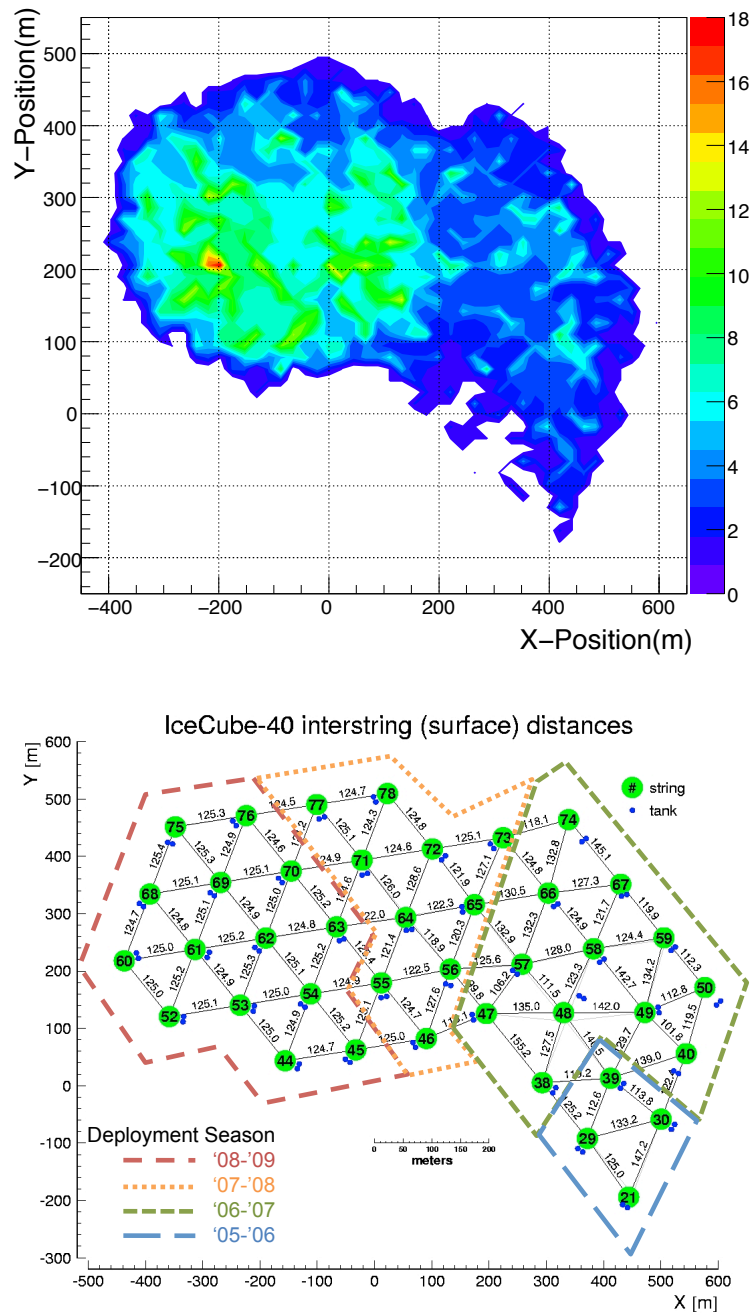


Figure 8.4: Figure 8.4(a) shows the reconstructed shower core location with a measure of rates as the colored z-axis. There is clearly a shortage of events in the right-hand half of the detector. A quick look at Figure 8.4(b) indicates that the right-hand half of the detector was built first, and has therefore had more of a chance to become buried under snow.

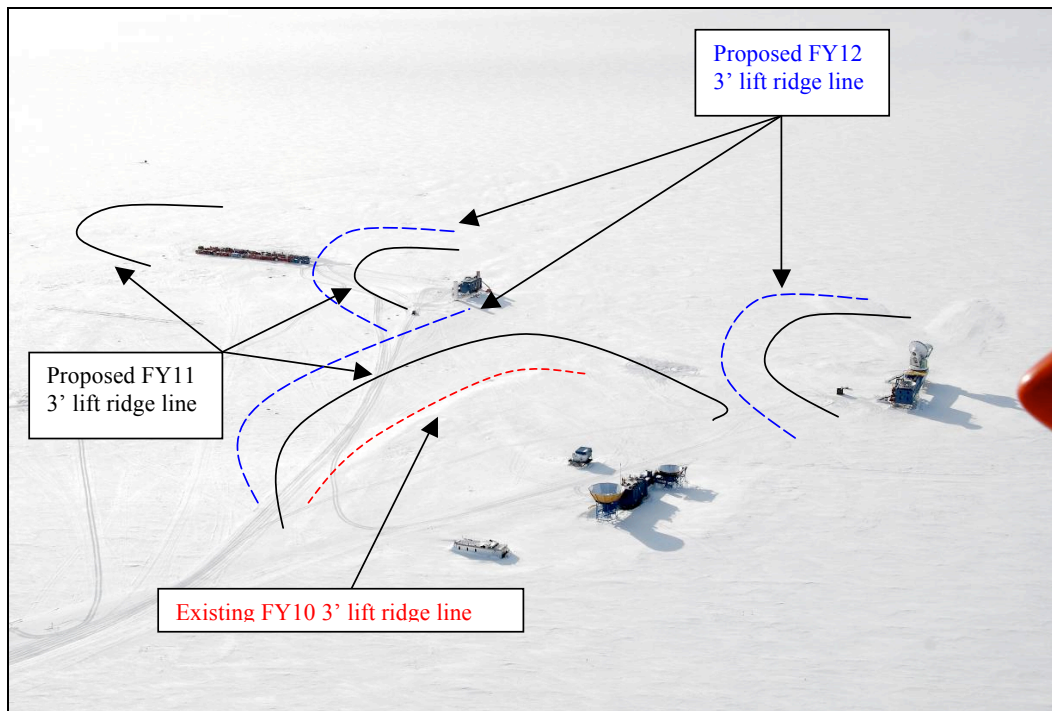


Figure 8.5: Here we show an aerial photo of the South Pole with the buildings visible. The drifting of the snow is clearly due to the wind blowing consistently from the bottom right corner of the photo, causing a predictable “wake-like” effect of snow drifts behind the buildings.

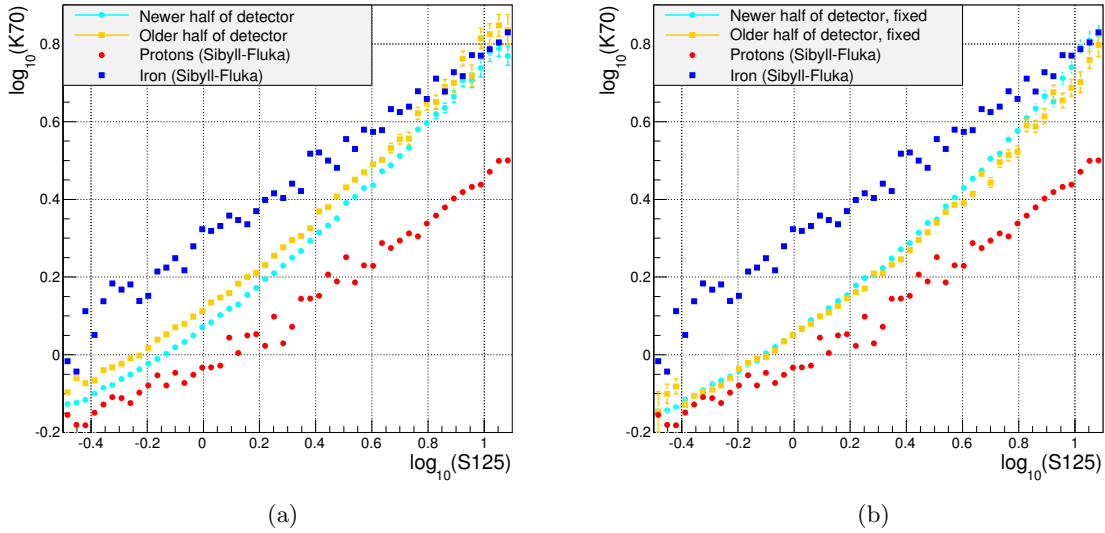


Figure 8.6: Effect of snow fix on  $K_{70}$  vs  $S_{125}$ . In Figure 8.6(a) it is clear that the “older” half of the detector (in gold) appears significantly more iron-like due to the effect of the snow on  $S_{125}$ . This can be fixed, as described in the text, and results in a much better match between the “older” half of the array and the “newer” half, as seen in Figure 8.6(b).

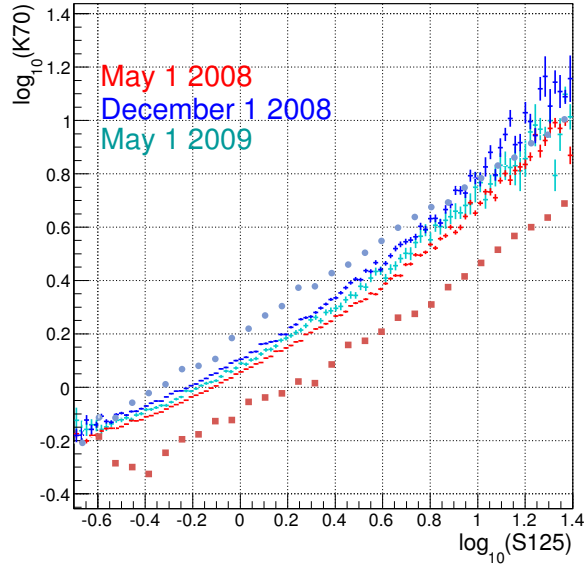


Figure 8.7: Effect of yearly atmospheric variations on  $K_{70}$  vs  $S_{125}$ . The data shown here include the newer half (x-location of shower core  $<200$  m) of the detector only. The slight shift between May 1 2008 and May 1 2009 can be explained as a decrease in  $S_{125}$  due to an increase in the snow depth over the course of the year: the depths used were measured in January of 2008. The larger shift between May 1 2008 and Dec 1 2008 is clearly not explainable in the same way, since it exceeds the shift over the course of the year. Thus, it must be due to atmospheric effects. It is clear that these effects are difficult to decouple from the effect of increasing snow at this point in time. Thus, to minimize an effect which is not well understood, we chose to use only data from August 2008 for this analysis, for reasonable comparison to the summer atmosphere that was simulated.

## 8.6 DOM Efficiency

The last effect that needs to be accounted for is the DOM efficiency in the ice. The efficiency of the DOMs depends on a number of factors, including the PMT quantum efficiency, the transmission of the glass and the gel, and even the refrozen ice from the deployment hole (which is less clear than the bulk ice). Measurements of the DOM efficiency in a controlled setting at Chiba University in Japan have estimated the uncertainty at approximately 8%, which we apply to the  $K_{70}$  parameter as a possible shift up or down of 0.035 in the  $\log_{10}$  scale.

## 8.7 Summary of Systematic Uncertainties

In summary, we have a number of effects which can cause systematic uncertainties in our sample. Problems that are well-understood we have simply fixed (such as the VEM calibration), those that we cannot account for have been mitigated (such as the snow-depth and the atmospheric effects), and those that will contribute to the systematic uncertainty of this analysis are listed below:

- DOM Efficiency: possible systematic **increase or decrease** in data by 0.035 in  $\log_{10}(K_{70})$  with respect to  $\log_{10}(S_{125})$ ,
- Hadronic Interaction Model: possible systematic **increase** in data by 0.04 in  $\log_{10}(K_{70})$  with respect to  $\log_{10}(S_{125})$ ,
- Ice Model: possible systematic **decrease** in data by 0.04 in  $\log_{10}(K_{70})$  with respect to  $\log_{10}(S_{125})$ .

These uncertainties are added in quadrature and the maximum and minimum possible  $K_{70}$  parameter is then used as an input into the neural network to find the error bands, as shown in Figure 8.8.

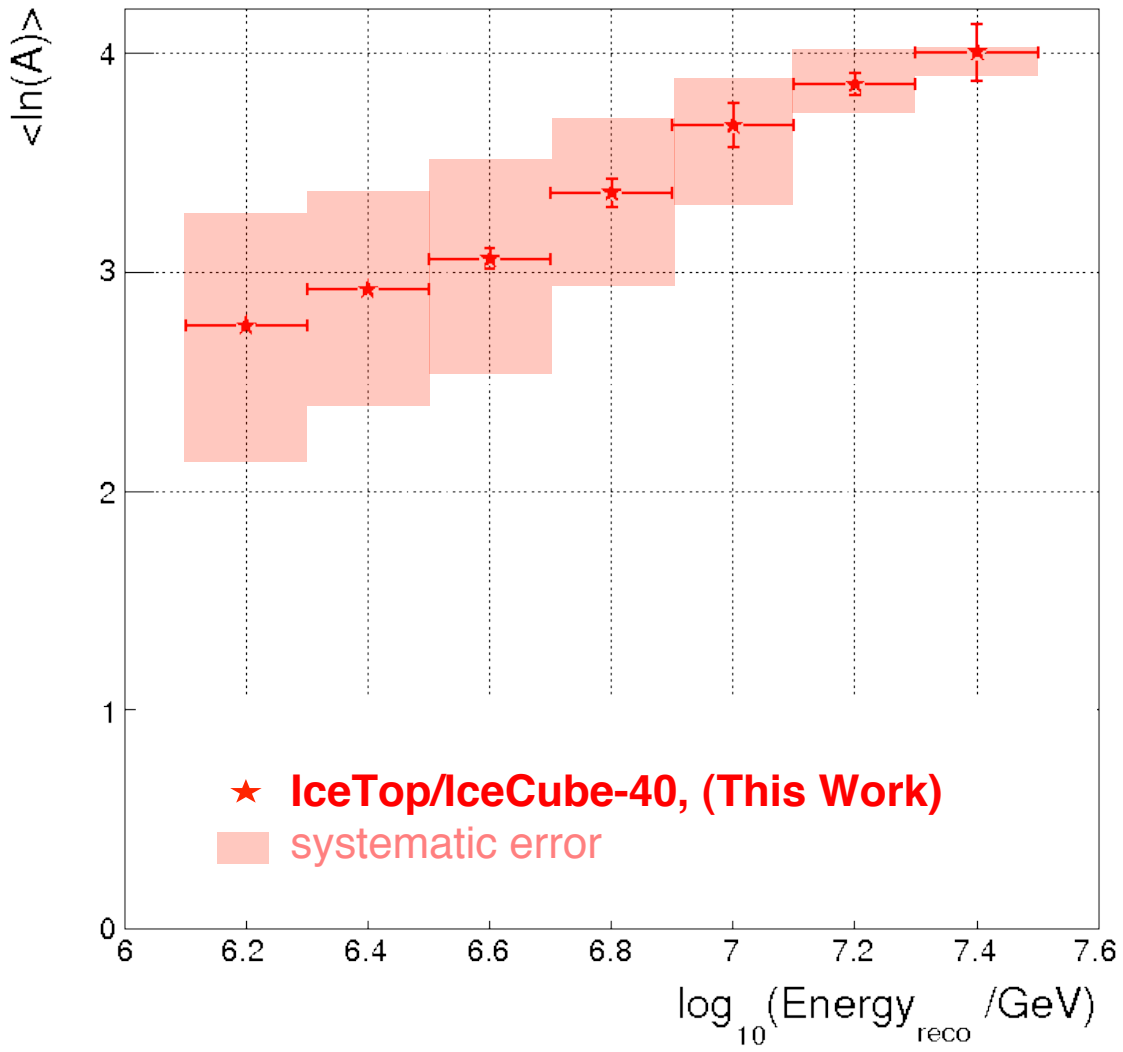


Figure 8.8: The mean log mass vs primary energy results of this analysis. The error bars on the data points are statistical, while the shaded region is that included by systematic uncertainties.

## Chapter 9

### Results and Conclusions

#### 9.1 Results

In summary we have used the combined IceCube and IceTop detectors from the 2008 40-string/40-station configuration to measure cosmic ray energy spectrum and composition at energies in the range of 1-50 PeV. Using a measurement of the electromagnetic component of the air shower at the surface,  $S_{125}$ , and the muonic component of the shower in the ice,  $K_{70}$ , we have developed an appropriate set of quality cuts and used our CORSIKA simulation to develop a non-linear mapping technique using a neural network in conjunction with a  $\chi^2$  minimization algorithm to extract the relevant physical parameters: primary mass and primary energy.

##### 9.1.1 Energy Spectrum

The neural network technique enabled us to reconstruct primary energy with a very small energy resolution and a minimal bias by primary type. This led to an energy spectrum measurement which compares favorably with other experiments, as seen in Figure 9.1. In particular, using the Poly-Gonato model [38] to fit our spectrum, we find a knee at 5.068 PeV, with gradual transition (i.e.,  $\epsilon = 3.947$ ) from a spectral index  $\alpha = 2.546$  below the knee to index  $\alpha = 3.271$  above the knee. For comparison, the results of other recent experiments can be found in Figure 9.2(a) and Table 9.2(b). A table of the values found using this analysis can be located in Appendix C.

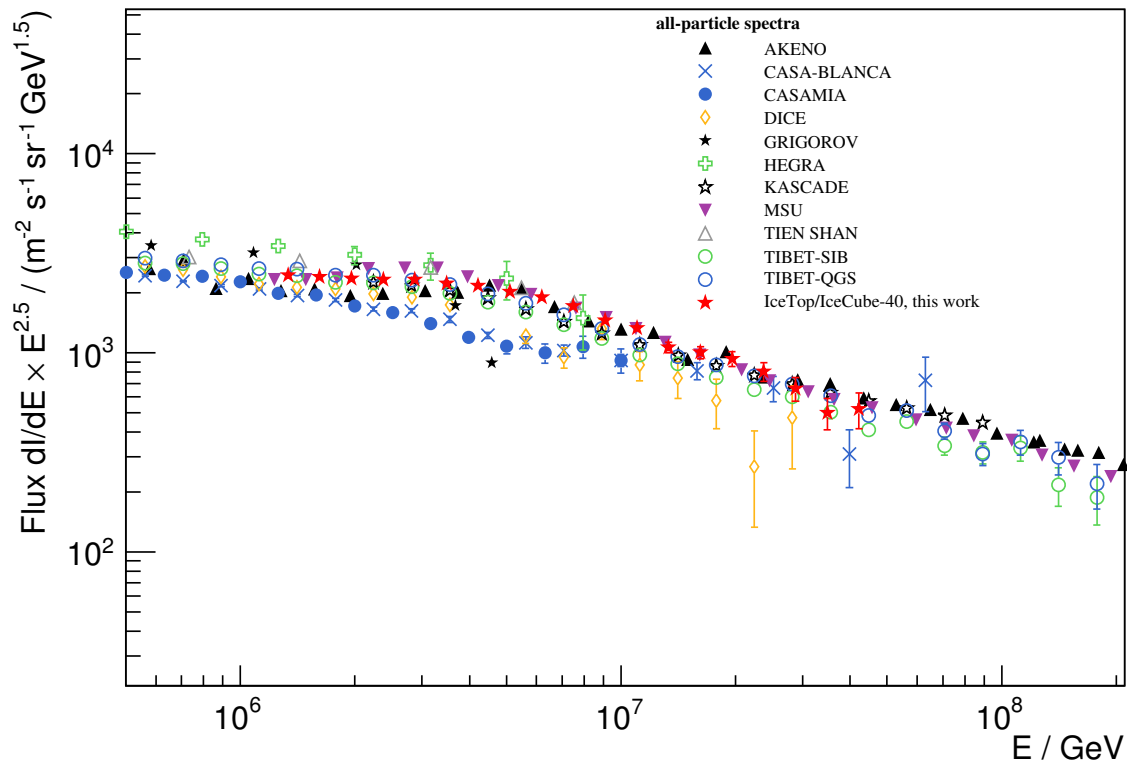
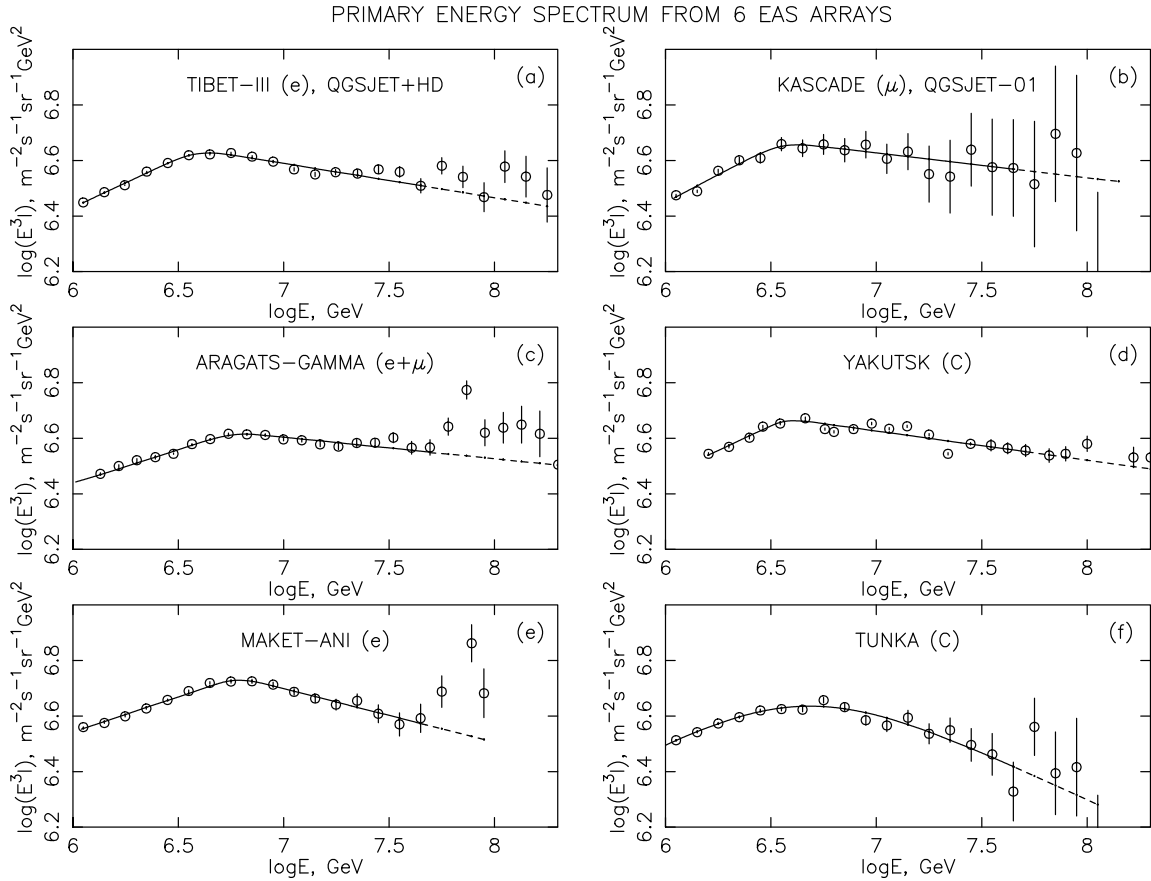


Figure 9.1: The all particle cosmic ray spectrum using the neural network technique as described in the text. The flux is multiplied by  $E^{2.5}$ . We find a very similar overall flux and shape to many other experiments. The error bars on all experiments are statistical only.



Array	$\log_{10}(E_{knee})$	$\gamma$	$\Delta\gamma$	$\epsilon$
Tibet-III	6.59	2.64	0.48	8.85
KASCADE	6.55	2.60	0.49	8.43
GAMMA	6.76	2.76	0.32	10.0
Yakutsk	6.57	2.64	0.46	15.7
Maket-ANI	6.78	2.75	0.44	12.9
Tunka	6.64	2.59	0.75	1.64
IceCube/IceTop (this work)	6.71	2.53	0.71	3.98

Figure 9.2: In Figure 9.2(a) we show the cosmic ray energy spectra of the recent experiments Tibet-III, KASCADE, GAMMA, Yakutsk, Maket-Ani, and Tunka. The observable EAS component for each experiment is indicated in the brackets (with  $\mu$  for muon,  $e$  for electromagnetic, and  $C$  for Cherenkov light). Each of the spectra has been fit to the Poly-Gonato model in black (the dashed line is an extrapolation), with the best fit parameters found in Table 9.2(b). The best fit parameters from this analysis compare favorably. (Table and Figure after [74])

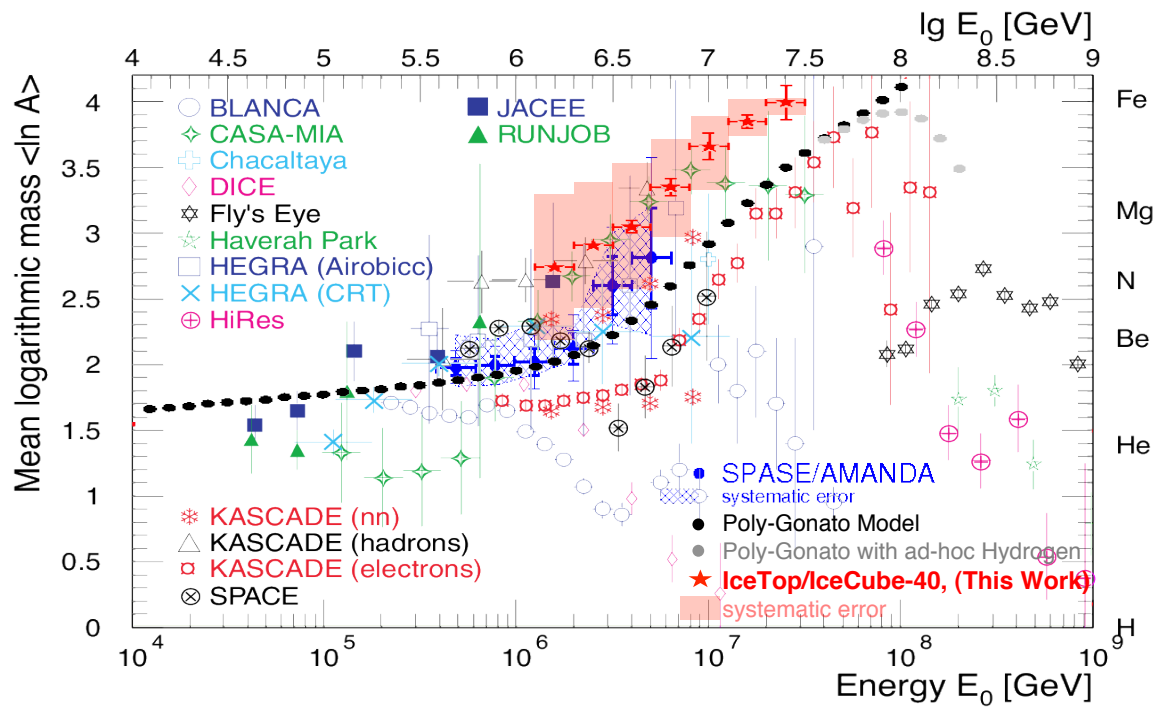


Figure 9.3: Mean logarithmic mass vs primary energy for a number of experiments, as labeled. The results of this analysis are on the heavier end of the measured results, and exhibit a strong preference for an increasing mass through the knee. Our systematic errors are included in the shaded red region, while the marked error bars are statistical.

### 9.1.2 Mass Composition

The neural network technique also enabled us to reconstruct a mass parameter which, combined with a minimization analysis, provides a measurement of cosmic ray composition: the mean log mass,  $\langle \ln A \rangle$ . The results of this analysis compared with many others can be seen in Figure 9.3. The mass measured by this analysis is on the heavier side of the observed masses and trends strongly toward an increase in mass through the knee. The results of our predecessor experiment, SPASE-2/AMANDA-B10 (which were normalized to the directly measured result of  $\langle \ln A \rangle = 2$  in the lowest energy bin), fall within the systematic error bars of the present analysis and show a similar overall trend, as seen in Figure 9.4. When compared with only experiments which measure similar shower components our results compare very favorably with the slope of previous measurements, and once more is on the heavier end in terms of  $\langle \ln A \rangle$  for each slice in energy, as seen in Figure 9.5. Furthermore, when compared with the Poly-Gonato model the results of this analysis exhibit a strikingly similar trend in slope, which is most easily seen by artificially removing the overall offset of 0.714 in  $\langle \ln A \rangle$  between the observation and the model, as seen in Figure 9.6. This slope only deviates in the highest energies, where the experimental results are limited by a maximum mass of iron. (A table of the values found can be located in Appendix D.)

## 9.2 Lessons Learned and Future Work

This analysis has produced remarkable first measurements of the energy spectrum and primary composition of cosmic rays using the combined IceCube and IceTop detectors. Using only one month of data, the all-particle energy spectrum has been measured with extremely tight energy resolution, exhibits a clearly visible knee, and compares very favorably with previous results. The mass composition measurement has also proven to be quite interesting, showing a very strong increase in mass through the knee as well as a strikingly similar slope to a commonly used model. Though this result still has significant systematic error bars, these errors come from sources which are becoming better-understood, which should enable us to pin-down the normalization more readily thereby allowing for a strong statement as to the mean log mass.

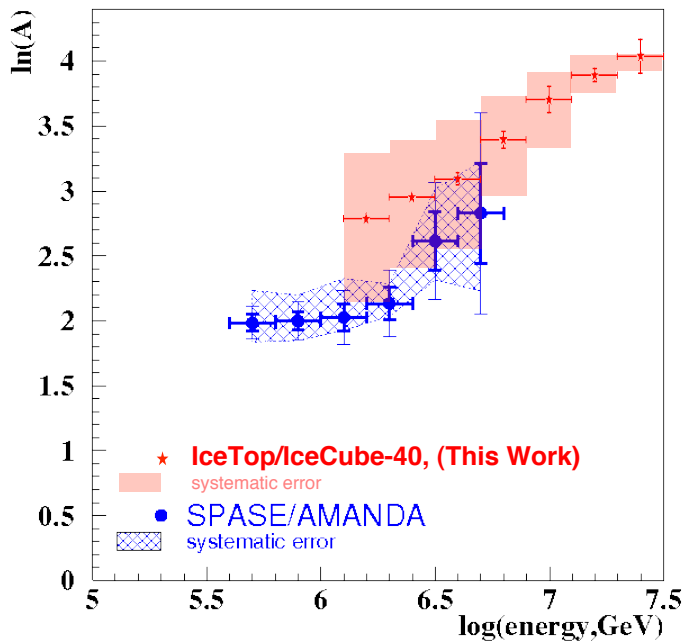


Figure 9.4:

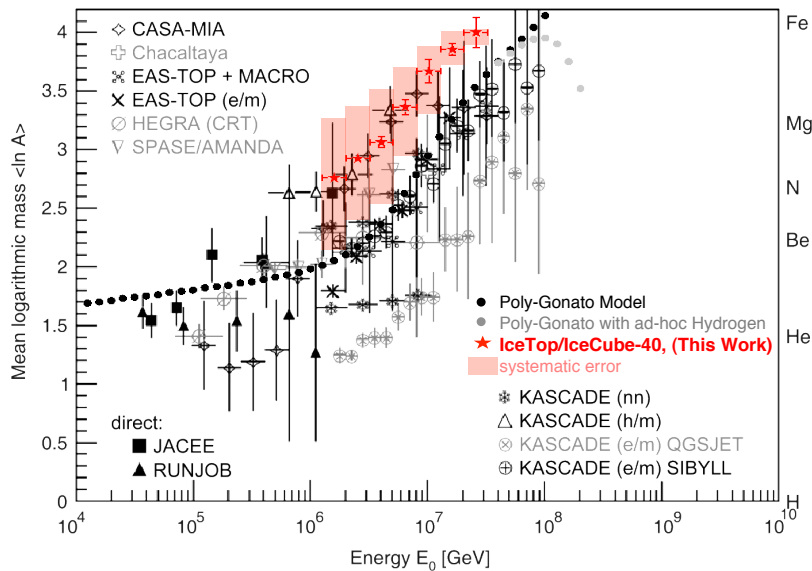


Figure 9.5: Comparison of final  $\langle \ln A \rangle$  results (after combined neural network and minimization analysis) with other experiments which find composition using similar analysis techniques. The slope of the mass increase with respect to energy is similar to most other experiments shown, and we show good overall agreement with CASA-MIA and the KASCADE neural network analysis.

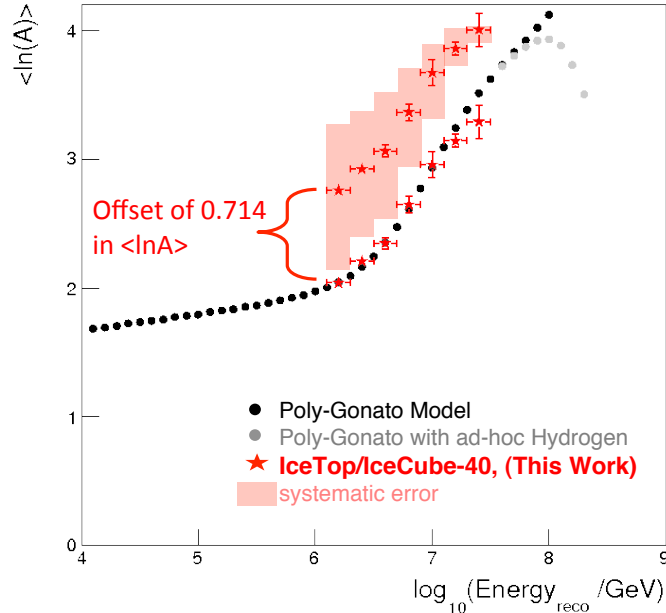


Figure 9.6: Comparison of final  $\langle \ln A \rangle$  results (after combined neural network and minimization analysis) with the well-known Poly-Gonato model of knee composition. To aid the eye, the results of this analysis have been re-plotted with an artificial downward shift of 0.714 in  $\langle \ln A \rangle$ .

Further, this analysis has exposed several measurement shortcomings which can be addressed in the future. Among these, snow covering the surface detectors has been discovered to play an important role in surface array data signal, and one method to deal with this issue has been developed and care must be taken with this effect in future analyses. Additionally, IceTop is now preparing techniques to develop a much larger simulation sample size as simulation statistics are a major limitation in the minimization technique.

In addition to providing an interesting result, a technique has been developed which has laid the groundwork for future analyses using the IceCube and IceTop arrays. A clear follow-up of this analysis is to include more parameters which are currently being developed, such as:

- Shower curvature
- Shower age
- Muon bundle energy loss
- Lateral distribution of low energy surface muons

which, together with a much larger simulation sample will allow for the possibility of reconstructing energy spectra of individual primary types. The techniques developed here were designed with flexibility in mind and therefore this analysis method should adapt easily to these natural extensions. Further, incorporating data from the full array will allow the IceCube Neutrino Observatory to measure primary energy spectrum and mass composition from energies which overlap with direct measurements to energies nearing the ankle. It is indeed an exciting time in cosmic ray physics, and especially for the IceCube Neutrino Observatory.

## Appendix A

### Glossary of Some Acronyms and Units

#### DOM

Digital Optical Module, the basic component of the IceCube and IceTop arrays.

#### DLP

Double Logarithmic Paraboloid, a function which is a parabola on a double logarithmic axis. A specific DLP function was developed to describe the signal size in IceTop.

#### eV

Electron-volts, the energy an electron gains as it crosses a one volt potential. This is the basic unit of energy used throughout this work. Furthermore, we often utilize the common prefixes GeV ( $10 \times 10^9$  eV), TeV ( $10 \times 10^{12}$  eV), PeV ( $10 \times 10^{15}$  eV), and EeV ( $10 \times 10^{18}$  eV).

#### FCU

Freeze Control Unit, specially designed to make (optically clear and bubble-free) ice in the IceTop tanks at the South Pole.

#### GZK

Greisen Zatzeputin K , usually in reference to the GZK cutoff, a commonly accepted but not yet experimentally proven theory describing the cut off of particles above  $\sim 10 \times 10^{20}$  eV.

#### $K_{70}$

The parameter used to describe the fitted amount of light in ice a perpendicular distance of

70 m from the reconstructed track at a reference depth of 1950 m (the center of the detector).

**LC**

Local Coincidence, a trigger condition requiring that a certain number of neighboring DOMs are hit within a certain time window.

**LDF**

Lateral Distribution Function, any function describing the lateral distribution of a specified type of particles in a cosmic ray air shower.

**NKG**

Nishimura, Kamata and Greisen, typically in reference to the function they developed to describe the lateral distribution of electromagnetic particles at the surface.

**PDF**

Probability Distribution Function, used for example when calculating the likelihood of a track in the IceCube array.

**PE**

The standard unit of measure for the amplitude of the light in the ice. A photoelectron is typically considered to be an electron ejected by an incident photon, as in our PMTs.

**PMT**

Photomultiplier Tube, the light-detecting component of all IceCube and IceTop digital optical modules (DOMs).

 $S_{125}$ 

The parameter used to describe the fitted shower size at the surface a distance of 125 m from the reconstructed shower core.

**SMT**

Simple Majority Trigger, a trigger condition requiring a certain number of hit DOMs before

an event is read out.

## **VEM**

Vertical Equivalent Muons, defined as the average energy deposited by a vertical muon passing through the center of an IceTop tank. This is the standard unit for the IceTop signal size.

## Appendix B

### Niessenian Energy Binning Scheme

Table B.1: The energy binning scheme chosen by Peter Niessen. For the current analysis we generated 3000 events of each primary particle type (proton, helium, oxygen, silicon, and iron) within each of these bins. We have recommended that future analyses use bin-widths of 1/10 of a decade in  $\log_{10}(E)$  instead of 1/3 of a decade in  $\log_{10}(E)$  as was chosen here.

Energy Bin	$\log_{10}(E/\text{GeV}) \geq$	$\log_{10}(E/\text{GeV}) <$	$E \geq$	$E <$
8	4.00	4.33	10 TeV	21.5 TeV
9	4.33	4.66	21.5 TeV	46.4 TeV
10	4.66	5.00	46.4 TeV	100 TeV
11	5.00	5.33	100 TeV	215 TeV
12	5.33	5.66	215 TeV	464 TeV
13	5.66	6.00	464 PeV	1 PeV
14	6.00	6.33	1 PeV	2.15 PeV
15	6.33	6.66	2.15 PeV	4.64 PeV
16	6.66	7.00	4.64 PeV	10 PeV
17	7.00	7.33	10 PeV	21.5 PeV
18	7.33	7.66	21.5 PeV	46.4 PeV

## Appendix C

### Energy Spectrum Results

Table C.1: Flux vs. Energy. The flux listed is for each energy slice (in logarithmic energy space): each slice is 1/12 of a decade in  $\log_{10}(\text{Energy}/\text{GeV})$ . The errors on the flux are statistical only.

$\log_{10}(E/\text{GeV})$	Flux ( $\text{m}^2 \text{ sr s GeV}^{-1}$ )
6.167 – 6.250	$7.27 \times 10^{13} \pm 5.74 \times 10^{15}$
6.250 – 6.333	$4.42 \times 10^{13} \pm 4.02 \times 10^{15}$
6.333 – 6.417	$2.70 \times 10^{13} \pm 2.85 \times 10^{15}$
6.417 – 6.500	$1.67 \times 10^{13} \pm 2.04 \times 10^{15}$
6.500 – 6.583	$9.88 \times 10^{14} \pm 1.43 \times 10^{15}$
6.583 – 6.667	$5.96 \times 10^{14} \pm 1.01 \times 10^{15}$
6.667 – 6.750	$3.44 \times 10^{14} \pm 7.01 \times 10^{16}$
6.750 – 6.833	$2.00 \times 10^{14} \pm 4.87 \times 10^{16}$
6.833 – 6.917	$1.11 \times 10^{14} \pm 3.31 \times 10^{16}$
6.917 – 7.000	$5.85 \times 10^{15} \pm 2.19 \times 10^{16}$
7.000 – 7.083	$3.31 \times 10^{15} \pm 1.50 \times 10^{16}$
7.083 – 7.167	$1.64 \times 10^{15} \pm 9.65 \times 10^{17}$
7.167 – 7.250	$9.58 \times 10^{16} \pm 6.73 \times 10^{17}$
7.250 – 7.333	$5.50 \times 10^{16} \pm 4.65 \times 10^{17}$
7.333 – 7.417	$2.94 \times 10^{16} \pm 3.10 \times 10^{17}$
7.417 – 7.500	$1.50 \times 10^{16} \pm 2.02 \times 10^{17}$
7.500 – 7.583	$7.01 \times 10^{17} \pm 1.26 \times 10^{17}$
7.583 – 7.667	$4.52 \times 10^{17} \pm 9.22 \times 10^{18}$

## Appendix D

### Mass Results

Table D.1: Number of entries vs. Energy. The energy is listed in slices, the other 5 columns are the number of entries in that final reconstructed slice in energy for data and simulation.

$\log_{10}(E / \text{GeV})$	Data	proton	helium	oxygen	iron
6.1-6.3	39578	143	133	149	104
6.3-6.5	20166	150	134	150	150
6.5-6.7	9315	165	142	132	133
6.7-6.9	4003	125	174	134	151
6.9-7.1	1428	121	150	130	158
7.1-7.3	529	148	144	147	152
7.3-7.5	192	112	124	151	143

Table D.2:  $\langle \ln A \rangle$  vs. Energy. The energy is listed in slices, the  $\langle \ln A \rangle$  is the final result of the analysis described in this work, and the last two columns are the minimum and maximum  $\langle \ln A \rangle$  values calculated by adding the systematic errors in quadrature and rerunning the neural network and the minimization procedure for the adjusted  $K_{70}$  values.

$\log_{10}(E / \text{GeV})$	$\langle \ln A \rangle$	systematic min $\langle \ln A \rangle$	systematic max $\langle \ln A \rangle$
6.1-6.3	2.75	2.14	3.26
6.3-6.5	2.92	2.38	3.37
6.5-6.7	3.06	2.54	3.52
6.7-6.9	3.36	2.94	3.70
6.9-7.1	3.67	3.31	3.88
7.1-7.3	3.86	3.72	4.01
7.3-7.5	4.00	3.89	4.03

Table D.3: Ratio of particles vs. Energy. The energy is listed in slices, the ratios of each particle type, as reconstructed by the neural network, are given.

$\log_{10}(E / \text{GeV})$	ratio protons	ratio helium-oxygen	ratio iron
6.1-6.3	0.32	0.00	0.68
6.3-6.5	0.23	0.10	0.67
6.5-6.7	0.20	0.08	0.72
6.7-6.9	0.15	0.03	0.82
6.9-7.1	0.08	0.02	0.90
7.1-7.3	0.04	0.00	0.96
7.3-7.5	0.01	0.00	0.99

## Appendix E

### Supplemental Details About Cuts

I thought it best to include some information about the method I used to chose the cuts to help explain the order in which I chose them. So in the next pages I'm including the panel I was using to choose cut parameters. It often changed as I tested other parameters, but the ones included presently are the ones used in the final cut selection. In all of these plots, the first row is generally indicator plots: true core position,  $K_{70}$  vs  $S_{125}$ ,  $S_{125}$  vs True Energy, efficiency (in histogram form, as well as numbers). The last plot in that row is the LineFit IcetopSiz parameter vs  $S_{125}$ . The second row is parameters drawn with respect to  $S_{125}$ , and the third row is the same parameters drawn with respect to  $K_{70}$ . As described in the section on event selection, for this analysis it can be expected that the angular resolution of this detector is very good. Therefore, I use the angular resolution as a way to gauge which cuts I should make. So, in all cases, the colored contours are angular resolution between the surface fit and the true track. The gray dots are protons, and the black points are iron. The cuts are then made as described in the chapter, with explanations in the figure captions.

(Note: A similar method can be used with position resolution, because a goal of cuts is to improve that core position reconstruction. I have also made these plots but they're redundant here, and I based the cuts in this analysis mainly on angular resolution.)



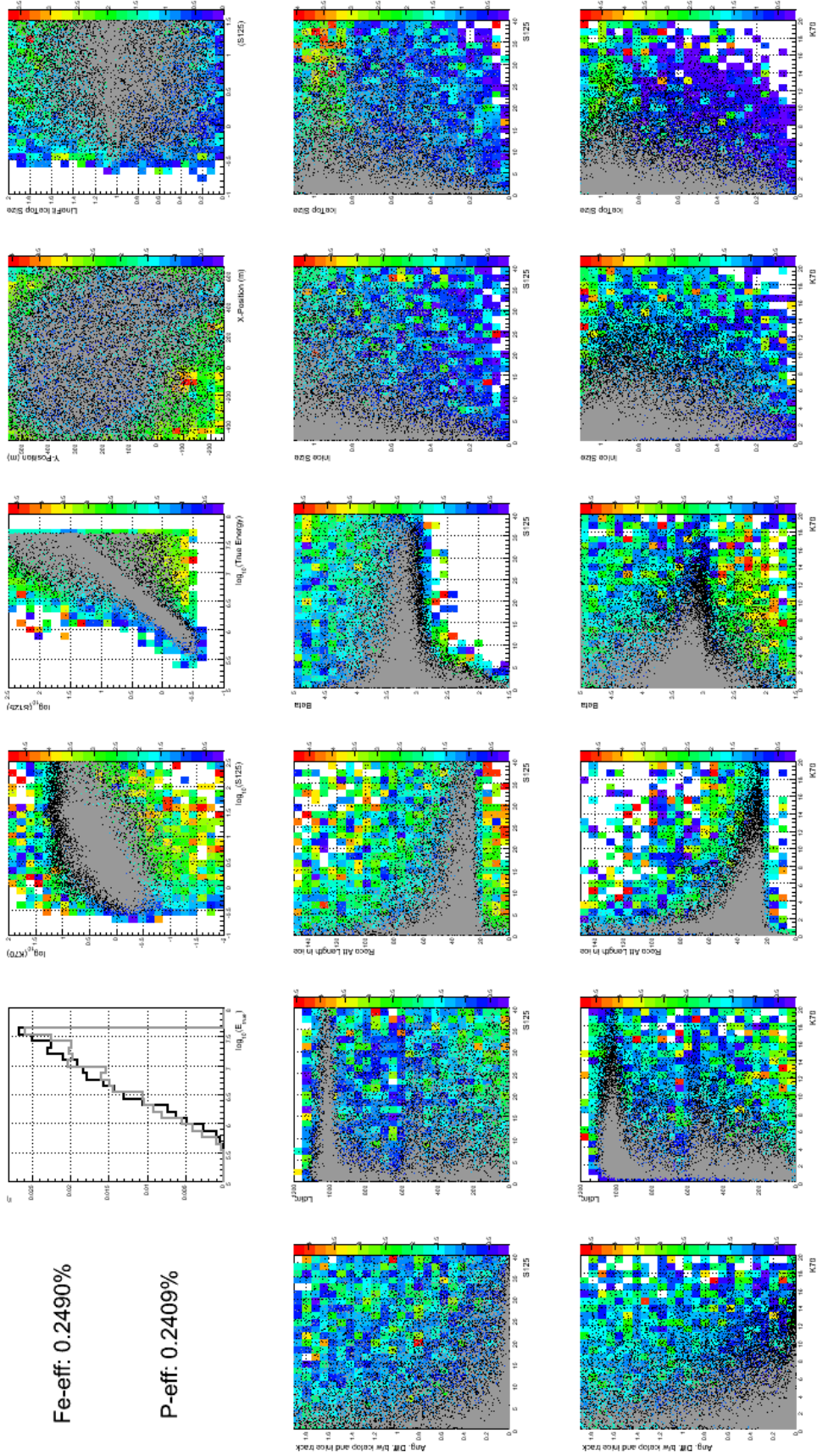
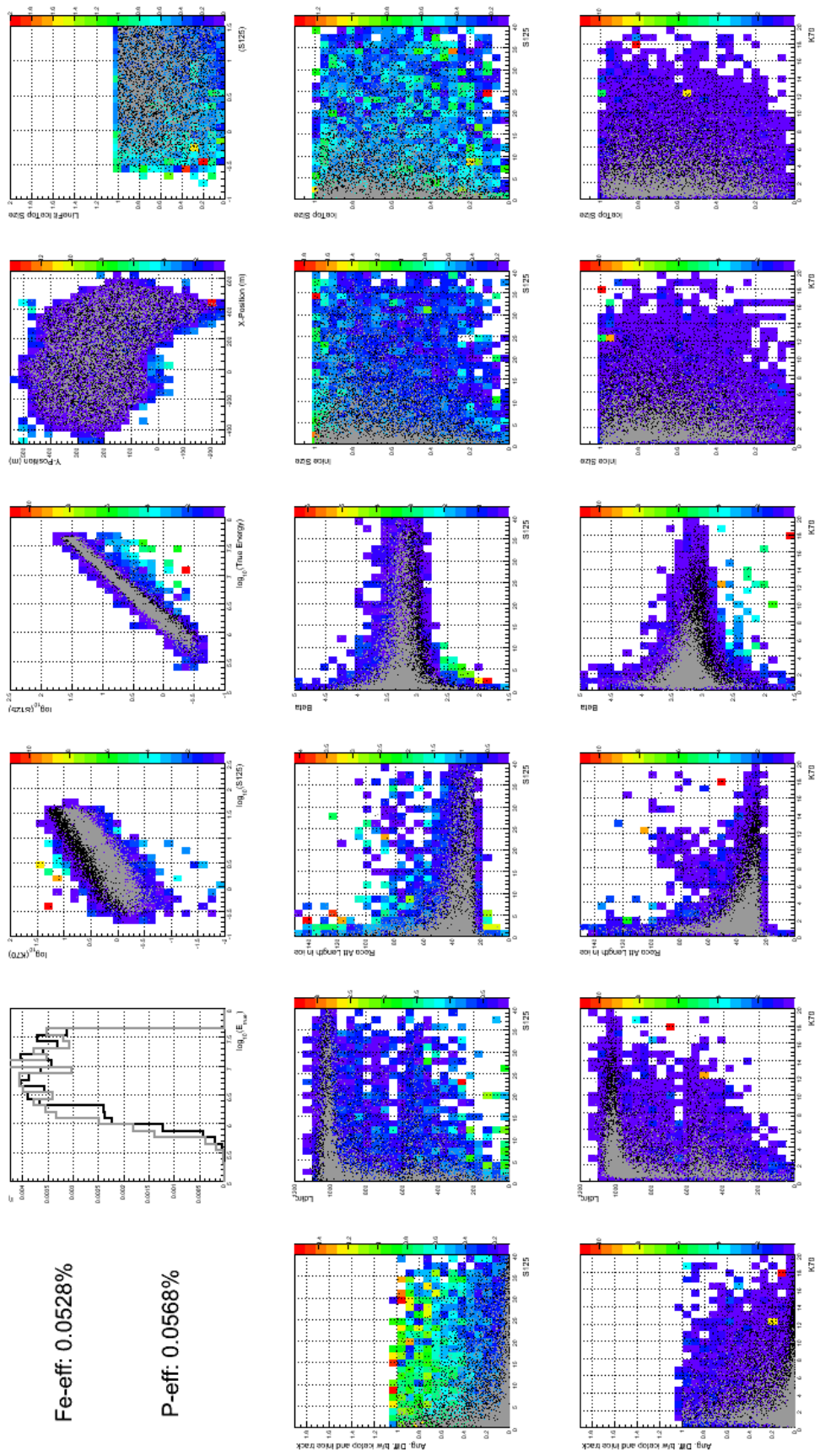


Figure E.2: ...I restrict the angular resolution to  $\pm 5$  degrees. This makes it clear that angular resolution is a good parameter to be looking at in the contours, as all the outlying events in the indicator plots in the top row have poor resolution. It also becomes obvious that containment cuts are the next choice for cuts.









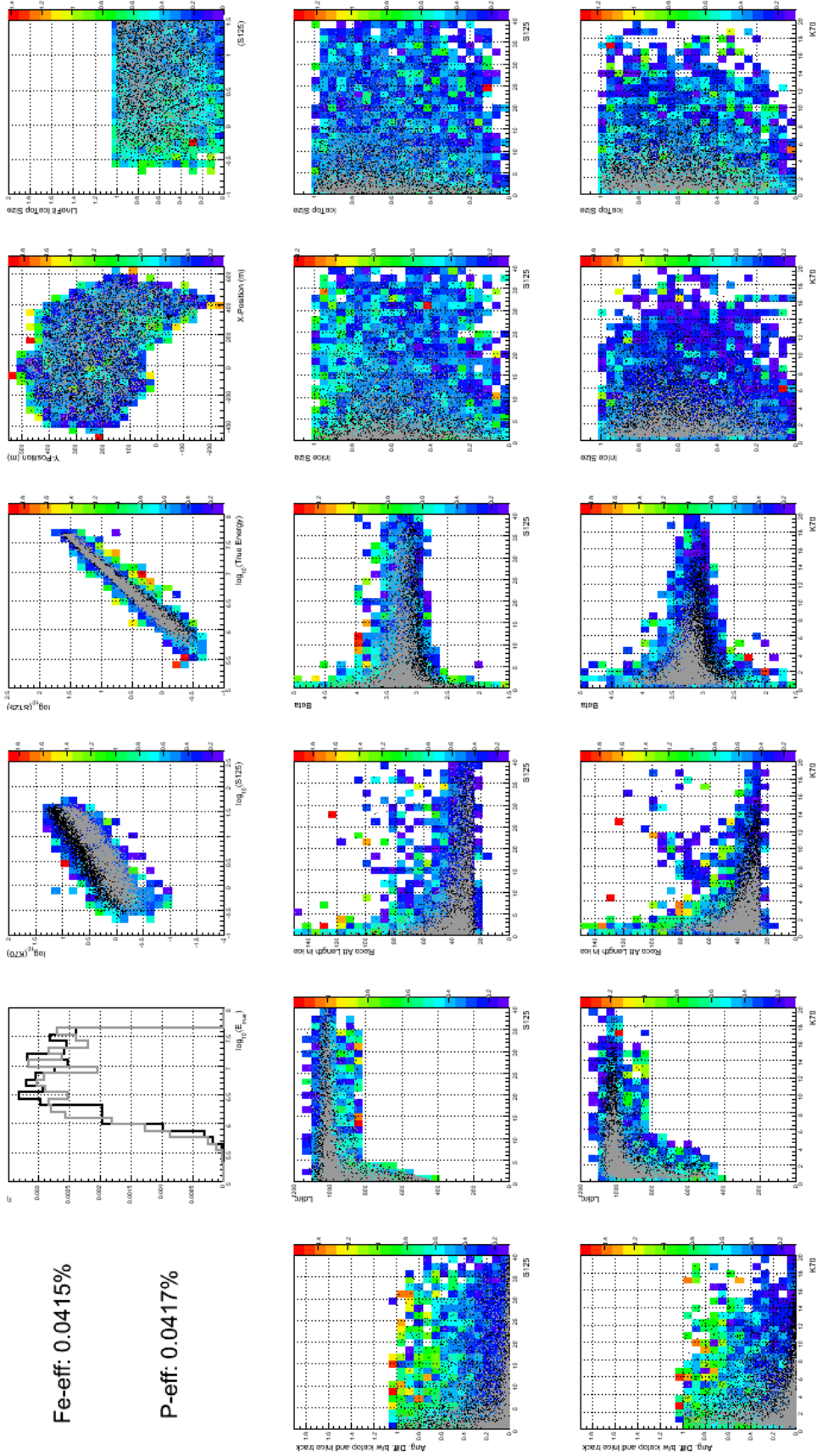


Figure E.7: ...again I restrict the angular resolution to 2 degrees, and make as loose a cut as possible on the length. I cut with respect to K and to S this time, since that way I can make the cut looser and still get most outlying events.



## Bibliography

- [1] V. Hess, “Penetrating radiation in seven free balloon flight,” *Z. Phys*, Jan 1912.
- [2] T. Gaisser, “From the knee to the ankle, theory and experiment,” *Physics at the End of the Galactic Cosmic Ray Spectrum 2005 Conference Proceedings*, 2005.
- [3] W. Bothe and W. Kolhörster, “The nature of the penetrating radiation,” *Nature*, Jan 1929.
- [4] J. Clay, “Penetrating radiation,” *Proceedings of the Amsterdam Academy*, vol. 33, p. 1721, 1930.
- [5] P. Auger *et al.*, “Extensive cosmic-ray showers,” *Reviews of Modern Physics*, Jan 1939.
- [6] W. Kolhörster, “Das verhalten der hohenstrahlung bei den magnetischen storungen vom januar 1938,” *Naturwissenschaften*, Jan 1938.
- [7] M. Schein and W. Jesse, “The nature of the primary cosmic radiation and the origin of the mesotron,” *Physical Review*, Jan 1941.
- [8] H. L. Brandt and B. Peters, “Investigation of the primary cosmic radiation with nuclear photographic emulsions,” *Physical Review*, vol. 74, pp. 1828–1837, Dec 1948.
- [9] H. Brown, “A table of relative abundances of nuclear species,” *Reviews of Modern Physics*, vol. 21, pp. 625–634, Oct 1949.
- [10] G. B. Hristiansen and G. V. Kulikov, “On the number of particles spectrum of extensive air showers,” *Il Nuovo Cimento*, vol. 8, no. 2, pp. 742–745, 1958.

- [11] J. Linsley, "Evidence for a primary cosmic-ray particle with energy  $10^{20}$  eV," *Physical review letters*, Jan 1963.
- [12] M. Nagano *et al.*, "Energy spectrum of primary cosmic rays above  $10^{17}$  eV determined from extensive air shower experiments at AKENO," *Journal of Physics G*, Jan 1992.
- [13] D. Bird *et al.*, "Evidence for correlated changes in the spectrum and composition of cosmic rays at extremely high energies," *Physical review letters*, Jan 1993.
- [14] E. Fermi, "On the origin of the cosmic radiation," *Physical Review*, Jan 1949.
- [15] T. K. Gaisser, *Cosmic rays and particle physics*. Cambridge University Press, Jan 1990.
- [16] T. Stanev, "Ultra high energy cosmic rays: Origin and propagation," *Proceedings of the 30th International Cosmic Ray Conference, Merida, Mexico*, 2007.
- [17] W. I. Axford, E. Leer, and G. Skadron, "Acceleration of cosmic rays at shock fronts," *15th International Cosmic Ray Conference, Budapest*, vol. 2, p. 273, 1977.
- [18] G. Krymsky, "A regular mechanism for accelerating charged particles at the shock front," *Dokl. Akad. Nauk. SSSR*, 1977.
- [19] A. Bell, "The acceleration of cosmic rays in shock fronts-ii," *Royal Astronomical Society, Monthly Notices*, vol. 182, p. 443, Feb 1978.
- [20] R. Blandford and J. Ostriker *Astrophysical Journal (Letters)*, vol. 221, p. 229, 1978.
- [21] R. Blandford and D. Eichler, "Particle acceleration at astrophysical shocks: A theory of cosmic ray origin," *Physics Reports*, vol. 154, no. 1, pp. 1–75, 1987.
- [22] F. Rieger and V. Bosch-Ramon, "Fermi acceleration in astrophysical jets," *The Multi-Messenger Approach*, Jan 2008.
- [23] L. A. Anchordoqui and D. F. Torres, "Astrophysical origins of ultrahigh energy cosmic rays," *Reports on Progress in Physics*, vol. 67, p. 1663, 2004.

- [24] A. M. Hillas, “The origin of ultra-high-energy cosmic rays,” *Ann. Rev. Astron. Astrophys.*, vol. 22, pp. 425–44, 1984.
- [25] NASA, “Supernovae,” <http://imagine.gsfc.nasa.gov/docs/science/known2/supernovae.html>, 2010.
- [26] K. Brecher, “Supernova,” *World Book at NASA*, [http://www.nasa.gov/worldbook/supernova\\_worldbook.html](http://www.nasa.gov/worldbook/supernova_worldbook.html), 2010.
- [27] Wikipedia, “Supernova,” <http://en.wikipedia.org/wiki/Supernova>, 2010.
- [28] J. Hörandel, “Cosmic rays from the knee to the second knee:  $10^{14}$  to  $10^{18}$  eV,” *Modern Physics Letters A*, vol. 22, no. 21, p. 1533, 2007.
- [29] K. W. Weiler and R. A. Sramek, “Supernovae and supernova remnants,” *Ann. Rev. Astron. Astrophys.*, 1988.
- [30] R. Diehl, “Particle acceleration in cosmic sites,” *The European Physical Journal D*, vol. 55, no. 2, pp. 509–518, 2009.
- [31] V. Berezhinsky, P. Blasi, and V. Ptuskin, “Clusters of galaxies as storage room for cosmic rays,” *The Astrophysical Journal*, vol. 487, pp. 529–535, 1997.
- [32] V. Ptuskin, “Cosmic ray transport in the galaxy,” *Journal of Physics: Conference Series*, Jan 2006.
- [33] T. Stanev, *High Energy Cosmic Rays*. Springer, 2009.
- [34] K. Greisen, “End to the cosmic ray spectrum?,” *Physical review letters*, vol. 16, no. 17, p. 7480750, 1966.
- [35] G. T. Zatsepin and V. A. Kuzmin, “Upper limit of the spectrum of cosmic rays,” *Journal of Experimental and Theoretical Physics Letters*, vol. 4, pp. 78–80, 1966.

- [36] J. Hörandel, “Models of the knee in the energy spectrum of cosmic rays,” *Astroparticle Physics*, Jan 2004.
- [37] J. Blumer, R. Engel, and J. Hörandel, “Cosmic rays from the knee to the highest energies,” *Progress in Particle and Nuclear Physics*, vol. 63, pp. 293–338, 2009.
- [38] J. Hörandel, “On the knee in the energy spectrum of cosmic rays,” *Astroparticle Physics*, vol. 19, no. 2, pp. 193–220, 2003.
- [39] K.-H. Kampert, “Methods of determination of the energy and mass of primary cosmic ray particles at extensive air shower energies,” *Journal of Physics G: Nuclear and Particle Physics*, vol. 27, p. 1663, Jul 2001.
- [40] K. Rawlins, *Measuring the Composition of Cosmic Rays with the SPASE and AMANDA Detectors*. PhD thesis, University of Wisconsin-Madison, 2001.
- [41] K. H. Kampert, “Some basics about extensive air showers (talk),” *International School on Astroparticle Physics*, 2007.
- [42] T. K. Gaisser and A. M. Hillas, “Reliability of the method of constant intensity cuts for reconstructing the average development of vertical showers,” *International Cosmic Ray Conference*, 1977.
- [43] L. Anchordoqui *et al.*, “High energy physics in the atmosphere: Phenomenology of cosmic ray air showers,” *Annals of Physics*, 2007.
- [44] K. Griesen, “Prog. in cosmic ray phys,” *N. Holland Publishing Co., Amsterdam*, vol. 3, 1956.
- [45] J. W. Elbert, “Multiple muons produced by cosmic ray interactions,” *DUMAND Summer Workshop, La Jolla, CA*, 1979.
- [46] I. Frank and I. Tamm, “Coherent radiation of fast electrons in a medium,” *C. R. Ac. Sci U.S.S.R.*, vol. 14, p. 107, 1937.

- [47] R. Abbasi *et al.*, “Calibration and characterization of the IceCube photomultiplier tube,” *Nuclear Instruments and Methods in Physics Research Section A*, vol. 618, p. 139, Jun 2010. Elsevier B.V.
- [48] R. Abbasi *et al.*, “The IceCube data acquisition system: Signal capture, digitization, and timestamping,” *Nuclear Instruments and Methods in Physics Research Section A*, 2008.
- [49] Achterberg *et al.*, “First year performance of the IceCube neutrino telescope,” *Astroparticle Physics*, 2006.
- [50] S. Klepser, *Reconstruction of Extensive Air Showers and Measurement of the Cosmic Ray Energy Spectrum in the Range of 1-80 PeV at the South Pole*. PhD thesis, Humbolt-Universität zu Berlin, 2008.
- [51] M. Ackermann *et al.*, “Optical properties of deep glacial ice at the south pole,” *J. Geophys. Res.*, vol. 11, 2006.
- [52] K. Woschnagg, “Ice properties and systematics.” [http://wiki.IceCube.wisc.edu/index.php/Ice\\_properties\\_systematics](http://wiki.IceCube.wisc.edu/index.php/Ice_properties_systematics).
- [53] K. Woschnagg, “Aha.” <http://wiki.IceCube.wisc.edu/index.php/Aha>.
- [54] E. Strahler, *Searches for Neutrinos from Gamma Ray Bursts with the AMANDA-II and IceCube Detectors*. PhD thesis, University of Wisconsin-Madison, 2009.
- [55] R. Abbasi *et al.*, “Time-integrated searches for point-like sources of neutrinos with the 40-string IceCube detector,” *Astrophysical Journal*, 2011.
- [56] S. Grullon, *A Search for a Diffuse Flux of Astrophysical Muon Neutrinos with the IceCube Neutrino Observatory in the 40-String Configuration*. PhD thesis, University of Wisconsin-Madison, 2010.
- [57] T. Kuwabara *et al.*, “Heliospheric physics with IceTop,” *Proceedings of the 30th International Cosmic Ray Conference, Merida, Mexico*, 2007.

- [58] L. Gerhardt, “Study of high pt muons in IceCube,” *Proceedings of the 31st International Cosmic Ray Conference, Lodz, Poland, 2009*.
- [59] F. Kislat, S. Klepser, and A. van Overloop, “A lateral distribution function and fluctuation parametrisation for IceTop.” IceCube Internal Report, Feb 2007.
- [60] F. Kislat *et al.*, “Measurement of the all-particle cosmic ray energy spectrum with IceTop.” Prepared for Astrophys. Space Sci. Trans.
- [61] A. van Overloop, “Simulation of air shower waveforms.” Internal Cosmic Ray Workshop, Bartol Research Institute, June 2006.
- [62] B. Ruzybayev, “Small air showers in IceTop,” *Proceedings of the 31st International Cosmic Ray Conference, Lodz, Poland, 2009*.
- [63] T. K. Gaisser and T. Stanev, “Cosmic rays,” *Particle Data Group*, 2009 (revised).
- [64] K. Andeen *et al.*, “Measuring cosmic ray composition at the knee with spase-2 and amanda-ii,” *Proceedings of the 30th International Cosmic Ray Conference, Merida, Mexico, 2007*.
- [65] K. Andeen *et al.*, “Cosmic ray composition using spase-2 and amanda-ii,” *Proceedings of the 31st International Cosmic Ray Conference, Lodz, Poland, 2009*.
- [66] T. Feusels, “Private communication.”
- [67] D. Chirkin, “Neutrino search with IceCube,” *distributed internally*, 2008.
- [68] D. Chirkin and W. Rhode, “Muon Monte Carlo: A high-precision tool for muon propagation through matter,” *preprint*, 2004. hep-ph/0407075.
- [69] J. Lundberg, “Light tracking for glaciers and oceans: Scattering and absorption in heterogeneous media with photonics,” *Nuclear Instruments and Methods*, vol. A581, no. 619, 2007.
- [70] C. M. Bishop, “Neural networks and their applications,” *Review of Scientific Instruments*, vol. 65, p. 1803, Jun 1994.

- [71] C. Song, *Study of Ultra High Energy Cosmic Rays with the High Resolution Fly's Eye Prototype Detector*. PhD thesis, Columbia University, 2001.
- [72] P. Niessen, "Weighting scheme for IceTop MC simulations." Internally Distributed, 2006.
- [73] D. Chirkin, "Study of ice transparency with IceCube flashers." IceCube internally distributed report, July 2010.
- [74] A. D. Erlykin and A. W. Wolfendale, "The knee in the cosmic ray energy spectrum," *eprint arXiv*, vol. 0906, p. 3949, Jun 2009.
- [75] G. Hill, "Private communication."
- [76] S. R. Klein *et al.*, "IceCube: A cubic kilometer radiation detector," *Presented at SORMA*, 2008.
- [77] J. Ahrens *et al.*, "IceCube preliminary design document," <http://IceCube.wisc.edu/>, 2001.
- [78] F. Halzen and S. R. Klein, "IceCube: An instrument for neutrino astronomy," *Review of Scientific Instruments*, vol. 81, 2010.
- [79] H. Corp., "Hamamatsu tentative data (v.4) photomultiplier tube r7081-02 for IceCube experiments," 2003.
- [80] R. Abbasi *et al.*, "Search for muon neutrinos from gamma-ray bursts with the IceCube neutrino telescope," *Astrophysical Journal*, 2010.
- [81] R. Abbasi *et al.*, "A search for a diffuse flux of astrophysical muon neutrinos with the IceCube 40-string detector," *Physical Review D*, 2011.
- [82] J. Hörandel, "On the knee in the energy spectrum of cosmic rays," *Proceedings of the 27th International Cosmic Ray Conference*, 2001.
- [83] G. B. Yodh, "The knee: Theory and experiment," *Journal of Physics: Conference Series*, vol. 47, p. 1, 2006.

- [84] M. Unger, R. Engel, F. Schüssler, and R. Ulrich, “Study of the cosmic ray composition above 0.4 EeV using the longitudinal profiles of showers observed at the Pierre Auger observatory,” *Astronomische Nachrichten*, vol. 328, p. 614, 2007.
- [85] S. P. Swordy and D. B. Kieda, “Elemental composition of cosmic rays near the knee by multiparameter measurements of air showers,” *Astroparticle Physics*, vol. 13, no. 2-3, pp. 137–150, 2000.
- [86] L. G. Sveshnikova *et al.*, “All particle spectrum and average mass obtained by runjob experiment,” *International Cosmic Ray Conference*, vol. 3, p. 49, 2005.
- [87] T. Shibata, “Energy spectrum and primary composition from direct measurements,” *Nuclear Physics B Proceedings Supplements*, vol. 75, pp. 22–27, 1999.
- [88] M. Shibata, Y. Katayose, J. Huang, and D. Chen, “Chemical composition and maximum energy of galactic cosmic rays,” *ApJ*, vol. 716, pp. 1076–1083, May 2010.
- [89] S. Paling, A. Hillas, and D. Berley, “Results from the CACTI experiment: Air Cerenkov and particle measurements of PeV air showers at Los Alamos,” *Proceedings of the 25th International Cosmic Ray Conference, Durban (South Africe)*, 1997.
- [90] M. Nagano and A. Watson, “Observations and implications of the ultrahigh-energy cosmic rays,” *Reviews of Modern Physics*, vol. 72, no. 3, pp. 689–732, 2000.
- [91] S. Knurenko, V. Kolosov, Z. Petrov, I. Sleptsov, and S. Starostin, “Cerenkov radiation of cosmic ray extensive air showers. part 1. lateral distribution in the energy region of  $10^{15}$ - $10^{17}$  eV,” *Proceedings of ICRC*, vol. 2001, p. 177, 2001.
- [92] J. Kirk and R. Dendy, “Shock acceleration of cosmic rays-a critical review,” *Journal of Physics G: Nuclear and Particle Physics*, vol. 27, p. 1589, 2001.

- [93] N. N. Kalmykov, L. A. Kuzmichev, G. V. Kulikov, V. V. Prosin, V. P. Sulakov, and Y. A. Fomin, "Spectrum and composition of cosmic rays at energies of  $10^{15}$ - $10^{18}$  eV," *Moscow Univ. Phys.*, vol. 65, pp. 275–282, Aug 2010.
- [94] J. Hörandel, "Cosmic-ray composition and its relation to shock acceleration by supernova remnants," *Advances in Space Research*, vol. 41, no. 3, pp. 442–463, 2008.
- [95] M. Glasmacher *et al.*, "The cosmic ray energy spectrum between  $10^{14}$  and  $10^{16}$  eV," *Astroparticle Physics*, vol. 10, no. 4, pp. 291–302, 1999.
- [96] J. Dickinson *et al.*, "Studies of the mass composition of cosmic rays with the spase-2/vulcan instrument at the south pole," *Proc. 26th Int. Cosmic Ray Conf., Salt Lake City*, vol. 3, pp. 136–139, 1999.
- [97] V. Derbina *et al.*, "Cosmic-ray spectra and composition in the energy range of 10-1000 TeV per particle obtained by the runjob experiment," *The Astrophysical Journal Letters*, vol. 628, p. L41, 2005.
- [98] M. Cha *et al.*, "Study of UHE primary cosmic ray composition with atmospheric Cherenkov light observations," *Proceedings of ICRC*, vol. 2001, p. 132, 2001.
- [99] D. Bird *et al.*, "The cosmic-ray energy spectrum observed by the fly's eye," *ApJ*, vol. 424, pp. 491–502, 1994.
- [100] K. Bernlöhr, W. Hofmann, G. Leffers, V. Matheis, M. Panter, and R. Zink, "Changes of the cosmic-ray mass composition in the  $10^{14}$ - $10^{16}$  eV energy range," *Astroparticle Physics*, vol. 8, no. 4, pp. 253–264, 1998.
- [101] J. Arteaga *et al.*, "Cosmic ray measurements with the cascade-grande experiment," *en.scientificcommons.org*, Jan 2009.

- [102] F. Arqueros, “Energy spectrum and chemical composition of cosmic rays between 0.3 and 10 PeV determined from the cherenkov-light and charged-particle distributions in air showers,” *Arxiv preprint astro-ph/9908202*, 1999.
- [103] A. Apanasenko *et al.*, “Composition and energy spectra of cosmic-ray primaries in the energy range  $10^{13}$ - $10^{15}$ eV/particle observed by Japanese-Russian joint balloon experiment.,” *ICRR Rep (Inst Cosm Ray Res Univ Tokyo)*, p. 34P, 2000.
- [104] T. Antoni *et al.*, “Kascade measurements of energy spectra for elemental groups of cosmic rays: Results and open problems,” *Astroparticle Physics*, vol. 24, no. 1-2, pp. 1–25, 2005.
- [105] T. Antoni, “The information from muon arrival time distributions of high-energy eas as measured with the kascade detector,” *Arxiv preprint astro-ph/0204266*, 2002.
- [106] M. Amenomori *et al.*, “Cosmic-ray energy spectrum around the knee obtained by the tibet experiment and future prospects,” *Advances in Space Research*, pp. 1–11, Aug 2010.
- [107] M. Albrow, “Accelerator data for cosmic ray physics,” *Arxiv preprint arXiv:1009.4178*, 2010.
- [108] E. Ahn, R. Engel, T. Gaisser, P. Lipari, and T. Stanev, “Cosmic ray interaction event generator sibyll 2.1,” *Physical Review D*, vol. 80, no. 9, p. 94003, 2009.
- [109] T. Abu-Zayyad *et al.*, “Measurement of the cosmic-ray energy spectrum and composition from  $10^{17}$  to  $10^{18.3}$  eV using a hybrid technique,” *Astrophysical Journal*, vol. 557, no. 2, pp. 686–699, 2001.
- [110] T. Abu-Zayyad *et al.*, “A multi-component measurement of the cosmic ray composition between  $10^{17}$  eV and  $10^{18}$  eV,” *Arxiv preprint astro-ph/9911144*, 1999.
- [111] T. Abu-Zayyad *et al.*, “Evidence for changing of cosmic ray composition between  $10^{17}$  and  $10^{18}$  eV from multicomponent measurements,” *Physical review letters*, vol. 84, no. 19, pp. 4276–4279, 2000.

- [112] R. Abbasi *et al.*, “A study of the composition of ultra-high-energy cosmic rays using the high-resolution fly’s eye,” *ApJ*, vol. 622, p. 910, 2005.
- [113] T. Stanev, “Ultra-high-energy cosmic rays and the large-scale structure of the galactic magnetic field,” *The Astrophysical Journal*, Jan 1997.
- [114] J. Hörandel *et al.*, “Dissecting the knee–air shower measurements with kascade,” *Nuclear Physics B*, Jan 2005.
- [115] J. Hörandel *et al.*, “The end of the galactic cosmic-ray energy spectrum—a phenomenological view,” *Journal of Physics*, Jan 2006.
- [116] D. Griffiths, *Introduction to elementary particles*. Wiley-VCH, Jan 2008.
- [117] R. Abbasi *et al.*, “IceCube collaboration contributions to the 2009 international cosmic ray conference,” *eprint arXiv*, vol. 1004, p. 2093, Apr 2010.
- [118] T. Feusels, J. Eisch, and C. Xu, “Reconstruction of IceCube coincident events and study of composition-sensitive observables using both the surface and deep detector,” *Proceedings of the 31st International Cosmic Ray Conference, Lodz, Poland, 2009*.
- [119] J. A. Nousek and D. R. Shue, “Chi-squared and c statistic minimization for low count per bin data,” *Astrophysical Journal*, vol. 342, p. 1207, Jul 1989.
- [120] S. Riggi *et al.*, “A neural network approach to event-by-event cosmic ray primary mass identification,” *Citeseer*, Jan 2007.
- [121] A. D. Supanitsky and G. Medina-Tanco, “Effect of multiple reusing of simulated air showers in detector simulations,” *Astroparticle Physics*, vol. 30, p. 264, Dec 2008.
- [122] P. Berghaus, “Ic40 energy estimators.” IceCube Internal Wiki.
- [123] J. Ochab, “Test of shower reconstruction procedures with the IceTop-a, IceTop-b subarrays.” IceCube internally distributed report, Sep 2007.

- [124] J. Madsen *et al.*, “IceTop: The surface component of IceCube.” IceCube internally distributed report, 2009.
- [125] F. James, “Interpretation of errors.” CERN internal circulation, 2004.
- [126] H. Stephens, *Electron Temperature Structures Associated With Magnetic Tearing Modes in the Madison Symmetric Torus*. PhD thesis, University of Wisconsin-Madison, 2010.
- [127] D. Ruck, S. Rogers, and M. Kabrisky, “Feature selection using a multilayer perceptron,” *Journal of Neural Network Computing*, Jan 1990.
- [128] R. Scrimaglio *et al.*, “Analysis of sileye-3/alteino data with a neural network technique: Particle discrimination and energy reconstruction,” *Advances in Space*, Jan 2006.
- [129] J. Ridky and P. Travnicek, “Cosmic multi-muon bundles detected by DELPHI,” *Nuclear Physics B Proceedings Supplements*, vol. 122, p. 285, Jul 2003.
- [130] J. Hörandel, “On the knee in the energy spectrum of cosmic rays,” *American Physical Society*, p. 3002, Apr 2002.
- [131] T. Antoni *et al.*, “Preparation of enriched cosmic ray mass groups with cascade,” *Astroparticle Physics*, vol. 19, p. 715, Sep 2003.
- [132] M. Gardner and S. R. Dorling, “Artificial neural networks (the multilayer perceptron)—a review of applications in the atmospheric sciences,” *Atmospheric Environment*, Jan 1998.
- [133] M. Richard and R. Lippmann, “Neural network classifiers estimate bayesian a posteriori probabilities,” *Neural computation*, Jan 1991.
- [134] M. B. Amelchakov *et al.*, “Muon bundles produced by uhe cosmic rays at large zenith angles,” *Physics of Atomic Nuclei*, vol. 70, p. 175, Jan 2007.
- [135] S. Bussino and S. M. Mari, “Gamma-hadron discrimination in extensive air showers using a neural network,” *Astroparticle Physics*, vol. 15, p. 65, Mar 2001.

- [136] A. K. O. Tiba, G. A. Medina-Tanco, and S. J. Sciutto, “Neural networks as a composition diagnostic for ultra-high energy cosmic rays,” *eprint arXiv*, p. 2255, Feb 2005.
- [137] A. D. Supanitsky, G. Medina-Tanco, and A. Etchegoyen, “On the possibility of primary identification of individual cosmic ray showers,” *Astroparticle Physics*, vol. 31, p. 116, Mar 2009.
- [138] T. Antoni *et al.*, “A non-parametric approach to infer the energy spectrum and the mass composition of cosmic rays,” *Astroparticle Physics*, vol. 16, p. 245, Jan 2002.
- [139] R. Glasstetter, “Analysis of electron and muon size spectra of EAS,” *Proceedings of the 26th International Cosmic Ray Conference. August 17-25*, vol. 1, p. 222, Jan 1999.
- [140] M. Ambrosio *et al.*, “Comparison between methods for the determination of the primary cosmic ray mass composition from the longitudinal profile of atmospheric cascades,” *Astroparticle Physics*, vol. 24, p. 355, Dec 2005.
- [141] A. Jain, J. Mao, and K. Mohiuddin, “Artificial neural networks: A tutorial,” *Computer*, Jan 1996.
- [142] F. Halzen and A. D. Martin, *Quarks and leptons: an introductory course in modern particle physics*. Wiley (New York), Jan 1984.
- [143] A. Krogh, “What are artificial neural networks?,” *Nature biotechnology*, Jan 2008.